Kinematic study of the molecular environment in the early phases of massive star formation

Ammonia observations and modeling

Juan Manuel Mayén Gijón
Oct 2015

Advisor
Guillem Anglada Pons
Instituto de Astrofísica de Andalucía (CSIC)

Universidad de Granada
Programa de doctorado en Física y Matemáticas

Editor: Universidad de Granada. Tesis Doctorales
Autor: Juan Manuel Mayén Gijón
ISBN: 978-84-9125-298-6
URI: http://hdl.handle.net/10481/42788

El doctorando Juan Manuel Mayén Gijón y el director de la tesis Guillem Anglada Pons garantizamos, al firmar esta tesis doctoral, que el trabajo ha sido realizado por el doctorando bajo la dirección de los directores de la tesis y hasta donde nuestro conocimiento alcanza, en la realización del trabajo, se han respetado los derechos de otros autores a ser citados, cuando se han utilizado sus resultados o publicaciones.

Granada, 13 de Octubre de 2015.

Director de la Tesis	Doctorando
Dr.Guillem Anglada Pons	Dn. Juan Manuel Mayén Gijón

Se lo dedico a mi familia

Agradecimientos

Quiero dar un agradecimiento especial a mi esposa, por su comprensión, por sus ánimos y por acompañarme en todo momento.

Quiero, también, agradecer especialmente a mi padre, a mi madre y a mi hermano por su paciencia y por el soporte que me han proporcionado.

Gracias a mis amigos por aguantarme en estos años duros.

Gracias a Luis Felipe por adoptarme en Morelia como su estudiante y por su sabiduría.

Gracias a Charly por enseñarmelo casi todo.

Gracias a todos los que fueron mis compañeros de despacho por saber escucharme.

Gracias a José Francisco por sus buenos consejos y su inestimable ayuda en la redacción.

Gracias a Susana por su ayuda en las partes más teóricas y por su interés.

Gracias a Robert por acogerme en Barcelona.

Gracias a Mayra por su insistencia,

y gracias a Guillem por sus lecciones y por darme la oportunidad de doctorarme.

Resumen

Las estrellas se forman a partir del colapso de fragmentos de nubes interestelares de gas molecular. Para entender los procesos físicos que dominan durante las primeras etapas de la formación estelar se requiere un conocimiento detallado de la cinemática de la envolvente de gas y polvo que rodea a la (proto)estrella naciente durante su formación. Sin embargo, el estudio de la cinemática de dicha envolvente es especialmente difícil ya que tanto los movimientos de rotación como los de colapso y de expansión están presentes en las primeras etapas de la formación estelar, y todos ellos pueden presentar características observacionales similares, lo que hace que sea difícil identificarlos correctamente. Esta situación es aún más problemática cuando consideramos la formación de estrellas de alta masa. Esto es debido a que la estrellas de alta masa se encuentran a mayores distancias que las de baja masa y suelen encontrarse formando grupos, lo que hace que el riesgo de confusión sea mayor y que se requiera para su estudio una mejor resolución angular. Además, al encontrarse agrupadas, las interacciones entre ellas son más frecuentes que en el caso de baja masa, dificultando la interpretación de los datos. Puesto que las estrellas muy jóvenes aparecen obscurecidas por el polvo que las rodea, no pueden ser estudiadas en el longitudes de onda ópticas. Por todo ello, resulta conveniente contar con improntas características de cada tipo de movimiento que sean observables en longitudes de onda radio y que nos permitan identificar dichos movimientos con la menor ambigüedad posible.

En esta tesis hemos abordado el estudio de la cinemática de las envolventes en colapso de gas y polvo, tanto teóricamente como observacionalmente. En una primera parte teórica, hemos propuesto nuevos rasgos observacionales que pueden servir para identificar los movimientos de colapso y de colapso con rotación. Además, hemos estudiado cómo se modifican dichos rasgos cinemáticos característicos de acuerdo con los diferentes modelos de colapso existentes en la literatura. Nos hemos centrado especialmente en poder distinguir entre aquellos modelos de colapso que parten de condiciones iniciales de equilibrio y aquellos que parten de condiciones iniciales fuera del equilibrio. En una segunda parte de la tesis, mediante observaciones de la emisión de la molécula de amoniaco, hemos estudiado la cinemática de dos “núcleos moleculares calientes” (NMC). La fase de NMC se considera una de las primeras etapas de la formación de estrellas de alta masa, en la cual la estrella se encuentra aún profundamente inmersa en su nube parental. Nuestra intención es, además de estudiar en detalle las propiedades físicas de cada NMC, comprobar si los rasgos característicos obtenidos teóricamente en la primera parte de la tesis se pueden identificar observacionalmente en dichos NMCs. Y cuando no sea así, construir un nuevo modelo que explique las características observadas del NMC.

Rasgos característicos fundamentales de colapso protoestelar

Para el estudio de los rasgos característicos cinemáticos de colapso a partir de los modelos nos hemos basado, especialmente, en el trabajo de Anglada et al. (1991) (en adelante A91). En una condensación que está colapsando para formar una estrella central, definiendo como superficie de isovelocidad a la superficie que forman aquellos puntos de la condensación que tienen la misma componente de velocidad proyectada a lo largo de la línea de visión, A91 muestran que, las superficies de isovelocidad para el modelo de colapso esférico de Larson (1972), cuyo campo de velocidades se comporta como el de caída libre, son superficies cerradas, y están anidadas unas dentro de otras, siendo las de mayor velocidad las más internas, y por lo tanto las más pequeñas. En el caso de una transición molecular ópticamente gruesa, las superficies de isovelocidad cerradas producen mapas de intensidad de línea bien diferenciados entre pares de velocidades simétricamente corridas al rojo y al azul. Por el contrario, las superficies de isovelocidad abiertas presentan mapas de intensidad similares para pares de velocidades simétricamente corridos al rojo y al azul. Para el caso de una envolvente en colapso angularmente resuelta y que se encuentra en la fase de acreción (cuando la protoestrella ya se ha formado), A91 deducen que, para una transición molecular ópticamente gruesa, en los mapas de intensidad de línea a velocidades corridas al azul respecto a la velocidad sistémica de la condensación, la intensidad aumenta abruptamente hacia el centro de la condensación, mientras que, a velocidades corridas al rojo, la distribución de intensidad permanece prácticamente constante. Además, la extensión de la emisión decrece conforme la velocidad se aleja de la velocidad sistémica de la nube. Dicha asimetría fue sugerida como un sello característico de colapso y su potencial deriva de que posee información tanto espacial como espectral.

El sello característico de colapso propuesto por A91, originalmente, se obtuvo adoptando el campo de velocidades que el modelo numérico de colapso de Larson (1972) predecía en las regiones más internas de la condensación. Sin embargo, dicho campo de velocidades no reproduce el comportamiento del campo de velocidades a grandes distancias. En esta tesis hemos recopilado algunos de los modelos de colapso más usados en la literatura, hemos obtenido sus campos de velocidades (y de densidad) a partir de sus desarrollos en variables autosimilares y hemos estudiado como varía el sello característico de colapso propuesto por A91 al cambiar el campo de velocidades. En definitiva, hemos realizado el análisis acerca de cómo varía la intensidad de las transiciones moleculares ópticamente gruesas en función de la distancia al centro de la condensación, a diferentes velocidades, siguiendo, entre otros, el formalismo de A91. Además, hemos ampliado el estudio del sello característico de colapso propuesto por A91 a modelos que describen el colapso durante la etapa pre-estelar, es decir, antes de la formación de la (proto)estrella.

En lo que respecta a los modelos de la etapa pre-estelar, el modelo de colapso de una esfera de Bonnor-Ebert (BE) (Bonnor 1956, Ebert 1957) parte de una condición inicial de equilibrio y presenta superficies de isovelocidad cerradas. Por otro lado, el modelo LP (Larson 1969, Penston 1969) tiene como condición inicial una configuración fuera de equilibrio y presenta todas sus superficies de isovelocidad abiertas. Durante esta etapa pre-estelar, debido a la ausencia de una fuente de calentamiento interno, y debido al calentamiento externo de los rayos cósmicos, la temperatura decrece hacia el interior de la condensación. En el caso del colapso de una esfera de BE esto hace que los perfiles radiales de intensidad de los canales de velocidades corridas al azul tengan un mínimo de intensidad en la posición central (suponiendo que la emisión está termalizada), mientras que los perfiles en los canales de velocidades corridas al rojo permanecen prácticamente planos. Al integrar sobre toda la condensación, la emisión corrida al rojo resulta ser más intensa que la corrida al azul. Por tanto, los perfiles de las líneas espectrales serán asimétricos, con la parte roja más intensa que la azul. Esto es importante puesto que, comúnmente, se suele usar como identificador de colapso la detección de una mayor intensidad en el lado azul del perfil de línea espectral. Sin embargo, nuestro estudio revela que en la fase pre-estelar, una envolvente en colapso tendría el lado rojo más intenso. En el caso de colapso según el modelo LP, la intensidad, tanto a velocidades corridas al azul como al rojo, muestra un leve decrecimiento hacia el centro de la condensación.

Durante la etapa de acreción, los modelos isotermos de colapso con condiciones iniciales de equilibrio como el SIS (Singular Isothermal Sphere; Shu 1977, Shu et al. 1987) o el SLS (Singular Logatropic Sphere; McLaughlin & Pudritz 1996, 1997) predicen la existencia de regiones estáticas en las zonas más externas de la nube. Sin embargo, los modelos isotermos con condiciones iniciales fuera del equilibrio, como el LPH (Larson 1969, Penston 1969, Hunter 1977) y el "colapso rápido" (Mac Low & Klessen 2004), predicen velocidades radiales supersónicas a grandes distancias del centro de la nube. En las zonas más cercanas a la (proto)estrella, donde se alcanzan las mayores velocidades, ambos tipos de modelos predicen un campo de velocidades similar al de caída libre.

Para obtener los mapas de intensidad de línea como función de la velocidad utilizamos una aproximación que consiste en obtener la estructura dinámica a partir de los modelos isotérmicos de colapso, mientras que la estructura térmica se fija separadamente con una cierta base empírica. Esta aproximación es similar a la utilizada por Zhou et al. (1993b) y Gao et al. (2009). La distribución de temperatura dentro de la condensación vendría determinada por el calentamiento interno debido a la acreción y la radiación estelar. En este trabajo se ha utilizado un campo de temperatura similar al que predice el modelo de Larson (1972), $T \propto r^{-1/2}$.

Si consideramos solo la emisión de mayor velocidad (relativa a la sistémica), todos los modelos predicen la presencia del sello de colapso propuesto por A91, tanto aquellos con condiciones iniciales en equilibrio como los de condiciones iniciales fuera de equilibrio. Sin embargo, sí existen discrepancias entre los modelos que describen un colapso que se inicia desde el equilibrio y los que describen un colapso que nunca pasa por una situación de equilibrio. Los campos de velocidades con valores a grandes radios diferentes de cero (como los de los modelos con condiciones iniciales fuera de equilibrio), producen para esas velocidades superficies de isovelocidad abiertas, mientras que aquellos campos de velocidad que predicen la existencia de una región externa estática (como los de modelos con condiciones iniciales de equilibrio) tienen todas sus superficies de isovelocidad cerradas. Esto implica que, a velocidades bajas respecto de la velocidad sistémica de la condensación, los modelos con condiciones iniciales de equilibrio predicen la existencia del sello característico de colapso propuesto por A91, que consiste en que los perfile radiales de intensidad (intensidad en función de la distancia proyectada al centro) son distintos para las velocidades corridas al rojo y al azul. Por el contrario, los modelos con condiciones inciales fuera de equilibrio predicen que, a velocidades bajas, los perfiles radiales de intensidad a velocidades corridas al rojo y al azul serían parecidos.

Esto parecería indicar que según se detecte observacionalmente o no el sello característico de colapso propuesto por A91 a bajas velocidades podríamos conocer si las condiciones iniciales del colapso eran o no de equilibrio. Sin embargo, puede suceder que el tamaño de las superficies de isovelocidad cerradas más extensas (las cuales corresponden a las de menor velocidad) sea mayor que el tamaño de la región emisora. En este caso, dichas superficies de isovelocidad estarían incompletas y, por lo tanto, a efectos prácticos se comportarían como superficies abiertas, perdiendo así la capacidad de producir las diferencias en los perfiles radiales de intensidad de los canales de velocidad de signo opuesto. Por lo tanto, ambos tipos de modelos, de equilibrio y fuera de equilibrio, producirían perfiles radiales de intensidad similares. En conclusión, si la asimetría en los perfiles radiales de intensidad se pierde a bajas velocidades, entonces, no podremos discernir entre modelos con condiciones iniciales de equilibrio o fuera de equilibrio, pero si, por el contrario, se observasen las asimetrías de A91 a bajas velocidades, entonces, tales evidencias parecerían apuntar a un modelo de colapso en el cual exista una zona externa estática, como la que predicen los modelos con condiciones iniciales de equilibrio.

Sin embargo, el modelo de colapso LPH, con condiciones iniciales fuera de equilibrio, en su generalización politrópica y para ciertos valores de su constante politrópica γ, predice que todas sus superficies de isovelocidad son cerradas, por lo que, aún siendo un modelo de colapso con condiciones iniciales fuera de equilibrio, se comportaría igual que los modelos de colapso que predicen condiciones iniciales de equilibrio. Al contrario que el modelo LPH, el modelo de colapso denominado “colapso rápido”, el cual explica la formación estelar a partir de flujos de gas supersónicos que chocan entre sí estocásticamente, dada su propia formulación, no puede nunca producir superficies cerradas a bajas velocidades y, por lo tanto, no puede presentar la asimetría de A91 a velocidades pequeñas. Así pues, si en una región se observaran las asimetrías de A91 a bajas velocidades indicaría que podríamos descartar el modelo de “colapso rápido” de entre los posibles escenarios de formación estelar pero, en general, no podríamos descartar unas condiciones iniciales de colapso fuera del equilibrio.

Con un código de transporte radiativo propio se calcularon los perfiles radiales de intensidad que predice cada modelo de colapso. Los resultados obtenidos de esta modo confirman los obtenidos a partir del formalismo aproximado de A91. El análisis indica que todos los modelos predicen el sello característico de colapso propuesto por A91 si se consideran velocidades al azul y al rojo relativamente altas. Por lo tanto, concluimos que el sello característico de colapso propuesto por A91 es robusto y que se puede generalizar a un amplio rango de modelos de colapso.

Rasgos adicionales característicos de colapso y de colapso con rotación

Basándonos en el resultado de que el sello característico de colapso propuesto por A91 es robusto, proponemos una nueva impronta cinemática derivada directamente de él. Este nuevo rasgo característico de colapso consiste en el predominio de la emisión corrida al azul hacia el centro de la condensación en los mapas de velocidad promedio (momento de orden 1). Por su apariencia, denominamos a dicha impronta "mancha azul central" y su principal ventaja frente al sello característico de colapso propuesto por A91 es su fácil identificación.

Tanto la predicción del sello de colapso propuesto por A91, como la "mancha azul central" se obtienen a partir de modelos de colapso esféricos. Sin embargo, el colapso de una condensación de gas molecular, en realidad, no ocurre radialmente sino que, debido a que la condensación tiene cierto momento angular, las fuerzas centrífugas asociadas a dicho momento angular hacen que el gas caiga sobre un disco de acreción en rotación en lugar de hacerlo directamente sobre la estrella. Dicho disco puede incluso estar soportado centrífugamente. Mediante mecanismos de expulsión de materia en forma bipolar a lo largo del eje de rotación se consigue que una fracción del momento angular se redistribuya hacia el exterior permitiendo a la estrella continuar creciendo en masa. Hemos utilizado el modelo de colapso desarrollado por Terebey, Shu y Cassen (1984) (TSC), que incluye en su formulación la rotación de la envolvente de gas y polvo, para, basándonos en la metodología de A91, calcular los perfiles radiales de intensidad en función de la velocidad en condiciones de alta opacidad. Nuestra intención era comprobar como se modifican los rasgos característicos de colapso esférico (en particular los propuestos por A91 y la "mancha azul central") en presencia de rotación. Encontramos que la rotación no enmascara el rasgo característico de colapso propuesto por A91, sino que lo modifica haciendo que los perfiles radiales de intensidad pierdan su simetría axial. Los perfiles radiales de intensidad correspondientes a velocidades corridas al azul se estiran en la mitad de la condensación donde la rotación tiende a acercar el material al observador, mientras que se encogen en la mitad opuesta, donde la rotación tiende a alejar el material. Lo contrario sucede con los perfiles radiales de intensidad correspondientes a velocidades corridas al rojo. Pero, tal y como sucedía en el caso sin rotación, los perfiles de velocidades corridas al azul continúan siendo intensos y picudos hacia el centro de la condensación, y los corridos al rojo continuan siendo prácticamente planos, por lo que el sello característico de colapso no se pierde en presencia de rotación. El colapso y la rotación pueden identificarse de modo independiente.

Nuestro estudio también indica que la rotación produce mapas de intensidad integrada que no están centrados en el centro geométrico de la condensación, sino que el máximo de emisión está desplazado hacia la mitad de la condensación donde la rotación tiende a acercar el material al observador. También obtenemos como resultado que, en el mapa de velocidad promedio, la rotación aumenta el corrimiento al azul de la "mancha azul central" respecto del caso sin rotación, y que la desplaza del centro de la condensación hacia la mitad de la condensación donde la rotación tiende a acercar el material al observador. Además, acompañando a la "mancha azul" en este mapa de velocidad promedio, aparece una "mancha roja" secundaria menos prominente que la azul. Ambas "manchas" están situadas simétricamente respecto del centro de la condensación. De acuerdo con nuestros resultados, estas características se mantienen para inclinaciones del eje de rotación intermedias entre el plano del cielo y la línea de visión, e incluso en presencia de flujos bipolares de alta velocidad. Proponemos que estos efectos producidos por la rotación superpuesta al colapso, como son el desplazamiento del máximo de emisión y de la "mancha azul" con respecto al centro de la condensación, y/o la orientación del par de manchas "azul y roja" en el mapa de velocidad promedio, pueden ser utilizados como improntas para determinar la orientación del plano ecuatorial, y en consecuencua la del eje de rotación. La orientación derivada de estas improntas probablemente es más fiable que la que se deriva de los gradientes de velocidad a gran escala que pueden resultar de la combinación de varios tipos adicionales de movimiento (flujos bipolares, precesión del eje de rotación, influencias externas a la envolvente, etc).

Detección de los rasgos característicos de colapso en el núcleo molecular caliente G31 HMC

En la segunda parte de la tesis estudiamos dos NMCs, prestando especial atención a su cinemática. Los NMCs son condensaciónes de gas denso y caliente que supuestamente contienen una protoestrella masiva en su interior. El primer NMC que estudiamos se encuentra en las proximidades de la región HII conocida como G31.41+0.31, a 7.9 kpc de distancia de la Tierra. Para su estudio realizamos observaciones de la molécula de amoniaco con el interferómetro Expanded Very Large Array (EVLA). Obtuvimos los perfiles radiales de intensidad para los diferentes canales de velocidad, para las transiciones de inversión de la molécula de amoniaco (2,2), (3,3), (4,4), (5,5) y (6,6). Encontramos que todas ellas presentan evidencia del sello característico de colapso porpuesto por A91. Es decir, dado un par de canales con velocidades simétricas respecto de la velocidad sistémica del NMC, en el canal con velocidad corrida al azul la intensidad como función de la distancia proyectada al centro del NMC crece abruptamente hacia el centro, mientras que la emisión en el canal con velocidad corrida al rojo muestra una distribución de intensidad mucho más uniforme en la región emisora. Además, el tamaño de la región emisora disminuye al aumentar la velocidad, indicando aceleración hacia el centro. En los mapas de velocidad promedio encontramos que la región donde se produce el máximo de emisión integrada presenta una velocidad promedio más azul que su entorno. Interpretamos estos resultados como la detección del sello de colapso propuesto por A91 y de la "mancha azul central", respectivamente. Dicha detección constituye la primera detección observacional de estos rasgos característicos de colapso. Estos rasgos son de difícil confusión con los de otros tipos de movimientos sistemáticos que no sean colapso, por lo que su presencia parecería indicar que los movimientos de colapso están jugando un papel fundamental en la cinemática del gas que conforma el NMC.

Osorio et al. (2009) desarrollaron un modelo de colapso esférico que lograba reproducir la distribución espectral de energía, así como los espectros de la transición de inversión (4,4) del amoniaco observados en G31 HMC. A partir de este modelo hemos calculado los perfiles radiales de intensidad esperados para diferentes canales y transiciones, y los hemos comparado con los observados. Obtenemos que los perfiles observados y teóricos son parecidos, tanto en forma como en valores, lo cual apoya la tesis de que el colapso es el movimiento dominante en la envolvente de G31 HMC. El parecido entre las predicciones del modelo y las observaciones en todas las transiciones es un resultado a destacar puesto que el ajuste del modelo solo se realizó usando la distribución espectral de energía (SED) en el continuo debido al polvo y los espectros de la transición (4,4) del amoniaco.

A pesar de que el colapso sea dominante en la región G31 HMC, se observa un gradiente de velocidad en dirección noreste-suroeste (emisión al azul al suroeste y emisión al rojo al noreste) en todas las transiciones del amoniaco estudiadas aquí. La orientación de dicho gradiente coincide con la del observado por otros autores en otras líneas moleculares. La razón de dicho gradiente ha sido y es un tema de debate, de modo que unos autores defienden que es debido a un flujo molecular bipolar, mientras que otros piensan que es producido por rotación. Hemos estudiado los perfiles radiales de intensidad observados calculando por separado el promedio de la emisión en función de la distancia al centro en la mitad noreste y en la mitad suroeste. Encontramos que en los canales con velocidades corridas al azul la emision se hace más extensa hacia la parte suroeste y se encoge hacia la mitad noreste, mientras que en los perfiles radiales de intensidad de los canales con velocidades corridas al rojo sucede lo contrario. Este comportamiento es compatible con la presencia de rotación según los resultados teóricos predichos en la primera parte de la tesis.

Encontramos, además, diferentes indicadores que sugieren que el eje de rotación se encuentra en dirección este-oeste, como son: el hecho de que la "mancha azul" y el máximo de intensidad integrada de las diferentes transiciones de amoniaco aparezcan sistemáticamente al sur de las dos radiofuentes de continuo (que tomamos como el centro del NMC); el hecho de que, en los mapas de velocidad promedio obtenidos con las líneas satélites (las cuales se espera que tracen mejor la parte más interna del NMC, precisamente donde la rotación puede adquirir más importancia) haya indicios de la presencia de la "mancha roja compañera" al norte de las radiofuentes; y el hecho de que el máximo gradiente de velocidad en el entorno del centro del NMC tenga una dirección norte-sur. La combinación de un movimiento de rotación norte-sur y del flujo bipolar este-oeste, revelado por un reanálisis que hemos realizado de la emisión de la molécula de CO, produciría un gradiente a gran escala noreste-suroeste similar al observado. Por ello, proponemos que G31 HMC es una estructura dominada por el colapso radial hacia el centro pero que presenta además un movimiento de rotación y un flujo molecular bipolar cuyo eje está en dirección este-oeste.

Estudio cinemático del núcleo molecular caliente W3(H_2O)

El segundo NMC que estudiamos se denomina W3(H_2O), y está en la proximidad de la región HII ultracompacta W3(OH), situada a 2 kpc de distancia de la Tierra. En el NMC hay dos radiofuentes de continuo centimétrico separadas entre sí aproximadamente $1''$ ($\sim$ 2000 UA) en dirección este-oeste. La fuente situada más al este tiene un índice espectral negativo, está alargada en direción este-oeste y se ha venido interpretando como un jet de emisión sincrotrón. La fuente situada más al oeste se ha interpretado como otro objeto protoestelar. Estas dos fuentes parecerían estar asociadas respectivamente con dos condensaciones de polvo observadas a longitudes de onda submilimétricas. Nuestras observaciones de la transición de inversión (4,4) de la molécula de amoniaco, realizadas con el VLA, muestran que la emisión de amoniaco procede de dos condensaciones, W3(H_2O)-E y W3(H_2O)-W, que parecen estar asociadas con las condensaciones de polvo observadas en el submilimétrico. Los mapas de intensidad integrada de la emisión de NH_3(4,4) muestran que tanto W3(H_2O)-E como W3(H_2O)-W presentan un doble pico de emisión. En el caso de W3(H_2O)-E los dos picos se encuentran a ambos lados del máximo de emisión submilimétrica, mientras en el caso de W3(H_2O)-W los dos picos se encuentran a ambos lados de la fuente de radiocontinuo centrimétrica. En ambas condensaciones, el doble pico de emisión de amoniaco se observa en los mapas de intensidad integrada tanto de la línea principal como de las satélites, pero la orientación de la estructura de doble pico en uno y otro mapa no coincide. Los mapas de velocidad media presentan gradientes de velocidad complejos, existiendo diferencias de velocidad entre las dos condensaciones (W3(H_2O)-E y W3(H_2O)-W) y entre los dos picos de emisión dentro de cada condensación, así como gradientes de velocidad en torno a cada pico de emisión. Dichas características observacionales no siguen los patrones simples de rotación o expansión, pero tampoco siguen el patrón de colapso, ni el de colapso con rotación que se estudiaron en la primera parte de la tesis.

Nuestra interpretación de los campos de velocidad y de la morfología de la emisión observada en los mapas de intensidad integrada requiere que, el amoniaco, tanto en la condensación W3(H_2O)-E como en W3(H_2O)-W, esté distribuido formando estructuras toroidales en rotación y en colapso. Para probar dicha hipótesis, modelamos las condensaciones W3(H_2O)-E y W3(H_2O)-W como envolventes aplanadas de gas molecular utilizando los modelos de colapso con rotación TSC (Terebey, Shu y Cassen 1984) y "colapso en láminas" ("sheet collapse", Hartmann et al. 1994, 1996), a los cuales les imponemos una condición de abundancia del amoniaco nula en la parte más interna de la envolvente, para así imitar el agujero interno de un toroide. La inclusión de un "agujero" o vacío de amoniaco en la parte central diferencia a este modelo respecto de los estudiados en la primera parte de la tesis. Nuestro modelo es capaz de reproducir las SEDs, los espectros observados de la transición (4,4) de amoniaco, los mapas de velocidad media, la morfología de doble pico de emisión en los mapas de intensidad integrada, e incluso el cambio de orientación de la estructura de doble pico entre los mapas de la línea principal y los de las satélites, producido por la diferencia de opacidad. El mejor ajuste del modelo predice valores de la masa de las protoestrellas de 2.2 y 6 $M_\odot$, tasas de masa en colapso de 7.4×10^{-3} $M_\odot$ año^{-1} y 9.8×10^{-3} $M_\odot$ año^{-1}, y masas de las envolventes de 20 $M_\odot$ y 16 $M_\odot$, para las condensaciones W3(H_2O)-E y W3(H_2O)-W respectivamente. Mientras que los valores obtenidos para la masa de las protoestrellas son típicos de estrellas de masa intermedia, los valores de las tasas de masa en colapso son altos y son más característicos de las estrellas de alta masa. Nuestra interpretación de dichos resultados es que estamos observando dos estrellas que llegarán a ser masivas, pero que todavía se encuentran en una etapa temprana de su proceso de formación, de modo que aún no han adquirido de las envolventes que las rodean toda su masa final.

Las dos envolventes modeladas resultan tener sus ejes de rotación coincidentes con los ejes de dos flujos bipolares muy colimados, con ángulos de posición PA=$-140°$ y PA=$15°$, observados en CO (Zapata et al. 2011), que parecen originarse en W3(H_2O)-E y W3(H_2O)-W respectivamente. Nuestro modelo es, además, capaz de predecir el signo de la velocidad (rojo o azul) de los lóbulos del flujo bipolar que sería eyectado en la dirección del eje de rotación de cada una de las envolventes modeladas. La predicción de nuestro modelo para los casos de W3(H_2O)-E y W3(H_2O)-W coincide con la distribución observada de los lóbulos rojo y azul de los dos flujos bipolares presentes en la región.

También predecimos que al menos dos objetos estelares jóvenes están presentes en la condensación W3(H_2O)-E, puesto que concluimos que la fuente excitadora del jet sincrotrón no puede ser la misma que la excitadora del flujo molecular bipolar que se origina en W3(H_2O)-E (PA=$-140°$). Para llegar a esta conclusión nos basamos en que el origen del jet se encuentra fuera de la estructura trazada por el amoniaco, y en que la dirección del jet no coincide con la dirección del flujo bipolar de CO, cuyo eje coincide con el eje de rotación de la estructura trazada por el amoniaco. Por lo tanto, además de la fuente excitadora del radiojet, debe existir un segundo objeto joven, asociado con la mayor parte de la emisión submilimetrica observada, que se encontraría en el centro de la estructura de amoniaco y sería la fuente excitadora del flujo bipolar de CO.

Nuestros modelos, además, ponen de manifiesto que la morfología de la emisión observada en los mapas de intensidad integrada depende de la profundidad óptica y no tiene por qué reflejar directamente la verdadera orientación de la estructura de densidad donde se origina dicha emisión. También concluimos que, en presencia de gradientes de velocidad, densidad y temperatura, se requieren modelos detallados para estimar de modo confiable las masas de las envolventes y de sus correspondientes protoestrellas centrales.

Conclusiones

En resumen, hemos sido capaces de predecir nuevos rasgos característicos de la cinemática de colapso y de colapso con rotación detectables en las imágenes de la emisión molecular. Hemos analizado cuál sería la influencia esperada de los diferentes modelos de colapso en el resultado de las observaciones. Hemos encontrado que, en general, el sello característico de colapso propuesto por A91 es robusto y se puede generalizar a un amplio rango de modelos, si se consideran velocidades (relativas a la sistémica) suficientemente altas. Hemos prestando especial atención a si era posible distinguir entre aquellos modelos de colapso que parten de condiciones iniciales de equilibrio y aquellos que parten de condiciones iniciales fuera del equilibrio. De este modo, hemos encontrado un posible procedimiento para descartar eventualmente, a través del estudio de los perfiles radiales de intensidad observados a bajas velocidades (relativas a la velocidad sistémica), el modelo de “colapso rápido” como posible proceso de formación estelar.

Hemos encontrado, por primera vez, evidencia observacional de los rasgos característicos de

colapso y de colapso con rotación en las imagenes de alta resolución angular del NMC en la región de G31.41+0.31. Hemos caracterizado las propiedades físicas de dicho NMC, y propuesto una solución al debate sobre su gradiente de velocidad a gran escala, que nosotros interpretamos como combinación de rotación y flujo bipolar. Así mismo, hemos caracterizado las propiedades físicas del NMC W3(H_2O), el cual hemos modelado satisfactoriamente como dos estructuras de gas y polvo en rotación y colapso, separadas entre sí ~2000 UA. Ambas deben tener una parte central donde el amoniaco está ausente, característica que no se precisaba en el estudio/modelaje del NMC en G31.41+0.31.

Contents

Chapter 1

Star formation

Stars form as a result of fragmentation and gravitational collapse of large interstellar clouds. The main components of these interstellar clouds are molecular gas ($\sim$ 99% of the mass) and dust ($\sim$ 1% of the mass). These clouds have been called “dark clouds” due to the high extinction at optical wavelengths produced by the presence of dust. Nowadays, they are commonly designated as “molecular clouds” because molecular hydrogen is the main component. According to Bergin & Tafalla (2007) typical molecular clouds have masses of $\sim 10^3 - 10^4$ $M_\odot$, sizes of $\sim$ 2-15 pc, and mean densities of $50 - 500$ cm^{-3}. These clouds have a hierarchical structure with smaller subunits called clumps and cores. Clumps have typical masses of $\sim 50 - 500$ $M_\odot$, sizes of $\sim 0.3 - 3$ pc, and mean densities of $\sim 10^3 - 10^4$ cm^{-3}, while cores have typical masses of $\sim 0.5 - 5$ $M_\odot$, sizes of $\sim 0.03 - 0.2$ pc, and mean densities of $\sim 10^4 - 10^5$ cm^{-3}. Temperatures are extremely low, with typical values in the range $10 - 20$ K. Williams et al. (2000) define a star-forming clump as a massive region of molecular gas out of which a star cluster is forming; and a core as a region of molecular gas that will form a single star (or multiple- star system such as a binary). However, the process leading to the formation of cores and clumps from the parental molecular cloud is not yet well understood, and is one of the most important challenges in the field of star formation.

Observationally, the star formation process is best studied at long wavelengths (radio and infrared), which are less affected by dust obscuration. Thus, physical properties of the protostellar environment can be studied through the dust emission at radio and infrared wavelengths while the kinematics and other physical properties can be studied through molecular transitions, mainly at radio wavelengths. To form a star, the cloud must be compressed by about 7 orders of magnitude in size, temperature would increase by about 6 orders of magnitude and the density by about 20 orders of magnitude. Thus, star formation is a very complex process and a challenging subject of study.

One of the outstanding properties of the star formation process is that, because of the initial rotation of the core, matter does not fall directly onto the central (proto)star but through a rotating circumstellar disk (accretion disk) that is developed in the equatorial plane at scales of $\sim$ 100 AU. A fraction of the infalling matter is ejected in the polar direction, in the form of a collimated bipolar outflow (or a jet) that removes the excess of mass and angular momentum, and allows the formation of the star. In its turn, a planetary system can be formed as a result of the evolution of the accretion disk.

1.1 The agents counteracting gravitational collapse in the interstellar molecular clouds

In order the collapse to occur and ensue star formation, gravity must overcome the support of thermal pressure, magnetic forces, internal turbulence and rotation. All of them act to prevent, suppress or slowdown the core collapse. The degree of support and the role of the different opposing forces in the star formation process is a matter of current debate.

- **Thermal pressure:** In the simplest case of gravity versus gas pressure, one can define the "Jeans mass", which can be understood as the minimum mass needed for cloud fragmentation. For a given radius and temperature, a cloud is stable for a sufficiently small mass but once the critical mass is exceeded, it will begin a process of runaway contraction until some other force could impede the collapse. The physical basis of the Jeans instability can be easily understood in terms of time-scales. In the absence of a pressure gradient, the collapse of a uniform sphere of gas occurs in the free-fall time $t_{ff} = (3\pi/32G\rho)^{1/2}$, defined as the time required for a core to collapse to infinite density from a state of rest (Spitzer 1978), and where ρ is the density. On the other hand, one can define the sound-crossing time as:

  $$t_s = r_{cl}/c_s = r_{cl}\ (\mu m_H/k_b T)^{1/2}\ , \tag{1.1}$$

  where T is the temperature, k_b is the Boltzmann constant, r_{cl} is the cloud radius, c_s is the sound speed, μ is the mean molecular weight, m_H is the mass of the hydrogen atom. If the sound-crossing time is less than the free-fall time, any density perturbation is smoothed away by pressure waves, but when the free-fall time is less than the sound-crossing time, gravity wins pressure forces, and the region undergoes gravitational collapse. Considering the critical distance where t_s equals t_{ff}, one obtains a critical perturbation length, $\lambda_{crit} = (3\pi c_s^2/32G\rho)^{1/2}$. Assuming that such a critical distance has the same value in the three spatial dimensions, we can estimate a corresponding minimum mass for which gravity can become dominant by setting $M_{crit} = \rho\lambda_{crit}^3$, where ρ is the density which is assumed constant. This critical mass was first studied by Jeans (1902, 1928) and is normally called the "Jeans mass". The original works of Jeans (1902, 1928) studied the growth of plane-wave density perturbations in an infinite uniform medium that has a finite pressure but has not rotation, nor magnetic fields, nor turbulence. Later on, further calculations of the critical mass adding rotation, magnetic fields, or using different geometries were carried out (Chandrasekhar & Fermi 1953, Stodolkiewicz 1963, Larson 1985). These results lead to the conclusion that, in general, the minimum mass needed for cloud fragmentation may be written as:

$$M_{crit} = \kappa \frac{c_s^3}{G^{3/2} \rho^{1/2}} \tag{1.2}$$

where κ is a constant of the order of unity that depends on the exact geometry, equation of state, or state of equilibrium of the fragmenting configuration assumed in the calculation.

The dependence of the “Jeans mass” on density suggests the possibility of fragmenting ever smaller masses out of the original larger self-gravitating cloud. At the same time, the t_{ff} dependence with ρ indicates that the denser inner regions always collapse faster than the less dense outer regions. Thus, the density distribution becomes increasingly peaked. When the central densest part becomes optically thick, the gas begins to heat up adiabatically, the temperature increases and so does the gas pressure. As consequence, the sound speed increases and so it does the “Jeans mass”. When the “Jeans mass” becomes larger than the centrally concentrated mass the thermal pressure becomes large enough to resist gravity. Consequently, the thermal pressure might not be negligible near the center (Larson 1969; Bate 1998). This happens at distances very close to the center, and it seems likely that, at larger distances, rotation (through conservation of angular momentum) becomes the most important agent in stopping the collapse.

- **Rotation:** Most star-forming cloud cores are observed to be rotating. Typical angular velocities of molecular clouds are $\omega \sim 10^{-14} - 10^{-13}$ rad s^{-1} (Goodman et al. 1993). That implies that the rotation velocity at the outer edges of a cloud of radius 0.1 pc would be $\sim 0.3 - 3$ km s^{-1}, which is comparable to the thermal support velocity. In general, such a rotation does not appear to provide much support for a molecular cloud core against their self-gravity. However, this rotation must strongly influence the later stages of collapse if angular momentum is conserved.

  The observed angular momentum of a prestellar core is ∼3 orders of magnitude greater than that of a single star. If angular momentum is conserved, a core of 0.1 pc in diameter that collapses to the size of the Sun will spin up in rotation frequency by a factor of about 10^{13} greater than initially. Because of the very high angular velocity, the centrifugal force would exceed the gravitational force by orders of magnitude, and the star will rotate faster than at breakup speed. This is known as “the angular momentum problem”. Even a slowly rotating prestellar cloud core has too much angular momentum for all of its mass to fall directly into a star; instead, flattened structures and disks are expected to be formed. As the core contracts, the centrifugal forces associated with the angular momentum eventually become as important as gravity, what makes most of the mass to end up in a centrifugally supported disk around the protostar. These circumstellar disks are frequently seen around young low-mass stars, and may be precursors of planetary systems. Collapse is halted unless a fraction of the angular momentum is redistributed or transported outwards by some mechanism, allowing to drive an inflow onto a central object. Several mechanisms were proposed as the responsible of the angular momentum redistribution: magnetic fields, spiral density fluctuations, orbital motions in a multiple system, but it was in 1980 when collimated bipolar molecular outflows emerging from young stars were discovered (Snell, Loren & Plambeck 1980; Rodríguez, Ho & Moran 1980). These bipolar outflows transfer angular momentum outwards (e.g. Königl & Pudritz 2000) and magnetic fields are thought to play an important role in the collimating and driving mechanisms of these outflows (Mouschovias 1977, 1991).

- **Magnetism:**

  Molecular clouds are significantly magnetized, and magnetic fields can also be important for the dynamics and evolution of these clouds (Heiles et al. 1993; McKee et al. 1993). In the case of being sufficiently strongly magnetized, their internal motions might be predominantly wavelike, consisting basically of magnetohydrodynamic (MHD) waves such as Alfvén waves, which involve only transverse and non-compressional motions. Wavelike "MHD turbulence" can supplement thermal pressure and help to support molecular clouds for a significant time against gravity (Myers & Goodman 1988; McKee et al. 1993; McKee & Zweibel 1995). However, it can be demonstrated that in the absence of magnetostatic support, MHD waves cannot completely prevent collapse, although they can retard it to some degree (e.g. Heitsch et al. 2001).

  The magnetostatic energy opposes to the gravitational collapse of the cloud. Mouschovias & Spitzer (1976) found that a critical mass-to-flux ratio can be defined, so that, in a cloud with a mass-to-flux ratio greater than that limit the gravitational attraction can overwhelm magnetostatic repulsion. The critical mass-to-flux ratio is:

$$\frac{M}{\Phi} = \frac{\zeta}{3\pi}(\frac{5}{G}) \ , \tag{1.3}$$

  where M is the mass of the cloud, ζ is a constant that depends on the geometry (ζ is 0.53 for a uniform sphere), $\Phi = \pi R^2 B$ is the magnetic flux through the cloud, R is the radius of the cloud, and B is the magnetic field. A cloud is termed subcritical if its mass-to-flux ratio is under the critical value (when the magnetic energy overwhelms gravity) and a cloud is supercritical if it is not magnetically stable (mass is high enough to overcome the magnetic support and set the collapse).

  Faraday's law tell us that, as long as the cloud is a good conductor, the number of field lines crossing the cloud's surface stays constant as the cloud compresses (flux freezing). It happens that most molecular clouds can be considered as good conductors because they are partially ionized by cosmic rays. Thus, clouds in which, originally, the magnetic forces cannot overcome gravity will remain supercritical as contraction proceeds and the field compresses, and subcritical cores would tend to remain subcritical in time, and therefore resisting to collapse. However, even in subcritical cores the collapse may end up occurring. Ions and magnetic field are frozen to each other, while neutrals are collisionally coupled to ions. But ions and neutrals not always stay perfectly mixed. In the interior of the clouds, where the ionizing radiation fields do not penetrate, the ion-to neutral fraction drops to values where collisional coupling is not efficient. Ions drift with respect to the neutrals, and neutral gas slips through the field line. If this happens, the mass-to flux ratio increases and eventually the core would accumulate enough mass for the gravitational energy to overcome the magnetic energy; then, the core becomes supercritical and collapses to form stars (Shu 1977, Shu et al. 1987, Lizano & Shu 1989). This process is known as ambipolar diffusion (Mestel & Spitzer 1956) and has been considered traditionally the classical model for the very early stages (prior to protostar formation) of low-mass star formation. The gradual contraction driven by ambipolar diffusion is a slow process, what makes core formation to be quasi-static. In conclusion, the main effect of the magnetic support is to retard the onset of collapse.

Shock compressions created by large-scale turbulent flows can also alter the mass to flux ratio of the core depending on the direction of the compression with respect to the direction of the magnetic field lines. If the magnetic field is boosted, then the resulting clump or core will be stabilized by magnetic forces against gravitational collapse. If the magnetic field is weakened, then the compressed clump is quickly set up for collapse.

- **Turbulence:**

Molecular clouds and massive clumps display line-widths much greater than would be expected from thermal motion given their inferred temperatures of only 10-20 K. These non-thermal line-widths have been traditionally interpreted as indicating the presence of supersonic random motions rather than large-scale systematic motions such as infall, outflow or rotation of the cloud. Such internal random motions in molecular clouds are often referred to as 'turbulence'.

The internal velocity dispersion inferred from the line width, σ_V, is well correlated with the size of the region, l:

$$\sigma_V \propto l^q \ , \tag{1.4}$$

where $q = 0.2$ for high-mass clumps (Larson 1981; Caselli & Myers 1995). In contrast, low-mass cores show wholly thermal line-widths near the core center, and $q = 0.5$ (Solomon et al. 1987). Larson (1981) reported two additional relations regarding the mass and average density, $M \propto l^2$, and $\langle\rho\rangle \propto l^{-1}$. These three relations have been called the "Larson relations" and imply that low-mass cores are smaller and have a smaller non-thermal velocity component than high-mass cores.

The existence of some kind of hierarchy of turbulent motions is suggested by the fact that the velocity dispersion inferred from the line width increases systematically with the size of the region (equation 1.4). Turbulence is a multiscale phenomenon in which the bulk of the kinetic energy remains at large scales and it cascades down to small scales. The effect of turbulence is two-fold. Under typical molecular cloud conditions, supersonic turbulence is energetic enough to prevent the global collapse of the cloud, but at the same time, turbulence is responsible of areas of density enhancement due to shock compression of large-scale turbulent flows (Klessen et al. 1998, Klessen 2000, Klessen & Burkert 2000, 2001, and Heitsch et al. 2001). While subsonic turbulence (at small scales) cannot produce substructure (Larson 1981, Padoan et al. 2001a), supersonic turbulent velocities (at large scales) induce density enhancement within the flow that can be large enough for the onset of gravitational collapse. The fact that turbulent motions become subsonic on the smallest scales, suggests that there may be a lower limit to the size of the compressed structures that can be created by turbulence. The transition from supersonic to subsonic motions occurs at a scale of the order of 0.05-0.1 pc, which is approximately the size of the observed massive prestellar cores.

The filamentary structure of molecular clouds suggests that they may form by some kind of compression. Sheets and filaments would form by the shocks of two converging flows; and cores would form at the converging point of three turbulent flows. Recent numerical simulations support the hypothesis that the morphology and kinematics of molecular clouds are dominated by the encountering of several large-scale turbulent streams in the interstellar medium (Ballesteros-Paredes et al. 1999). However, the origin of the observed large-scale motions is not yet fully understood. Some likely sources are random magnetic fields, and stellar feedback such as ionization, winds, or supernova explosions. However, some authors argue against the turbulent interpretation of the non-thermal line-widths in molecular clouds, and suggest that the observed large line-widths are mainly caused by gravitationally driven motions on large scales (Goldreich & Kwan 1974, Vázquez-Semadeni et al. 2009).

In summary, turbulence and/or magnetic fields may be the most important agents counteracting gravity at large scales. After the core has begun to collapse, the centrifugal force associated with its angular momentum eventually becomes important at intermediate and small scales and may halt its contraction, originating a centrifugally supported disk. On scales of a few solar radii, thermal pressure becomes the most important force opposing gravity. The magnetic field also plays an important role in mediating the accretion of the gas and in launching the bipolar jets that are outstanding signpost of the birth of a new star. Note that while the magnetic field support leads to core formation in a quasi-static way, large-scale supersonic turbulence leads to core formation in a much more dynamical way, via shock compression.

Many models have been proposed so far to describe the collapse of a molecular cloud core to form a star. They mainly differ in the importance of the above opposing agents, what later determines the initial characteristics of the core and the way collapse proceeds. Among the models of protostellar collapse most common in the literature we find:

- The Larson-Penston-Hunter model (LPH; Larson 1969, Penston 1969, Hunter 1977). In this model only hydrodynamic and thermal pressures oppose against gravity. Its initial condition is constant density. The initial absence of pressure gradients makes it a highly non-equilibrium configuration.

- The collapse of a Bonnor-Ebert sphere (BE-sphere; Bonnor 1956, Ebert 1957). A BE-sphere is a hydrostatic structure confined by pressure whose density profile has a central flat region and an outer region that behaves as r^{-2}. It differs from the LPH model in that the core is initially at equilibrium.

- Ambipolar diffusion and the Singular Isothermal Sphere model (SIS; Shu 1977, Shu et al. 1987). This model has become the classical picture of star formation. It considers that the core formation is magnetically regulated through the ambipolar diffusion process, which sets slowly a density profile as r^{-2} and the pressure support begins to substitute the magnetic support in opposing the gravitational collapse.

- The Singular Logatropic Sphere model (SLS; Lizano & Shu 1989; McLaughlin & Pudritz 1996, 1997) describes the case in which non-thermal support (likely MHD turbulence) is the main opposing force against gravity before and after the collapse is set. It predicts a cloud core initially at equilibrium with a density profile that is flat at the center and behaves as r^{-1} in the outer region.

- The rapid collapse model (Mac Low & Klessen 2004), in which cores are formed by large-scale turbulent inflows converging at supersonic velocities.

- The Terebey-Shu-Cassen model (TSC; Terebey, Shu & Cassen 1984), which describes self-consistently the collapse when a small component of rotation is taken into account. The matter falls onto the star in the polar direction but accumulates in a flattened rotating structure in the equatorial plane.

- The Sheet collapse model (Hartmann et al. 1996), which is a generalization of the TSC model for the case of intrinsically flattened density distributions by considering the collapse from a sheet initially in hydrostatic equilibrium.

In Chapter 3 we describe in more detail these models in the different phases of the protostellar collapse.

1.2 Initial conditions of collapse

First theoretical studies of gravitational collapse considered static or stationary core initial conditions and therefore cores should be long-lived. That idea laid mainly on the fact that spectral line observations towards low-mass starless cores show narrow lines, with nearly thermal widths (a few tenths of km s^{-1}). This implies that gas velocities are subsonic (e.g., Jijina et al. 1999; Lee et al. 1999, 2001; Gregersen & Evans 2000; Tafalla et al. 2004), what, in its turn, means that the inertial forces are small and that there is nearly balance between the thermal and gravitational forces (Keto & Field 2005).

In recent years, however, some observations have been interpreted as indicative of some molecular cloud cores displaying nonzero, inward motions (Lee et al. 1999, 2001) before they contain infrared sources. One interpretation of this is that the cores must begin their collapse from a pre-existing inward flow. Thus, the question that arises is whether star formation is a dynamic, relatively rapid process, or if it proceeds by slow quasi-static evolution.

Observations suggest that the density profile of prestellar cores has a central flattening. A popular approach is to describe these cores as pressure-confined, hydrostatic spheres (BE-spheres) (Bonnor 1956; Ebert 1957), which often provides a good fit to the data (Alves et al. 2001; Bacmann et al. 2001; Kandori et al. 2005). However, the observed morphologies of the starless cores are not always spherical and aspect ratios of 2:1 are common (Myers et al. 1991). Additionally, a centrally flattened density structure is not unique of equilibrium. Numerical calculations of the dynamical evolution of supersonically turbulent clouds show that transient cores forming at the stagnation points of convergent flows may exhibit a column density profile with the appearance of the BE profile (Ballesteros-Paredes et al. 2003). Also, the observed density contrast between the core center and its edge often exceeds the maximum value of 14 allowed for stable BE-spheres (Bacmann et al. 2000; Evans et al. 2001). The latter indicates either the presence of an additional force component, apart from the thermal, or the lack of equilibrium.

Studies of the chemistry of molecular clouds suggest young ages and short lifetimes (of the order of 1 Myr or less), in contrast with the long-lived cores predicted by theories that assume static initial conditions. As discussed by Stahler (1984), Prasad et al. (1987), Herbst (1994), and van Dishoeck & Blake (1998), molecular clouds and cloud cores appear to be chemically relatively unevolved, since the observed abundances of various molecules are often far from those expected to prevail in chemical equilibrium. Also, most of the molecules in dense molecular clouds have not yet frozen out on the dust grains as would be expected if these clouds were stable long-lived objects.

Moreover, very few giant molecular clouds are known that are not forming stars, and the most massive and dense ones all contain newly formed stars. This means that there cannot be any significant "dead time" between the formation of a massive dense molecular cloud and the onset of star formation in it; therefore, there cannot be any long period of slow quasi-static evolution before stars begin to form. Statistical studies of the observed ratio of starless cores and stellar cores have been made in order to determine the life-time of cores. If cores are stable, and therefore long-lived, there should be many more cores without stars that cores with young stars. Wood, Myers & Daugherty (1994) found that about 25% of a sample of $\sim$ 50 cores contained IRAS sources, suggesting that cores evolve rapidly. However, according to the simulations of Ballesteros-Paredes et al. (2003) and Klessen et al. (2005) the number of starless cores might be overestimated as many of them will not end up forming stars. So, the starless-to-stellar cores ratio in the statistical study of Wood, Myers & Daugherty (1994) would be as well overestimated, suggesting that cores should evolve even faster. In opposition to the dynamic, rapid hypothesis of star formation, Tassis & Mouschovias (2004) argue that the phase of cloud evolution prior to core formation has been ignored, and by taking this long phase of evolution into account the observations are consistent with the scenario of slow, quasi-static magnetically controlled star forming scenario.

The observed morphological structure of molecular clouds does not resemble any kind of equilibrium configuration, but instead is highly irregular and filamentary and often even wind-blown in appearance, suggesting that these clouds are actually dynamic and rapidly changing structures, possibly formed from the encountering of two or more converging large-scale flows. Additionally, molecular clouds display line-widths much greater than would be expected from thermal motion. These non-thermal line-widths have been interpreted as indicating the presence of supersonic turbulent motions, rising the question on whether it is possible to get quasi-static cores in the supersonic turbulent medium that (possibly) governs molecular clouds.

On one hand, Keto & Field (2005) and Nakamura & Li (2005) argue that quiescent cores can form in a turbulent environment if the starless cores, with their narrow line-widths, are at the subsonic bottom of the turbulent cascade. In this picture stable cores (magnetically subcritical cores) cannot easily be destroyed and may persist indefinitely oscillating in size and density around an equilibrium mean until external conditions change or they merge with other cores to become supercritical. On the other hand, unstable cores follow a progression toward greater densities and infall velocities.

Klessen et al. (2005) analyze the results from non-magnetic numerical simulations of the fragmentation of supersonically turbulent, self-gravitating molecular gas, and conclude that about 25% of the cores formed in these simulations are quiescent (understood here as having the non-thermal component of the line-widths smaller or equal to the thermal component). These authors point out, however, that if the external turbulent compression ends before the core reaches the state where it is dominated by self-gravity, then the core will re-expand and merge with the lower-density ambient molecular cloud material, and thus, such quiescent cores won't be able to give birth to new stars. Vázquez-Semadeni et al. (2000, 2005) also support the idea that structures created by turbulence are generally transient. Similarly, Padoan et al. (2001b) argue that, even if an equilibrium core is formed from a turbulent environment, it is highly unlikely that it is left undisturbed for as long as the ambipolar drift time-scale. According to Padoan et al. (2001b), for local collapse to actually result in the formation of stars, shock-generated cores must collapse to sufficiently high densities on time scales shorter than the typical time interval between two successive shock passages. Only then, the new generated cores can decouple from the ambient flow and survive subsequent shock interactions. The shorter the time between shock passages, the less likely these fluctuations are to survive. Only cores with gravitational energy in excess of the sum of thermal and magnetic energy, i.e. the supercritical cores, would collapse. As we will also mention later, according to Padoan et al. (2001b), if clouds are turbulence dominated then the classical picture of ambipolar diffusion does not apply, and both low- and high-mass stars should form from supercritical cores.

Contrary to Keto & Field (2005) and Nakamura & Li (2005), Ballesteros-Paredes et al. (1999, 2003, 2006) argue that the actual cloud conditions do not meet the requirements to form equilibrium cores from a dynamic medium, and conclude that quasi-hydrostatic configurations cannot be produced out of turbulent fluctuations.

In conclusion, the uncertainties in observations and simulations have prevented to confirm the hypothesis of whether cores are built up over many dynamical timescales, so that hydrostatic equilibrium is a reasonable approximation, or are formed dynamically.

1.3 Modes of star formation

1.3.1 Low-mass star formation

There is evidence that the low-mass stars can form from the collapse of gravitationally bound cores in molecular clouds (**monolithic collapse models**). The theoretical works of Shu (1977), Shu et al. (1987), and Larson (1969, 1972) have been widely used to explain how a dense core evolves into a star. The Shu theory establishes that, before the formation of the protostar and the onset of the main accretion phase, the process of ambipolar diffusion sets quasi-statically a centrally condensed density distribution, that ultimately reaches the form $\rho \propto r^{-2}$. If this equilibrium configuration is perturbed, collapse initiates at the center and a rarefaction wave expands outwards setting the mass behind it into inward motion.

On the other hand, the Larson theory begins with a state of uniform density and the lack of pressure support sets the whole core into collapse. Matter becomes increasingly concentrated at the center until a density distribution of $\rho \propto r^{-2}$ is set. At that point the protostar is formed, the prestellar phase ends, and the main accretion phase begins. However, in contrast with the Shu scenario, where large-scale infall motions are not expected at the protostar formation instant, the Larson scenario predicts large-scale inflow motions in the whole cloud. In both cases the core collapse is assumed to be isothermal. This is a valid approximation since the temperature is predicted to decrease with increasing gas density because of the increasing efficiency of atomic and molecular line cooling, but, at the same time, at higher densities the gas becomes thermally coupled to the dust, which then controls the temperature by its thermal emission; so, the temperature begins to rise slowly with increasing density. The two effects balance and the temperature does not change too much while the density increases by many orders of magnitude.

During the collapse, because of the initial rotation of the cloud and the angular momentum conservation, part of the material will be accumulated in an equatorial disk orbiting around the star. This disk would be the precursor of a planetary system. Also, these disks are intimately related to the presence of jets, which are powerful collimated ejections of material along the rotation axis of the disk, and outflows, which are interpreted as the result of the interaction of the jet with the ambient molecular gas (Raga & Cabrit 1993, Raga et al. 1993). It is through these ejections of material that the protostar can remove the excess of angular momentum, consequence of the initial rotation of the cloud, which otherwise would make the star to rotate too fast and to disintegrate.

The protostellar evolution proceeds in subsequent phases which can be distinguished observationally by their spectral energy distribution (SED). SEDs of young stellar objects (YSOs) are divided into four classes based on the slope of the SED over the range between 2.2 μm and 10-25 μm (Lada 1987; Adams, Lada & Shu 1987; André, Ward-Thompson & Barsony 1993) (Figure 1.1),

$$\alpha_{IR} \equiv \frac{d\ \log(\lambda F_\lambda)}{d\ \log\lambda}\ . \tag{1.5}$$

The SEDs of low-mass young stellar objects in these four classes have been reproduced using monolithic collapse models (Kenyon et al. 1993; Osorio et al. 2003; Adams et al. 2012; Furlan et al. 2014). Also, there is some evidence that some prestellar/starless cores follow a BE-density distribution (Alves et al. 2001). The characteristics of theses four classes can be summarized as follows:

- Class 0: Sources of this type are extremely faint in the optical and near-IR and have a significant submillimeter luminosity. Their SEDs are very similar to that of a black-body with a low temperature ($\sim 10-30$ K). These characteristics suggests that we are observing a cold dusty envelope around the protostar. A protostar in this embedded phase is believed to acquire a significant fraction of its mass by accreting gas from its surrounding envelope through an accretion disk, and drives bipolar outflows.

- Class I: A source of this class is characterized by a positive value of α_{IR}. Its SED is wider than that of a black-body, which suggests the presence of large amounts of circumstellar dust. A source of this type is believed to be a relatively evolved protostar still with both a circumstellar disk and an envelope. In this phase, an outflow creates cavities in the envelope, the protostar increases its temperature and becomes visible in the IR.

- Class II: A source of this class has -1.5 $< \alpha_{IR} <$ 0. Its SED is also wider that that of a black-body, with an IR excess, but the negative slope indicates that the source is surrounded by considerably less circumstellar dust than a Class I source. The stars of this class have almost stopped accretion and are observable in the IR and optical. The SEDs

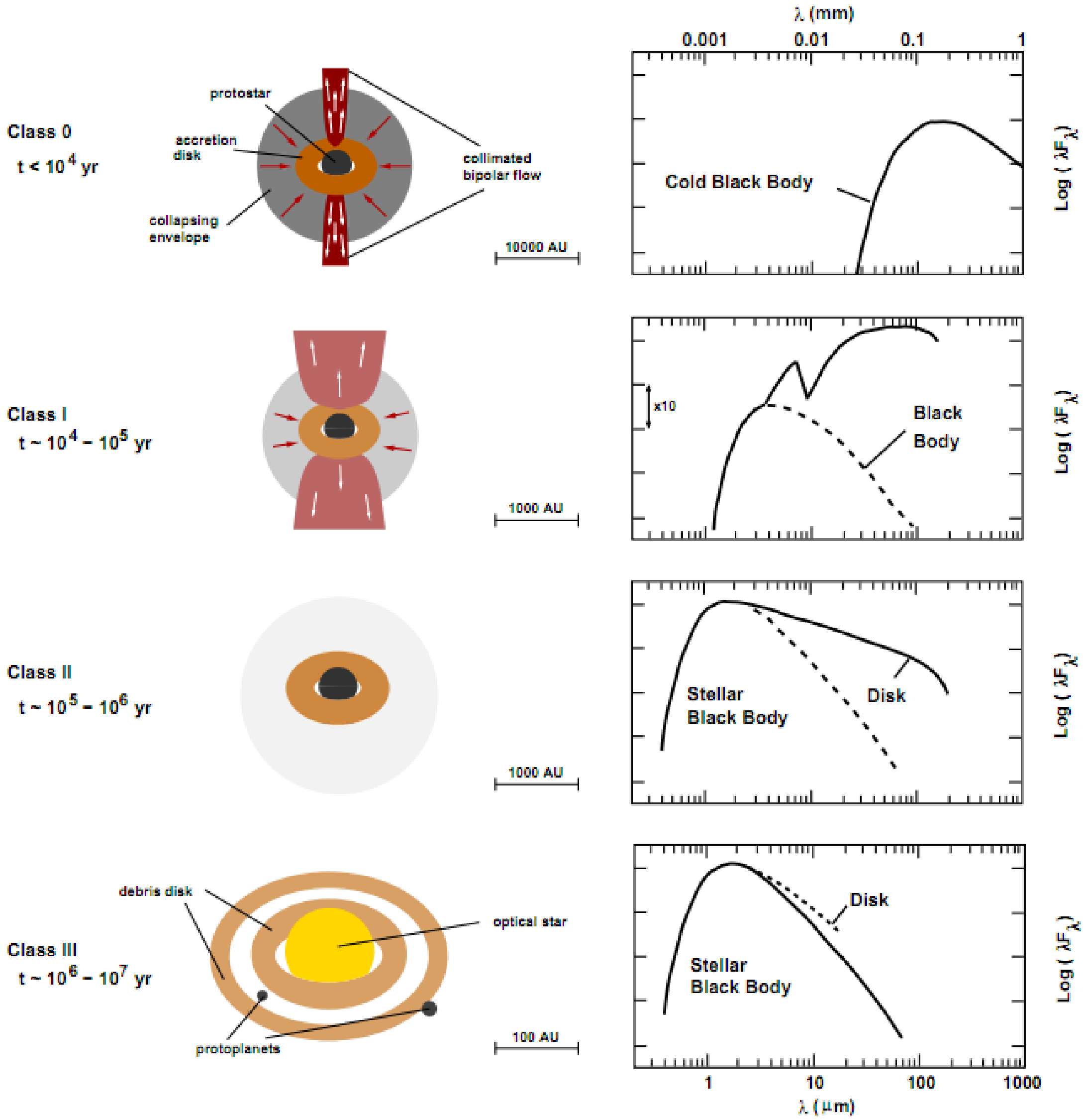

Figure 1.1: Observational classification of low-mass young stellar objects based on the shape of their SED. This classification is usually taken as the standard evolutionary scheme of how low-mass star formation proceeds. Protostars would evolve from a phase in which they are surrounded by large amounts of material (Class 0) to a phase in which most of the material of the envelope has been incorporated to the star (Class III). Figure adapted from Carrasco-González (2010).

can be modeled as the combination of a pre-main sequence star with a dusty circumstellar disk. Stars of this class correspond to classical T-Tauri stars.

- Class III: A source of this class has -3 $< \alpha_{IR} <$ -1.5. The SED is similar to that of a black-body with a single temperature, consistent with observing the photosphere of a young star. The source is observable at optical wavelengths and it presents very little circumstellar dust. The small amount of matter in the circumstellar disk may indicate that the formation of a planetary system is in an advanced phase. It is believed that Class III objects are pre-main sequence stars that are no longer accreting significant amounts of matter. The main source of energy is their gravitational contraction. When the central temperature is sufficient to ignite hydrogen fusion, a main sequence star is born.

1.3.2 Why high-mass star formation differentiates from the low-mass case?

Even though massive stars are fundamental in the evolution of galaxies, since they produce the heavy elements, energize the interstellar medium, and possibly regulate the star formation rate, their formation process is currently a matter of intense debate (e.g., Zinnecker & Yorke 2007). This contrasts with our understanding of low-mass star formation, which is better known. High-mass star-forming regions (HM SFRs) are characterized by more extreme physical conditions than their low-mass counterparts. Clumps and cores within HM SFRs have sizes, masses, and velocity dispersions roughly an order of magnitude larger than cores in low-mass regions (e.g., Jijina et al. 1999; Lee et al. 1999; Garay & Lizano 1999; Kurtz et al. 2000; Beuther et al. 2007). The velocity dispersion in high-mass cores has typical values of 1.5-4 km s^{-1}. Such high values are generally interpreted as resulting from strong turbulence that manages to support the clumps against gravity (e.g., Garay & Lizano 1999; McKee & Tan 2003).

Besides the above observational differences, from a theoretical point of view, there have been reasons to, traditionally, think that high-mass stars may form in a different way than low-mass stars. According to the classical theory of ambipolar diffusion (Shu & Adams 1987; Lizano & Shu 1989), cores are long-lived quasi-static objects formed from subcritical clouds. However, in HM SFRs, where highly supersonic turbulent velocity dispersions are observed (Plume et al. 1997), large-amplitude density fluctuations are expected to continually form and grow. If massive stars were to form in magnetically stabilized clumps, which take much longer for collapse to begin (because of the low process of ambipolar diffusion), their large internal turbulent structure would make the clumps to subfragment before the massive stars have time to form, and therefore preventing massive stars to form via monolithic accretion in subcritical clouds. Thus, only supercritical compression would lead to massive star formation (Shu et al. 1987). Consequently, the classical model of star formation introduces a dichotomy in the formation process of low-mass (from subcritical clouds) and high-mass stars (from supercritical clouds).

Also, historically, considerations on the stellar radiation pressure have lead to a dichotomy between high and low-mass star formation. Massive stars are believed to reach the zero-age main sequence (ZAMS) when they are still accreting and deeply embedded in their parental cores (Palla & Stahler 1993), while low-mass stars spend a considerable part of their youth as contracting pre-main sequence (PMS) objects after they have finished the accretion process. Thus, it was suggested that once the massive star has started hydrogen burning, the radiation pressure and ionization can halt the accretion, which determines an upper limit of the stellar mass function (Larson & Starrfield 1971; Kahn 1974; Wolfire & Cassinelli 1987). A reanalysis of these calculations using updated properties of dust grains (opacity and sublimation temperature) sets an upper limit of about 35 $M_\odot$ for the mass of a star assembled through spherical accretion (Osorio et al. 1999). Although non-spherical accretion can increase this upper limit (Jijina & Adams 1996; see below), these considerations motivated the suggestion that massive stars or, at least, the most massive ones, may form via the **coalescence** of previously formed low-mass stars (Bonnell et al. 1998). This coalescence scenario was supported by the fact that the most massive stars are usually found in the central region of the clusters, where stellar collisions are more frequent.

However, the problems associated with the strong turbulence and with the radiation pressure that motivated the dichotomy between low- and high-mass star formation have been revised recently. Regions of high-mass star formation like the Orion Nebula Cluster, which has been determined to be magnetically supercritical, also form low-mass stars in great abundance. In fact, not only high-mass star-forming regions but most cloud cores are magnetically supercritical (Bourke et al. 2001; Crutcher 1999; Crutcher & Troland 2000; Crutcher & Troland 2008). The fact that many low-mass stars form in supercritical conditions calls into question the importance or need of ambipolar diffusion in star formation. High-mass stars might not form via magnetically-dominated quasi-static process, but low-mass stars may neither. Regarding the radiation pressure problem, analytic treatments of the problem suggest that the solution lies in the non-sphericity of the accretion process. In the more realistic scenario of mass growth via an accretion disk, as expected when rotation comes into play, the radiation pressure could blow away the tenuous polar regions but not the massive disk (Nakano, Hasegawa & Norman 1995). In this situation, the central object may emit radiation isotropically but the radiation can scape along the polar direction, becoming anisotropic farther from the center (Yorke & Bodenheimer 1999). Also, the disk would redirect the IR radiation towards the poles, reducing the radiative force in the disk plane and permitting mass accretion to continue from the disk onto the star over a substantial range of solid angles (Jijina & Adams 1996; Krumholz et al. 2005c; Nakano 1989). Recent 3D calculations suggest that radiation pressure does not set a limit in the final mass of the stars formed in a non-spherical accretion scenario (Krumholz et al. 2005a, 2009; Kuiper et al. 2013). As stellar collisions require extreme stellar densities, $\sim 10^8$ pc^{-3}, larger than the values observed so far, monolithic accretion appears to be favored over coalescence. Thus, massive-stars may form via processes that involve an accretion disk (and beaming of radiation along the polar direction), just as ordinary low-mass stars (McKee & Tan 2002).

To try to unify the treatment of low- and high-mass star formation, McLaughlin & Pudritz (1996) proposed a **monolithic collapse model**, similar to those of the low-mass star formation case of Shu (1977) and Larson (1969, 1972) but, in which a non-thermal component manages to support the cloud against gravitational collapse. These authors created a model for the internal structure of molecular cores that was able to explain qualitatively and naturally: 1) the different behavior of the velocity dispersion between high-mass cores, $\sigma_V \propto l^{0.2}$, and low-mass cores, $\sigma_V \propto l^{0.5}$ (Caselli & Myers 1995); 2) the mass-radius and size-radius relationships of Larson (1981) (see Section 1.1); and 3) the typical mass and density contrasts between Giant Molecular Clouds and the clumps within them. These authors achieve these results by introducing a phenomenological equation of state, $P = P_0\left[1 + A\ln\left(\rho/\rho_0\right)\right]$ (similar to the one first introduced by Lizano & Shu 1989). Because of the logarithmic dependence on the density of the pressure, this model is known as logatropic. The equilibrium density profile of a logatrope behaves as $\rho \propto r^{-1}$ outside of a constant-density central region. However, Motte & André (2001) found that low-mass isolated cores tend to exhibit a density profile like $\rho \propto r^{-2}$, which coincides better with the prediction of the classical model (SIS model; Shu 1977 and Shu et al. 1987) once the pressure support has taken over the magnetic support. These authors also found that low-mass clustered cores have a density distribution that resembles that of a BE-sphere, which is a self gravity equilibrium configuration in approximate pressure balance. Both things suggest that, at least in low-mass cores, thermal support is the most important opposing agent against gravity. In contrast, in the high-mass regime, studies of massive hot cores indicate shallower density distributions, $\rho \propto r^{-\alpha}$, with $1.0 < \alpha < 1.5$ (van der Tak et al. 2000; Hatchell et al. 2000), which are more similar to the predictions of the logatropic model with non-thermal support.

Observations have also revealed that, unlike low-mass stars, massive stars are gregarious, namely that they tend to be born in groups (e.g. Ho & Haschick 1981; Welch et al. 1987; Rudolph et al. 1990; Garay et al. 1993), that they show a high frequency of binary or multiple systems (Preibisch et al. 2001), and that they are often centrally located in the cluster in which they form (Hillenbrand & Hartmann 1998). The SLS model, and also the rest of monolithic collapse models (SIS, BE-spheres, LPH, etc), do not take into account that high-mass stars form in clusters. In the monolithic collapse models the formation of clusters of stars is simply accounted by considering a larger and more massive molecular cloud, which having highly inhomogeneous density structures, would fragment into several subregions. As high-mass stars form in dense clusters, the interaction with other protostars and newly formed stars may be important in their evolution. Perhaps because of such interaction, regions of massive star formation are more complex in structure and dynamics.

The fact that high-mass stars are located often at the center of stellar clusters (Bonnell & Davies 1998), where the high density and pressure result in a small thermal "Jeans mass" that is only a fraction of a solar mass (at the typical densities and temperatures of a molecular cloud that has not yet begun to collapse), motivated the following question: If massive stars form preferentially at the centers of stellar clusters, where the thermal "Jeans mass" is considerable smaller than the mass of OB stars, why would a massive clump collapse coherently into a single star rather than fragmenting into many objects and form a cluster of low-mass stars (Dobbs et al. 2005)?

The so-called **competitive accretion** scenario addresses the fragmentation and clustering issues. According to this theory for high-mass star formation, fragmentation occurs without any restriction. All the gas fragments down to roughly the “Jeans mass”, forming a cluster of low-mass cores. The high-mass stars form via a second phase in which “Jeans mass” protostars compete for gas at the center of a dense cluster. The cluster gravitational potential channels mass toward the center, so stars that remain at the center grow to large masses, while those that are ejected from the cluster center by N-body interactions remain with a low-mass (Bonnell et al. 2004, 2006; Klessen & Burkert 2000). The competitive accretion picture has been challenged on the grounds that the kinematic structure observed in star-forming regions is inconsistent with the idea that protostars have time to strongly interact with one another before they completely accrete their parent cores (André et al. 2007; Krumholz et al. 2005b).

Other explanations have been proposed to answer why massive clumps would collapse coherently into a single massive star rather than fragment in many objects. The idea that motivated the above question rests on the assumption that the cloud temperature in massive clumps is similar to that observed in low-mass stars, $T \simeq 10$ K. However, it has been argued that more massive fragments could form if the gas temperature is higher. The accretion luminosity produced by the collapse of a dense core in a massive star-forming region is sufficient to heat the environmental cloud and suppress a high level of fragmentation, converting a collapse that might have produced 100 small stars into one that produces only a few massive ones (Krumholz 2006; Krumholz & McKee 2008). Another possibility is that the heating of the environmental gas comes from the luminosity of one or several external stars. It is possible that the temperature of massive cores increases gradually with time as energy is injected in the surrounding medium by low- and intermediate-mass stars formed during an initial stage of star formation, and that the massive stars are formed last, during a late “hot” stage of star formation (Garay & Lizano 1999). On the other hand, Larson (1982) suggested a different explanation, where tidal forces from an association of stars produce the disruption of incipient condensations within the remaining gas. The gas, then, settles toward the center of the forming cluster and becomes progressively more dense. Much of this dense gas may then give rise to a few massive stars.

As commented in Section 1.2, there is evidence of molecular clouds being dynamic and rapidly changing, with structures dominated by large-scale turbulence. This idea lays on the assumption that the superthermal line widths present in molecular clouds are due to turbulent motions. The turbulent-shock scenario described by the **rapid collapse scenario** proposes a unified description of both low-mass and high-mass star formation and, at the same time, it can explain in a natural way the clustering behavior of high-mass stars as a result of the degree of support provided by the supersonic turbulence. According to this theory, the hierarchical nature of turbulence produces that, at large scales, turbulence would prevent the global collapse of the clumps, but at small scales, shock compressions can create areas of enhanced density that are prone to collapse. Thus, high global support tends to produce local collapse and low star-formation rate, exactly as seen in low-mass star formation regions. Conversely, lack of global turbulent support results in regions that can collapse freely and form a web of density enhancements in which star formation can proceed efficiently, as seen in regions of massive star formation (Mac Low & Klessen 2004). Numerical simulations show that supersonic turbulent flows generate supercritical cores, from which both types, low- and high-mass stars, would form (see Section 1.2). Therefore, in this scenario there is no need to form low-mass stars from subcritical cores, thus removing the dichotomy introduced by the ambipolar diffusion mediated collapse model. In this rapid collapse scenario, the magnetic field is relegated only to provide an additional contribution to the support.

Recently, Vázquez-Semadeni et al. (2008, 2009) have challenged the interpretation of molecular clouds being turbulence dominated. These authors argued that it is difficult to imagine a turbulent velocity field inside the clouds that is completely random in such a way as to only provide support against gravity. Instead, the compressive component of turbulence may foster core contraction rather than support against gravity. The results of Vázquez-Semadeni et al. (2008, 2009), which are consistent with those of Hartmann & Burkert (2007) and Peretto et al. (2007), suggest that molecular clouds and clumps may be in a state of gravitational collapse. If confirmed, these suggestions point towards a return to the original proposal by Goldreich & Kwan (1974) that the observed line-widths in molecular clouds are due primarily to large-scale gravitational contraction. Vázquez-Semadeni et al. (2008, 2009) present numerical simulations that show that the physical conditions in both low- and high-mass star forming regions can arise from hierarchical gravitational collapse. The former regions arise from small-scale fragments in the collapse (which, however, occur first, because they originate from local high-amplitude density fluctuations that have a shorter free-fall time), while the latter may appear when the global, large-scale collapse is completed.

The 3D simulations of Girichidis et al. (2011) (Figure 1.2) give similar results to that of Vázquez-Semadeni et al. (2008, 2009). Their simulations suggest that whether forming stars are low- or high-mass stars depends strongly on the initial density of the cloud and the turbulent field. They compare four different initial density profiles of the cloud (uniform, Bonnor-Ebert type, $\rho \propto r^{-1.5}$, and $\rho \propto r^{-2}$) combined with three different supersonic turbulent velocity fields (compressive, solenoidal and mixed). The simulations show that, during the collapse of the cloud, two different gravitational processes compete with each other. First, the collapse towards the center of mass and secondly the collapse of dense regions into filaments, induced by the turbulence. Initially concentrated density profiles ($\rho \propto r^{-1.5}$ and $\rho \propto r^{-2}$) always lead to the formation high-mass stars at the center of the cloud. While the $\rho \propto r^{-2}$ profile produces only one high-mass star, the $\rho \propto r^{-1.5}$ profile can form more than one massive star after filamentary structures have formed and collapse. Low-mass stars are created surrounding the massive central one. Initial density profiles with a flat inner region do not produce any central massive star, but they produce hundreds of low-mass stars, either distributed throughout the entire cloud or in subclusters, depending on the initial turbulence.

The results of Girichidis et al. (2011) and Vázquez-Semadeni et al. (2008, 2009) explain why massive cores tend to have larger velocity dispersions than low-mass ones, since the latter only begin contracting when they decouple from the global flow, while the former have been

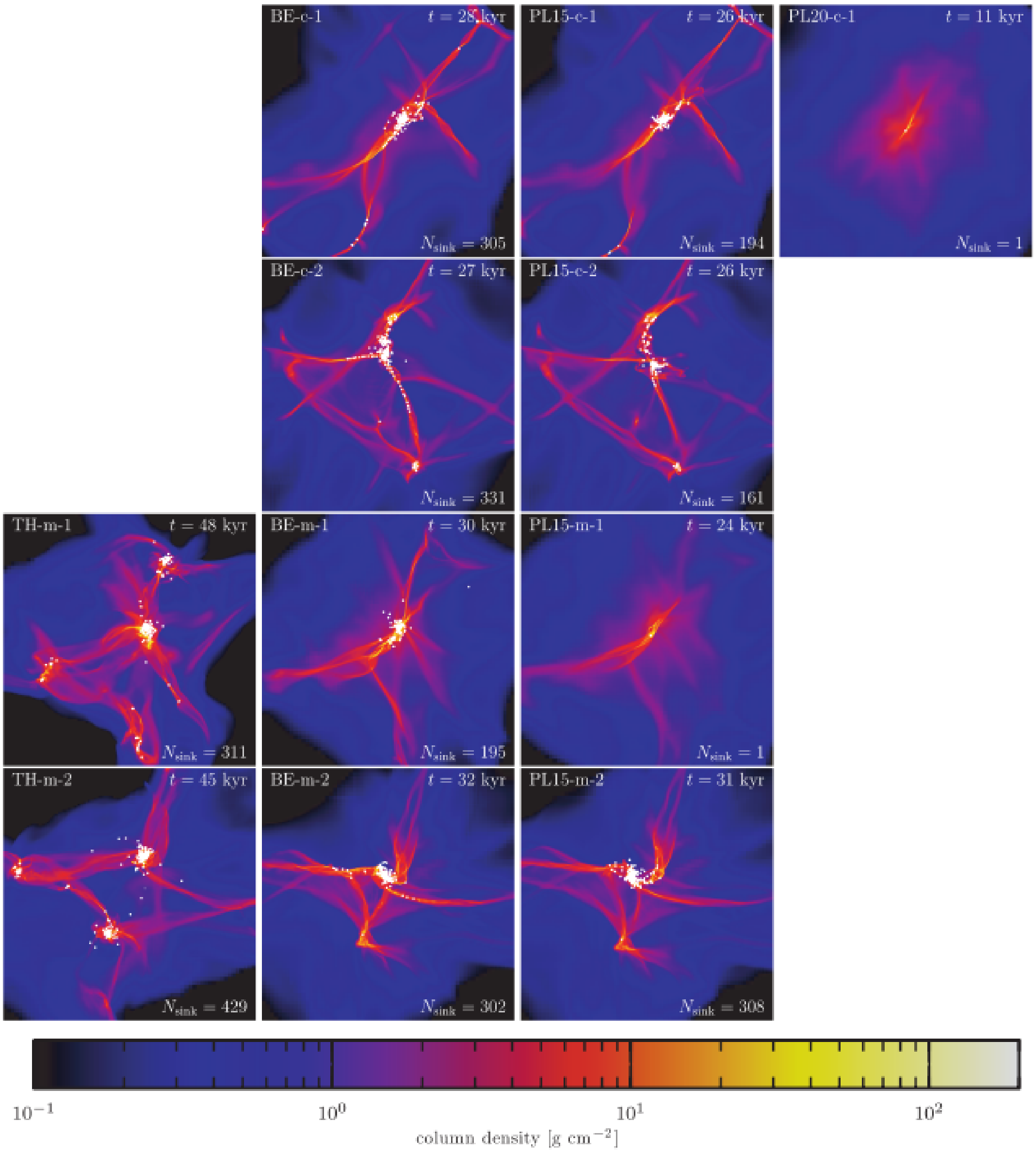

Figure 1.2: Column density plots of a collapsing cloud (Girichidis et al. 2011). Each column corresponds to different initial density configurations of the collapsing cloud. TH stands for Top Hat, meaning uniform density, BE stands for density distributions of the kind of a Bonnor-Ebert sphere, PL15 stands for density distribution of the form $\rho \propto r^{-1.5}$, and PL20 stands for density distribution of the form $\rho \propto r^{-2.0}$. Each row corresponds to different modes of initial turbulence. Only the TH runs develop several subclusters. All setups show filamentary structures but differently spread in the box. The box in all cases spans 0.13 pc in both x and y directions. Figure adapted from Girichidis et al. (2011).

accelerating in their contraction for a longer time. Also, these kind of models predict that massive stars tend to be located at the center of the cloud, whereas stars with lower masses form further out, in agreement with observations (Hillenbrand & Hartmann 1998; Gouliermis et al. 2004, Stolte et al. 2006). Another worthy result from the study of Girichidis et al. (2011) is that it shows the strong importance of the initial conditions on the final product of cloud collapse.

There are several additional pieces of evidence suggesting that massive stars can form in a similar way as low-mass stars, favoring the **monolithic collapse** as a common scenario for the formation of both low- and high-mass stars. Observations have shown that high-mass YSOs are associated with collimated jets, bipolar outflows, and more recently, with circumstellar accretion disks, similarly to what happens in low-mass YSOs. These observational results suggest that these objects have been formed in a monolithic collapse scenario, as it seems difficult that a collimated jet/accretion disk system would survive after the violent stellar collisions that should characterize the coalescence scenario.

Both low- and high-mass protostars are associated with colimated radio jets (e.g., Martí et al. 1993; Garay et al. 1996; Rodríguez et al. 2008; Anglada 1996; Anglada et al. 2015) with similar (but scaled) properties. It is well known that photoionization (the ionizing mechanism of HII regions) does not work for radio jets associated with low-mass YSOs since these objects lack, by several orders of magnitude, the number of ionizing UV photons required to produce the observed radio luminosities (Rodríguez et al. 1989; Anglada 1995). Instead, ionization by shocks (Curiel et al. 1989) is the preferred ionizing mechanism, as suggested by the observed correlation between the radio luminosoty of the jets and the momentum rate in the outflow (Anglada et al. 1992, 1998). Since all radio jets, both those associated with low-mass and those associated with high-mass objects, follow the same observed correlations between radio luminosity, outflow momentum rate and bolometric luminosity, a common origin for the ionization and launching mechanisms of all radio jets is suggested (Anglada et al. 2015).

Also, bipolar molecular outflows appear ubiquitously associated with both high-mass (e.g., Gómez et al. 1999; Beuther et al. 2002a; Davis et al. 2004; Shepherd et al. 1998) and low-mass YSOs. The dynamical ages of the outflows in massive star forming regions are similar to those associated with low-mass YSOs, although their masses, outflow rates and energetics are substantially larger (Churchwell 1997). However, the outflow momentum rate correlates well with source luminosity across a very wide range in luminosity (Rodríguez et al. 1982; Cabrit & Bertout 1992). These results support the hypothesis that low- and high-mass protostars show a common wind launching mechanism (Cabrit & Bertout 1992; Shepherd & Churchwell 1996; Wu et al. 2004).

Low-mass stars present accretion disks oriented perpendicular to the direction of the outflow (e.g., Burrows et al. 1996; Lee et al. 2009; Carrasco-González et al. 2012). In the last two decades, some candidates of accreting disks around high-mass stars with luminosities typical of B-type ($< 25 M_{\odot}$) stars have been reported in the literature (Shepherd et al. 2001; Patel et al. 2005; Torrelles et al. 2007; Beltrán & de Wit 2015). However, around more luminous and massive objects (presumed O-type stars) there is still no clear evidence for accretion disks. Instead, gravitationally unstable, elongated, large molecular structures that exhibit smooth velocity gradients suggesting rotation have been detected (Cesaroni et al. 1999; Sandell et al. 2003; Beuther et al. 2004; Sollins & Ho 2005; Sollins et al. 2005; Beltrán et al. 2005, 2006, 2011; Furuya et al. 2008; Beuther & Walsh 2008; Zapata et al. 2009; Beltrán & de Wit 2015). While typical disks in low-mass stars have radii of 60-150 AU (Rodríguez et al. 1992; Wilner, Ho & Rodríguez 1996; Padgett et al. 1999; Kitamura et al. 2002) and masses of several tenths of a solar mass, these molecular structures around O-type stars have radii of several thousand of AU and their masses range from 10 to 2000 $M_\odot$, corresponding to interstellar toroids rather than to circumstellar disks.

The above exposed pieces of evidence would suggest that massive stars, at least those of B-type, may form in a similar manner to low-mass stars, motivating the use of monolithic collapse models for both low- and high-mass stars. It is worth noting that the turbulent-dominated and/or of the hierarchical gravitational collapse scenarios (Vázquez-Semadeni et al. 2008, 2009) discussed above may be better suited regarding the question on how star formation is onset on molecular clouds, while the monolithic collapse models are better suited to describe how the collapse proceeds within a given core once gravity has managed to prevail over the rest of forces. In that sense, monolithic collapse models are very useful tools to determine the physical properties of a given star-forming core, and have been proved successful in describing the observed SED and molecular line emission of high-mass star forming regions (Osorio et al. 1999, 2009; de Buizer et al. 2005; this work).

1.3.3 High-mass star formation

One of the main differences between low- and high-mass star formation is that the formation of high-mass stars happens on much shorter time scales and that they reach the main sequence before they have finished accreting all their mass. In addition, massive stars are usually born in clusters or groups, hence their individual study is usually affected by confusion, particularly because they are found at greater distances from the Sun than the sites of low-mass star formation. The advent and development of aperture synthesis radio telescopes in the last three decades have provided high angular resolution, sensitivity, and spectral resolution, and has open up this field for investigation.

Although at present there is no well-established evolutionary scheme for the formation of massive stars, observations have allowed to identify several successive stages in the formation of a massive star (e.g., Carrasco-González 2010):

- **Infrared Dark Clouds (IRDCs)**: These clouds are so dense that they are observed in absorption even at mid-IR wavelengths against the galactic background emission. They were first recognized in mid-infrared images from the Infrared Space Observatory (ISO) by Perault et al. (1996), and the Midcourse Space eXperiment (MSX) by Egan et al. (1998). They are characterized by very high densities ($n \sim 10^5$ cm^{-3}) and very low temperatures ($T \sim$ 10-20 K) (Carey et al. 1998, Pillai et al. 2006). It is though that these objects represent the initial conditions of high-mass star formation.

- **Hot Molecular Cores (HMCs)**: HMCs are small ($\sim$ 0.1 pc), dense (n $\sim$ 10^6-10^8 cm^{-3}), luminous (L $\sim$ 10^3-10^5 L$_\odot$), and hot (50-200 K) condensation with a significant extinction (A$_v$> 10^3 mag). HMCs are detected through dust emission at mm wavelengths, and through the compact emission of high excitation molecular lines, like the NH_3 inversion transitions. They are found near other young massive stars, are associated with water masers or methanol masers and present radio jet and outflows. HMCs are considered the cradles of massive stars, since it is thought that an OB-type protostars must be hosted in its interior, acting as the internal heating source. The dust emission and the molecular line emission from HMCs have been successfully modeled as an infalling envelope of gas and dust with a central massive star (Osorio et al. 1999, 2009; de Buizer et al. 2005). Despite their large luminosities, HMCs lack of strong free-free emission. This is interpreted as an effect of a very intense on-going accretion flow able to confine the bubbling photoionized region. Mass accretion rates as high as 6×10^{-3} M$_\odot$ yr^{-1} have been estimated in collapsing cores associated with high-mass star forming regions (eg., W51e2: Zhang & Ho 1997), whereas those associated with the formation of low-mass stars are typically $\sim$ 10^{-6} M$_\odot$ yr^{-1}. Despite the high luminosity and ionizing radiation of OB stars, neither radiation pressure nor thermal pressure are able to reverse such intense accretion flow (Keto & Wood 2006). Because of the compact size of massive cores and the typical large distances they are located, > 1 kpc, the typical angular diameter of a HMC is of $\sim$ 2 arcsec. So, high angular resolution observations are needed in the study of HMCs.

- **Hypercompact and Ultracompact HII regions**: Once the accretion rate decreases, the large amount of Lyman continuum photons are able to produce a detectable photoionized region. The first to be ionized is the material in the vicinity of the massive star, that is a thin layer in the surface of the accretion disk. Close to the star where the escape velocity is much greater than the sound speed, the ionized gas remains bound. Hypercompact HII regions, which are regions of $\sim$ 0.01 pc of size and electron densities greater than 10^6 cm^{-3} (Kurtz et al. 2000), may represent that evolutionary stage (Keto 2007). On the other hand, Ultracompact HII regions, which have sizes of 0.1 pc, electron densities greater than 10^4 cm^{-3} (Kurtz et al. 2000), are probably a later evolutionary stage, where the accretion disk has been destroyed and the molecular cloud has begun to dissipate, since the stellar wind and ionizing radiation of the massive star interacts with the lower dense and more poorly gravitationally bound molecular material (Zinnecker & Yorke 2007). It seems that either jets and outflows are destroyed by processes associated with the ionization, or survive the formation of the HII region but are difficult to detect (Tan & McKee 2003).

- **Classical HII regions**: They are characterized by gas photoionized globally, often by several ionizing sources. They expand hydrodynamically as a whole and disrupt the parent molecular cloud, revealing both the embedded high-mass and lower mass stellar population for optical and near-IR observations (Carpenter et al. 1993; Zinnecker, McCaughrean, Wilking & Moneti 1993). These objects are one of the first historical signatures used to search for sites of massive star formation (e.g. Mezger et al. 1967, Yorke 1986, Wood & Churchwell 1989)

1.4 Goals and work scheme

An understanding of the physical processes that dominate during the early stages of massive star formation requires a detailed knowledge of the physical conditions of the gas environment prior to and during the formation of the (proto)star. In this work we study the physical conditions of the environmental gas around massive (proto)stars paying special attention to its kinematics. By doing so, we intend to engage in the two open questions exposed in this chapter: Are cores initially quasi-static equilibrium configurations, or are they rapid evolving structures? And, how do massive stars form?

Examples of how the characterization of the kinematics can help in understanding massive star formation are the detection of rotating structures or large-scale infall. Evidence of rotating structures like accretion disks around massive stars rules out the coalescence formation scenario since this kind of structures are not expected to survive after shocks of stars. Also, detections of large-scale infall in early stages of the formation process would point directly to the monolithic collapse scenario since, in the competitive accretion scenario, infalling signatures would be likely blurred by the large tangential velocities and the velocity dispersion present in the complex cluster environments (Bonnell & Bate 2006).

As noted before, infall and outflow are expected to be present in the early stages of the star formation process and both may produce similar observational features in the spectral line profiles of molecular transitions (see Chapter 2), making them difficult to distinguish observationally. Also, the presence of rotation makes more difficult the identification of these motions. Characterizing the different systematic motions via unequivocal signatures is important to better understand the dynamic processes in star formation. For example, the HMC in G31.41+0.31 presents a SW-NE velocity gradient which has been observed in many molecular transitions but there is still an on-going controversy about the rotation or bipolar outflow nature of such a velocity gradient (Beltrán et al. 2005, Araya et al. 2008, Cesaroni et al. 2011). Also, two cores close in projection but with different systemic velocities produce features similar to a rotational or a bipolar outflow gradient. This might be the case of the molecular gas in W3(H_2O) (see Chapter 5), where the three different scenarios have been proposed: rotation (Shchekinov & Sobolev 2004), outflow (Alcolea et al. 1993), and two clumps with different radial velocities (Wilner et al. 1999).

The purpose of this work is twofold: to provide useful signatures that help to characterize the kinematics of the cores that will give birth to massive stars, and also to dissect the kinematics of two particular HMCs through a detailed observational study and modeling. This thesis is structured as follows:

- In Chapter 2 we introduce the "spectral imaging infall signature" predicted by Anglada et al. (1991). We explore the effect of rotation on that signature, and propose new kinematic signatures, "the central blue spot", which traces infall, the "blue spot and dimmer red spot pair" and "the roller coaster", which trace rotation plus infall.
- In Chapter 3 we use the formalism of Anglada et al. (1991) to obtain the kinematic features predicted by core equilibrium models and compare them with those predicted by non-equilibrium models. We compare the kinematic features derived through the Anglada et al. (1991) formalism with those obtained through a radiative transfer code.
- In Chapter 4 we analyze ammonia observations towards the HMC in the region G31.41+0.31. We present evidence of the "spectral imaging infall signature", the "central blue spot", "the blue spot and dimmer red spot pair", and "the roller coaster" signatures described in Chapter 2. We compare our observational results with the detailed predictions of a previous model of the source (Osorio et al. 2009).
- In Chapter 5 we present ammonia observations towards the HMCs in W3(H_2O). We model these sources and we estimate their physical conditions by fitting the SEDs and the ammonia emission. For the latter we developed a radiative transfer code to calculate the expected ammonia emission given the density, temperature and velocity fields.
- In Chapter 6 we present the main conclusions of this Thesis work.
- In Appendix A we describe the radiative transfer code developed in this work and its application to the ammonia molecule.

Chapter 2

In the search of kinematic signatures of infall

The earliest phases of star formation should be characterized by infall dominated motions. However, obtaining observational evidence for these motions associated with the star forming process constitutes a long-standing problem. The study of this kinematics is specially tricky since rotation, infall and outflow motions all together are present in the earliest phases of star formation and since they may produce similar observational features, what makes them easy to confuse. This situation worsens in the high-mass regime where the effects of embeddedness, large distances, multiplicity and interaction between stars are more important. Infall and outflow are difficult to distinguish observationally (Figure 2.1) unless high opacity effects, together with temperature and velocity gradient come into play. Bipolar outflows and rotation can result in similar features with red-shifted and blue-shifted areas in velocity maps (intensity-weighted mean velocity maps or centroid velocity maps), and are prone to lead to misinterpretation. Even two different regions close in projection but with slightly different systemic velocities can mimic a rotational or a bipolar outflow gradient.

Traditionally, most of the infall signatures have been based on the spectral line profile (1D), that gives the total flux density as a function of the velocity but lacks of any spatial information. In this sense, mapping signatures (2D) can provide a more complete information. In this chapter we will review the most used techniques to claim for observational evidence of infall motions. We will focus on the most complete infall signature (3D) based on spectral imaging suggested by Anglada et al. (1991), whose first observational evidence is presented here in this Thesis work. We will also explore how this signature is modified in the presence of rotation, and we will propose two new mapping signatures (consequence of the 3D signature of Anglada et al. 1991), one that evidences the existence of infall and a second that characterizes the equatorial plane of an infalling and rotating structure.

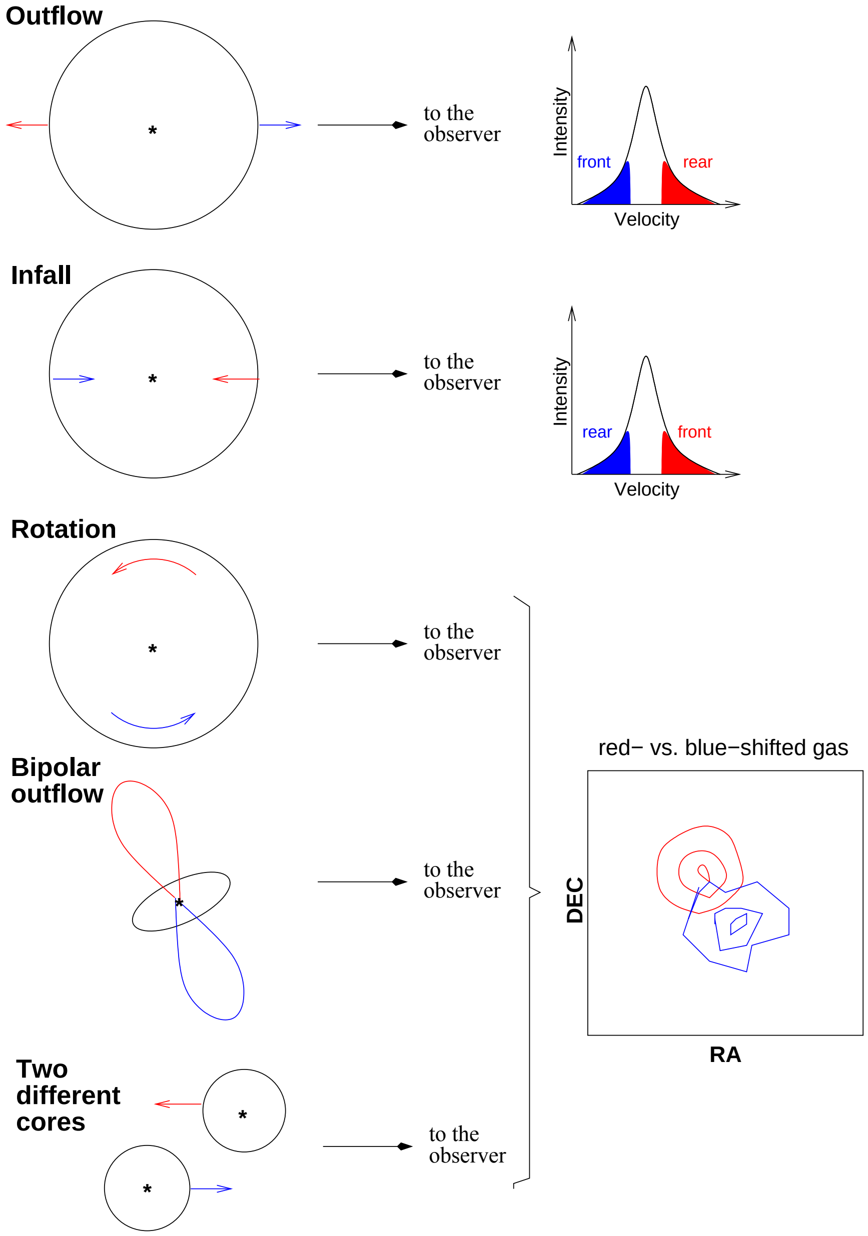

Figure 2.1: Sketch of the observation of different kinematic scenarios. *Upper panels:* Comparison of the spectral line profiles observed in case of outflow and infall motions. Line profiles are similar if temperature and velocity gradients are not considered. If the emission is optically thin, the line profile is symmetric and there is no way to distinguish the front from the rear side emission. Also, opacity effects alone would not produce distinguishable asymmetries since the front and the rear side emissions are decoupled because of the large difference in velocity. *Lower panels:* Expected map of the velocity-integrated red-shifted emission overlapped with the velocity-integrated blue-shifted emission in case of rotation, bipolar outflow, and different cores. The three scenarios result in similar maps.

2.1 Previously proposed infall signatures

The most used method to claim for the detection of infall is based on the so-called "blue-asymmetry". This signature consists in the appearance of two peaks in the spectral line profiles, being the blue-shifted peak stronger than the red-shifted peak. Snell & Loren (1977) were the first to propose that the observation of such feature in the CO line profile seen towards embedded stars may serve as evidence of collapse in dense interstellar clouds. They were able to explain the line profile in terms of geometric considerations under assumptions of temperature and the velocity gradient increasing inward. They proposed that under such conditions, a small red-shifted self-absorption in the line profile was produced given the aspect of double-peaked (see Figure 2.2).

Soon afterwards, the interpretation of Snell & Loren (1977) was criticized by Leung & Brown (1977), who argued that the Sobolev approximation (Sobolev 1957) used in the Snell & Loren (1977) calculations was invalid for the velocity fields considered, and therefore, they could not have used geometrical arguments to obtained the brightness temperature of the line. Instead, Leung & Brown (1977) calculated the line profile by solving the radiation transfer problem for a contracting core. They obtained a double-peaked line profile similar to those of Snell & Loren (1977) with the low velocity peak lower than the high-velocity peak and a minimum at small red-shifted velocities, even they used a velocity field with constant infall velocity. They argue that this skewing to lower velocities does not depend on the cloud geometry or on the form of the velocity field (as explained Snell & Loren 1977) but it occurs in optically thick lines as long as the excitation temperature increases inwards.

Myers et al. (1996) reproduce the "blue-asymmetry" simply by considering two plane parallel layers of gas at different excitation temperature approaching one another. This two-layer model has been widely used to determine infall and obtain physical characteristics of star forming regions. However, it has not been proved yet that such a simple 2-plane parallel model is a realistic approximation of the physical conditions in an infalling protostar, casting some doubts on some of the results found in the literature using this method.

The results of Leung & Brown (1977) and, the fact that a simple two-layer model can produce "blue-asymmetry", means that the "blue-asymmetry" analysis can say nothing about the velocity gradient inside a contracting sphere and nothing about the mode of accretion. In order to further constrain the velocity field, complementary observations are needed.

Additionally, the "blue-asymmetry" may not be even indicating collapse, as already pointed out by Leung & Brown (1977). Outflows, rotation, intrinsic asymmetries in the source, or the relative motion of unbound clouds could also produce a "blue-asymmetry" along a particular LOS of a given source. However, red asymmetries would be equally probable in these cases. Infall motion is the only process out of the three that would consistently produce the "blue-asymmetry" if the dynamics of cores are controlled by gravitational contraction. Then, in a large sample of sources the presence of infall should show a statistically significant excess of

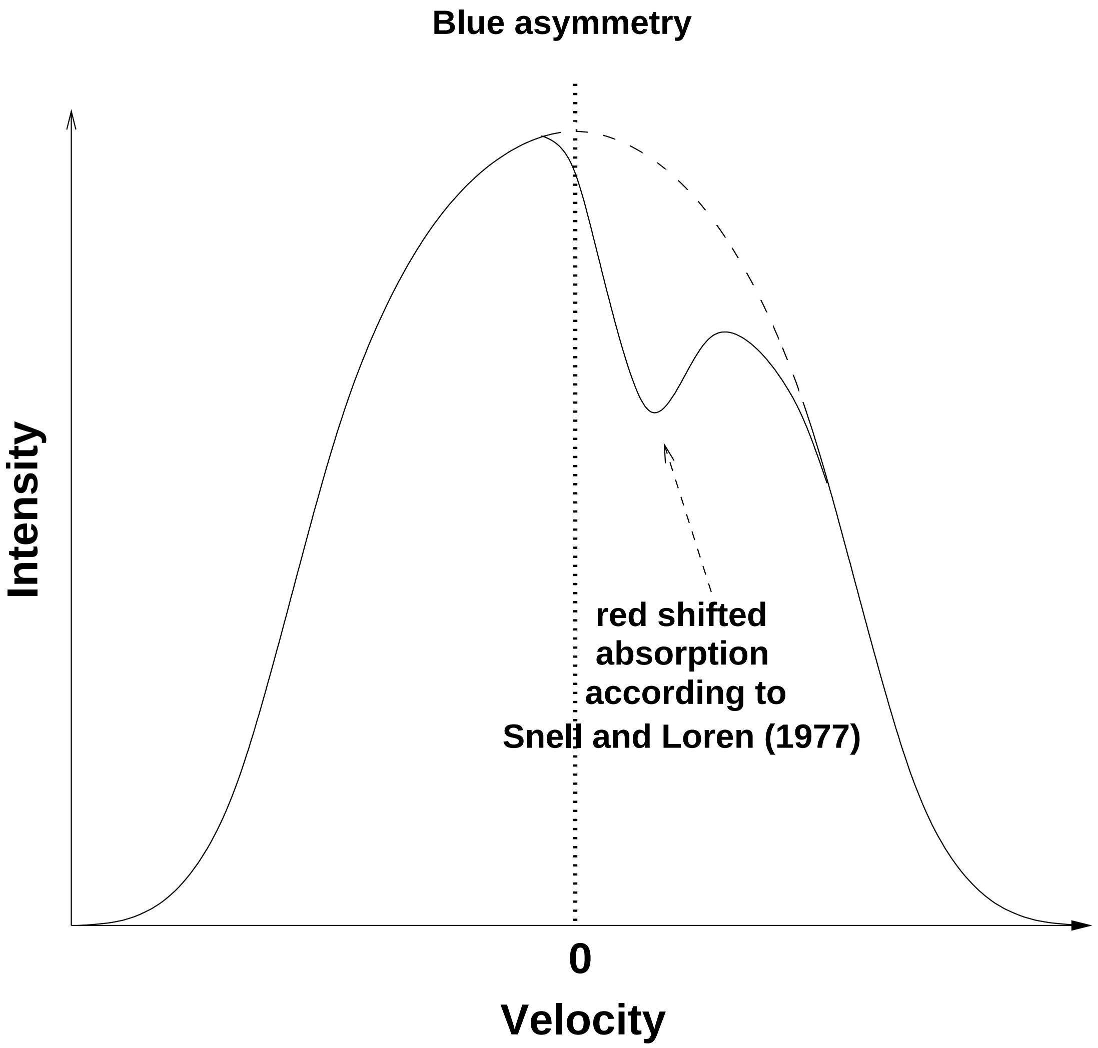

Figure 2.2: Line profile showing the "blue-asymmetry" signature, consisting in the presence of a double peak in the line profile, being the blue-shifted peak the stronger. According to Snell & Loren (1977), a red-shifted self-absorbed dip is produced, modifying the line profile, which adopts a double peak appearance. Because the dip is produced at red velocities, the peak at blue velocity results stronger than the one at red velocities.

blue asymmetries compared to red asymmetric profiles. However, some recent surveys (towards high-mass star forming sites) show approximately equal numbers of red and blue asymmetries (e.g., Purcell et al. 2006; Szymczak et al. 2007), what would indicate that the line profile is at least as sensitive to other systematic motions as to infall motions. The effect of protostellar collapse on molecular line emission can not be easily isolated from those of other dynamical processes. Moreover, the "blue-asymmetry" is based on the shape of the line profile at low velocities, but the emission at such velocities is couple with the emission of the ambient gas of the molecular cloud where the core is embedded, so the line profile as such velocities is expected to be affected by dynamics outside the core.

Despite all these impairments, the 1D "blue-asymmetry" signature, has been widely used to search for evidence of infall in low-mass star forming regions (e.g., Zhou et al. 1994; Mardones et al. 1997; Lee et al. 1999; Gregersen et al. 1997; 2000) and high-mass star forming regions (e.g., Wu & Evans 2003; Fuller et al. 2005; Klaassen & Wilson 2007; Wu et al. 2007).

Anglada et al. (1987) studied (still in a one dimensional analysis based only on the shape of the line profile) the infall signatures of an angularly unresolved protostellar core under the assumptions of optically thick line emission, gravitational infall motions dominating the kinematics over turbulent and thermal motions, infall velocity of the form $V \propto r^{-\alpha}$, and a temperature gradient increasing also towards the center. They focused on the asymmetries that occurs at high velocities in order to avoid confusion with emission from the ambient cloud at low velocities. They explained that, in an infalling spherical core where a protostar is forming, if the velocity increases towards the center (as it is expected because gravitational acceleration), then, the points with the same LOS velocity (V_z) will form closed surfaces, as it is illustrated in Figure 2.3a. Hereafter we will designate these isovelocity surfaces as "V_z-surfaces". In general, a given LOS intersects the same V_z-surface twice. All the V_z-surfaces have the same shape, they decrease in size with increasing magnitude of the LOS velocity, are nested, and converge at the core center. The intensity of the line profile at a given LOS velocity, $I(V_z)$, would arise from the material located in the corresponding V_z-surface. The assumption of large opacity allows to adopt a simple approach similar to the Sobolev approximation (see Appendix A.2 in Anglada et al. 1987). The Sobolev approximation means that, along a given line of sight, the gas contributing to the emission at a given radial velocity has negligible changes in its physical parameters. For simplicity, Anglada et al. (1987) assumed that the depth of the region of gas along the LOS that emits at a given radial velocity, which is determined by the thermal width (ΔV_{th}), is relatively small,

$$\Delta z_{th} < \left(\frac{dV_z}{dz}\right)^{-1} \Delta V_{th}; \tag{2.1}$$

this is equivalent to consider narrow isovelocity regions, or that radiatively coupled gas concentrates in a thin layer. This assumption implies that only a very thin edge of the V_z-surface, where physical properties are unlikely to vary significantly, would be observable and, hence, only the part of the surface facing the observer (Figure 2.3a; thick line) is observable, while the rear part (Figure 2.3a; thin line) is not observable. If the temperature also increases inwards, for the red-shifted velocities, the outer and colder part of the V_z-surfaces are in between the observer and the hotter inner side of the V_z-surfaces. On average, the blue-shifted emission comes from points that are closest to the protostar (and, therefore, hotter) than the corresponding red-shifted ones (see Figure 2.3a), and therefore this results in asymmetric line profiles (Figure 2.3b), with the blue-shifted side stronger than the red-shifted one. The authors calculated that such difference should be of the order of two.

Inverse P-Cygni profiles, which consist in the detection of absorption at red velocities against a bright background continuum source, are usually considered a reliable infall signature. In several cases, inverse P-Cygni profiles have been observed in molecular lines against a bright background HII region (e.g., Keto, Ho & Haschick 1987, 1988; Ho & Young 1996; Zhang & Ho 1997; Zhang, Ho & Ohashi 1998) or against the bright dust continuum emission of the hot protostellar core itself (e.g., Di Francesco et al. 2001; Girart et al. 2009) and have been interpreted as infall motions of the surrounding envelope. Nevertheless, it uniquely indicates that foreground matter is moving towards a hotter source, no matter how or if it is indeed gravitationally bound.

Mapping signatures can provide additional evidence of the existence of infall by providing a deeper description of the internal kinematics of the core. For instance, the "blue bulge" signature uses centroid velocity maps, $V(x, y)$, to identify infall signatures in rotating structures (e.g., Adelson & Leung 1988; Walker, Narayanan, & Boss 1994; Narayanan & Walker 1998) realized that, while only a rotational velocity field is present, then a centroid velocity map will show blue-shifted emission on one side of the rotation axis and red-shifted emission on the opposite side, but if infall is occurring, blue-shifted emission may be observed across the rotational axis through the core center on what would otherwise be the red-shifted side of the map. They proposed such an excess of blue-shifted emission towards the center as a signature to detect infall in a rotating structure and stated that it is preferentially detected in the equatorial plane (rotation axis in the plane of the sky). However, 2D signatures provide some spatial information but the shape of the line profile is not taken into account, resulting in an incomplete information on the kinematics and physical structure of the core.

2.2 The spectral imaging infall signature

2.2.1 Asymmetries in the spatial intensity distribution

Anglada et al. (1991) (hereafter A91) propose a more complete 3D signature of infall based on the spatial intensity distribution as a function of the velocity, $I_\nu(\alpha, \delta, V_z)$. These authors calculated the expected images for angularly resolved collapsing cores for different LOS velocities (channel maps) following the assumptions of Anglada et al. (1987). The V_z-surfaces are those of Figure 2.4a. If the opacity is high enough, then only a very thin edge of the V_z-surface, where physical properties do not vary significantly, would be observable and, hence, the intensity map at a given LOS velocity is in fact an image of the excitation temperature distribution in the side of the V_z-surface facing the observer (thick line in Figure 2.4a), while the emission from the rear side (thin line in Figure 2.4a) remains hidden. Since in protostellar

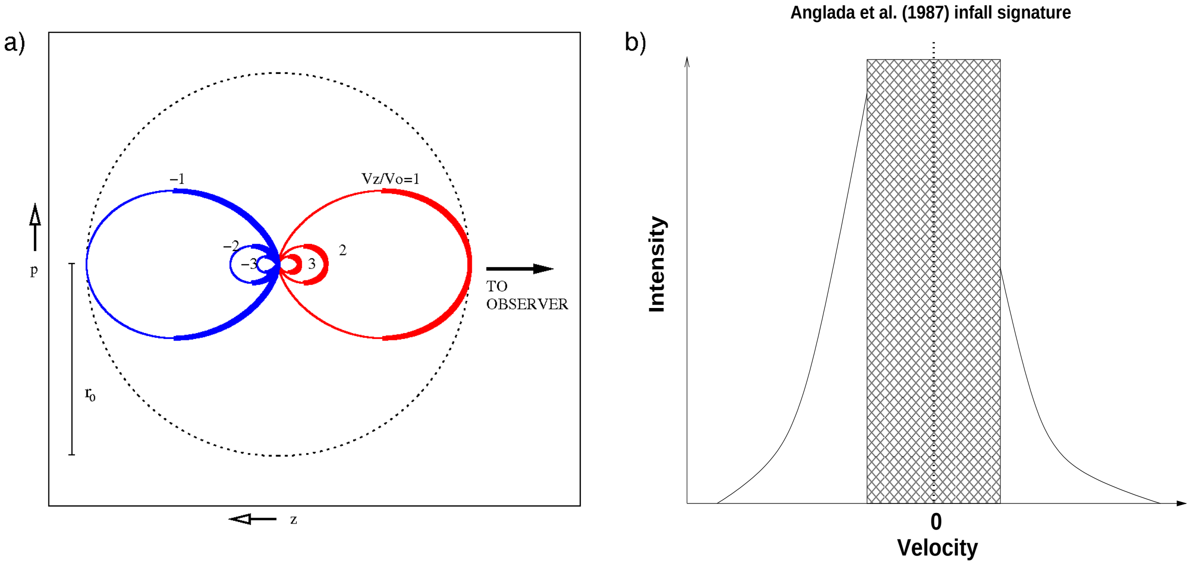

Figure 2.3: *(a)* Surfaces of equal LOS velocity for a collapsing protostellar envelope with a velocity field of $V \propto r^{-1/2}$. Note that a given LOS intersects an isovelocity surface at two points. The V$_z$-surfaces are nested having all the same shape, and decreasing in size with increasing LOS velocity. Also, all of them converge at the core center, where coordinates are (0,0). *(b)* Infall asymmetry predicted by Anglada et al. (1987) for a collapsing sphere under conditions of high line opacity is shown. It consists on a blue side of the line profile intrinsically stronger than the red side. If opacity is high enough, only the side of the V$_z$-surfaces facing the observer are visible, while the rear parts remain hidden. While for blue velocities the visible frontal side of the V$_z$-surface is the one closer to the central (proto)star (hotter), for red velocities the frontal side is the more external side (colder). Thus, the blue-shifted emission comes from points on averaged hotter and therefore its emission results stronger. The central part of the line profile is not shown since the emission at low velocities is easily confused with the ambient cloud emission.

collapse the temperature increases towards the center of the core, for red-shifted channels, the center of the image corresponds to a region that is slightly farther away from the center of the core and, thus, colder than the edges (Figure 2.4a). Conversely, for blue-shifted channels, the center of the image corresponds to the emission from a region very close to the center of the core and, therefore, very hot. This produces very different images in red-shifted and blue-shifted channels. In the image of a red-shifted channel, the intensity is almost constant over the emitting region, decreasing slightly towards the center, while in the corresponding blue-shifted channel the intensity increases sharply towards the center of the image (see Fig. 2.4b). Additionally, since the size of the V_z-surfaces decreases with increasing (relative) velocity, the emission becomes more compact at higher (relative) velocities for both, red- and blue-shifted channels. The detectability of these 3D infall signatures depends strongly on the beam-to-source size ratio since one needs to resolve angularly the infalling gas to obtain images.

Optically thin lines would have symmetric profiles and equal images in channel maps for symmetric red- and blue-shifted velocities. It should be noted that the set of "spatial intensity profiles" (intensity as a function of the projected distance to the core center) for different velocity channels shown in (Fig. 2.4b) is actually equivalent to a position-velocity (P-V) diagram. However, in a conventional P-V diagram the spatially resolved infall signatures are usually more difficult to identify.

While "1D spectral signatures" do not provide enough information on the spatial structure of the source, the three dimensional character of the "spectral imaging infall signature" of A91 can provide more complete information on the velocity field in the core, and it is not easily mimicked by other scenarios such as rotation, outflow, intrinsic asymmetries in the source, or the relative motion of unbound clouds. Observational evidence of this theoretically predicted signature has been obtained for the first time in this Thesis work (see Section 4.4.1).

2.2.2 The "central blue spot"

The infall signatures in the spatial intensity profiles produce an additional signature in the maps of the first-order moment of spectral lines (intensity-weighted mean velocity, equivalent to a centroid velocity map). This signature is easily identifiable, and consists in a compact spot of blue-shifted emission towards the peak of integrated intensity (zeroth-order moment) of the source. This spot of blue-shifted emission is a consequence of the differences in intensity and spatial distribution of the emission in the red- and blue-shifted channels. As it is illustrated in Figure 2.4b, the emission near the edges of the emitting region has a similar intensity in the pairs of red- and blue-shifted velocity channels that are symmetrically located with respect to the systemic velocity of the cloud. However, while the intensity distribution remains almost flat in the red-shifted channels, it rises sharply towards the center in the blue-shifted channels. As a consequence, the intensity-weighted mean velocity towards the central region will appear blue-shifted because of the higher weight of the strong blue-shifted emission. Additionally, the integrated intensity (zeroth-order moment) will peak towards the central position. As

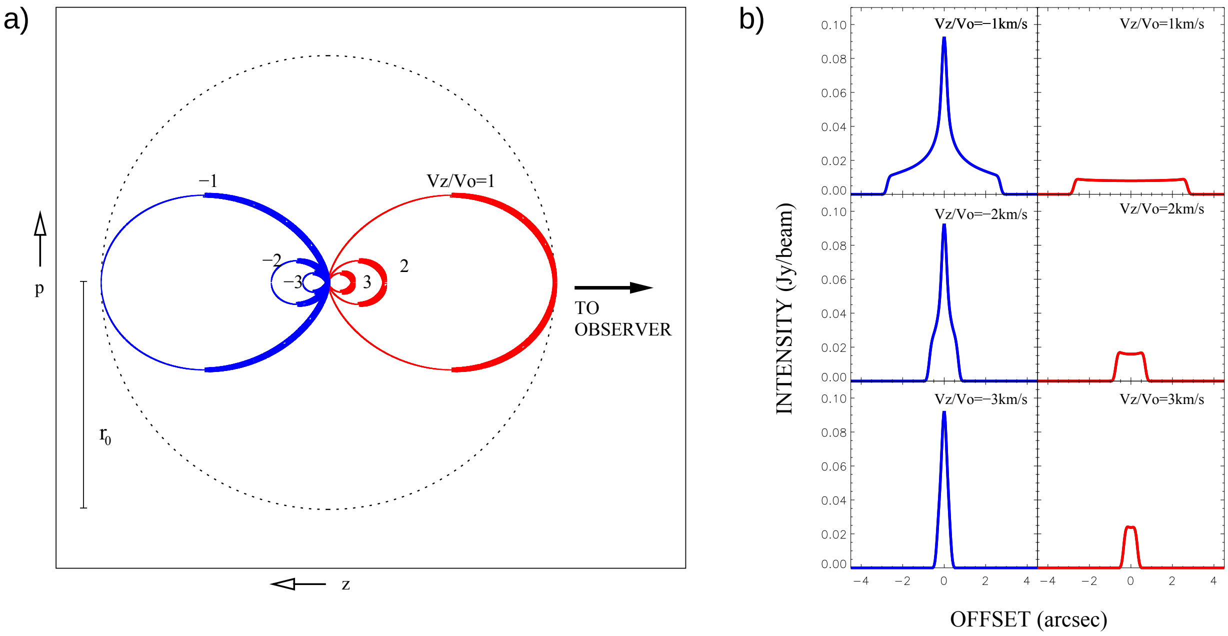

Figure 2.4: *(a)* Surfaces of equal LOS velocity for a collapsing core with a velocity field $V = V_o(r/r_o)^{1/2}$. Note that a given LOS intersects an isovelocity surface at two points. The V$_z$-surfaces are nested, having the same shape and decreasing in size with increasing LOS velocity. Also, all of them converge at the core center, where the coordinates are (0,0). *(b)* Intensity as a function of projected angular offset on the plane of the sky from the source center for channel maps of different velocities. If the emission at each velocity is optically thick, only the part of the surface facing the observer (thick line) is observable, while the rear part (thin line) is not observable and channel maps are, in fact, images of the temperature distribution in the side of the isovelocity surfaces facing the observer. For red-shifted channels, the center of the image corresponds to a region slightly farther away from the center of the core (and, thus, slightly colder) than the edges. Conversely, for blue-shifted channels, the center of the image arises from a region very close to the center of the core (and, therefore, very hot). This produces very different images in red-shifted and blue-shifted channels. In a red-shifted channel, the intensity is almost constant over the emitting region (decreasing slightly at the center) while in the corresponding blue-shifted channel the intensity increases sharply towards the center of the image. Additionally, the emission becomes more compact as the absolute value of the velocity increases. Calculations correspond to a simple model for an 1 M$_\odot$ protostar at 160 pc observed with a beam of $0\farcs2$ at the time when a central mass of $\sim$ 0.64 M$_\odot$ has been accreted (from Anglada et al. 1991).

one moves away from the center the integrated intensity decreases, the blue and red-shifted intensities become similar, and the intensity-weighted mean velocity approaches the systemic velocity of the cloud. Therefore, the first-order moment of an infalling envelope is expected to be characterized by a compact spot of blue-shifted emission towards the position of the zeroth-order moment peak (Figure 2.5). We will designate this infall signature the “central blue spot”. Note that the “central blue spot” is a 2D mapping signature since it is obtained by collapsing the velocity dimension of the “spectral imaging infall signature”. One of the advantage of the “central blue spot” it does not require an “a priori” knowledge of the systemic velocity of the cloud. An accurate knowledge of the systemic velocity is critical in searching for infall through the analysis of asymmetries in the line profiles. Note that, this problem is somehow alleviated in the “spectral imaging signature” of A91 because the comparison is not only made in terms of intensity but also the shape of the intensity profile is taken into account.

2.3 Kinematic signatures in the presence of rotation

2.3.1 Asymmetries in the spatial intensity distribution in the presence of rotation

The above model is spherically symmetric and rotation was not included. However, rotation plays a decisive role in star formation, it makes the matter to land on an accretion disk. Such accretion disk may be supported centrifugally, what makes rotation provides efficient support against further gravitational collapse. In the following, we will discuss how the “spectral imaging infall signature” of A91 is modified, if still stands, in the presence of rotation.

The combination of both motions, rotation and infall, produces four differentiated zones in the core, as is illustrated in Figure 2.6. In zones labeled as I and III the velocity projection along the LOS of rotation and infall movements have equal signs, but in zone II and IV, they have opposite signs. Let us consider now two generic points P1, and P2, which are symmetrically located respect the LOS that passes through the core center and are contained in a plane perpendicular to the rotation axis (assumed in the plane of the sky for simplicity). That is, for a given plane perpendicular to the rotation axis, P1 and P2 would have polar coordinates (r,-α) and (r,α) respectively, as indicated in Figure 2.6. In the non-rotating case both points have the same projected velocity, and therefore, form part of the same V$_z$-surface.

When rotation is added, the symmetry is broken down. While point P1 is placed in area I, where rotation and infall projections summed up, point P2 is placed in area II, where rotation and infall tend to compensate one another. Hence, it happens that the projected velocity in P1 is greater than in P2. If we further assume that infall velocity increases towards the center and also that the rotational velocity increases inwards, as it is expected because of conservation of angular momentum, then, a point along the radial direction of P2 that belongs to the same V$_z$-surface of P1 needs to be closer to the center than P2. And also, a point along the radial

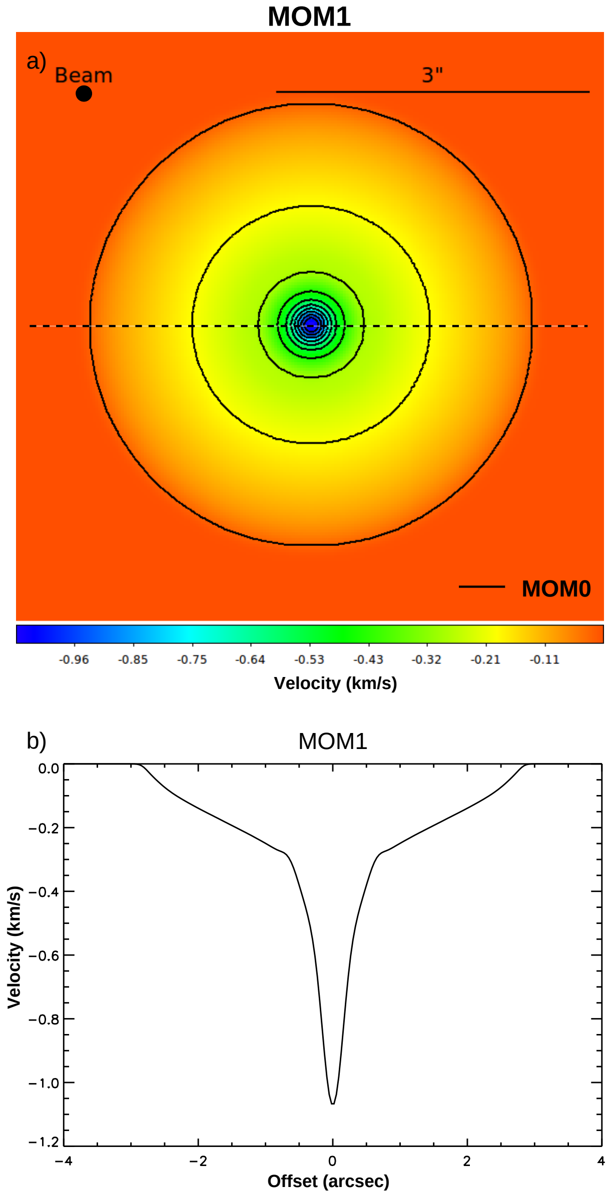

Figure 2.5: *(a)* Intensity weighted mean velocity map (first-order moment) in colors overlapped with the velocity integrated intensity map (zeroth-order moment) in contours. Contours are 0.021, 0.043, 0.085, 0.128, 0.170, 0.213, 0.255, 0.298, 0.34, and 0.383 mJy beam^{-1} km s^{-1}. *(b)* Plot of the first-order moment (intensity-weighted mean velocity) as a function of angular offset from the source center. Note that since calculations are done for a spherically collapsing core, the shown projection of the first-order moment map is valid for any PA. The systemic velocity of the cloud has been assumed zero. Calculations correspond to a simple spherically symmetric model for an 1 M$_\odot$ collapsing protostar at 160 pc observed with a beam of $0\farcs2$ at the time when a central mass of $\sim$ 0.64 M$_\odot$ has been accreted.

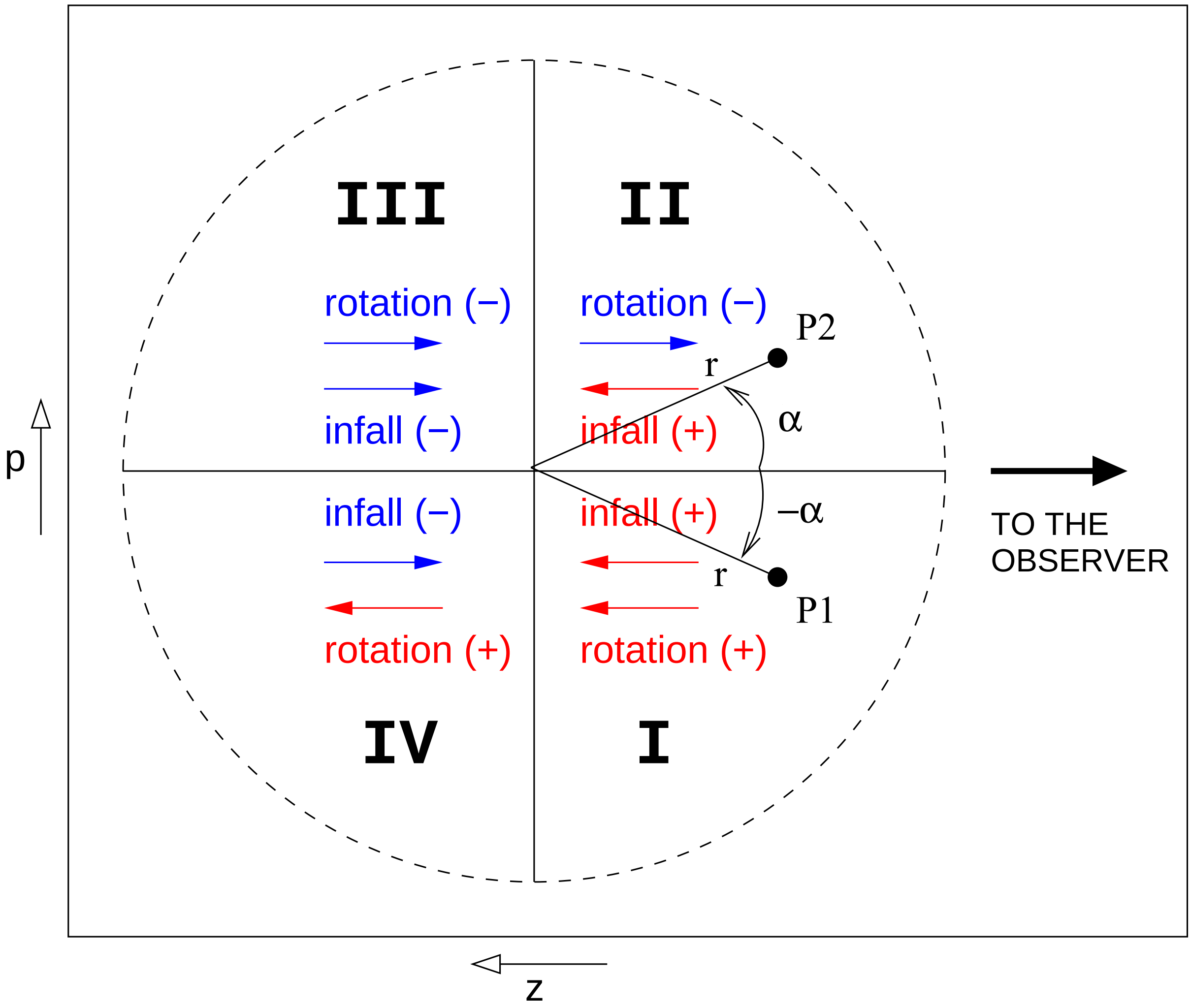

Figure 2.6: Sketch of the distribution of the velocity components in an infalling and rotating core. The combination of infall and rotation motions divides the core in four region. In regions I and III the projections along the LOS of infall and rotation motions have equal sign. In regions II, and IV they have opposite signs. Two generic points, P1 and P2, symmetrically placed with respect to the LOS that crosses through the center of the cloud, in the absence of rotation have the same projected velocity along the LOS and thus belong to the same isovelocity surface. When rotation is included the projected velocity along the LOS of P1 is greater than that of P2 and they no longer belong to the same V_z-surface. As rotation and infall velocity are assumed to increase inwards, the point along the radial direction of P2 with the same projected velocity of P1 (and thus belonging to the same V_z-surface) must be closer to the center. In the same way, a point along the radial direction of P1 with the same projected velocity as P2 must be further away from the center than P1. The result is that the isovelocity surfaces are asymmetric, they enlarge where the infall and rotation have equal sign along the LOS and shrink where have opposite sign.

direction of P1 that belongs to the same V$_z$-surface of P2, it is necessary further away from the center than P1. The final result is that V$_z$-surfaces are more extended to the side where rotation and infall have equal signs (zone I) than they are where rotation and infall have opposite signs (zone II). The same reasoning can be made for points in areas III and IV. As consequence, given a LOS velocity (channel velocity), the observed emission from a collapsing and rotating cloud will be asymmetric with respect to the rotation axis, and its spatial intensity profiles will be stretched on the side where the channel and rotation velocities are both red-shifted or both blue-shifted while they will shrunk on the opposite side.

To quantify this analysis of an infalling rotating envelope, and to compare it with the non-rotating case, we have considered a system with properties similar to those of the example described in A91 (Figure 2.4), but with the velocity field given by the TSC (Terebey, Shu, & Cassen 1984) prescription. The TSC formalism provides a generalized solution of the problem of the spherical collapse of a singular isothermal sphere (Shu 1977) that includes the effects of an initially uniform and slow rotation. The velocity field of the TSC formalism is given by equations 5.4. Note that it has azimuthal and polar velocity components different than zero. Matter does not fall radially onto the central protostar, but settles into a centrifugally supported disk around it (Terebey, Shu, & Cassen 1984; Shu et al. 1987). If the angular momentum of the infalling material, h, is conserved, then its final circular orbit has a radius, R, that follows:

$$R = \frac{h^2}{GM} \ . \tag{2.2}$$

If the core is initially in uniform rotation with an angular velocity Ω, then, the angular momentum of the material at a distance r_0 varies with the polar angle θ, as $h = \Omega r_0^2 sin\theta$. Thus, the material falling in from different θ but same r_0 will arrive at the plane perpendicular to the rotation axis at different radii. The material from regions $\theta \sim \pi/2$ is the one that lands at a largest radius. One can define a centrifugal radius that represents the maximum distance at which matter initially at a distance r_0 settles in the disk:

$$r_c = r_0^4 \Omega^2 / GM_\star \ . \tag{2.3}$$

Initially most of the mass falls close to the center, because the material that falls in first has small angular momentum. As collapse continues, material from larger radii, with much larger angular momentum, is added to the disk rather than to the central star. As shown by Hartmann (2008) the centrifugal radius increases with the square of the angular momentum, that goes as t^4, and decreases with the accumulated mass of the central star, that increases linearly with t, so finally the r_c is expected to increase rapidly with time, as t^3. In the inner region of the infalling envelope (near the centrifugal radius, r_c), the magnitude of rotation and infall velocities tend to equal, and the density adopts a flattened configuration towards the equatorial plane. At larger radii (much larger than the centrifugal radius), the density law tends to the free-fall form solution with nearly radial streamlines. For a further description of the model see Chapter 5.

Figure 2.7a shows the contours of equal LOS velocity of the TSC velocity field close to the equatorial z-p plane, for an example that considers $\mathrm{r_c} = 100$ AU. The TSC isovelocity contours are closed curves with sizes similar to those of radial infall shown in Figure 2.4a. However, in radial infall all the isovelocity contours are aligned and axially symmetric with respect to the LOS towards the center, while the TSC isovelocity contours are asymmetric with respect to this LOS, and they appear somewhat distorted. The axis going from the center of the core to the vertex (the point more distant from the center) of the TSC isovelocity contours is rotated with respect to the LOS towards the core center. The angle of rotation of this axis increases from the outer (lower) isovelocity contours to the inner (higher) isovelocity contours where it reaches $\sim 45°$. This is because in the TSC formalism the rotation velocity is small in the outer parts of the infalling region, that behave almost as free-fall, while in the proximity of the centrifugal radius, in the equatorial plane, it becomes comparable to the radial component.

Following the simplified analysis of A91, that assumes a high enough optical depth, the intensity map at a given LOS velocity is, in fact, an image of the excitation temperature distribution in the side facing the observer of the corresponding V_z-surface. Since the axes of the TSC isovelocity contours are misaligned with respect to the LOS, the observer will see an asymmetric source in each velocity channel. In the geometry defined in Figure 2.7 (rotation perpendicular to the LOS and positive position offsets in the areas with blue-shifted rotation), the emission in the red-shifted channels will be more extended at negative offsets and more compact at positive offsets, while in the blue-shifted channels the emission will appear more extended at positive offsets and more compact at negative offsets. Thus, the spatial intensity profiles will be asymmetric as illustrated in Figure 2.7b, where we show the spatial intensity profile along the equatorial direction, for different velocity channels. As in the non-rotating case, the images in blue-shifted channels present centrally peaked intensity distributions, while the red-shifted channels present flatter intensity distributions; and the emission becomes more compact with increasing LOS velocity, V_z. Then, the main difference with respect to the non-rotating case is the opposite asymmetry, with respect to the central position, of the red- and blue-shifted pairs of velocity channels (Mayen-Gijon et al. 2014). Although, for simplicity, this has been exemplified to the case of rotation perpendicular to the LOS ($i = 0$), it can be generalized to any inclination angle, except for $i = 0°$, in which rotation can not be detected.

It is important to note that rotation does not mask the spectral imaging signatures of infall proposed by A91, but just modifies these signatures by making the spatial intensity profiles asymmetric. The infall signature is maintained, in part, because of the relatively small value of the centrifugal radius considered (r_c=100AU). The TSC model predict practically radial infalling movements for $r \gg r_c$, therefore, by taking a small r_c in comparison with the core size we are, somewhat, forcing most of the core to be in the radial infall regime. However, the centrifugal support is supposed to grow as collapse proceeds, which results in an increase of the centrifugal radius with time as well, $r_c \propto t^3$ (Hartmann 2008). Effects of large r_c are studied in a later Chapter when exploring the region W3($\mathrm{H_2O}$).

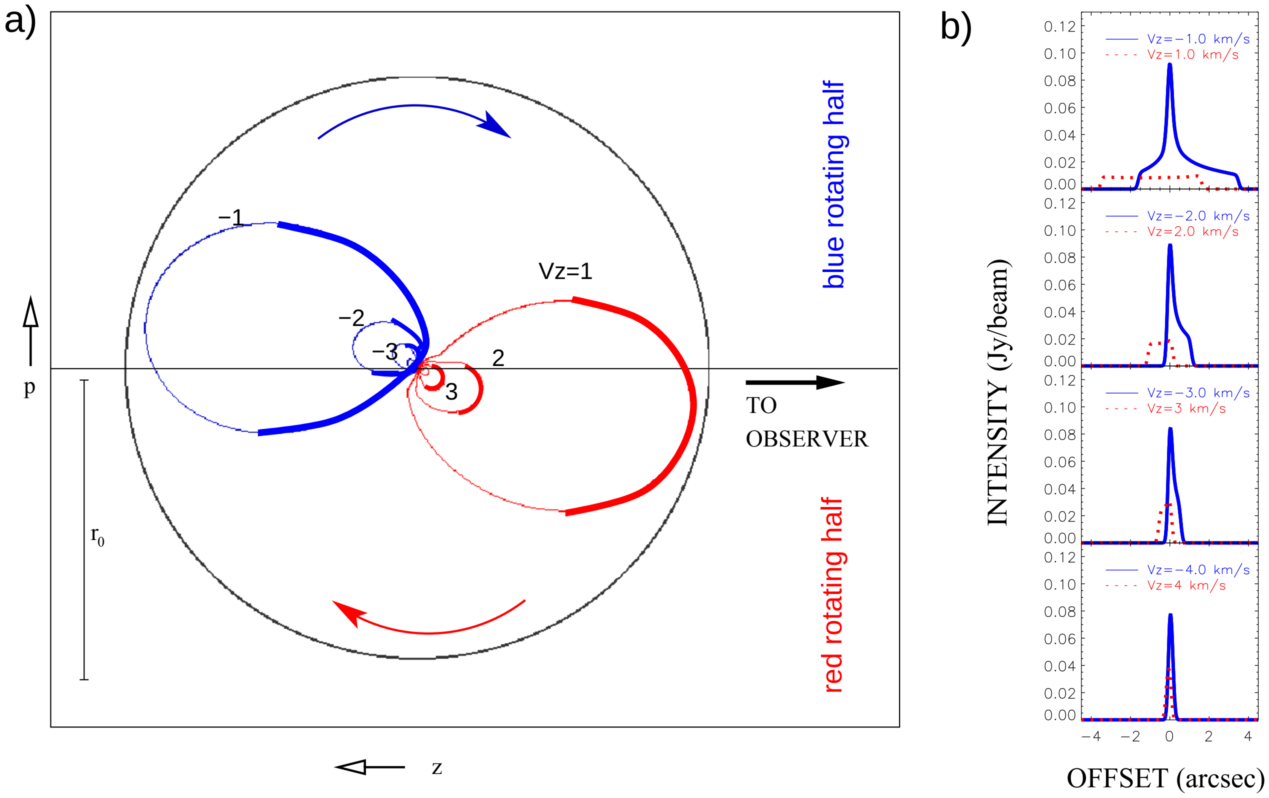

Figure 2.7: *(a)* Contours of equal LOS velocity for a collapsing and rotating core in a z-p plane close to the equator, as described by the TSC formalism (Terebey, Shu, & Cassen 1984). The (0,0) offset corresponds to the position of the central protostar. The angular momentum is assumed to be perpendicular to the z-p plane, and pointing inside the page (clockwise rotation, as seen from the reader). Note that, in general, a given LOS intersects a V_z-surface at two points. If the emission at each velocity is optically thick, only the part of the V_z-surface facing the observer (thick line) is observable, while the rear part (thin line) is not observable. In comparison with the radial collapse shown in Figure 2.4, where all the V_z-surfaces are symmetric with respect to the LOS to the center, the main effect of the rotation of the cloud is to rotate the axes of the V_z-surfaces in the sense of the cloud rotation. *(b)* Intensity as a function of angular offset from the source center, in the equatorial direction, for channel maps of different LOS velocity. As channel maps are, in fact, images of the temperature distribution in the corresponding V_z-surfaces, the misalignment of the axes of the V_z-surfaces with respect to the central LOS results in asymmetries in the observed spatial intensity profiles. Calculations correspond to the emission of an optically thick molecular line transition that is well thermalized, for a central protostar of ~ 0.64 M$_\odot$ at 160 pc observed with a beam of $0\farcs2$. A centrifugal radius of 100 AU has been assumed.

2.3.2 The effect of rotation on the "blue spot"

In order to understand better the effects of rotation on the “blue spot” we first show the case of pure rotation. Figure 2.8 shows the V_z-surfaces and their corresponding spatial intensity profile for an envelope undergoing pure Keplerian rotation for a central mass of 0.64 $M_\odot$. The V_z-surfaces are aligned in a direction perpendicular to the LOS. Red- and blue-shifted emission come from different sides of the rotation axis. The fact that the Keplerian velocity field monotonically decreases to zero with r makes the V_z-surfaces to be closed, similarly to what happened in the pure infall case (Figure 2.4), and so, in general each LOS intercepts a given V_z-surface twice. However, contrary to the case of infall, the spatial intensity profile for blue- and red-shifted channels are similar, indeed they have the same profile but with reflection symmetry one another (Figure 2.8b). We will refer to the half of the core where rotation shifts velocities to red (blue) as the red (blue) rotating half. A cut along the equatorial direction of the first-order moment is presented in Figure 2.9. It shows a “blue spot” and a “red spot” in the immediate vicinity of the core center. Such “blue” and “red spots” account for the strong emission of the high-velocity V_z-surfaces, smaller in size. Figure 2.10 shows an observational example of the presence of the “red and blue spots” in the first-order moment for a rotating structure around a central star (ALMA data; de Gregorio-Monsalvo et al. 2013).

It should be noted that, in pure radial infall all the isovelocity surfaces are aligned along the LOS towards the core center since they are axially symmetric with respect to this LOS (see Figure 2.4). This implies that, if emission at a velocity V_z is present along a given LOS then a counter-part of emission at velocity $-V_z$ will also be present (assuming the rest velocity of the cloud to be $V_{LSR} = 0$), but because the blue-shifted emission gets stronger than the red-shifted emission as one gets closer to the center (Figure 2.4b), the first-order moment shows a central blue spot.

The effect of rotation in a collapsing core is that the V_z-surfaces corresponding to blue-shifted velocities are stretched in the blue rotating half, and shrunk in the red rotating half. The contrary happens for the V_z-surfaces corresponding to red velocities (see Figure 2.7a). This effect gets more pronounced as the velocity increases since then, the relative contribution of the rotation component becomes more important. So, for large enough velocities, close to the core center, the emission of the V_z-surfaces of opposite sign velocities would come from different halves of the core (at both sides of the rotation axis), similarly to what happens in the pure rotating case. As a consequence, at the blue rotating half, the blue-shifted emission of high velocity creates in the vicinity of the core center a “blue spot”. Note that, this “blue spot” is bluer than the “central blue spot” in the pure infall case (assuming the same physical conditions of temperature, density and central mass) since there is no counterpart of red-shifted emission of high velocity at the blue rotating half of the core. Additionally, at the red rotating half, the high velocity red-shifted emission near the core center, which would not be counter-balanced by the corresponding blue-shifted emission of high velocity as it has been displaced towards the other side of the rotation axis, creates a “red spot”. Note that, because of the infall asymmetry the red-shifted emission is expected to be less intense than the blue-shifted emission (Figure

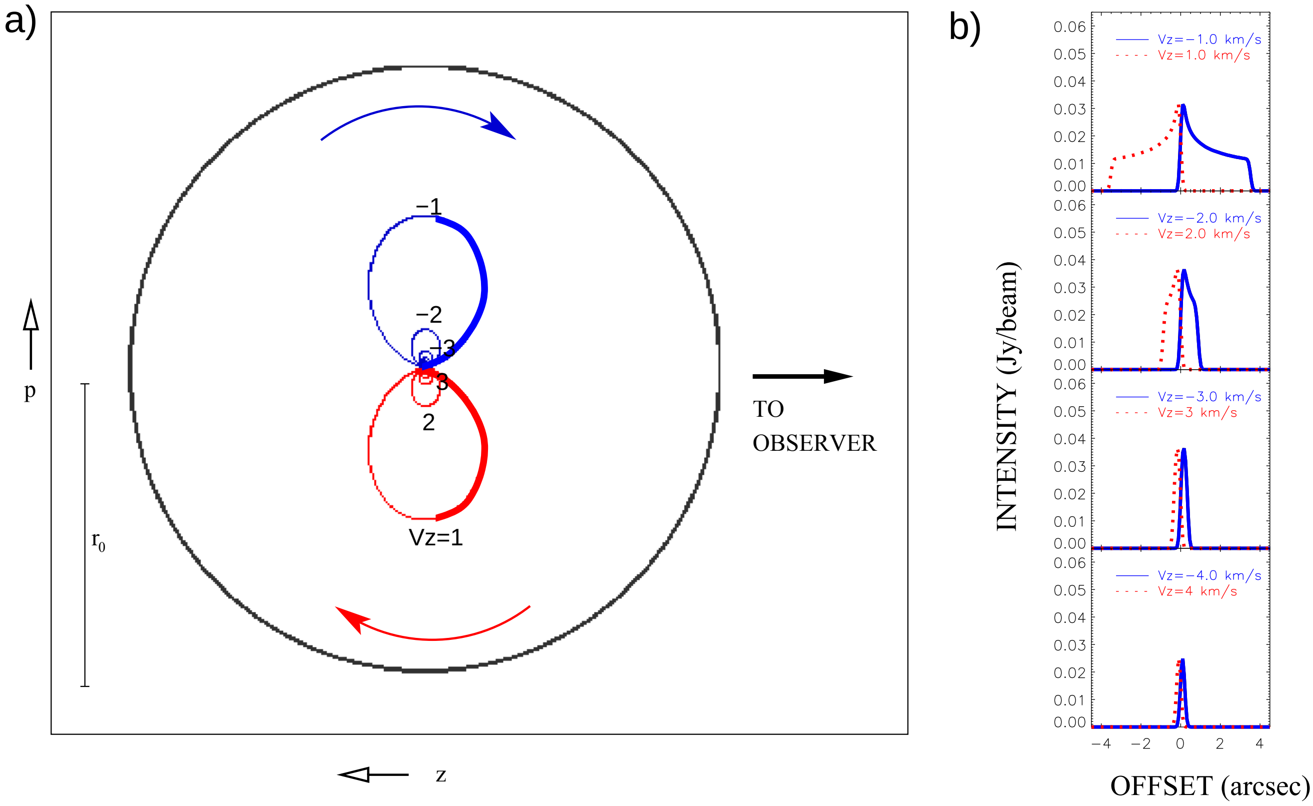

Figure 2.8: *(a)* Contours of equal LOS velocity for a rotating structure undergoing pure keplerian rotation in the equator plane. The (0,0) offset corresponds to the position of the central protostar. The angular momentum is assumed to be perpendicular to the z-p plane, and pointing inside the page (clockwise rotation, as seen from the reader). Note that, in general, a given LOS intersects a isovelocity contour at two points. If the emission at each velocity is optically thick, only the part of the isovelocity contour facing the observer (thick line) is observable, while the rear part (thin line) is not observable. In comparison with the radial collapse shown in Figure 2.4 in the equatorial plane, where all the isovelocity contours are aligned along the LOS towards the source center, in the pure rotation case, the isovelocity contours are aligned in the perpendicular direction to the LOS. *(b)* Intensity as a function of angular offset from the source center, in the equatorial direction, for channel maps of different LOS velocity. As channel maps are, in fact, images of the temperature distribution in the corresponding isovelocity contour, the spatial intensity profiles of the red-shifted emission is a mirror reflection of the blue-shifted emission. Calculations correspond to the emission of an optically thick molecular line transition that is well thermalized, for a central protostar of $\sim 0.64\ M_\odot$ at 160 pc observed with a beam of $0\farcs2$.

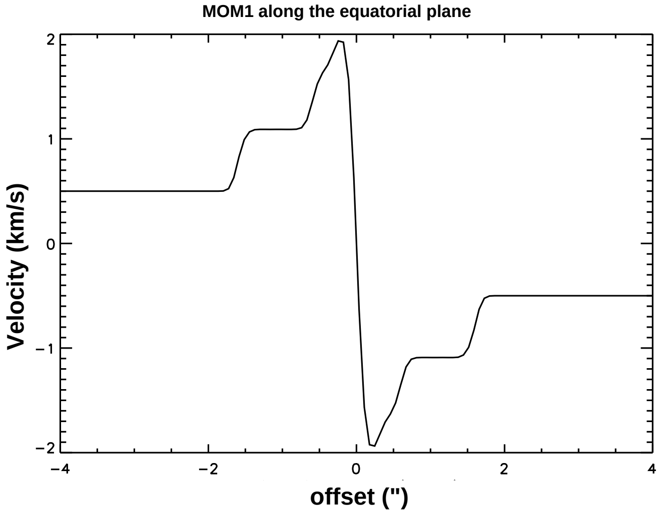

Figure 2.9: Cut of the intensity-weighted mean velocity (first-order moment) as a function of angular offset from the source center along the equatorial plane. The systemic velocity of the cloud has been assumed to be zero. Calculations correspond to the emission of an optically thick molecular line transition that is well thermalized, for a central protostar of ~ 0.64 $M_\odot$ at 160 pc observed with a beam of $0\rlap{.}''2$ and with spectral resolution of 1 km s^{-1}.

2.7), the "red spot" has a less absolute velocity than the “blue spot”. The final result is that rotation makes the “central blue spot” even bluer and moves it off the center towards the blue rotating half, additionally a “dimmer red spot” at the opposite side of the rotation axis appears.

It is important to note that the difference with respect to the pure rotating case resides in that in pure rotation, the “red” and “blue spot” have equal absolute values, but in the presence of infall, the “blue spot” is more pronounced than the “red spot”.

To quantify this effect we have computed the zeroth-order moment and first-order moment of the TSC example above ($r_c = 100$ AU). The result is shown in Figure 2.11. The zeroth-order moment shows that the integrated emission is not symmetric respect to the core center, being stronger in the blue rotating half. This is due to fact that the blue- and red-shifted emission extend towards opposite direction of the core center (see Figure 2.7), and because for a given distance from the core center, the blue-shifted emission in the blue rotating half in stronger than the red-shifted emission at the symmetric point in the red rotating half. This effect makes the actual core center (marked as a white point in 2.11) do not fall at the geometrical center of the contours of equal integrated intensity, what gives an impression of a misplacement of the core center. Note that this effects makes the core center not to coincide with the peak of integrated emission. Regarding the features that appear in the first-order moment, the “blue spot” and the “dimmer red spot” appear at opposite sides of the rotation axis in the vicinity of the core center. Note that the “blue spot”, at -1.7 km s^{-1}, is bluer than the “central blue

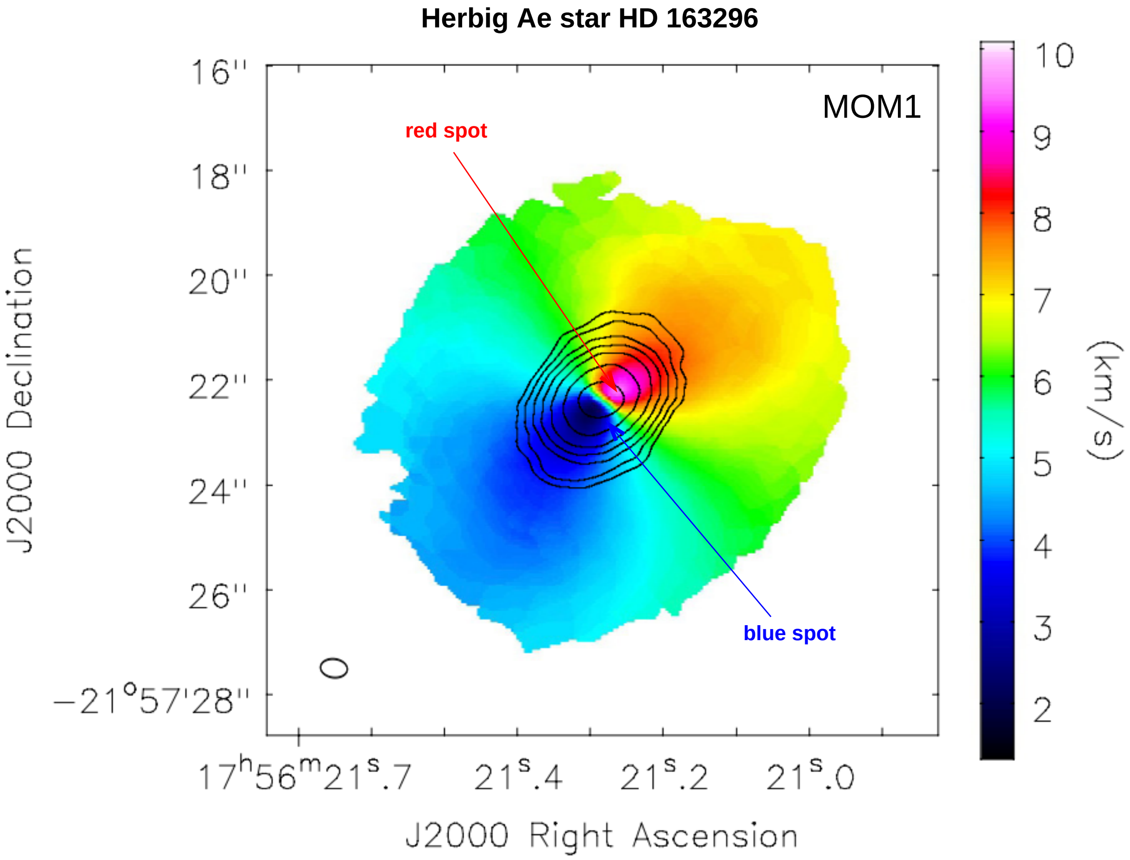

Figure 2.10: Snapshot of figure 1 of de Gregorio-Montsalvo et al. (2013). ALMA observations of the protoplanetary disk surrounding the Herbig Ae star HD163296. Colors represent the CO(3-2) first-order moment. Contours show the continuum emission at 850 μm with levels representing 5, 10, 20, 40, 80, 160, and 320 times the rms of the continuum map (0.5 mJy beam^{-1}).

spot" for the case of non-rotation, -0.9 km s^{-1} (despite both models have the same central mass, 0.64 M$_\odot$, and the same temperature law). The "dimmer red spot" is at a velocity of 1.0 km s^{-1}, which is lower in absolute value than the "blue spot".

The "blue spot and dimmer red spot pair" would be detectable as long as the most internal V$_z$-surfaces are angularly resolved and the opacity remains high in the innermost region (see Anglada et al. 1987). Note that, along the polar direction, the rotation component is negligible and, therefore, the "central blue spot" is expected to persist. Figure 2.12 shows a cut of the first-order moment along the projected direction of the rotational axis for the TSC example above (Figures 2.7 and 2.11). The cut evidences that the "central blue spot" is still present in the direction perpendicular to the equatorial plane. Note that we have not taken into account yet the possible presence of a bipolar outflow along the rotation axis.

A cut of the first-order moment along the equatorial plane (Figure 2.13) reveals another feature produced by the combined motions of infall and rotation. For simplicity, we will base the general explanation on the numerical TSC example described above. For consistency with this example (Figure 2.7) we will refer as "negative offsets" those of the red rotating half of the core, and as "positive offsets" those of the blue rotating half. In pure infall, at large offsets from the core center the intensity of the red-shifted emission at a given velocity $|V_z|$ tends to equal the blue-shifted emission at $-|V_z|$ velocity and thus the first-order moment tends to zero at such offsets (Figures 2.4 and 2.5). In contrast, in the rotating case, at negative offsets and away from the core center (LOS labeled A in Figure 2.13a), the red-shifted emission at a given velocity $|V_z|$ contributes to the first-order moment but the blue-shifted emission at $-|V_z|$ velocity has been "shifted" to more positive offsets and hence, is not longer detectable at such LOS as it has been replaced by emission of smaller $|V_z|$. Therefore, the blue-shifted contribution to the first-order moment decreases and the first-order moment adopts a positive (red) value. As the LOS get closer to the core center (LOS labeled B in Figure 2.13a), the blue-shifted emission get stronger but the red-shifted emission gets slightly weaker (Figure 2.7) so the first-order moment tends to adopt bluer values. At small negative offset (LOS labeled C in Figure 2.13a), the strong red-shifted emission of higher velocities, together with the absence of high-velocity blue-shifted emission (which has been "shifted" to more positive offset by rotation), produce the first-order moment to rise to redder values. Note that this rise corresponds to the "dimmer red spot". At the other side of the rotation axis, at small positive offsets (LOS named D in Figure 2.13a), the strongest blue-shifted emission at the highest velocities makes the first-order moment to decrease sharply towards bluer values producing the "blue spot". Such a large difference in velocity produces a steep velocity gradient at small scales. As the LOS gets away from the core center towards positive offset (LOS labeled E and F in the example Figure 2.13a), the high velocity blue-shifted contribution to the first-order moment disappears and the first-order moment increases to redder values. The final result is that successive ups and downs are created in the first-order moment along the equatorial plane, causing a "roller-coaster" profile. To quantify this effect we calculated a cut to the first-order moment (Figure 2.11) along the equatorial plane for the TSC example above ($r_c = 100$ AU). The result is shown in Figure 2.13b, where the "roller coaster" profile can be easily distinguished. Note that in the "roller-coaster" profile,

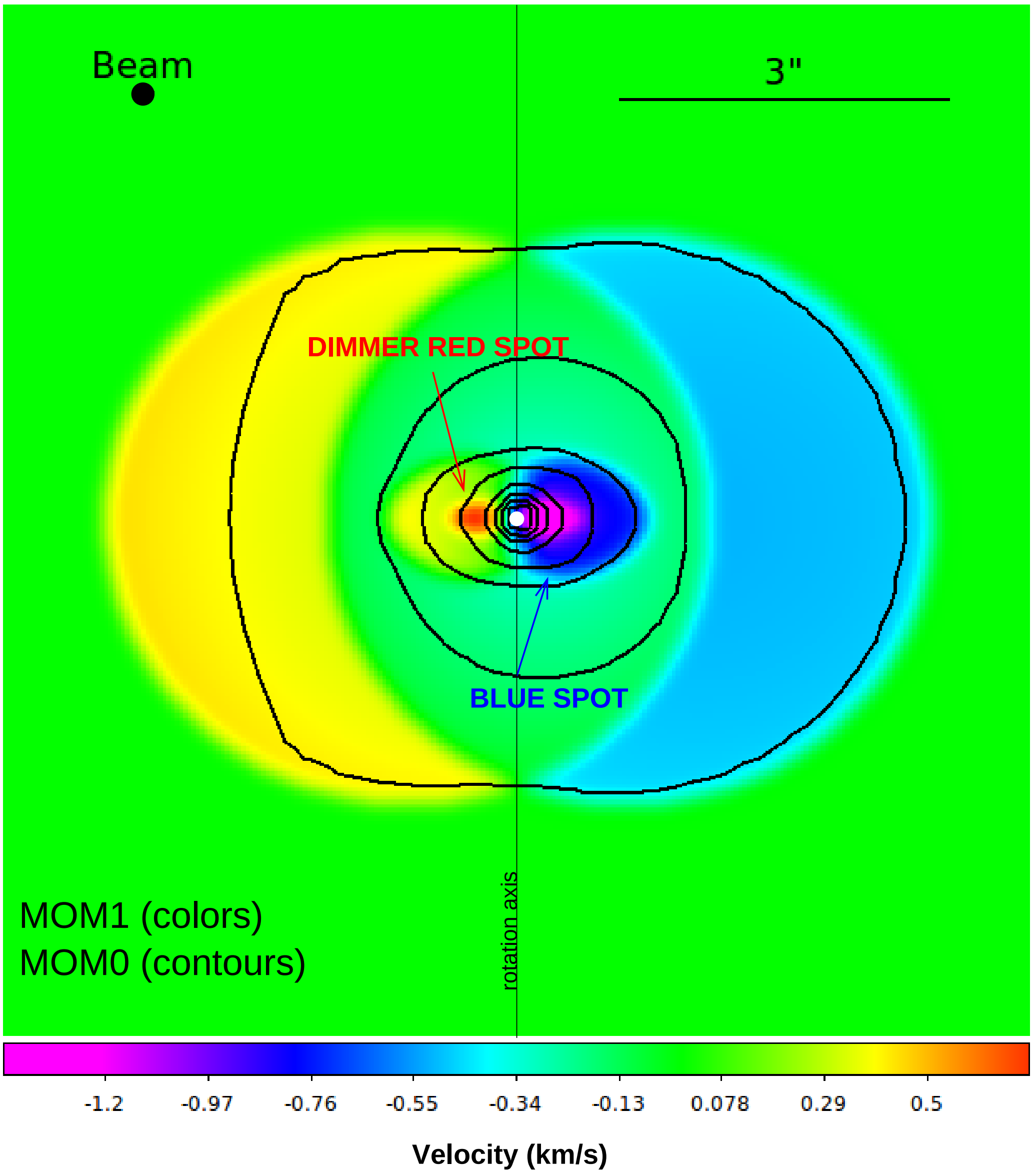

Figure 2.11: Intensity-weighted mean velocity maps (first-order moment) for a TSC core of centrifugal radius of 100 AU. The rotation axis is in the plane of the figure. The effects of possible outflows have not been considered. Contours represent the integrated velocity intensity map (zeroth-order moment). Contours are 0.021, 0.043, 0.064, 0.085, 0.128, 0.170, 0.213, and 0.255 mJy beam^{-1} km s^{-1}. Calculations correspond to the emission of an optically thick molecular line transition that is well thermalized, for a central protostar of $\sim$ 0.64 M$_\odot$ at 160 pc observed with a beam of $0\rlap{.}''2$. The rest velocity is assumed to be at V$_{LSR}$ = 0. Note that the color scale is not centered at zero in order to emphasize the red spot. The white spot represents the core center.

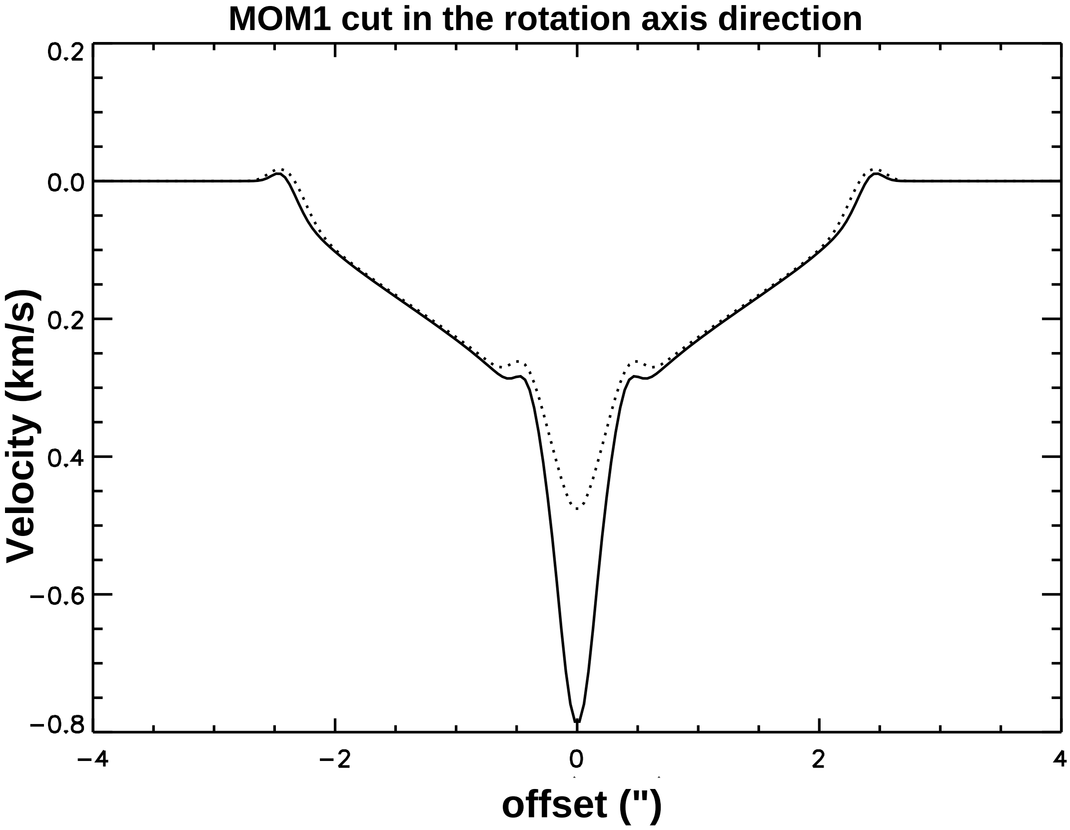

Figure 2.12: Cut of the first-order moment (intensity-weighted mean velocity map) along the projected direction of the rotation axis for a TSC core with a centrifugal radius of 100 AU as a function of angular offset from the source center (solid line). Dotted lines represent the cut along a strip of 1.″4 width ($\sim$ 20% of the core size) in the same direction. The effects of possible outflows have not been considered. The systemic velocity of the cloud has been assumed to be zero.

the valley and ridge at the sides of the core center indicate the presence of the "blue spot" and the "dimmer red spot pair" respectively. It is important to note that the "roller-coaster" feature is produced because of the different extension of the emission at different discrete V_z. In practice, the velocity discretization will result from the spectral resolution of the velocity channels of the observations.

Although these features, the "blue spot and dimmer red spot pair" and the "roller-coaster", are more prominent along the equatorial direction they appear even when the inclination angle of the rotation axis is large. Note also that these signatures are not expected to be affected by the presence of a bipolar outflow along the rotational axis. Figure 2.14 shows the expected first-order moment under the assumption of high line opacity and thermalization for a TSC envelope of $r_c = 100$ AU, an internal mass of 0.64 $M_{\odot}$, and the rotation axis at $i = 50°$ with respect to the LOS. We have also included the effect of a bipolar outflow of constant velocity, and opening angle of 15° along the rotation axis. Figure 2.15 shows a cut of the first-order moment along the rotational axis, and along its perpendicular direction. It is observed that despite the configuration largely departs from being edge-on, the "blue spots and dimmer red spot pair" rotation signature, and also the "roller-coaster" feature remain visible. The cut of the first-order moment along the rotation axis (equivalently, along the outflow direction) does not produce similar features. The outflow model used is very simple, though.

We propose that either the "roller coaster" feature, the presence of the "blue spot and dimmer red spot pair" at opposite sides of rotation axis, the direction of the shift in position of the "central blue spot", or the "visual displacement" of the core center respect the geometric center of the contours of equal integrated intensity could be used to infer the PA of the equatorial direction of a infalling and rotating molecular envelope. We believe that any of these signatures is more reliable in tracing rotation than large-scale velocity gradients, which can be flawed by low signal-to-noise ratios, or affected by bipolar outflows (that can even be precessing), or by other external agents as stellar winds of nearby stars, etc. Notwithstanding, high angular resolution observations, able to resolve the inner parts of the source, are needed in order to be able to detect such features.

We note that the "central blue spot" and the "blue spot and dimmer red spot pair" infall signatures are related to the "blue bulge" signature introduced by Walker, Narayanan, & Boss (1994). These authors realized that, when only a rotational velocity field is present, a centroid velocity map will show blue-shifted emission on one side of the rotation axis and red-shifted emission on the opposite side, but if infall is also occurring, the blue-shifted emission may be observed across the rotational axis through the core center on what would otherwise be the red-shifted side of the map. However, as these authors focused their study on cloud orientations more favorable for detection of rotation they did not discuss the case of a pole-on orientation. In the case of a pole-on orientation the contribution of the rotation velocity field goes to zero and the velocity centroid contours are concentric circles, recovering our "central blue spot" signature (Figure 2.5).

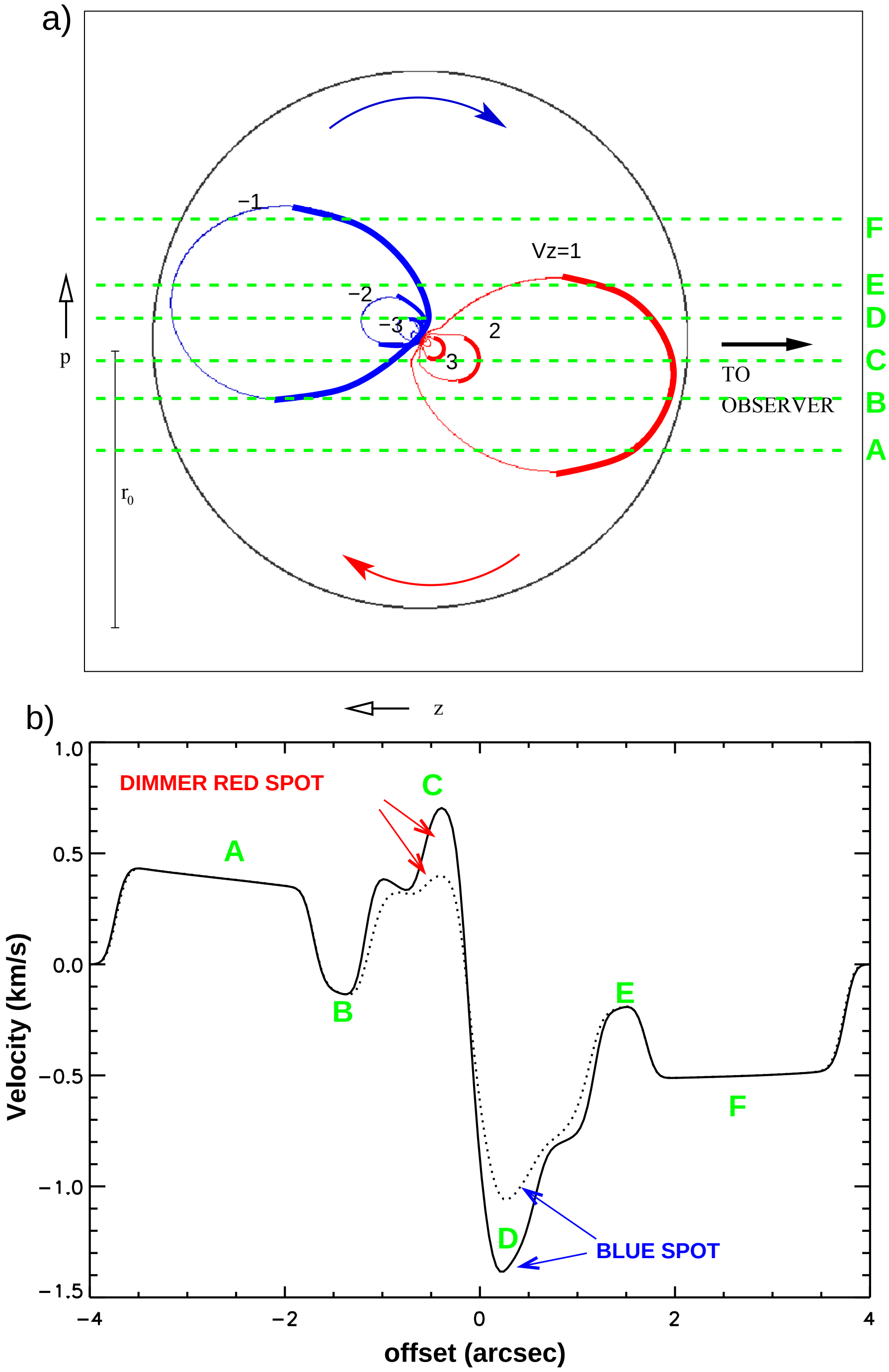

Figure 2.13: *(a)* Same as Figure 2.7a, but for the V_z-surfaces of a rotating and collapsing core are shown. Green dashed lines labeled A, B, C, D, E and F correspond to different LOS. *(b)* Cut of the intensity-weighted mean velocity maps (first-order moment) along the equatorial plane. Dotted lines represent the cut along a strip of $1.''4$ width ($\sim$ 20% of the core size) in the same direction. Calculations correspond to the emission of an optically thick molecular line transition that is well thermalized, for a TSC core of centrifugal radius of 100 AU with a central protostar of $\sim 0.64\ M_\odot$ located at 160 pc and observed with a beam of $0.''2$.

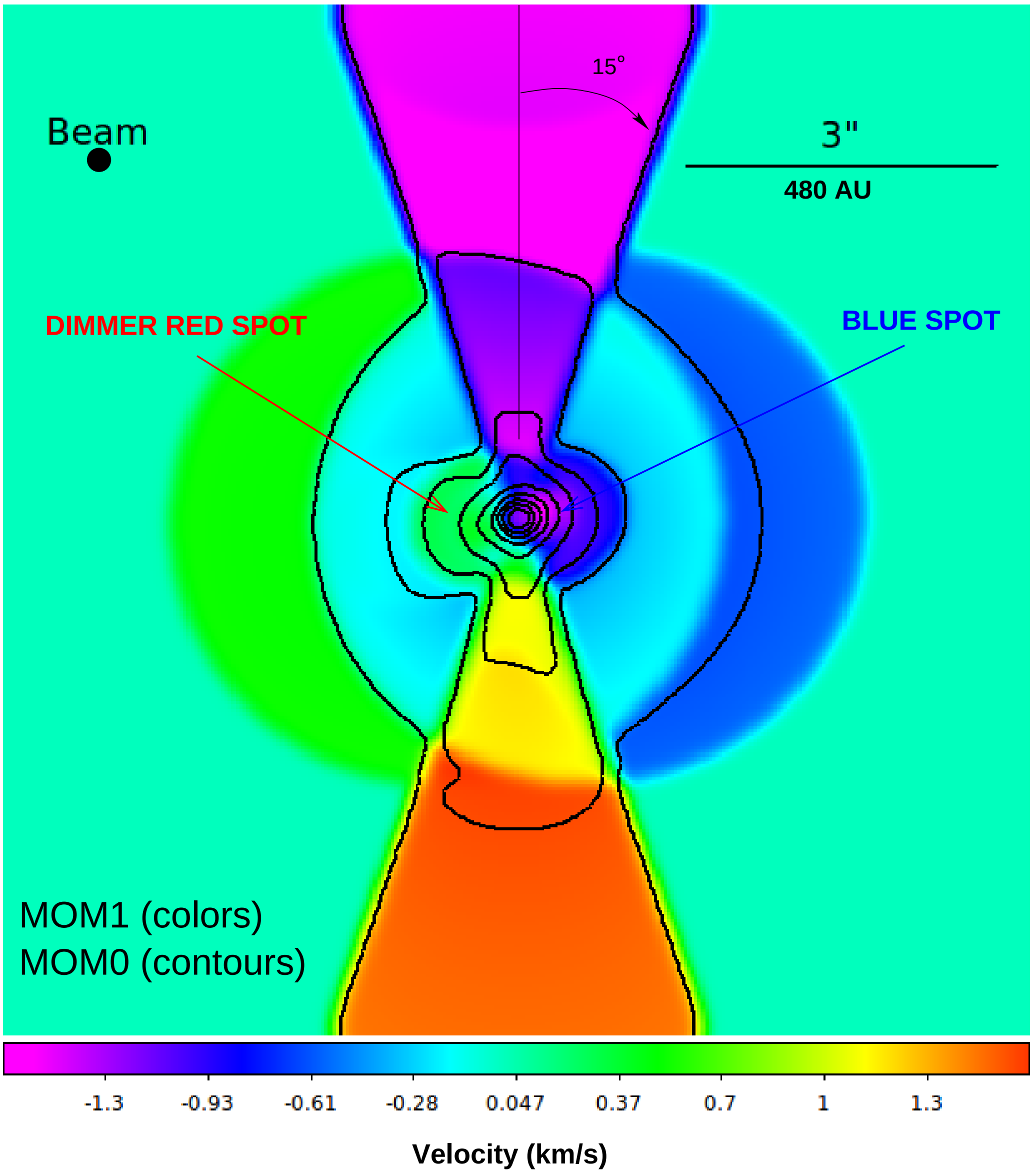

Figure 2.14: Intensity weighted mean velocity map (first-order moment) in colors. The integrated intensity map (zeroth-order moment) is shown in contours. Contours are 0.021, 0.043, 0.064, 0.085, 0.128, 0.170, 0.213, 0.255, 0.298, 0.34, and 0.383 Jy beam^{-1} m s^{-1}. Calculations correspond to the emission of an optically thick molecular line transition that is well thermalized, for a TSC core of $r_c = 100$ AU with a central protostar of ~ 0.64 M$_\odot$ located at 160 pc and observed with a beam of $0\farcs2$ and spectral resolution of 1 km s^{-1}. The inclination angle is 50° (respect the LOS). The effects of an outflow have been introduced ad hoc along the rotation axis. The opening angle of the outflow is 15° and the velocity of the outflow is 5 km s^{-1}.

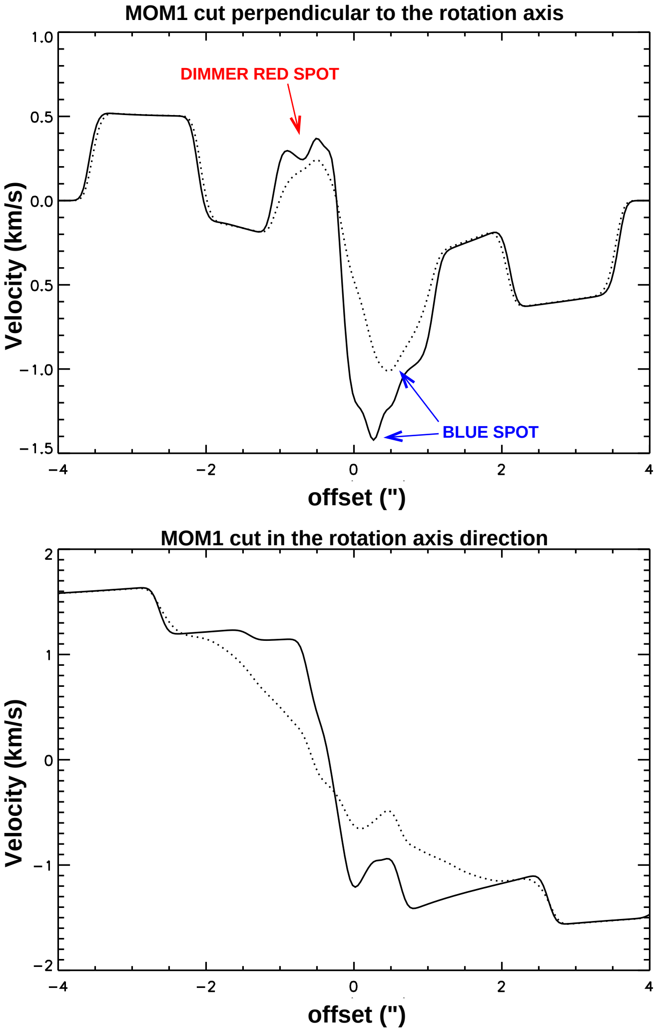

Figure 2.15: *(a)* Cuts of the first-order moment shown in Figure 2.14 along the perpendicular direction to the rotation axis for the case in Figure. *(b)* Cut of the first-order moment shown in Figure 2.14 along the direction of the rotation axis (equivalent to the outflow direction). Dotted lines represent the cut along a strip of 1.″4 width (∼ 20% of the core size) in the same direction. The systemic velocity of the cloud has been assumed to be zero.

Because the “blue bulge” is a signature for the combined infall and rotation motions, we will compare it with the infall and rotation signature that we have derived in this chapter, the “blue spot and dimmer red spot pair”. The “blue bulge” signature was first identified by Walker, Narayanan, & Boss (1994) using a “self-consistent” three-dimensional hydrodynamic model from Boss (1993), but it was also found using the TSC formalism (Narayanan & Walker 1998). We note that apparently our results do not coincide with the description of the “blue bulge” signature of Narayanan & Walker (1998), despite we are using also the TSC formalism. Although there are several differences (Narayanan & Walker 1998 use a different temperature law, $\sim r^{-1}$, in contrast to the $\sim r^{-1/2}$ used here; also, they use a radiative transfer code to calculate the emergent intensity while here we have assumed the high line opacity simplified formalism of A91), the main reason for the discrepancy is the angular resolution. Narayanan & Walker (1998) set the model source at 160 pc, exactly as we do in our modeling, and explored centrifugal radii that range from 0.4 AU to 440 AU. Nevertheless, they used beam sizes of $5''$ and $14''$, which cannot resolve the inner region of the core, where rotation becomes important. Because their beam size is too large, the “blue spot” and its companion “dimmer red spot” fit both together in a single beam size, so they could only detect an excess of blue-shifted emission towards the core center as a consequence of the fact that the “blue spot” is more pronounced than the “dimmer red spot”. In order to check that the main source of discrepancy is the angular resolution we enlarged the beam size and the centrifugal radius in our example and found that we were able to reproduce the features characteristic of the “blue bulge” (Figure 2.16). Thus, the “blue spot and dimmer red spot pair” and the “blue bulge” both have a similar origin, but the former contains a more detailed information and, as commented earlier, it is a feature that is expected to be detected only if the angular resolution is able to resolve the V_z-surfaces of highest velocities.

2.4 Conclusions

We introduced a new mapping signature of infall, that we call the “central blue spot”, consisting in a spot of blue-shifted emission in the first-order moment (intensity-weighted mean velocity map) towards the peak position of the zeroth-order moment (integrated intensity map). This signature is produced as a result of the difference in intensity and spatial distribution of the emission in the red- and blue-shifted channels predicted by the “spectral imaging infall signature” of A91. The signature is easily identifiable and does not require an accurate determination of the systemic velocity of the core.

We studied how rotation affects the spatial intensity profiles of an infalling envelope. The spatial intensity profile of the image in a given velocity channel (red- or blue-shifted) is stretched towards the side where rotation has the same sign (red- or blue-shifted, respectively) as the channel velocity, and it is shrunk on the opposite side. Nevertheless, as in the non-rotating case, the images in blue-shifted channels present a centrally peaked intensity distribution, while in the red-shifted channels they present a flatter intensity distribution. Thus, we concluded

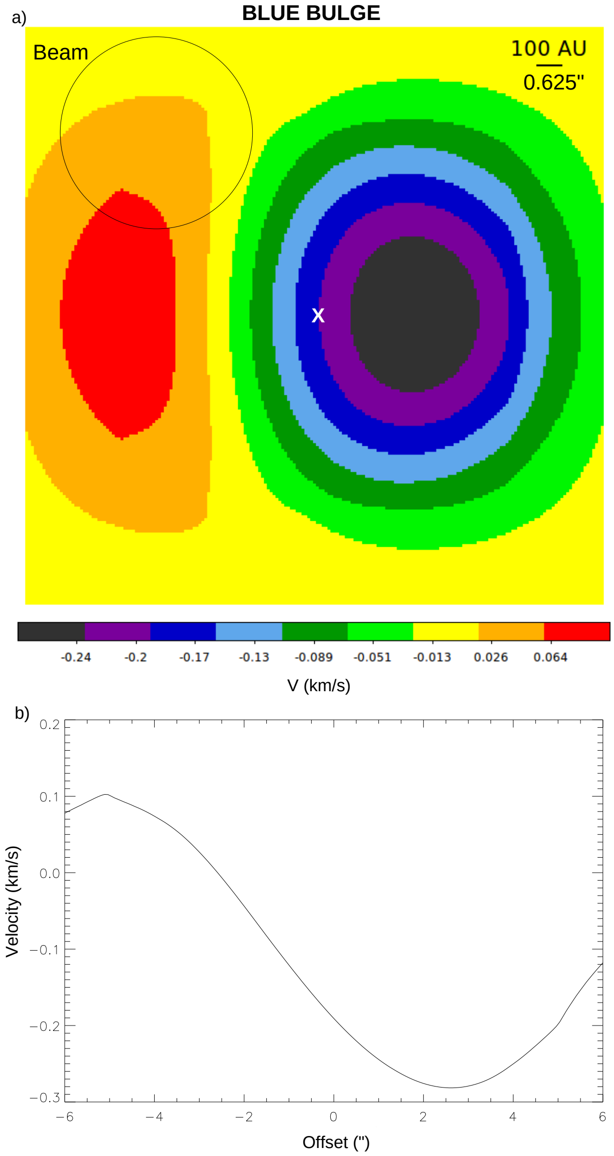

Figure 2.16: *(a)* Intensity-weighted mean velocity maps (first-order moment) for the same core as in Figure 2.11 but observed with a beam of 5″. The "blue bulge" signature is shown as described by Narayanan & Walker (1998) since towards the core center the blue-shifted emission invades the area that would otherwise be red-shifted by rotation in the map. Note that because of the poor angular resolution, the "blue spot and dimmer red spot pair" at the immediate sides of the core center do not appear. The white cross indicates the core center. *(b)* Cut of the first-order moment along the equatorial direction. Note that the absence of the "blue spot" and "the dimmer red spot" at opposing sides of the core center also produces that the "roller-coaster" feature disappears.

that the rotation signature makes the spatial intensity profiles asymmetric with respect to the central position but it does not mask the A91 infall signatures.

We also explored how the "central blue spot" in the first-order moment of an infalling envelope is modified by the presence of rotation. We found that rotation makes the "central blue spot" even bluer and moves it off the center towards the blue rotating half (the half of the core where rotation tends to shift velocities to the blue). Additionally, a "dimmer red spot" appears symmetrically located on the opposite side of the rotation axis. The "blue spot" and the "dimmer red spot" originate, respectively, from the blue- and red-shifted V_z-surfaces of highest $|V_z|$, which do not coincide in the same line-of-sight because of the distortion of the V_z-surfaces produced by rotation. We propose that the orientation of the "blue spot and dimmer red spot pair" and/or the shift of the "blue spot" off the core center could be used to infer the equatorial direction of an infalling and rotating molecular envelope. We believe that these small-scale signatures are more reliable in tracing the rotation axis than large-scale velocity gradients. These signatures are detectable even at large inclinations of the rotation axis. Notwithstanding, high angular resolution observations are needed in order to be able to detect such features.

We obtained an additional signature that should characterize a rotating and infalling envelope. A cut of the first-order moment along the equatorial plane shows a sequence of successive valleys (bluer values) and ridges (redder values). This feature is a direct consequence of the presence of the "blue spot" and the "dimmer red spot", together with the fact that the "spectral imaging infall signature" is not masked by rotation, and therefore blue-shifted emission sharply increases towards the center but red-shifted emission does not. We call this new feature the "roller-coaster" signature. It could be used to determine the direction of the equatorial plane by searching for this signature in cuts of the first-order moment made along different position angles.

Chapter 3

Kinematic study of core collapse models

3.1 Introduction

In the previous chapter we introduced the "3D spectral imaging infall signature" of A91, which is based on the spatial distribution of the line emission intensity in the images as a function of the velocity, $I_\nu(\alpha, \delta, V_z)$. Under the assumptions of increasing infall velocity and temperature towards the core center, thermalized lines, high opacity of the line, and enough angular resolution to resolve the collapsing core, the intensity images at blue-shifted velocities are strongly peaked towards the center, while they are nearly flat at red-shifted velocities. Additionally, the emission size becomes smaller at larger velocities. This infall signature is expected even in the presence of small rotation, and, unlike the 1D signatures (Section 2.1) based on the line spectral profile, $I_\nu(V_z)$, it can not be easily mimicked by other scenarios.

The power of the (3D) spectral imaging signatures goes beyond of merely finding reliable signatures of infalling gas. It is possible that these signatures are sensitive to subtle differences in the velocity field that, in its turn, depends on the initial conditions of clouds. In particular, it may provide information on whether or not cores are initially in quasi-static equilibrium. In general, contraction from quasi-static equilibrium would evolve from the inside out, i.e., collapse begins at the core center, and a rarefaction wave moves outwards setting the gas behind it into motion towards the central protostar, while the gas outside the wave remains static. In a contraction from a non-equilibrium states, the whole core, even the outermost parts, would begin to move at once. Hence, evidence of extended infall may indicate that the core started from a non-equilibrium state.

A91 obtained their "spectral imaging infall signature" (Figure 2.4) adopting the velocity field from the numerical calculations of Larson (1972), whose velocity field behaves as free-fall ($V \propto r^{-1/2}$). This velocity field is only valid close to the central object, where gravity dominates over other forces that oppose collapse. Notwithstanding, as mentioned above, the main difference between initial equilibrium and non-equilibrium states happens to occur at large distances from the center. Moreover, in the very early stages of core collapse, the velocity field might not increase inwards, as required to produce the A91 spectral imaging infall signature.

As an extreme example, in the free-fall collapse of a sphere of uniform density (which is far from an equilibrium configuration), the whole sphere begins to move inward at once and after a short time, as the acceleration is largest in the outer region (the internal mass goes as r^3 and acceleration goes as M/r^2) the velocity will be higher at longer distances from the center. Some questions may arise at this point. One is how V$_z$-surfaces change when modifying the velocity fields. And second, how spatial intensity profiles (the intensity as a function of the projected distance to the core center) change as a consequence of that.

Figure 3.1 shows the different V$_z$-surfaces for a power-law velocity field $V = V_o(r/r_o)^a$ when changing the index a. Note that $a = -0.5$ was the case explored in Anglada et al. (1987, 1991) (Figure 2.4). For $a < 0$ the V$_z$-surfaces are closed and nested, with the ones of higher velocities being smaller, what makes the extent of the spatial intensity profiles to decrease with increasing $|V_z|$. The shapes of the V$_z$-surfaces change with a: the lower a, the more oblate. When a is closer to zero, V$_z$-surfaces are more prolate. Note also that all V$_z$-surfaces meet at the center of the core. This also happens for $a = 0$, although in this case the V$_z$-surfaces are open and take the shape of cones. For $a > 0$, infall velocities increase with increasing radius (as expected in the free-fall collapse of a uniform sphere), the V$_z$-surfaces are open, adopt a paraboloid shape, and they do not coincide at any point.

Figure 3.2 shows an example of the spatial intensity profiles corresponding to the V$_z$-surfaces shown in Figure 3.1 when only the velocity field is changed and the rest of the conditions in A91 have been held unmodified. These are high line opacity, thermalized transition, and temperature and density fields of the form $T \propto r^{-1/2}$, and $n \propto r^{-3/2}$. Note that the "spectral imaging infall signature" of A91 is visible as long as V$_z$-surfaces are closed ($a < 0$; upper panels Figure 3.2). In this case, each LOS crosses a given V$_z$-surface twice. If the optical depth is high the crossing point of the V$_z$-surface closer to the observer hides the emission from the crossing point at the rear part (left column in Figure 3.1). Then, only the emission from the front side is visible. In the case of red-shifted surfaces, the front side is further from the core center, and thus colder. The temperature varies little along that side of the surfaces, and therefore their spatial intensity profile is practically flat. On the contrary, the front side of blue-shifted surfaces is the one closer to the protostar. The temperature increases sharply towards the center, so the temperature in the blue V$_z$-surface varies significantly with the central part being very hot. Therefore, the spatial intensity profiles of the V$_z$-surfaces are sharply peaked towards the center of the core (upper panels in Figure 3.2). Note also that, since closed V$_z$-surfaces get smaller at larger velocities (in absolute value), the extent of the area of emission decreases with increasing V_z (left column in Figure 3.1).

If V$_z$-surfaces are open then each LOS only crosses a given V$_z$-surface once, and there are not hidden parts of the collapsing core. The whole V$_z$-surface is exposed to the observer and therefore, there is no difference between the red- and blue-shifted spatial intensity profiles (lower panels in Figure 3.2). Note that the spatial intensity profiles shown in Figure 3.2 have not been obtained in a physically self-consistent mode, since the velocity has been introduced ad hoc and thus is not necessarily consistent with the temperature and density fields; they are only

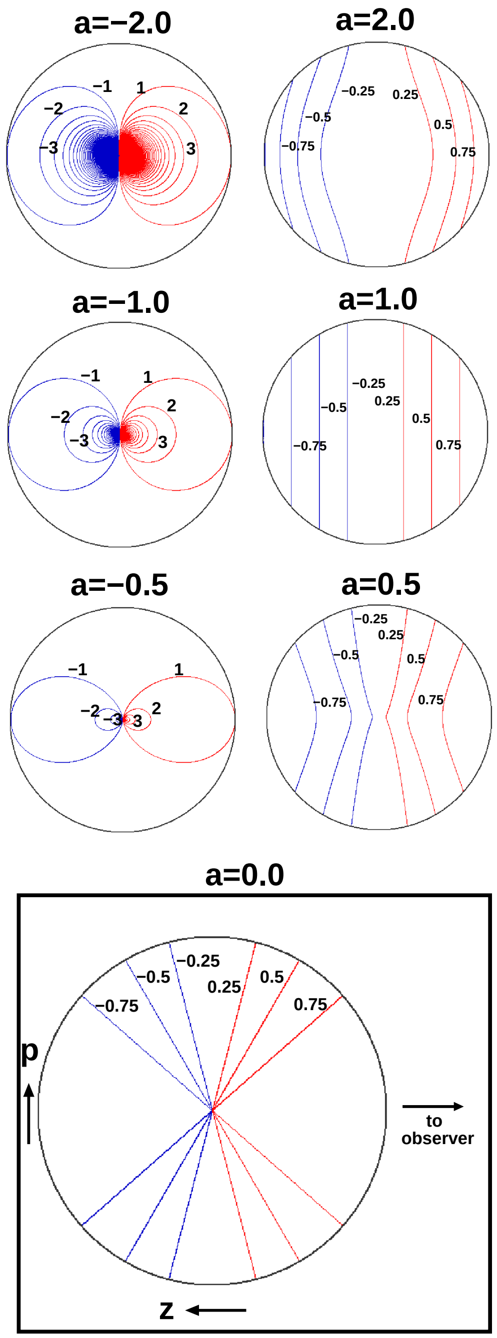

Figure 3.1: Surfaces of equal LOS velocity for a collapsing core with velocity field $V = V_o(r/r_o)^a$, where V_o =1 km s^{-1} and r_o =1.7 × 10^{16} cm. The outer radius of the core (solid black line) is set at $r = r_o$.

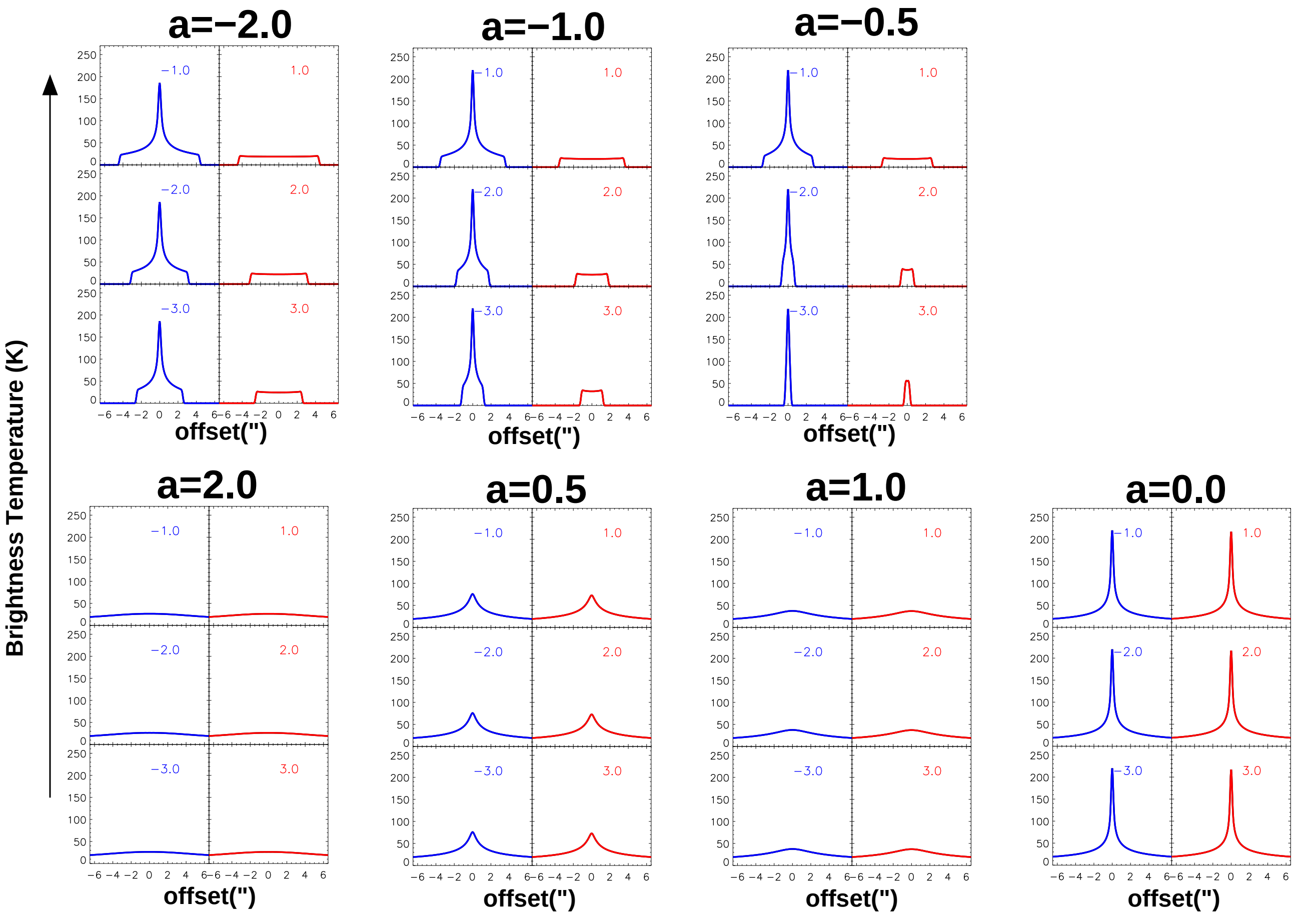

Figure 3.2: Spatial intensity profiles as a function of LOS velocity for power-law velocity fields, $V = V_o(r/r_o)^a$, with different values of the index a, where $V_o = 10^5$ cm s^{-1} and $r_o = 1.7 \times 10^{16}$ cm. As in the example of A91, it is assumed an optically thick thermalized molecular transition, $T = T_o(r/r_o)^{-1/2}$, and $n = n_o(r/r_o)^{-3/2}$, where $T_o = 19$ K and $n_o = 1.9 \times 10^5$ cm^{-3}. The number at the upper right corner of each panel indicates the LOS velocity of the channel in units of km s^{-1}. The infall signature of A91 is seen as long as $a < 0$.

shown for illustrative purposes.

In the following we will analyze the presence of infall signatures for different self-consistent models of protostellar collapse. We will use models from the literature that are described by the so-called "self-similar" formalism (see below), whose mathematical simplicity will allow us to obtain the physical properties of the core. We will calculate the images as a function of the LOS velocity, $I_\nu(\alpha, \delta, V_z)$, and check if such images show the infall signatures or not through two methods: The first one uses a simplified formalism similar to that of A91. In this formalism, high line opacity is assumed, so we consider that the gas contributing to the emission at a given LOS velocity originates in a thin layer of such gas near the corresponding isovelocity regions (V_z-surface) where the physical characteristics vary little. Thus, the velocity channel maps, $I_\nu(\alpha, \delta, V_z)$, can be considered as the images of the temperature distribution over the visible side of the corresponding V_z-surfaces (see Sections 2.1 and 2.2). The second method uses a radiative transfer code which does not need of any previous assumption.

For a given transition, the conditions of opacity and thermalization needed for the "spectral imaging signature" to emerge are more likely to be fulfilled in the high-mass star formation regime because of the higher densities and temperatures involved compared with the low-mass regime. For this reason, we will compare the different models under the typical physical conditions of massive star-formation. Our aims are twofold, the first is to determine if significant differences emerge in the spatial intensity profile between equilibrium and non-equilibrium models. The second is to check if the "spectral imaging infall signature" of A91 is of general application or if it is valid only for some specific velocity fields.

The outcomes of the different collapse models have important implications beyond the kinematics of the cores. The different models predict different time-scales, stellar initial mass functions, star formation rates, etc. These predictions could also be tested with observational results in order to discriminate between models. However, this is beyond the scope of this thesis work and we will focus on the kinematics. This chapter is structured as follow:

- In Section 3.2, we explain the self-similar formalism, which is commonly used in the literature to describe models of core collapse.
- In Section 3.3, we summarize the self-similar models that describe the prestellar phase, prior to the formation of a central protostar. We pay special attention to their kinematics and their self-similar transformations and solutions. The kinematic features in the velocity images predicted by these models are presented.
- In Section 3.4, we present an analogous analysis, but with self-similar models that describe the main accretion phase, after the formation of a central protostar.
- In Section 3.5, we summarize the results and present the conclusions of this chapter. We focus on the possible differences in the results between models that evolve from the

equilibrium and those that evolve from non-equilibrium, and on the presence or absence of the “spectral imaging infall signature”.

3.2 The self-similar formalism in the modeling of the gravitational collapse

3.2.1 Self-similar solutions

The collapse of an interstellar molecular cloud has typically been studied using two approaches: self-similar or numerical methods. Under the assumption of spherical symmetry, the dynamics of a non-magnetized cloud of gas in spherical polar coordinates is described by the equations of mass conservation,

$$\frac{\delta M}{\delta r} = 4\pi r^2 \rho \quad \text{and} \quad \frac{\delta M}{\delta t} + V\frac{\delta M}{\delta r} = 0 \ , \tag{3.1}$$

the equation of continuity,

$$\frac{\delta \rho}{\delta t} + \frac{1}{r^2}\frac{\delta}{\delta r}(r^2 \rho V) = 0 \ , \tag{3.2}$$

and the force equation,

$$\frac{\delta V}{\delta t} + V\frac{\delta u}{\delta r} = -\frac{1}{\rho}\frac{\delta P}{\delta r} - \frac{GM}{r^2} \ , \tag{3.3}$$

where V is the radial component of the velocity, ρ is the density, $M(r,t)$ is the total mass within a given radius, r, at a time t, and P is the pressure.

Solving the problem numerically has traditionally been difficult because of the need of treating very large scales in the initial phase of the collapsing cloud along with very small scales once the prestellar core has formed and contracted several orders of magnitude. That has historically imposed great demands on the accuracy of numerical solutions. Early simulations showed that the density and velocity distributions in the inner part of the collapsing cloud approach constant limiting forms, with only their scale changing with time. That suggested that there had to be a “similarity” solution for the collapse of a spherically symmetric cloud. In a similarity solution, nondimensional functions for the physical properties are used to describe the flow motion at any time by applying some appropriate scaling. The time dependence is introduced by scale factors. The nondimensional functions are obtained by using a self-similar transformation:

$$r = a(t)x \ , \quad V = b(t)v(x) \ , \quad \rho = c(t)\alpha(x) \ , \quad P = d(t)\beta(x) \ , \quad M = e(t)m(x) \ , \tag{3.4}$$

where a, b, c, d and e are scaling factors, that are a function of time only, and the reduced fluid fields (v, α, β, m) are dimensionless functions of the (single) dimensionless similarity variable x.

If one adopts $a(t) \propto t^n$, then, for consistency, the general similarity transformation calculation leads to (Suto & Silk 1988, Fatuzzo et al. 2004, Lou & Wang 2006, Wang & Lou 2007, Wang & Lou 2008):

$$a = k^{1/2}t^n \ , \quad b = k^{1/2}t^{n-1} \ , \quad c = \frac{1}{4\pi G t^2} \ , \quad d = \frac{kt^{2n-4}}{4\pi G} \ , \quad e = \frac{k^{3/2}t^{3n-2}}{(3n-2)G} \ , \tag{3.5}$$

where n and k are constants. The scaling factor e is meaningless when $3n-2 \leq 0$. In these cases the self-similar transformation should be modified slightly, the constant $(3n-2)^{-1}$ changes to $(2-3n)^{-1}$. Similarly, it should be changed to 1 when $n = 2/3$ (see Lou & Wang 2006). Note that a similarity transformation is not unique; one can always rescale the coefficients a, b, c, d and e by a set of dimensionless numbers and obtain new equations of motion with different numerical coefficients. The time benchmark t=0 corresponds to the instant when the mass of the central protostar is zero, i.e., $M(r=0,t=0)=0$. Using these similarity transformations one can reduce the system of differential equations in the variables (r, t), to a set of ordinary differential equations in a new similarity variable x. The mass conservation equations become:

$$(nx - v)\frac{dm}{dx} = (3n-2)m \quad \text{and} \quad \frac{dm}{dx} = x^2\alpha \ . \tag{3.6}$$

Both equations yield:

$$m = \alpha x^2(nx - v). \tag{3.7}$$

The equation of continuity becomes:

$$(nx - v)\frac{d\alpha}{dx} - \alpha\frac{dv}{dx} = -2\frac{x-v}{x}\alpha \tag{3.8}$$

and the reduced radial momentum equation become:

$$\frac{1}{\alpha}\frac{d\beta}{dx} - (nx - v)\frac{dv}{dx} = -(n-1)v - \frac{nx - v}{3n-2}\alpha. \tag{3.9}$$

The problem can be simplified by assuming some particular thermodynamic condition for the collapsing gas, what translates in an extra relation between β and α. For instance, we may assume isothermality, $P = K\rho$ (where K is constant), or in general, a polytropic equation of state of the form $P = K(t)\rho^\gamma$ where K can be a function of time, and γ is a constant. The new equations of motion (equations 3.7 to 3.9) may have some direct analytical solutions, but in general they must be solved numerically. Further simplifications to the system of equations can be made by assuming a particular behavior for the velocity and density fields at the limit $x \rightarrow 0$, and/or at $x \rightarrow \infty$. For example, if one assumes quiescent material at large distances ($v \rightarrow 0$ at $x \rightarrow \infty$), equation 3.8 reduces to:

$$\frac{d\alpha}{dx} = -\frac{2\alpha}{nx} \ , \tag{3.10}$$

which is easily integrated to give:

$$\alpha = Ax^{-2/n} \ , \tag{3.11}$$

where A is an integration constant. The solutions obtained this way are the so-called "asymptotic solutions".

Numerical simulations of the collapse problem, which can be used to verify the semi-analytic results of the self-similarity solutions, seem to indicate that the collapse approaches the similarity solution asymptotically in time (Hunter 1977) and that this occurs relatively rapidly and smoothly (Fatuzzo et al. 2004). The mathematical simplicity of the similarity solutions leads to a basic understanding of many essential physical features. Given the relation between x, r and t, $x = r/k^{1/2}t^n$, the variable x can be understood as a spatial variable at a fixed time (if $n \neq 0$) and the similarity solutions would then provide the behavior of the flow at a given time for any value of r, i.e. a still photograph of the flow conditions at any r. But x also can be considered as a time variable for a fixed distance and the similarity solution would then tell us how the conditions at a particular point in space change with time (the Eulerian formalism) as the flow passes by. Another important implication is that, if the collapse indeed proceeds self-similarly, then the result of an observation would not be strongly biased by the moment in which it is made since the shape of the velocity and density fields remains constant with time, only the scale changes. Hence, similarity solutions provide an important theoretical framework within which to explore the dynamics of star formation.

The original self-similar collapse calculations (Larson 1969; Penston 1969; Shu 1977) considered isothermal spherical flows. Since then, many generalizations of the collapse problem have been made: adding the effects of rotation (Ulrich 1976; Cassen & Moosman 1981; Terebey, Shu, & Cassen 1984), magnetic fields (Galli & Shu 1993a, 1993b; Li & Shu 1996, 1997); shocks from "champagne flows" of HII regions (Shen & Lou 2004); expansion of the external envelope of the collapsing core (Lou & Shen 2004); or introducing different equations of state (Cheng 1978; McLaughlin & Pudritz 1997). Moreover, symmetries other than spherical have been explored, such as the collapse of magnetized singular isothermal toroids (Allen, Shu, & Li 2003; Allen, Li, & Shu 2003) or the study of cylindrical cloud geometries with dynamic equations of state (Holden et al. 2009). As stated before, we will restrict our discussion to the spherically symmetric problem.

3.2.2 The calculation of the temperature distribution in the models

An important condition required for the presence of the 3D infall signatures described in A91 is the existence of a temperature gradient. Otherwise, all velocity channels would have flat spatial intensity profiles, and the only difference would be the size of the emitting region at different velocities. However, many of the "self-similar" collapse models in the literature assume isothermal conditions and therefore, would not produce any red- vs blue-shifted asymmetry in the spatial intensity profiles. These collapse models do not include the temperature distribution within the core. In the high-mass regimen, the central YSO is thought to begin burning hydrogen while still deeply embedded in its parental cloud, and even earlier, the strong luminosity associated with the intense accretion process heats the gas from inside the core. To account for this temperature gradient, most molecular line-profile calculations follow the approximation that the density and velocity profiles are taken from an isothermal dynamic model but the temperature profile is assigned separately, obtained empirically or inferred from the total luminosity and dust properties (Osorio et al. 2009, Gao et al. 2009). This approximation was termed **"hybrid approximation"** by Gao et al. (2009). Its reliability is based on the fact that heating the gas and introducing a pressure gradient in the inner part of the infalling cloud should not affect the collapse as long as the thermal pressure is much lower than the hydrodynamic pressure of the infalling gas, $nk_bT << \rho V^2$, i.e., as long as the gas motion is supersonic, $V >> c_s$. This condition is easily met at the inner region of a collapsing core during the main accretion phase. Additionally, the outer parts remain relatively unaffected by the central heating and so the isothermal approximation is still valid.

On the other hand, polytropic models use a softer (less restrictive) equation of state than pure isothermal, what allows for variability in the temperature distribution. The polytropic models assume the following equation of state:

$$P = K(t)\rho^{\gamma} \ , \tag{3.12}$$

where γ is the polytropic index and the coefficient $K(t)$ can vary with time. Introducing the relationship between the density, ρ and the reduced density, α, in equation 3.12, one gets:

$$P = \frac{K(t)}{(4\pi G)^{\gamma} t^{2\gamma}} \alpha^{\gamma}(x) \ , \tag{3.13}$$

which, if compared with the reduced similarity transformation for P, $P = kt^{2n-4}(4\pi G)^{-1}\beta(x)$, implies:

$$K(t) = k(4\pi G)^{\gamma-1} t^{2(n-2+\gamma)} \ , \tag{3.14}$$

$$\beta(x) = \alpha^{\gamma}(x) \ . \tag{3.15}$$

If $n = 2 - \gamma$, then K no longer depends on time, and it is referred to as the "usual" or "conventional" polytropic equation of state. Note that the isothermal case can be recovered by setting $n = 1$, and $\gamma = 1$.

In a polytrope, the effects of all energetic processes (for instance the heating by dust-coupling) are included in the polytropic index γ. If one assumes that there is no turbulent nor magnetic pressure (all pressure is thermal), then, using the ideal gas law, one can obtain a relationship between the temperature and the density of the core, for a given γ:

$$T = \frac{\mu m_H}{k_b} \frac{p}{\rho} = \frac{\mu m_H}{k_b} K \rho^{\gamma-1}. \tag{3.16}$$

In this work we will study different collapse models and will explore how their different kinematic and physical conditions affects to the line spatial intensity profile. To do that we will use, in general, the hybrid approximation. To set the temperature distribution in the model we differentiate two phases of the core collapse, prior the formation of the central object (prestellar phase), and after the formation of it (main accretion phase). As we will show later, the temperature distributions are different in these two phases. Many of the isothermal self-similar collapse models found in the literature have been generalized to polytropic cases (Cheng 1978, Suto & Silk 1988, Yahil 1983, Fatuzzo et al. 2004). Whenever a polytropic solution is available in the literature, we will use it to complement the study of the line spatial intensity profile. Gao et al. (2009) investigated the validity of the hybrid approximation by comparing their results with those of a polytropic analysis. These authors examine and compare three self-similar inside-out core collapse models (the isothermal model, the conventional polytropic model and the empirical hybrid model) for star-forming molecular clouds and obtain that both the conventional polytropic model and the hybrid one can reproduce asymmetric line profiles in collapsing cores, similar to those observed.

3.3 Kinematic features of collapse during the prestellar phase

3.3.1 Descriptions of the models

Here we summarize the self-similar solutions of two models that describe the core collapse prior to the formation of a central protostar:

- **Larson-Penston (LP) and Larson-Penston-polytropic (LP-p) collapse models**

  The LP isothermal model (Larson 1969, Penston 1969) assumes an initial configuration of constant density, which is a highly non-equilibrium configuration. Only hydrodynamic and thermal pressures act against the gravitational collapse. No magnetic field nor turbulence are considered. In this model, for a given time, the absolute value of the velocity increases monotonically with r, and approaches an asymptotic value of 3.3 times the sound speed, c_s. As the collapse proceeds, the density, $\rho(r)$, becomes gradually centrally peaked, and tends to approach the form $\rho \propto r^{-2}$. For a given value of r, the velocity increases with time and at the moment of the protostar formation ($t = 0$), when the $\rho \propto r^{-2}$ regime is established throughout the core, the entire core is moving at $3.3c_s$.

  Larson (1969) already pointed out that the isothermal similarity solution could be generalized to the polytropic case (LP-p model), however, we will use the formulation of the polytropic generalization of the problem by Suto & Silk (1988). Their self-similar transformation coincides with the one shown in equations 3.4 and 3.5. The asymptotic solutions for $x \gg 1$ are:

  $$\alpha(x) \propto x^{-2/n} \tag{3.17}$$

$$v(x) \propto x^{(n-1)/n} \tag{3.18}$$

For $x \ll 1$ the solutions are not asymptotic, but the reduced density, α, and the reduced velocity, v, are expanded as:

$$\alpha = \alpha_* + \alpha_1 x + \alpha_2 x^2 + ... \quad , \tag{3.19}$$

$$v = v_0 + v_1 x + v_2 x^2 + ... \quad , \tag{3.20}$$

by introducing them in equations 3.8 and 3.9, one obtains the following limiting solutions:

$$\alpha = \alpha_* - \frac{\alpha_*^{(2-\gamma)}}{6\gamma}(\alpha_* - \frac{2}{3})x^2 + ... \quad , \tag{3.21}$$

$$v = \frac{2}{3}x - \frac{\alpha_*^{(1-\gamma)}}{15\gamma}(\alpha_* - \frac{2}{3})(n - \frac{2}{3})x^3 + ... \quad , \tag{3.22}$$

and from equation 3.7

$$m = \alpha_*(n - 2/3)x^3 \; . \tag{3.23}$$

The original isothermal calculations of Larson (1969) are recovered by setting $n = \gamma = 1$ and $\alpha_* = 5/3$.

Note that while the velocity in the isothermal LP model tends to approach the constant value of $-3.3c_s$, the velocity in the polytropic generalization of the LP model depends on n. For a conventional polytropic gas, $n = 2 - \gamma$, we have $v \propto r^{(1-\gamma)/(2-\gamma)}$. In this case, if $1<\gamma<2$ the velocity tends to zero at large radii. Also note that the isothermal model predicts a density law in the outer region going as $\rho \propto r^{-2}$, while the conventional polytropic model predicts $\propto r^{-2/(2-\gamma)}$. Thus, an observational characterization of the density radial distribution of the cores at large radii would allow the determination of γ.

- **Bonnor-Ebert (BE) sphere**

  The BE model describes the collapse of an hydrostatic confined sphere. Thus, in this model the prestellar phase starts from an initial equilibrium configuration, in contrast to the non-equilibrium LP model. Only the pressure forces opposing the gravitational collapse are considered. The density distribution of a BE-sphere is flat in its inner region while in the external region it decreases rapidly as r^{-2} down to the density of the external interstellar medium. At the center of a BE-sphere any density perturbation is rapidly smoothed out by pressure waves, which maintain constant the density around the center. The transition between the flat inner region and the outer envelope ($\rho \propto r^{-2}$) happens approximately where the sound-crossing and the free-fall times are equal (Keto & Caselli 2010):

$$r_{in} = \frac{c_s}{(32\rho_c G/3\pi)^{1/2}} \ , \tag{3.24}$$

where c_s is the sound speed. In our study of the collapse of a BE-sphere we follow the formalism of Foster & Chevalier (1993), who, in order to find the solution for this model, used different nondimensional transformations to that in equation 3.5, instead the nondimensional variables are written as:

$$\alpha = \rho/\rho_c \ \ ; \quad v = V/c_s \ \ ; \quad \xi = \frac{r}{c_s}(4\pi G\rho_c)^{1/2} \ ; \tag{3.25}$$

$$\tau = t(4\pi G\rho_c)^{1/2} \ \ ; \quad m = GM(4\pi G\rho_c)^{1/2}/c_s^3 \ , \tag{3.26}$$

where ρ_c is the central density. Using these nondimensional variables, the fluid equations 3.1 to 3.3 become:

$$m = \int \alpha\xi^2 d\xi \ , \tag{3.27}$$

$$\frac{\delta\alpha}{\delta\xi} + \frac{1}{\xi^2}\frac{\delta(\xi^2\alpha v)}{\delta\xi} = 0 \ , \tag{3.28}$$

$$\frac{\delta v}{\delta\tau} + v\frac{\delta v}{\delta\xi} = -\frac{1}{\alpha}\frac{\delta\alpha}{\delta\xi} - \frac{m}{\xi^2} \ . \tag{3.29}$$

On the other hand, for the case of an hydrostatic sphere the equation:

$$\frac{1}{\rho(r)}\frac{dP}{dr} = -\frac{d\Phi(r)}{dr} \tag{3.30}$$

is satisfied, which, together with the equation of state $P = \rho c_s^2$ makes:

$$\frac{d\ln\rho(r)}{dr} = -\frac{d}{dr}\left(\frac{\Phi(r)}{c_c^2}\right) \ . \tag{3.31}$$

Writting the last equation in terms of the reduced density and gravitational potential,

$$\alpha = e^{-\phi(\xi)} \ , \tag{3.32}$$

and substituting it into equations 3.27 to 3.29 one obtains:

$$\frac{d^2\phi}{d\xi^2} + \frac{2}{\xi}\frac{d\phi}{d\xi} = e^{-\phi} \quad ; \qquad \phi(0) = \frac{d\phi}{d\xi}(0) = 0. \tag{3.33}$$

The spheres described by these equations depend only on the extent of the sphere where the pressure equals the external pressure, ξ_{max}. Bonnor (1956) derived a critical extent, $\xi_{crit} = 6.451$, which if $\xi_{max} < \xi_{crit}$ the cloud is stable and if $\xi_{max} > \xi_{crit}$ the cloud is unstable to collapse. The relationship between ξ and ρ/ρ_c (equations 3.25 and 3.32) allows the critical condition to be written in terms of the ratio between the central density and the external density. For ratios of central to external density greater than 14.4 the cloud is unstable.

Once the collapse in a BE-sphere starts, the $\rho \propto r^{-2}$ envelope falls in, creating a shock at the boundary of the flat inner region. The density in the inner constant-density region grows, and therefore, its boundary at r_{in} (equation 3.24) decreases. The inner region gets smaller and smaller in time while the outer region (with $\rho \propto r^{-2}$) extends inward. A velocity field increasing with the distance to the center is established in the inner flat region; whereas, in the outer region, the velocity decreases outwards. This makes the velocity field adopts a $\wedge$-shape as a function of distance (see below). Once the radius of the inner flat region is reduced to zero, the protostar is considered to be formed, and the $\wedge$-shape of the velocity field is lost. Foster & Chevalier (1993) found that at the time of the central protostar formation, when the central density has a singularity, the central inflow velocity approaches to $-3.3c_s$, and the central density approaches to an $\rho \propto r^{-2}$ profile, as in the LP model, but that only occurs at the center and not at all radii. Since then on, a new inner region with $v \propto r^{-1/2}$ growing with time develops. The collapse is considered dynamic as the whole cloud is already in motion when the protostar is formed.

3.3.2 Results for the prestellar phase

Here we will explore the shape and size of the V_z-surfaces for the above mentioned models of collapse, and calculate their corresponding spatial intensity profiles under the assumptions of high line opacity and thermalization (as in A91). For this purpose we use the velocity and density fields of the models from the original papers. In this prestellar phase there is no central heating source. Cosmic radiation heats the external part of the core, while in the interior, at higher densities, the increasing efficiency of atomic and molecular line cooling maintains the temperature low. Moreover, since massive stars tend to form in multiple systems, hot cores are affected by the presence of nearby massive YSOs, whose luminosity will increase the temperature of the surrounding dust and gas. Under such circumstances, a temperature gradient increasing outwards is set in the core.

For the study of the **Larson-Penston (LP)** model we use its **polytropic generalization (LP-p)** with $\gamma < 1$. The motivation for this choice is that it is consistent with the observed density structure, $n \sim r^q$, of high-mass cores. Van der Tak et al. (2000) find that $\sim q = -1.5$. Similar values are found by other authors in different massive star forming regions (Caselli & Myers 1995; Beuther et al. 2002b; Mueller et al. 2002). A value of $q \simeq -1.5$ corresponds to a polytropic index $\gamma = 2/3$ (equation 3.17), which we will be adopted in this work. By assuming

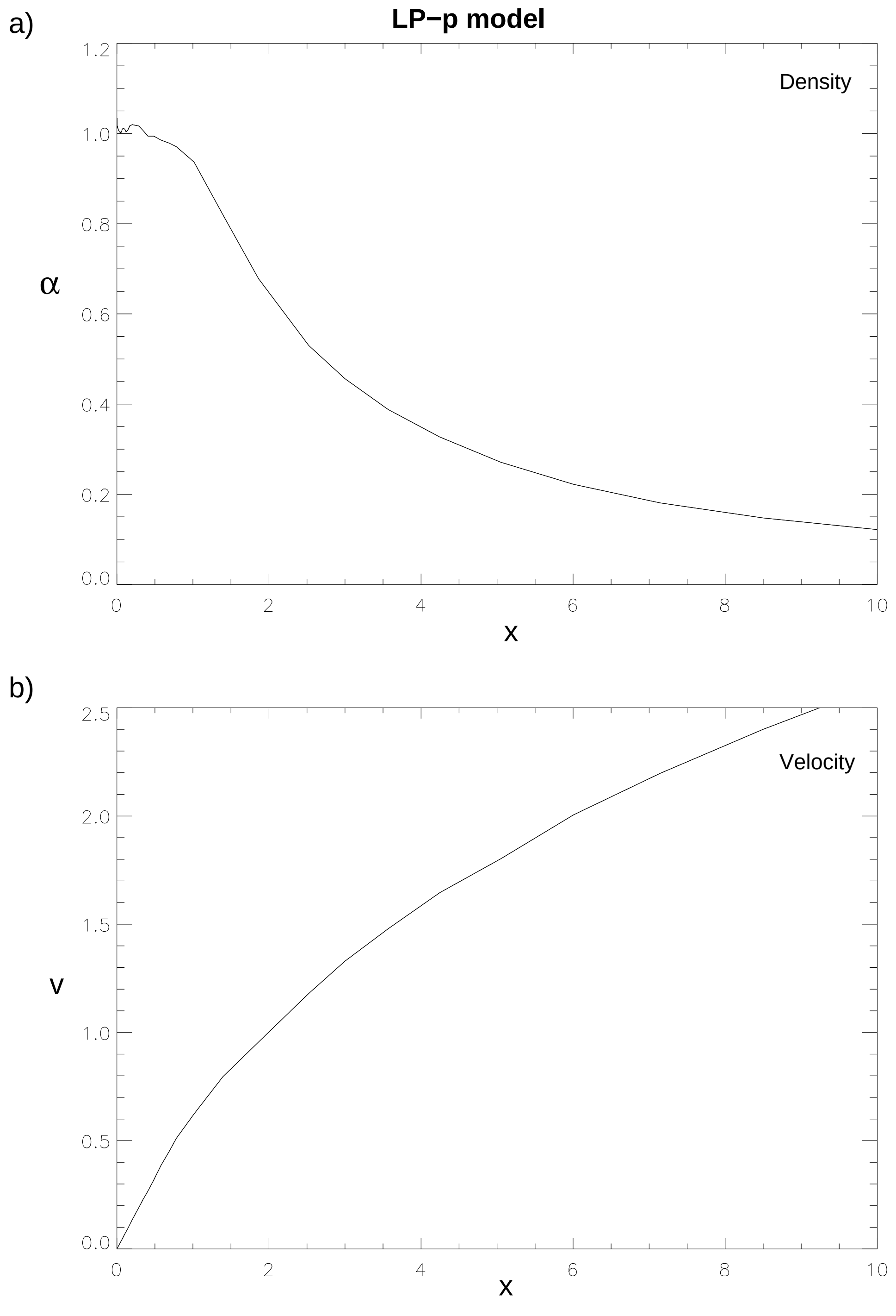

Figure 3.3: Nondimensional density *(a)* and velocity *(b)* fields during the prestellar phase of collapse ($t < 0$), as described by the LP-p ($\gamma = 2/3$) model. The values plotted here were obtained from figure 3 from Suto & Silk (1988).

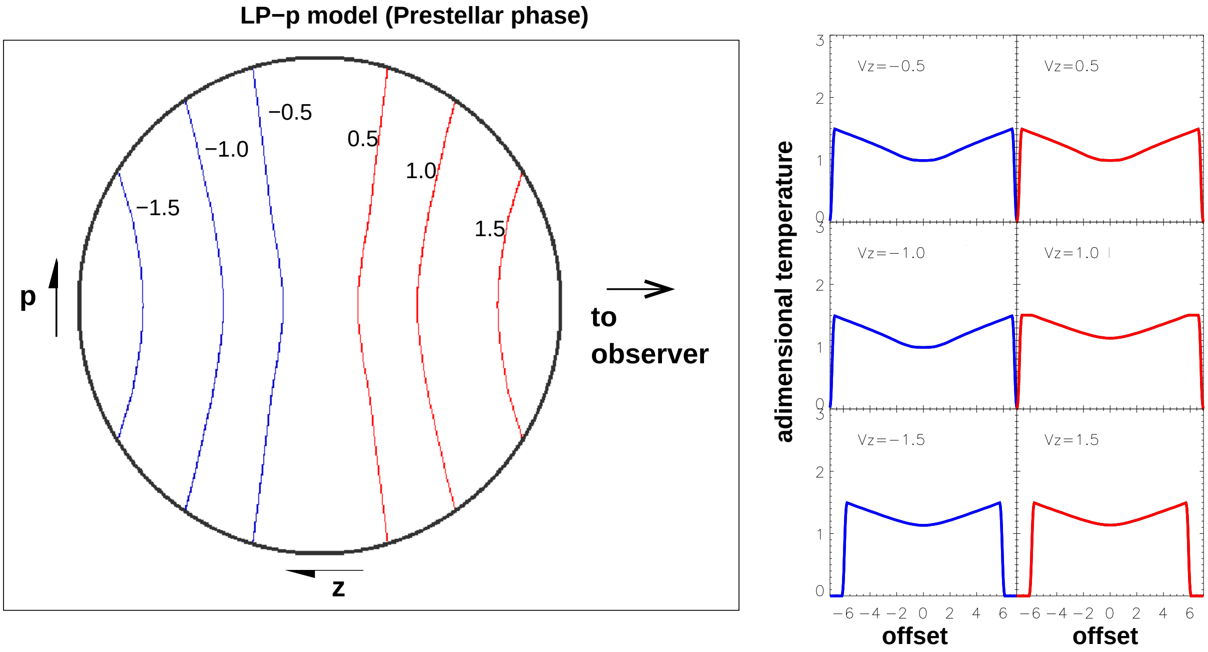

Figure 3.4: Nondimensional representation of surfaces of equal LOS velocity and their corresponding spatial intensity profiles (given a nondimensional temperature) during the prestellar phase of collapse ($t < 0$), as obtained from the velocity field of the LP-p ($\gamma = 2/3$) model (Figure 3.3).

the pressure to be purely thermal, the temperature follows equation 3.16, which yields:

$$T \propto x^2 \qquad (x << 1). \tag{3.34}$$

Note that the temperature increases outwards as required in this phase.

We consider the velocity field from figure 3 of Suto & Silk (1988) where $\alpha_* = 1$ and $\gamma = 2/3$ were assumed. The velocity field increases monotonically with x (Figure 3.3), so the V$_z$-surfaces are open and do not pass through the core center (see Figure 3.4), similar to those of the case $a > 0$ in Figure 3.2.

With respect to the images produced by the V$_z$-surfaces, the center of the images corresponds to regions closer to the core center than the edges and thus, colder. Consequently, intensity images will have a central dip. This happens for both, red- and blue-shifted velocity channels. Therefore, there is no asymmetry between the spatial intensity profiles at red- and blue-shifted velocities.

For the collapse of a **Bonnor-Ebert (BE) sphere** we used the results of Foster & Chevalier (1993) and adopted their velocity distribution from their figure 1a corresponding to the nondimensional time $\tau = -0.005$ (for visualization motives). Foster & Chevalier (1993) studied the isothermal case so we adopted the hybrid approximation to derive the line spatial intensity profile and use the same temperature law as the one derived in the LP-polytropic model. Since at large r the velocity tends to zero (Figure 3.5b), V$_z$-surfaces are closed and nested (Figure 3.6a), like those with $a < 0$ in Figure 3.1. However, this is not the case near the center of the core, where the velocity increases with increasing radius, and V$_z$-surfaces resemble those with $a > 0$ in Figure 3.2, i.e., the V$_z$-surfaces do not coincide at the core center. Regarding the images produced by such V$_z$-surfaces, for red-shifted velocities the center of the image corresponds to regions further away than the edges, hence slightly hotter, which produces spatial intensity profiles almost flat with a small increase at the center. For blue-shifted velocities, the center of the image correspond to regions that are closer to the center than the edges and thus colder, and therefore, the spatial intensity profile presents a central dip (Figure 3.6a).

Note that the hybrid approximation may not be a good approximation for the prestellar phase since the condition $V >> c_s$ migth not be met. Also the thermalization assumption ($T_{ex} \simeq T_k$) might not be true for starless cores, as pointed out by Keto & Caselli (2008). In order to avoid these problems we have used the self-consistent collapse model of Keto & Caselli (2010), who studied the dynamical evolution and the chemistry of non-isothermal supercritical cores taken as the initial state a BE sphere. With their hydrodynamic code, which assumes radiative equilibrium with dust, includes gas cooling by molecular lines, collisional coupling with the dust, as well as molecular chemistry, they are able to obtain the temperature, density and velocity fields in the core. The velocity field has the characteristic $\wedge$-shape (Figure 3.7), and therefore, the V$_z$-surfaces are closed and nested but with no point in common (see Figure 3.6b). The fact that they are closed V$_z$-surfaces makes the red and blue spatial intensity profiles asymmetric. For blue-shifted velocities, toward the center of the image, the visible part of the

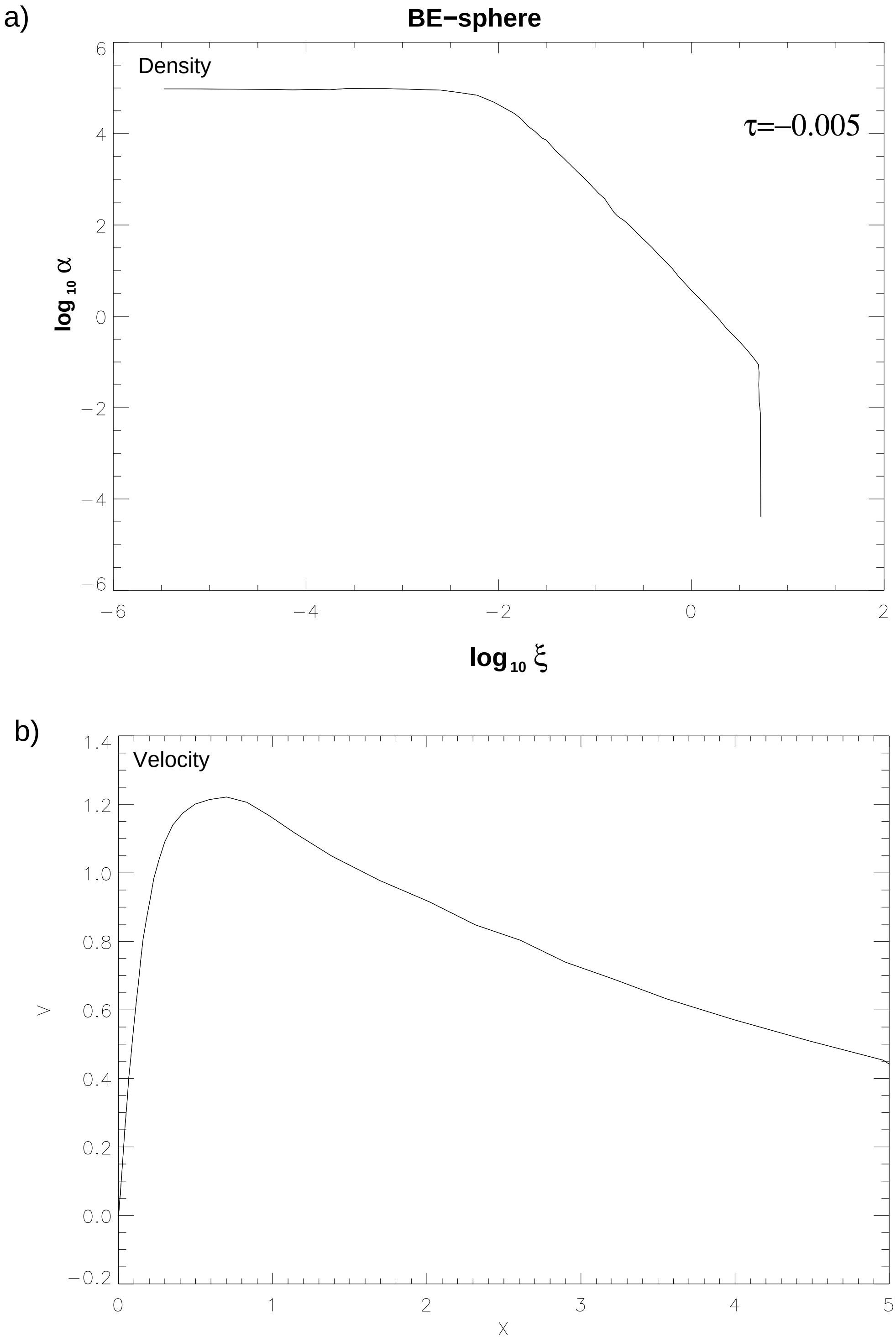

Figure 3.5: Nondimensional density *(a)* and velocity *(b)* fields during the prestellar phase of collapse, as described by the BE-sphere model. The values plotted were obtained from figure 1b from Foster & Chevalier (1993) and correspond to a nondimensional time $\tau = -0.005$.

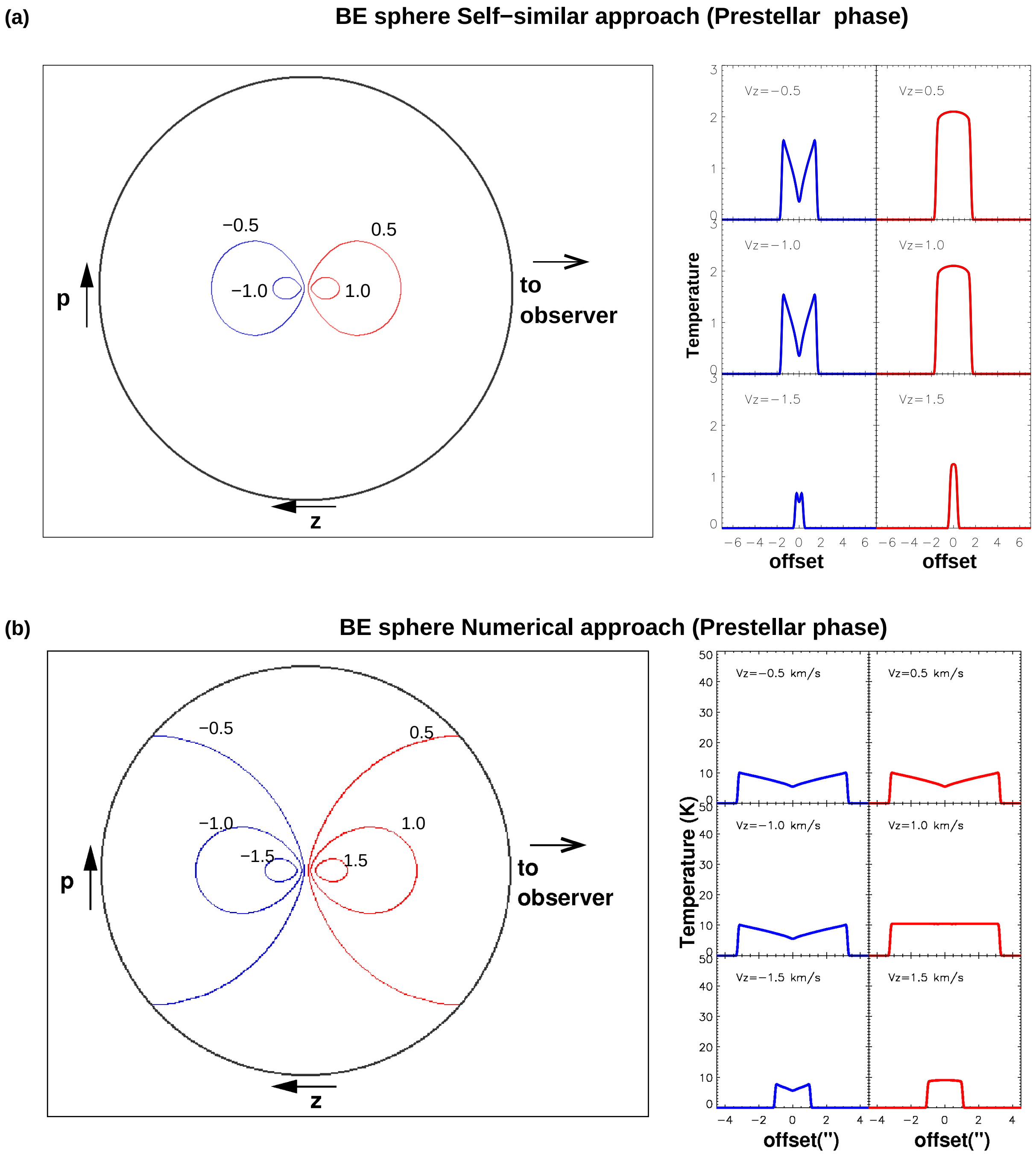

Figure 3.6: Nondimensional representation of surfaces of equal LOS velocity and their corresponding spatial intensity profiles during the prestellar phase of collapse ($t < 0$), as obtained from the velocity fields of the BE-sphere model given by *(a)* the self-similar solution of Foster & Chevalier (1993) (Figure 3.5), and by *(b)* the numerical solution of Keto & Caselli (2010) (Figure 3.7). All the magnitudes are nondimensional.

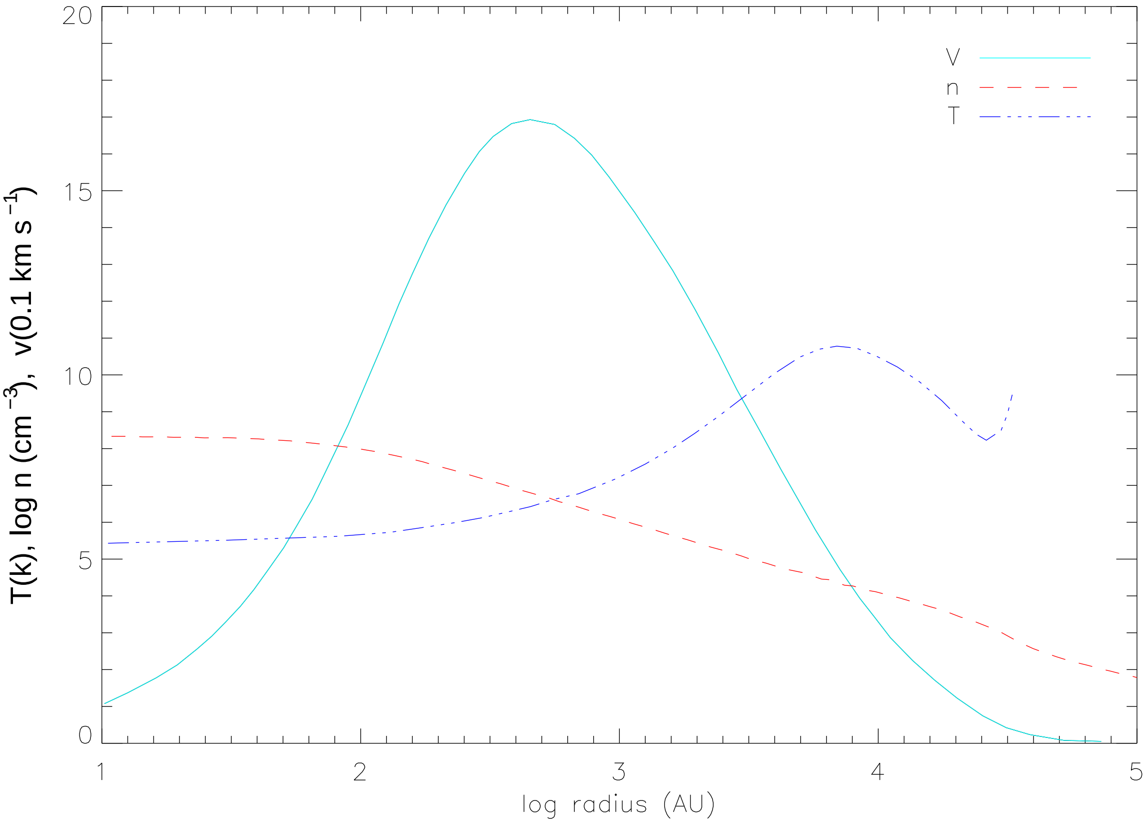

Figure 3.7: The temperature (blue line), the logarithm of the density (red line), and the inward velocity (cyan) as a function of the logarithm of the radius, for a contracting starless core when the central density is $\rho_c = 2 \times 10^8$ cm^{-3}. The temperature is in K, the density in cm^{-3}, and the velocity units are 0.1 km s^{-1}. The temperature, density and velocity distribution are taken from the lowest panel of figure 3 in Keto & Caselli (2010).

V_z-surfaces is closer to the core center (and colder) than at larger offsets, and as a consequence, the spatial intensity profile would tend to have a depression towards the center. Because of the temperature variation is small, this effect is almost inappreciable. On the other hand, for red-shifted velocities the temperature over the visible side of the V_z-surfaces varies little and the spatial intensity profiles is practically flat (see Figure 3.6b).

The main difference that we found between the initially equilibrium model (BE-sphere) and the initially non-equilibrium model (LP-polytropic) is that, while the non-equilibrium model has open V_z-surfaces, the equilibrium model has closed V_z-surfaces. This has two consequences. The first, and more evident one, is that the intensity profiles do not show any asymmetry in the LP model but they do in the BE-sphere model. Both models produce a central dip in the spatial intensity profile for blue-shifted velocities, but the BE-sphere produces flat profiles for red-shifted velocities, while those predicted by the LP-polytropic model present a central dip. However, we noted that the temperature profile obtained by setting $\gamma = 2/3$ is too steep for a starless core, and the decrease in temperature towards the center in a starless core is likely to be much gradual than predicted by the scaling law x^2. Under these conditions, the central dip in the images would be less pronounced and the predicted blue vs red differences in the spatial intensity profiles would be reduced significantly. These small differences may be easily masked by noise in observations. The second effect is related to the extension of the emission. Because closed V_z-surfaces are nested, being those of larger velocities the more internal ones, the size of the emitting region decreases with velocity, however, this is not necessary the case for open V_z-surfaces, which extend towards the limits of the core. Hence, large variation in emission size for consecutive velocity channels would point to closed V_z-surfaces, and favor equilibrium models.

3.4 Kinematic features of collapse during the main accretion phase

3.4.1 Descriptions of the models

Here we summarize the self-similar solutions of the models that describe the core collapse after the formation of a central protostar. Several of the models that we are going to explore predict a quasi-static stage prior to the formation of the protostar and therefore, we have not used them to explore kinematic features during the prestellar phase. The models for the main accretion phase together with those of the prestellar phase can be classified in a two-entry table depending on whether or not they are initially in an equilibrium state, and whether or not the core is at a (quasi-)static state at the moment of the protostar formation (Table 3.1).

During the main accretion phase, gravity dominates in the region closest to the central object and therefore, all the models predict a radial power-law scaling in the form: $\rho \propto r^{-3/2}$, and $V \propto r^{-1/2}$. This behavior in the inner collapsing part is in fact the free-fall state, and it

Table 3.1: Model Classification

		Initial state	
		Equilibrium	**Non-Equilibrium**
State at protostar formation	**Static**	SIS/SLS	...
	Dynamic	BE-sphere	LS/LPH(-p)

Notes: SIS = Singular Isothermal Sphere; SLS = Singular Logatropic Sphere; BE-sphere = Bonnor-Ebert Sphere; LS = Rapid collapse; LPH(-p) = Larson-Penston-Hunter-polytropic.

appears consistent with observations (Zhou et al. 1990). Meanwhile, in the outer part of the core the density and velocity fields will depend on the initial conditions assumed and on the polytropic index (Cheng 1978, Suto & Silk 1988, Ogino et al. 1999).

- **The Larson-Penston-Hunter (LPH) collapse model**

  Hunter (1977) extended the LP model to include the phase after the formation of the protostar ($t > 0$). We recall that the initial assumption in this model is uniform density and that only hydrodynamic and thermal pressures oppose gravity. At $t = 0$ the entire core is falling at a velocity of $3.3c_s$, and the density behaves as $\rho \propto r^{-2}$ (see Section 3.3.1). Afterwards, while material keeps falling at $3.3c_s$ at large r, the velocity in the innermost part will behave as $V \propto r^{-1/2}$. The transition between the two velocity regimes is smooth. The density in the innermost part also begins to resemble that of a free-fall case, $\rho \propto r^{-3/2}$. The similarity transformations used by Hunter (1977) are:

$$\xi = c_s t/r; \quad \rho(r,t) = \frac{c_s^2 \alpha(\xi)}{4\pi G r^2}; \quad V(r,t) = c_s v(\xi); \quad M(r,t) = \frac{c_s^3 t}{G} m(\xi) \ . \tag{3.35}$$

  Hunter (1977) applied a Taylor-series expansion in the neighborhood of the point $\xi = \xi_*$ where the condition $1/\xi = v$ is fulfilled:

$$\alpha(\xi) = -\frac{2}{\xi_*} + \frac{2(\xi - \xi_*)}{\xi_*^2} - \frac{(7\xi_*^2 + 6\xi_* + 1)(\xi - \xi_*)^2}{\xi_*^4(3\xi_* + 2)} \ , \tag{3.36}$$

$$v(\xi) = -(1 + \frac{1}{\xi_*}) - \frac{(\xi - \xi_*)}{\xi_*} + \frac{(\xi_*^2 - \xi_* - 1)(\xi - \xi_*)^2}{2\xi_*^3(3\xi_* + 2)} \ , \tag{3.37}$$

where $\xi_* = -0.4271$ for the LPH solution. For $\xi \to \infty$, which here correspond to small distances or large times, the nondimensional variables behave as:

$$m(\xi) = m_0; \quad \alpha(\xi) = (\frac{m_0}{2\xi})^{1/2}; \quad v(\xi) = -(2m_0\xi)^{1/2} \ , \tag{3.38}$$

where m_0 is the reduced mass of the internal protostar and has a value of $m_0 = 46.915$ in this model.

- **The LPH-polytropic (LPH-p) collapse model**

  This is the generalization of the LPH model to the polytropic case. We follow the formalism used by Yahil (1983), which assumes conventional polytropes, $n = 2 - \gamma$. The self-similar transformations used by this author are:

$$x = \frac{-r}{k^{1/2}t^{(2-\gamma)}G^{(1-\gamma)/2}}; \quad \rho(r,t) = \frac{\alpha(x)}{G(-t)^2} \ ; \tag{3.39}$$

$$V(r,t) = k^{1/2}G^{(1-\gamma)/2}(-t)^{1-\gamma}v(x); \quad M(r,t) = \frac{k^{3/2}(-t)^{(4-3\gamma)}}{G^{(3\gamma-1)/2}}m(x) \ . \tag{3.40}$$

  The main difference with the isothermal case (LPH) happens at large distances, where the velocity and density fields for the LPH-polytropic model take the form:

$$\alpha(x) \propto x^{-2/(2-\gamma)}; \quad v(x) \propto x^{(1-\gamma)/(2-\gamma)} \ . \tag{3.41}$$

  For $1 < \gamma < 2$, the velocity field tends to zero at large distances from the center, while for other values of γ the velocity increases with x at large x.

- **The Singular Isothermal Sphere (SIS) collapse model**

  The classical theory of star formation considers a core initially supported against gravity by the magnetic field (subcritical core), but the slow process of ambipolar diffusion makes neutrals become increasingly centrally concentrated, until a density distribution $\rho \propto r^{-2}$ is achieved. At that point, the protostar is formed and the hydrostatic pressure forces takes over magnetic support in preventing the gravitational collapse and maintaining the cloud in (highly unstable) equilibrium. This is the starting point for the SIS model. Once a perturbation breaks the equilibrium, the main accretion phase begins, the collapse starts at the center, and as matter in the inner part falls in, the matter in outer immediate layers, still at rest, find the bottom dropping out from beneath them, loses its pressure support against gravity, so it also begins to fall, that is, the falling process progresses outwards in the form of an "expansion wave". Such collapse front moves outwards at the speed of sound setting up the particles behind it into motion. In the inner growing region the velocity field behaves as $V \propto r^{-1/2}$ and the density field as $\rho \propto r^{-3/2}$, while outside the collapse front the matter is still at rest and the density follows $\rho \propto r^{-2}$. Such a way of collapse has been traditionally called the "inside-out" collapse. Note that, since the ambipolar diffusion is a quasi static process, during the prestellar phase and at the moment of the formation of the protostar, the gas core is almost static.

The self-similar transformation originally used by Shu (1977) is obtained by setting $n = 1$ and $k^{1/2} = c_s$ in equations 3.4 and 3.5:

$$x = \frac{r}{c_s t}; \quad \rho(r,t) = \frac{\alpha(x)}{4\pi G t^2}; \quad u(r,t) = c_s v(x); \quad M(r,t) = \frac{c_s^3 t}{G} m(x) \ . \tag{3.42}$$

The asymptotic solutions at large x of the SIS are obtained under the condition that the reduced radial velocity $v(x)$ is zero:

$$m(x) = 2x; \quad \alpha(x) = \frac{2}{x}; \quad v(x) = 0 \quad (x \geq x_{ew}). \tag{3.43}$$

Moreover, the asymptotic solution at small x is:

$$m(x) = m_0; \quad \alpha(x) = \left(\frac{m_0}{2x^3}\right)^{1/2}; \quad v(x) = -\left(\frac{2m_0}{x}\right)^{1/2} \quad (x << x_{ew}) \tag{3.44}$$

where x_{ew} is the position of the collapse front and $m_0 = m(0)$ is the reduced mass of the protostar. For this model, the collapse front is at $x_{ew} = 1$, and $m_0 = 0.975$.

- **The Singular Polytropic Sphere (SPS) collapse model**

  This is the generalization of the SIS to the conventional polytropic case ($n = 2 - \gamma$). We use the formulation of the problem given by Lou & Wang (2006). The self-similar transformations of the SPS are those in equations 3.4 and 3.5. The asymptotic solutions are obtained by considering quiescent material at large x, and that v and α are non-increasing functions of x at small x:

$$m(x) = n\left[\frac{n^2}{2\gamma(3n-2)}\right]^{1/n} x^{3-2/n}; \quad \alpha(x) = \left[\frac{n^2}{2\gamma(3n-2)}\right]^{1/n} x^{-2/n}; \quad v(x) = 0 \quad (x \gg 1) \tag{3.45}$$

$$m(x) = m_0; \quad \alpha(x) = \left(\frac{(3n-2)m_0}{2x^3}\right)^{1/2}; \quad v(x) = -\left(\frac{2m_0}{(3n-2)x}\right)^{1/2} \quad (x \ll 1) \tag{3.46}$$

- **The Singular Logatropic Sphere (SLS) collapse model**

  This model aims at providing a unified treatment for both low and high-mass star formation, as well as to explain the observed relation between the velocity dispersion (σ_V) and the size (l) of cores, $\sigma_V \approx l^q$, where $q = 0.2$ and $q = 0.5$ for low- and high-mass cores, respectively (Caselli & Myers 1995). This model considers that nonthermal random motions (turbulence) provide support against gravity additional to the thermal pressure and help to maintain the cloud in unstable equilibrium. These nonthermal motions have a hierarchical nature and are responsible for the $\sigma_V \approx l^q$ relationship. To account for this, the SLS model uses a phenomenological equation of state of the form (McLaughlin & Pudritz 1996, 1997):

  $$P = P_c \left[1 + 0.2 \ln \left(\frac{\rho}{\rho_c}\right)\right] \ , \tag{3.47}$$

  where P_c and ρ_c are the pressure and density at the center of the cloud. In the SLS model the density law in equilibrium behaves as $\rho \propto r^{-1}$ in the external region, in contrast to $\rho \propto r^{-2}$ in the case of pure thermal support (BE-spheres and SIS models). The formalism and interpretation are extensions of those in the SIS model: the core is essentially at rest when a perturbation sets the system out of equilibrium a collapse front moves outward into the external part at rest, and the gas behind it falls onto a protostar. Hence, the SLS is also an "inside-out" collapse model. The similarity transformations are the same as for the SIS (equations 3.42), except for the sound speed, which for the SLS is a time dependent function:

  $$c_s = [AP_c(4\pi G t^2)]^{1/2} \ . \tag{3.48}$$

  Note that this is the same as considering $k = 4\pi AP_cG$ and $n = 2 - \gamma$ with $\gamma \to 0$ in equations 3.4 and 3.5. The static solution of a SLS ($x > x_{ew}$) can be found by assuming both c_s and $|v|$ to be much smaller than x in equations 3.7 to 3.9:

  $$m(x) = \frac{x^2}{\sqrt{2}}; \quad \alpha(x) = \frac{\sqrt{2}}{x}; \quad v(x) = 0 \tag{3.49}$$

  The asymptotic solutions of the SLS at $x \to 0$ are:

  $$m(x) = m_0; \quad \alpha(x) = 4\left(\frac{m_0}{2x^3}\right)^{1/2}; \quad v(x) = -\left(\frac{2m_0}{x}\right)^{1/2} \tag{3.50}$$

  The collapse front is at $x_{ew} = \frac{1}{4\sqrt{2}}$, and $m_0 = 6.67 \times 10^{-4}$.

- **The Rapid Collapse models (LS)**

  The rapid collapse model describes the formation of cores as a consequence of shocks from random large-scale supersonic flows, which create local enhancements of density that may have enough mass to collapse. Lou & Shen (2004), hereafter LS model, found spherical isothermal self-similar solutions for initial conditions with non-zero inward velocity and non-equilibrium density structures. We take the solution of Lou & Shen (2004) as an approximation to the physical conditions of the rapid collapse model, by considering the non-zero inwards velocity as the velocity of the encountering flows, and the non-equilibrium density as the density structure formed after the shock, since an equilibrium density distribution would be rare to be formed via shocks. The self-similar transformation in the LS model is the same as in the SIS, with $n = 1$, $k = c_s^2$. For $x \ll 1$ the asymptotic solutions have the same form as in the SIS model. However, for $x \gg 1$, the asymptotic solutions are:

$$\alpha = \frac{A}{x^2} - \frac{A(A-2)}{2x^4} + \frac{(4-A)v_0 A}{3x^5}; \tag{3.51}$$

$$v = v_0 + \frac{(2-A)}{x} + \frac{v_0}{x^2} + \frac{(A/6-1)(A-2) + 2v_0^2/3}{x^3} + ... \tag{3.52}$$

where v_0 and A are constants. v_0 represents the velocity of the pre-existing large-scale external flow creating the shock, in units of sound speed. The parameter A sets the density structure of the core. Cores can be “overdense”, i.e., with densities higher than the maximum value for which pressure supported against collapse ($A > 2$); or “subdense” ($A < 2$). Note that the SIS solution can be recovered by simply setting $v_0 = 0$ and $A = 2$. For the case presented here we assume the initial infall velocity $v_0 = -2$ and two density states corresponding to $A = 0.436$ ($m_0 = 0.624$)(subdense) and $A = 2.2$ ($m_0 = 5.92$) (overdense), which we will denote as LS-sub and LS-over, respectively.

3.4.2 Results for the main accretion phase

In this section we will explore the shape and size of the V$_z$-surfaces for the above mentioned models of collapse; and calculate the corresponding spatial intensity profiles of molecular transitions under the assumptions of high line optical depth and thermalization (as in A91). For that analysis we will use the hybrid approximation (see Section 3.2.2), although we will complement it with polytropic models when possible.

The main accretion phase begins with the formation of the protostar, which is represented in the models by a singularity in the density field at $r = 0$. During the initial stages of this phase, the shock created by matter falling onto the protostar is the main heating source, and later on, the luminosity of the star itself will also be relevant. These two heating mechanisms will produce a temperature gradient increasing inwards. A power law dependence for the temperature as $T \propto r^{-1/2}$ has been implemented ad hoc for the hybrid approximation. This choice was motivated by several reasons. First, as a first approximation, in the case of optically thin limit for the dust opacity, the radiation field approaches that of a point source of luminosity L_{tot} at a distance r. In the case of a gray opacity obeying the Kirchhoff’s law, the temperature is independent of the dust opacity and is given by:

$$T^4 = \frac{L_{tot}}{16\pi\sigma r^2} \tag{3.53}$$

where L_{tot} is the luminosity of the central heating source, and σ is the Steffan-Boltzmann constant. Second, setting $T \propto r^{-1/2}$ facilitates the comparison with the original results of the 3D signature in A91, who adopted such a power-law dependence from the numerical results of Larson (1972) for the collapse of protostars with masses from 0.25 $M_\odot$ to 10 $M_\odot$. Third, Osorio (2000) modeled the Spectral Energy distribution of four high-mass cores, and obtained that the behavior of the temperature distributions ranges from $T \propto r^{-0.30}$ (in the outer part of the core) to $T \propto r^{-0.75}$ (in the inner part). Taking $T \propto r^{-1/2}$ is a compromise between the two limits. A more self-consistent analysis, which takes into account the dust opacity in the calculation of the temperature profile, will be presented in Chapter 4 for the source G31 HMC. We also assume for simplicity that the region under study has a systemic velocity $V_{LSR} = 0$. We analyze the behavior of the different models using three different approaches to calculate the intensity profile:

(i) The nondimensional approach: In this first approach we will work on the nondimensional space of the self-similar solutions, i.e., we will use the nondimensional velocity v to construct the V_z-surfaces, and consider the nondimensional variable, x, as the spatial variable. We use the formalism of A91, i.e., we assume optically thick thermalized molecular transitions in all positions to obtain the intensity images as a function of velocity. Although it is a crude approach, as we are also neglecting any time-dependence, it is illustrative and help to understand the results of more precise approaches.

(ii) Application to the specific physical conditions of HMCs and the NH_3 molecule: This second approach consists in changing from dimensionless functions (α, v, m and β) depending on x to physical functions (ρ, V, M, P) depending on (r, t) by specifying a time. By doing so, we will be able to take into account the density and the temperature distribution of each model and thus, we will be able to limit the region where the conditions of thermalization and high line opacity are fulfilled. We perform the analysis for the (4,4) inversion transition of ammonia, for which the critical density (the minimum density needed for thermalization) is $\sim 10^5$ cm^{-3} and the sublimation temperature is 60 K, above this temperature the ammonia is released to gas-phase and its abundance increases several orders of magnitude (Lee, Bergin & Evans. 2004). We obtain the spatial intensity profiles by using the formalism of A91, to do so we assume that the ammonia emission is optically thick where the molecules are in gas-phase, and consider that the NH_3(4,4) transition is thermalized over $\sim 10^5$ cm^{-3}.

(iii) Radiative transfer calculations: The third approach is to take the same velocity and density field as in the previous approach, and introduce them in our radiative transfer code to obtain the emergent ammonia emission for its (4,4) inversion transition. Here neither thermalization nor high line opacity are assumed beforehand. The main goal is to check if the spectral imaging signature of A91 is expected and observationally detectable according to the physical characteristic predicted by the models. The results of this approach also allows us to check

whether the formalism of A91 (used in the previous approaches) produces reliable predictions of the intensity image.

3.4.2.1 Results from the nondimensional approach

For the study of the V$_z$-surfaces we use the nondimensional velocity field of the different models described in Section 3.4.1. The nondimensional variable x, which relates r and t, is understood here as a spatial variable. In other words, we are considering that our assumptions and results are valid for all times. The density and velocity fields for the "equilibrium" models (SIS, SLS, SPS) are shown in Figure 3.8, and in Figure 3.9 for "non-equilibrium" models (LPH, LS). The V$_z$-surfaces considered are those of values $v_z = \pm 1, 2, 3$, and 4, which are shown in Figure 3.10. Note that, because of the use of nondimensional variables, velocities are not in km s^{-1}, but in units of sound speed, c_s. To obtain the spatial intensity profiles of the line emission corresponding to the different models, we will assume, as stated before, that we are observing a thermalized, optically thick molecular transitions. We assume that these conditions are fulfilled for the whole range of values of x and v_z considered. Thus, we assume that the intensity images (channel maps) are, in fact, maps of the T_{ex} over the corresponding V$_z$-surface. For computational reasons we have to limit the core radius to a maximum value, x_m. The choice of x_m has been made on the basis of a proper visualization of the model characteristics. For example, the core radius has been set equal to the collapse front position $x_m = x_{ew}$ for the inside-out models (SIS, SPS, and SLS). Moreover, we chose the beam-to-core size relationship to be fixed at 0.014 for all models, which corresponds to the one used originally in A91 for their highest angular resolution case. The temperature field, $\Gamma(x)$, is chosen to be nondimensional as well. For simplicity we have chosen $\Gamma(x) = x^{-1/2}$, a simplification of equation 3.53.

For the **Singular Isothermal Sphere (SIS)** the velocity field was obtained from table 2 of Shu (1977) (see also figure 2). All the V$_z$-surfaces are closed, nested (Figure 3.10) and pass through the core center. The hybrid approximation has been used to calculate the spatial intensity profiles, which show a blue-red asymmetry. The spatial intensity profiles at blue-shifted velocities are centrally peaked while the ones at red-shifted velocities are flat. Also the size of the emitting region decrees when $|v_z|$ increases (Figure 3.11). This is the spectral imaging infall signature described by A91 for spatially resolved cores.

The generalization to the polytropic case of the SIS model, the **Singular Polytropic Sphere (SPS)**, allows for variability of the temperature field without adopting the "hybrid approximation". The temperature field predicted by the polytropic model is $\Gamma \propto x^{-2(\gamma-1)/(2-\gamma)}$. In order to compare with the SIS model we need to set $\Gamma = x^{-1/2}$, which would correspond to $\gamma = 4/3 \simeq 1.333$. We took instead $\gamma = 1.3$, which predicts an nondimensional temperature distribution $\Gamma = x^{0.45}$, since the case $\gamma = 4/3$ is a particular case that needs a different treatment (Lou & Wang 2006). The velocity field was obtained from figure 1 of Lou & Wang (2006) where $\gamma = 1.3$, $n = 2 - \gamma = 0.7$, the collapse front is at $x_{ew} = 1.526$ and $m_0 = 0.273$. The core limit was set at the location of the collapse front $x_m = x_{ew} = 1.526$. Like in the SIS case, all the V$_z$-surfaces are closed surfaces (Figure 3.10) and therefore the spectral imaging infall

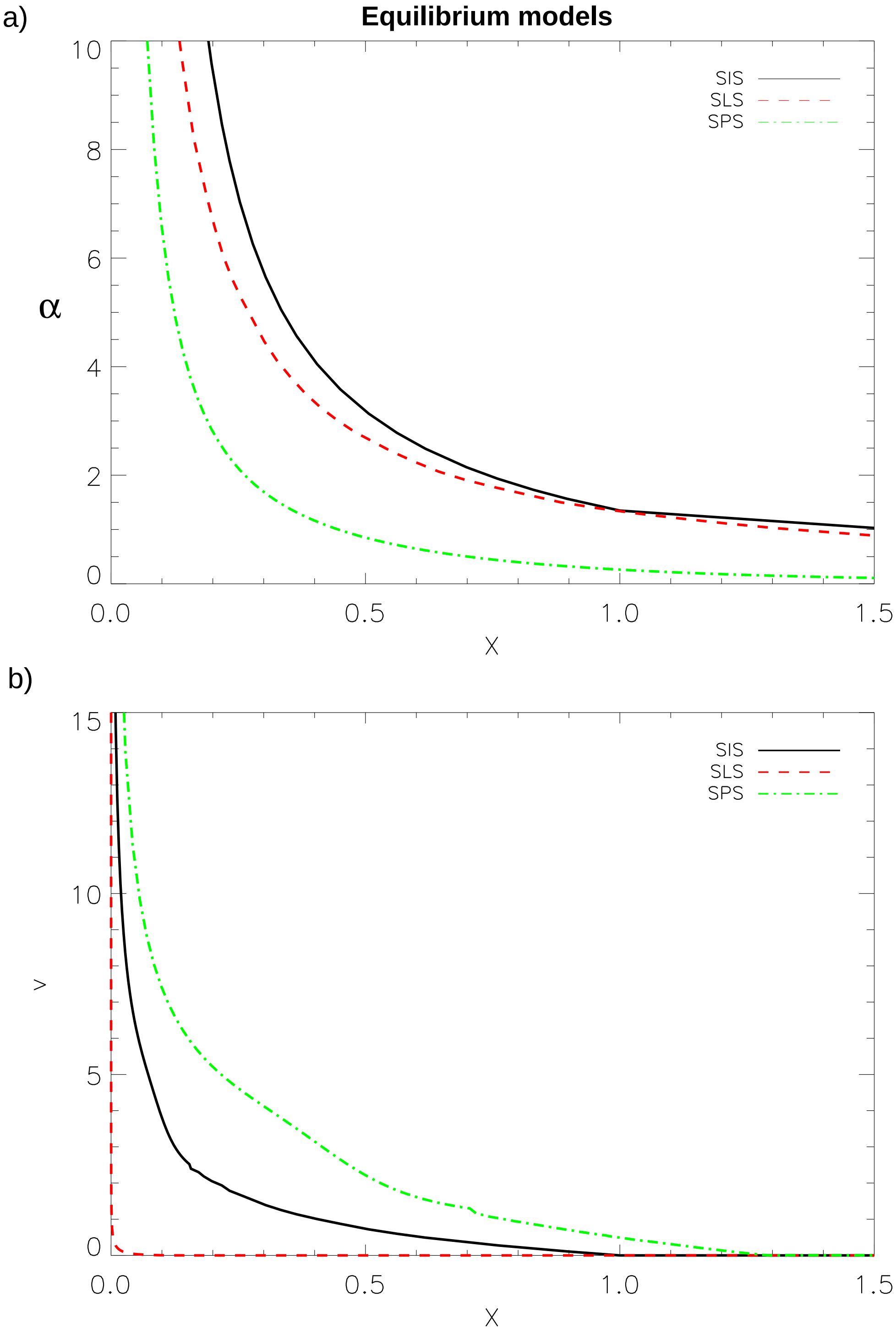

Figure 3.8: *(a)* Nondimensional density field and *(b)* nondimensional velocity field during the main accretion phase of the self-similar collapse models SIS, SLS, and SPS ($\gamma = 1.3$), for which the initial state is at equilibrium. The values of the fields have been obtained from Shu (1977), McLaughlin & Pudritz (1997) and Lou & Wang (2006), respectively.

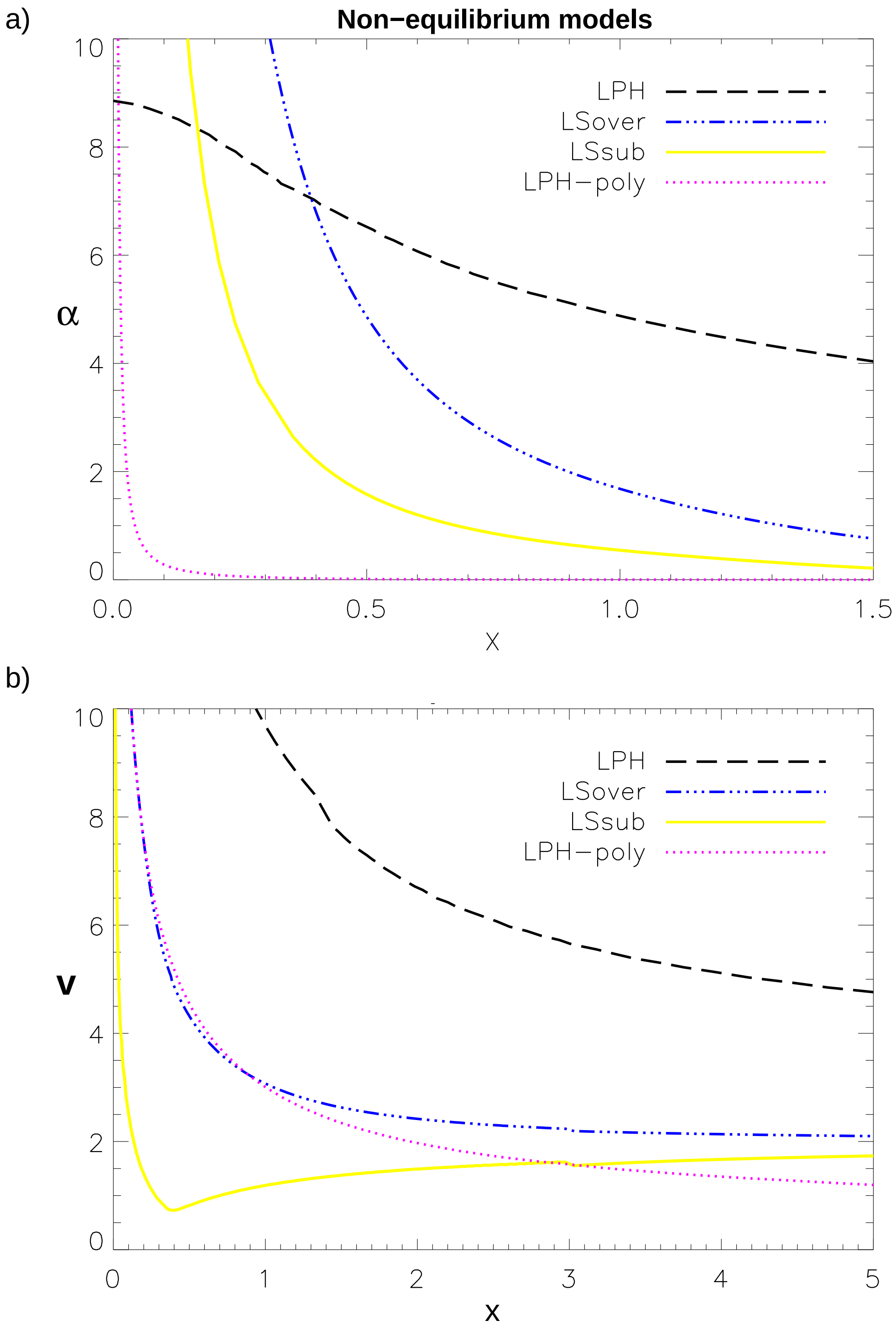

Figure 3.9: *(a)* Nondimensional density field and *(b)* nondimensional velocity field during the main accretionphase of the self-similar collapse models LPH, LPH-p ($\gamma = 1.3$), LS-over and LS-sub for which the initial state is at non equilibrium. The values of the fields have been obtained from Hunter (1977), Yahil (1983) and Lou & Shen (2004), respectively.

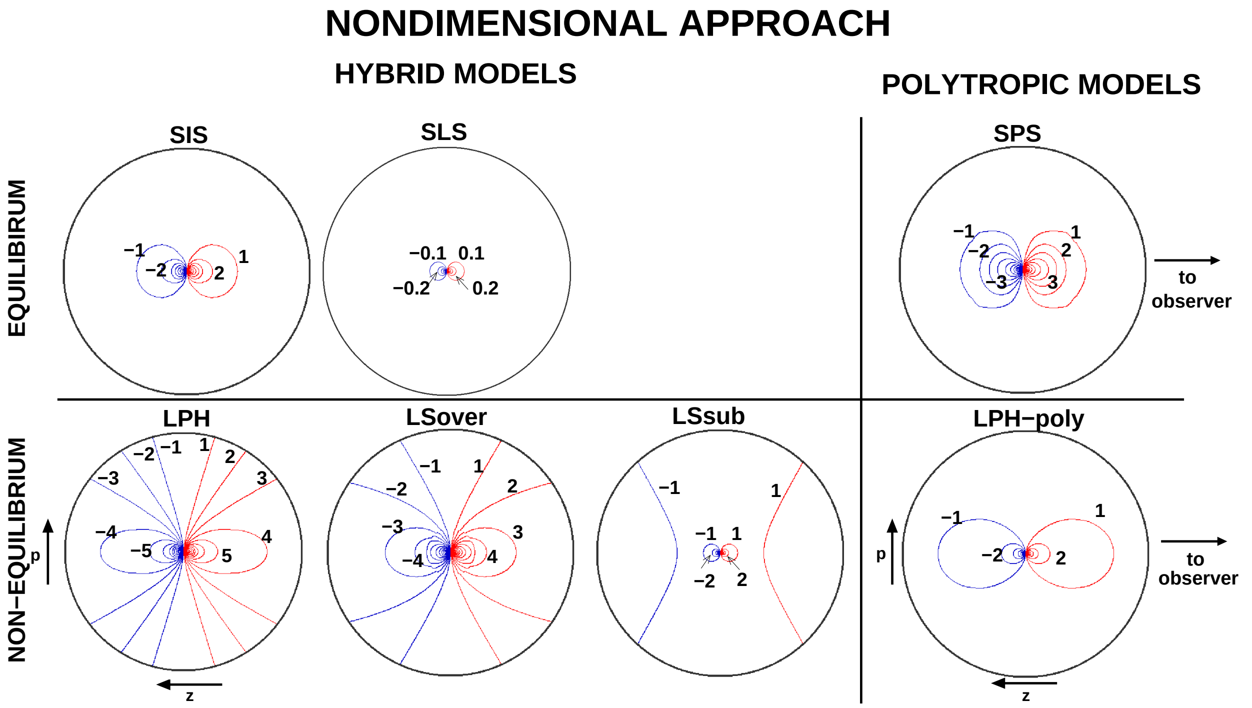

Figure 3.10: Surfaces of equal LOS velocity during the main accretion phase ($t > 0$), as obtained from the velocity field of the LP-p ($\gamma = 2/3$) model (Figure 3.3). All the magnitudes are nondimensional. Surfaces of equal LOS velocity for a collapsing protostellar envelope for the models SIS, SLS, SPS ($\gamma = 1.3$), LPH, LS-over, LS-sub, and LPH in its polytrope generalization for $\gamma = 1.3$. The isovelocity surfaces correspond to values of the nondimensional velocity of $v_z = \pm$ 1,2,3,4... except for the case of the SLS model, where such V$_z$-surfaces are too small to be visible because large velocities are accomplished only deep inside the collapse front. For the SLS model the V$_z$-surfaces shown correspond to $v_z = \pm 0.1$, 0.2, and 0.3.

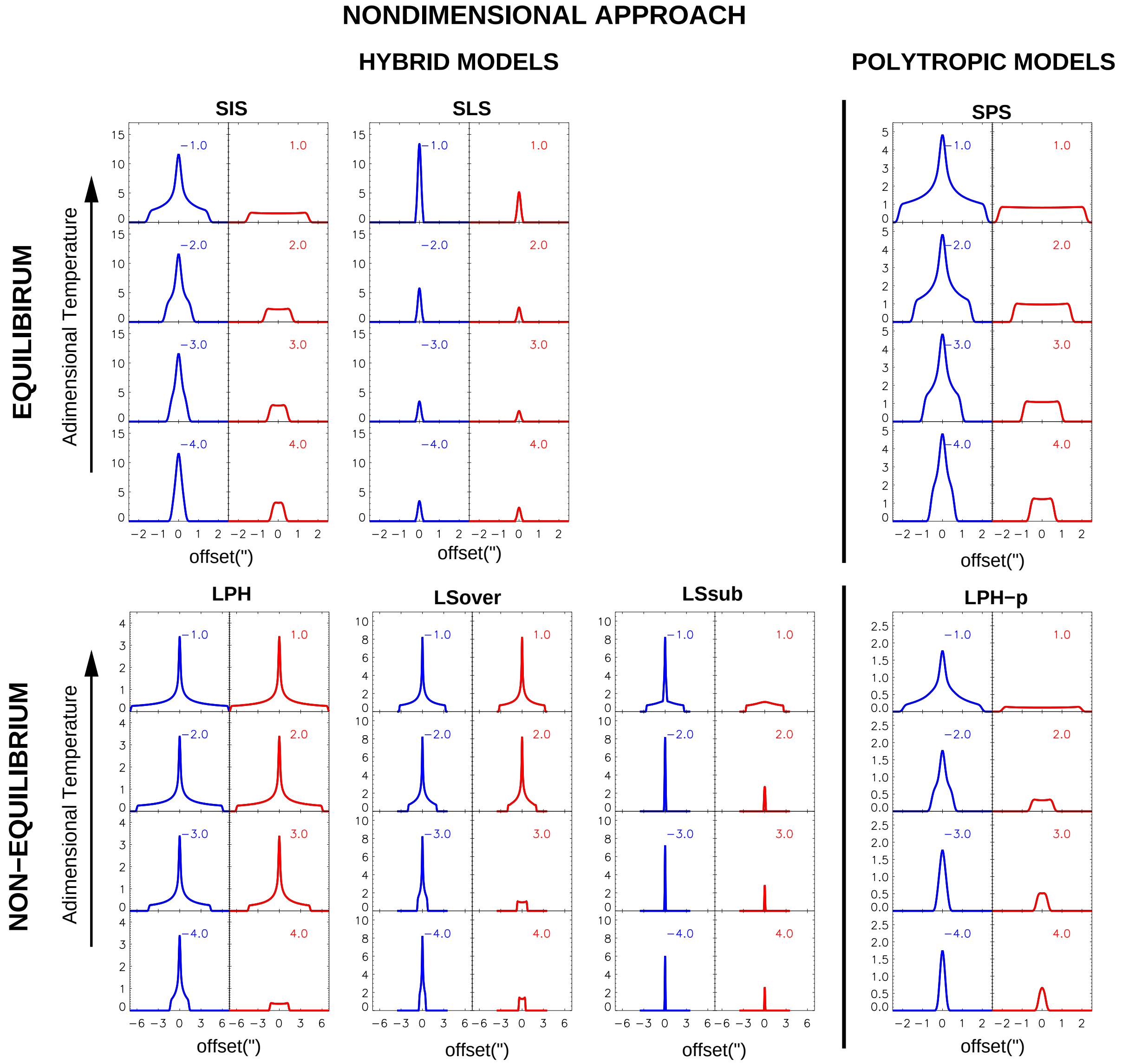

Figure 3.11: Intensity as a function of angular offset from the source center during the main accretion phase for channel maps of nondimensional velocities $v_z = \pm$ 1,2,3 and 4 (from top to bottom). The velocity in units of times the sound speed is shown in the upper right corner of the each panel.

signature is maintained (Figure 3.11).

For the **Singular Logatropic Sphere (SLS)** model the hybrid approximation is used. The velocity and density fields were obtained from figure 3 of McLaughlin & Pudritz (1997). The limit of the core was set to $x_m = x_{ew} = \frac{1}{4\sqrt{2}}$. The V$_z$-surfaces are closed so the infall signature of A91 is expected to be maintained, but the V$_z$-surfaces corresponding to $v_z = 1, 2, ...$ are more than one order of magnitude smaller than x_{ew} so that they are almost indistinguishable in Figure 3.10. This happens because most of the collapsing gas in this model has subsonic velocities, and only the central region of the collapsing core is accelerated to supersonic velocities by gravity. Therefore, the emission at the highest velocities in this example would not be spatially resolved by the beam and only the 1D signature in Anglada et al. (1987) (blue emission more intense than the red one) is detectable.

In the **Larson-Penston-Hunter (LPH)** model there is no separation between an inner collapsing zone and an outer one at rest; instead the whole core is moving at supersonic velocities. We have set the outer radius of the core at $x_m = 1/\xi_m = 15$. The velocity and density fields are obtained from figures 1 and 3 of Hunter (1977), respectively. Since at large x, the velocity approaches $3.3c_s$, the V$_z$-surfaces with $|v_z| < 3.3c_s$ are open surfaces and pass through the core center (Figure 3.10) as in the case of $a = 0$ of Figure 3.1. The hybrid approximation has been used to calculate the spatial intensity profile. Opened surfaces do not produce asymmetric spatial intensity profiles, but produce the intensity images to be centrally peaked for both red-shifted and blue-shifted velocities. Consequently, at the low velocities, the signature of infall of A91 is lost (Figure 3.11), and blue and red spatial intensity profiles are equal. However, for the higher velocities, surfaces are closed and the signature of infall of A91 is recovered.

For the **LPH-polytropic (LPH-p)** model (the polytropic generalization of the LPH model) we have taken $n = 2 - \gamma$ and $\gamma = 1.3$, as we did for the SPS model. We obtained the self-similar velocity and density distributions for this γ from figures 1 and 4 of Yahil (1983) respectively. We set the limit of the cloud at $x_m = 10$ for representation motives. As mentioned for the SPS, this γ predicts a nondimensional temperature distribution of $\Gamma = x^{-0.45}$, similar to the one we use for the models with the hybrid approximation. Note that this choice of γ also implies that the velocity goes to zero at large distances (equation 3.41). In that case, all the V$_z$-surfaces are closed (Figure 3.10), and therefore the 3D infall signature is maintained at all velocities (Figure 3.11).

For the **LS-over** and **LS-sub** models, which we consider representative of rapid collapse, the hybrid approximation has to be applied since they are originally isothermal models. The velocity fields were obtained from figure 2 in Lou & Shen (2004). The radius of the core was set at $x = 2$. The velocity field for the LS-over model monotonically decreases with increasing distance from the center down to a non-zero ($v = 2$) asymptotic value, like the LPH model. For the LS-over model, all the V$_z$-surfaces of $|v_z| > 2$ are closed (Figure 3.10), but the $|v_z| = 1$ and $|v_z| = 2$ V$_z$-surfaces are open. Hence, the infall asymmetry in the spatial intensity profiles is lost at the lowest velocities $|v_z| < 2$ while it is maintained at velocities $|v_z| > 2$. The velocity field of the LS-sub model is significantly different to that of any other model (Figure 3.9). The velocity fields in other models decreased monotonically with increasing radius (outwards), but the LS-sub velocity field decreases in the inner part, presents a local minimum at $x \sim 0.4$, and rises in the outer region. In the inner part of the core, where velocity decreases with radius, the V_z-surfaces are closed as in the case of $a < 0$ in Figure 3.1. However, for large x, where the velocity increases with x, they would be open paraboloids that do not intersect the core center, as in the case of $a > 0$ in Figure 3.1. For the case considered here, all V_z-surfaces with $|v_z| > 2$ are closed (Figure 3.10), but the $|v_z| = 1$ surfaces appears twice, one as a closed surfaces and a second time, at larger x, as a paraboloid surface that does not pass through the core center. The central part of the outer open V_z-surface of $v_z = -1$ (blue-shifted velocity) is hidden by the inner closed V_z-surface of the same velocity. This produces a sharp peak in the intensity images at $v_z = -1$, while the outer open-surface makes the emission to extend at large offsets. On the other hand, the outer open V_z-surface at $v_z = 1$ (red-shifted) completely hides the inner and closed V_z-surface at that velocity. Moreover, as this open V_z-surface does not pass through the core center, but it is located in the outer part, the temperature varies little all over its surface. As a consequence, the intensity image that produces is almost flat. The final result is that, although the LS-sub model present open V_z-surfaces, their location at the outer region of the core produces an effect that mimics the asymmetry in the spatial intensity profiles characteristic of infall (Figure 3.11). The closed surfaces in this numerical example become small, even at relatively low velocities, and would be spatially unresolved. So, the infall signature of A91 would be hardly visible in these spatial intensity profiles.

Using the hybrid approximation, there is a clear distinction between models that evolve from equilibrium configuration and those that do not. While for the former (as long as the outer radius of the core x_m is large enough) all V_z-surfaces are closed, the latter have open V_z-surfaces at low $|v_z|$. This has two effects. One is that, for non-equilibrium models, the extent of the emission at low $|v_z|$ is comparable with the size of the core. This may not happen for equilibrium models. The second is that at high $|v_z|$ the asymmetry in the spatial intensity profile is expected to be detected in all models while, for the non-equilibrium LPH and LS-over models, it is lost at low $|v_z|$.

We have also shown in Figure 3.10 that the conventional polytropic generalization of the non-equilibrium LPH model has all its V_z-surfaces closed if $1 < \gamma < 2$. Therefore, the asymmetries in the spatial intensity profile that characterize infall are present for all velocities even for this non-equilibrium model. This indicates that non-equilibrium models may not have open V_z-surfaces, however, it is important to note that, this can not be the case for the LS models, which will always have open V_z-surfaces. The fact that the LP model predict a non-zero velocity at large r is a prediction of the model when $\gamma \leq 1$ or $\gamma > 2$, but the fact that the LS model has supersonic velocities at large r is an intrinsic characteristic of the model as they represent the velocity of the supersonic encountering turbulent flows. Since the rapid collapse requires a non-zero inward velocity at large distances it will produce open V_z-surfaces. However, we also showed that even in the rapid collapse model, more specifically in the LS-sub model, asymmetric spatial intensity profiles are expected due to the relative location of the open V_z-surfaces.

This simple "self-similar approach" has some important advantages that make it illustrative. It does not require of the specification of a molecule to estimate the shape of the spatial intensity profile, it neglects any time dependence and it is independent of the temperature choice for the isothermal end of the hybrid model. Nevertheless its simplicity prevents a quantitative comparison between models. For instance, we have not set any spatial limit where the thermalization assumption loses validity, or where the high line opacity assumption is not meet. For a more realistic approach, these limiting factors needed to be taken into account. The thermalization radius, r_{therm}, will depend on the density distribution, which was not taken into account so far, and on the molecular transition of study. For example, the critical density (above which thermalization can be assumed) for the (1,1) inversion transition of the ammonia molecule is 3×10^4 cm^{-3}, but it is of 1.4×10^2 cm^{-3} for the CO (1→0) rotational transition. Time dependence was also not considered so far. The density distribution scales with time, as a consequence of the self-similarity. For example, for the SIS and SPS models the density at a given position r inside the collapse front decreases with time. So r_{therm} will decrease as well with time. On the contrary, for the SLS model, inside the collapse front, the density at a given r increases with time; so, r_{therm} will also increase. In the following approach we will compare models taking into account more realistic conditions. Finally, in order to compare models we force them to share a common characteristic that serves as a reference (a cornerstone or benchmark), and then look for possible differences. Ideally one would like the benchmark to be an observational one, that is, not to be something to be inferred from the models. Our benchmark parameter will be the luminosity. We will compare all the models when they reach a luminosity of 1.5×10^4 L$_\odot$.

3.4.2.2 Results from the application to specific physical conditions

In the self-similarly approach described above we explored the predicted kinematic features of some of the most used collapse models of star formation. However, the analysis was somewhat indefinite in the sense that parameters as the stellar mass, the time, or the molecule transition remained undefined. Here we will perform the analysis of the kinematic features of non-equilibrium and equilibrium models in the frame of high-mass star formation by estimating the expected emission of the (4,4) inversion transition of the ammonia molecule. This transition needs of high temperature and high density conditions to be excited, which makes this transition well-suited to the study of HMCs.

As commented earlier, in order to compare all the models we will force them to share some common characteristics, preferentially observational ones, that serve as reference. Typical luminosities and accretion rates measured in HMCs are in the range of $L_{tot} = 10^3 - 10^5$ L$_\odot$ and $\dot{M} = 10^{-4} - 10^{-3}$ M$_\odot$ yr^{-1}, respectively. We chose to compare all models when the luminosity of the central object is of $L_{tot} = 1.5\times10^4$ L$_\odot$, and the accretion rate is $\dot{M} = 10^{-3}$ M$_\odot$ yr^{-1}. For a young object, the total luminosity is approximately the sum of the stellar luminosity, produced by nuclear reactions in the star; and the accretion luminosity, produced on the (proto)star surface via accretion shocks:

$$L_{tot} = L_\star + L_{acc} \ . \tag{3.54}$$

We will assume that most of the luminosity comes from accretion, which luminosity is given by:

$$L_{acc} = \frac{G\dot{M}M_\star}{R_\star} \ , \tag{3.55}$$

where $M_\star$ is the mass of the (proto)star, $\dot{M}$ is the mass accretion rate, and $R_\star$ is the stellar radius, whose value is taken as $R_\star = 10^{12}$ cm (Osorio et al. 1999; Hosokawa & Omukai 2008). Through equation 3.55 we obtain that the (proto)stellar mass is of 6.8 $\mathrm{M}_\odot$. If a star of such mass would have entered in the main sequence then its stellar luminosity, according to the formula described by (Eddington 1924),

$$\frac{L_\star}{L_\odot} = 1.5(\frac{M_\star}{M_\odot})^{3.5} \ , \tag{3.56}$$

would be of $L_\star =\sim 10^3$ $\mathrm{L}_\odot$, which is much lower than the accretion luminosity considered ($L_{acc} = 1.5 \times 10^4$ $\mathrm{L}_\odot$), so our assumption of considering the total luminosity as coming mainly from accretion would remain valid.

>From the self-similar formalism, equations 3.4 and 3.5, the protostellar mass is:

$$M_\star = \frac{k^{3/2}t^{3n-2}}{(3n-2)G} m_0 \tag{3.57}$$

(in the more general case of a polytrope). The constants m_0, n, γ and k depend on the model. For example, in the case of a the SIS model $n = 1$, $\gamma = 1$, $m_0 = 0.975$, and $k^{1/2} = c_s$. By knowing $M_\star$, we can obtain t so we can change from nondimensional functions, depending on x, to real physical functions depending on (r). This way we obtain the density and velocity fields as a function of r from the self-similar solutions of the different models, the latter serves us to calculate the V_z-surfaces.

We have not found in the literature self-similar studies of the LPH-p model (the polytropic generalization of the Larson-Penston model; see 3.4.1) during the main accretion phase apart from that of Yahil (1983), but unfortunately this author did not provide the value of m_0, which we need to conduct our analysis (see equation 3.57). Therefore, we will restrict our analysis to the "hybrid" approximation for the models SIS, SLS, LP, and LS. The temperature profile used in the "hybrid" approximation is that of equation 3.53.

Given the physical conditions for each model we will estimate the expected emission of the (4,4) inversion transition of the ammonia molecule and calculate the kinematic features on the spatial intensity profiles. To do so we use a simplified formalism similar to those of A91 to obtain the images as a function of the LOS velocity. That is, under conditions of high opacity and thermalization, we will assume that the images as a function of LOS velocity are maps of the variation of temperature over the visible side of the corresponding V_z-surfaces. Hence, for the study of the kinematic features on the spatial intensity profiles we need first to delimited where the high opacity and thermalization conditions are met.

The ammonia molecules at temperatures below 100 K are mostly frozen in ice mantles onto the dust grain surfaces, but at higher temperatures the ice sublimate, drastically releasing the ammonia moleucles and, thus, increasing the ammonia abundance in gas phase, from which the molecular line emission arises. This increment in abundance can be of several orders of magnitude (Lee, Bergin & Evans 2004, Osorio et al. 2009) Taking into account typical abundances in the interstellar medium, and the physical conditions in HMCs it is reasonable to consider the NH_3(4,4) emission is optically thick at r where $T(r) > 100$ K. We will take as the emitting region that where most of the ammonia molecules are in gas phase. According to equation 3.53, at the time that the stellar luminosity is 1.5×10^4 $L_\odot$, such sublimation radius is of ~ 1000 AU. We will also take this radius as the limit radius of the core in computations and will assume high line opacity within it.

Regarding the thermalization condition, the critical density needed to thermalize the NH_3(4,4) transition is $\sim 1 \times 10^5$ cm^{-3} (Osorio 2000). >From the density distributions in terms of r we can calculate the radius at which such density is met, r_{therm}. It happens that for all the models studied, at the time when $L_{tot} = 1.5 \times 10^4$ $L_\odot$, the emitting region (r with $T(r) > 100$ K) have densities higher than 1×10^5 cm^{-3} so we can consider that the emission is thermalized and so $T_{ex} = T_k = T$.

In this analysis we assume that the region under study is located at 1000 pc, which is a typical distance for high-mass regions, and it is observed with a beam of 0.1 arcsec, what approximately corresponds to the angular resolution of the Very Large Array (NRAO) in its A-configuration at the frequency of the NH_3(4,4) transition.

The velocity and density fields of the models at the time when the total luminosity is of $L_{tot} = 1.5 \times 10^4$ $L_\odot$ are shown in Figures 3.12 and 3.13, respectively. The V_z-surfaces and the spatial intensity profiles are shown in Figures 3.14 and 3.15. Note that only the emitting region is represented in Figure 3.14.

We found that the velocity fields for all models are very similar, specially at small radii. This is so because the emitting region is predicted to be in the free-fall regime by all models at “relatively small” radii (see Section 3.4.1). At larger radii, some differences arise, and the non-equilibrium models show a bit higher velocities. Note that for the equilibrium models, SIS and SLS, the collapse front is predicted to be out of the emitting region, so the entire emitting region is at move. The similarity between the predicted velocity fields produces that also V_z-surfaces look similar between models.

The limit in size of the emitting region has important implications specially for cores evolving from equilibrium. It is important to note that the emitting region (assumed optically thick)

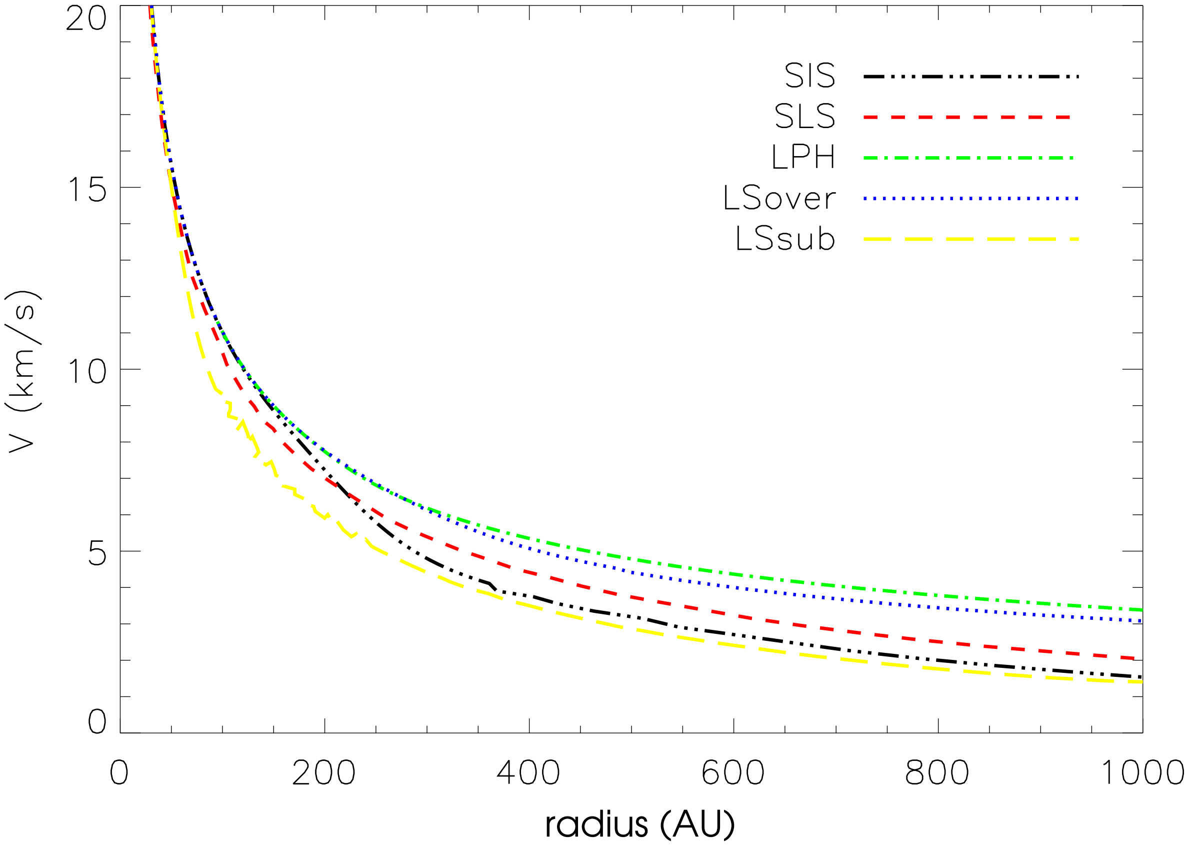

Figure 3.12: Velocity field of the models SIS, SLS, LPH, LS-over, and LS-sub, during the main accretion phase, at the moment when the total luminosity is $L_{tot} = 1.5 \times 10^4$ $L_\odot$.

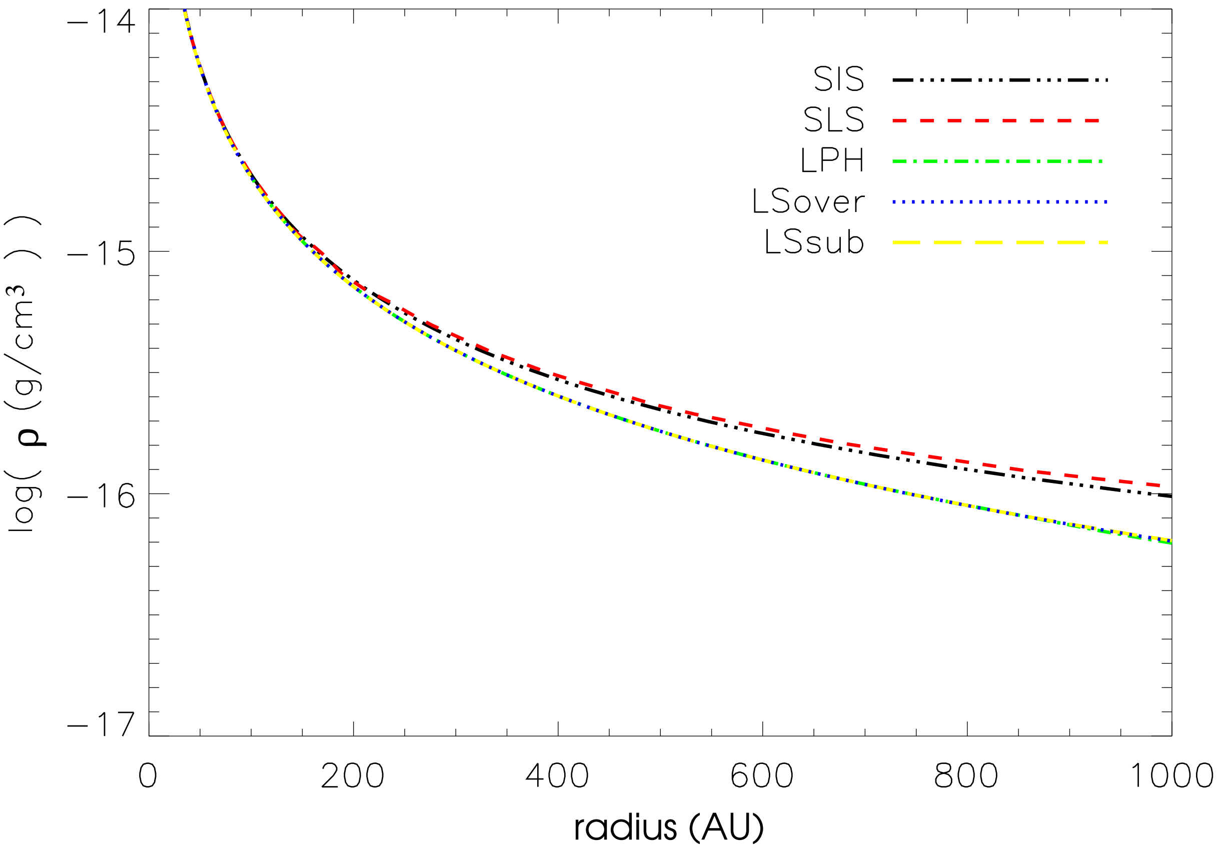

Figure 3.13: Density field of the models SIS, SLS, LPH, LS-over, and LS-sub, during the main accretion phase, at the moment when the total luminosity is $L_{tot} = 1.5 \times 10^4$ $L_\odot$.

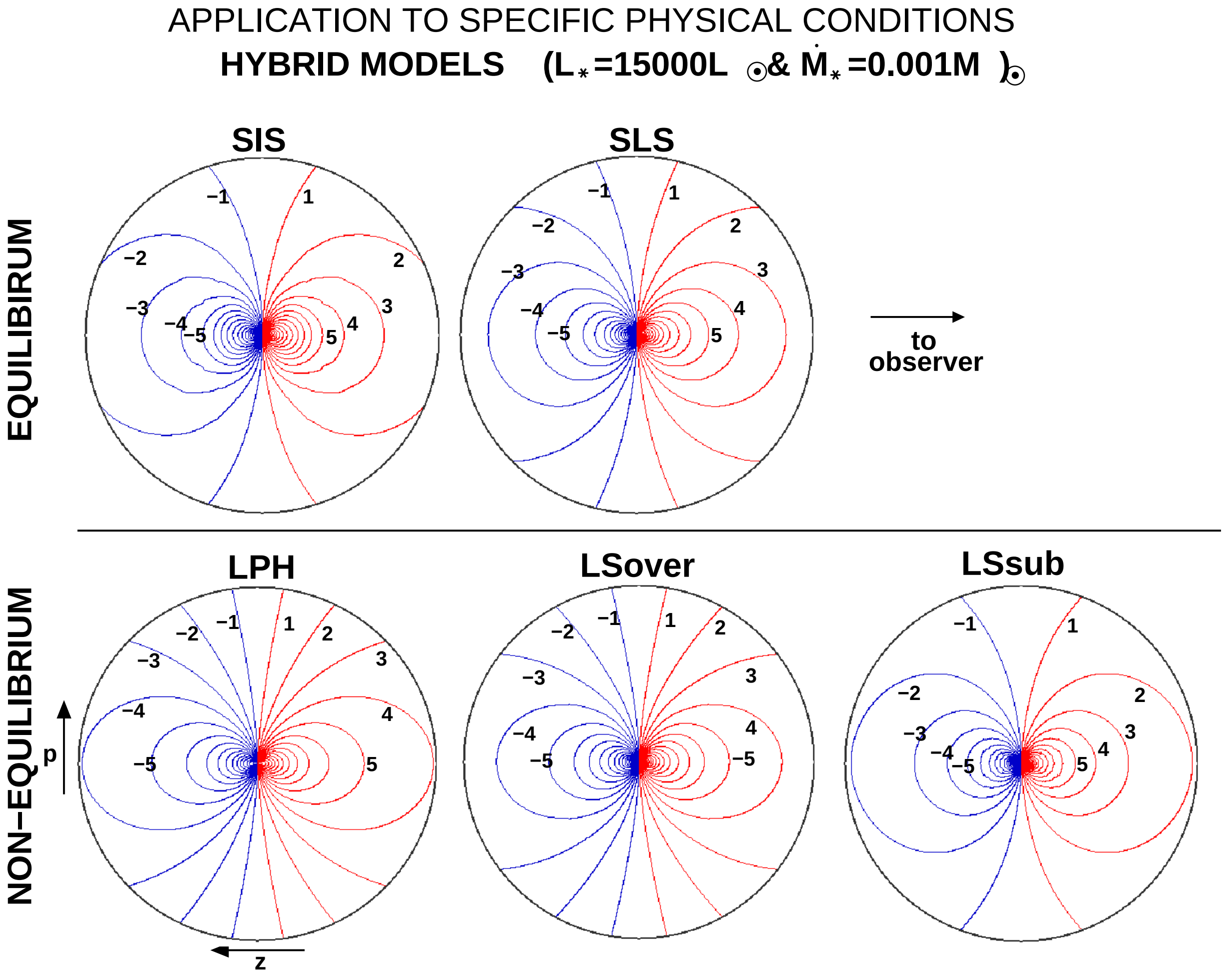

Figure 3.14: Surfaces of equal LOS velocity for a collapsing protostellar envelope for the hybrid models SIS, SLS, LPH, LS-over, and LS-sub for specific physical conditions during the main accretion pahse. A total luminosity of $L_{tot} = 1.5 \times 10^4$ L$_\odot$ and an accretion rate of $\dot{M} = 10^{-3}$ M$_\odot$ yr^{-1} has been assumed. The outer radius of the core is set to 946 AU for all models and corresponds to the radius where temperature reaches 100 K and ammonia is released by sublimation of ice mantles on dust grains. The isovelocity surfaces correspond to values of the velocity of $V_z = \pm 1, 2, 3, 4...$ km s^{-1}.

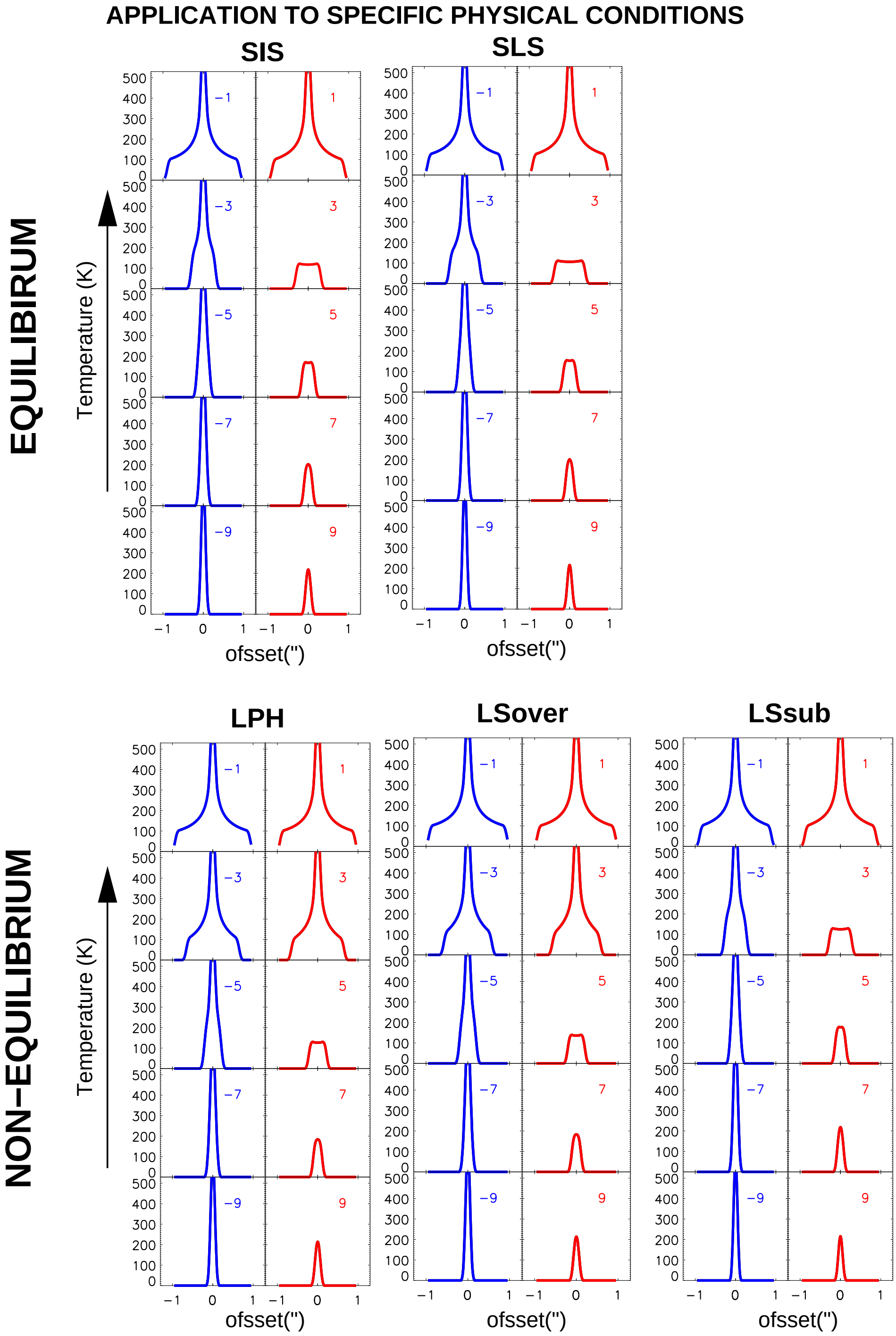

Figure 3.15: Intensity as a function of angular offset from the source center for specific physical conditions during the main accretion phase, for different channel maps. Results are shown for the hybrid models SIS, SLS, LPH, LS-over and LS-sub at the moment when the total luminosity is of $L_{tot} = 1.5 \times 10^4$ L$_\odot$ the accretion rate is of $\dot{M} = 10^{-3}$ M$_\odot$ yr^{-1}. The velocities of the channel maps are shown in the upper right corner of each panel in units of km s^{-1}.

for the SIS, SLS, and LS-sub is smaller than the size of the V_z-surfaces of ±1 and even than the V_z-surfaces of ±2 km s^{-1} (see Figure 3.14), which are to be closed surfaces (see Section). In consequence, these V_z-surfaces are missing their more external part and look "incomplete". Since V_z-surfaces are nested and those of higher $|V_z|$ are the more internal ones, the boundary of the emitting area does not affect the V_z-surfaces of high $|V_z|$. The fact that the outermost V_z-surfaces (correspondig to lower absolute velocities) are incomplete has little observational effect regarding the blue-shifted emission, since the missing part of the V_z-surfaces of blue-shifted velocities is in the background and would have been hidden anyway from the observer by the frontal side. However, the V_z-surfaces corresponding to low red-shifted velocities are missing the part of the surface closer to the observer, and therefore, the rear, inner (and thus hotter) part of such V_z-surfaces are no longer hidden. This produces centrally peaked and sharp intensity profiles at low red-shifted velocities, like the spatial intensity profiles of blue-shifted velocities. Therefore, the asymmetry in the spatial intensity profiles between red and blue channels is lost. For practical purposes, the "incomplete" V_z-surfaces of lowest velocities behave as open surfaces, as those in the non-equilibrium models. Nevertheless, the infall signature of A91 is maintained at large velocities since their V_z-surfaces are still complete closed surfaces.

It is important to keep in mind that these results are obtained for the ammonia molecule, which is a high density tracer and therefore is sensitive to the most internal parts of the core. It is possible, however, that other molecules sensitive to lower densities than ammonia might trace better the outer layers of the core, and thus, closed and large V_z-surfaces could be possibly fully contained within the emitting region of such molecule. In such case, the asymmetry in the spatial intensity profile should be detectable even at low velocities (except if the collapse proceeds as described by the "overdensity" rapid collapse model, which does not predict closed V_z-surfaces of low velocities).

In summary, both equilibrium and non-equilibrium models are expected to show the blue-red asymmetry in the spatial intensity profiles for large absolute velocities, but however, at low absolute velocities no asymmetry is expected since both blue- and red-shifted velocities produce centrally peaked and sharp spatial intensity profiles. Hence, no differentiation between both kind of models can be made on the basis of the behavior of the spatial intensity profiles.

3.4.2.3 Results from the radiative transfer calculations

In this new approach we will calculate the spatial intensity profiles under the same physical conditions as in Section 3.4.2.2 but using the radiative transfer code which does not take any assumption on thermalization or optically thickness. Besides provide us of more accurate spatial intensity profiles, this new approach will also help to check if the formalism of Anglada et al. (1987, 1991), used in the previous approaches to obtain the spatial intensity profiles, provides reliable results.

In Section 3.4.2.2 we assumed that the $NH_3(4,4)$ emission coming from outside of the sublimation radius was negligible, and that that coming from inside was optically thick. The latter, in its turn, allowed us to estimate the spatial intensity profiles by using a similar formalism to the one in Anglada et al. (1991) (see Section 3.4.2.2). The high line opacity assumption was used to assume that the radiatively coupled gas concentrates in a thin layer of the corresponding isovelocity surface, where there is little variation in the physical conditions. So, the images for different LOS velocities were assumed to correspond to the temperature distribution over the visible side of the isovelocity region. The validity of these approximations can be tested through radiative transfer calculations, which are described in the following.

Our own radiative transfer code calculates the expected NH_3(4,4) emission without the requirement of the above assumptions. The code uses the physical conditions of velocity, density and temperature fields from the models at the time when the central object has a luminosity of $L_{tot} = 1.5 \times 10^4$ $L_\odot$ and when the accretion rate is of $\dot{M} = 10^{-3}$ $M_\odot$ yr^{-1}, as in the previous approach. In addition to the density, temperature and velocity fields, the code needs as input parameters the ammonia abundance and the ammonia formation temperature (see Appendix A). Typical ammonia abundances for cold regions are about $10^{-8} - 10^{-7}$ (Herbst & Klemperer 1973, Ungerechts et al. 1980, Estalella et al. 1993) while typical abundances for hot and massive regions are of $10^{-6} - 10^{-5}$ (Millar et al. 1997, Walmsley 1997). Following Osorio et al. (2009), we explain this variation in abundance in terms of sublimation. We assume an abundance distribution that behaves nearly as a step-like function, with an outer (colder) region of low abundance, where the NH_3 molecules are frozen in the ice of dust grain mantles; and a inner (hotter) region of high abundance, where the ice has sublimated and NH_3 molecules are released in gas phase. We adopt a gas phase abundance of 10^{-5} for regions where $T > 100$ K (the ice sublimation temperature) and of 10^{-9} for those where $T < 100$ K. We have set extreme values of the abundance in the inner and outer zone in order to get, as much as we can, similar conditions to those assumed in the previous approach (see Section 3.4.2.2). The formation temperature, which sets the ratio of ortho-para species (see Appendix), has been found to be about $11-20$ K in massive star-forming regions (Nagayama et al. 2009). $T_{for} = 20$ K was taken here. The code also allows to add micro-turbulence. We have set a constant turbulent velocity widening of $\Delta V = 0.5$ km s^{-1} (FWHM) for all models except for the SLS, which includes intrinsically in its formulation a total dispersion that follows the relationship $\sigma_v \propto \rho^{-1/2}$. See Appendix A for a full description of the code.

For the computations presented here, the resolution of the computational grid was 8 AU, and the spatial coverage of the grid was of $\sim (2r_{sub})^3$, where r_{sub} is the radius of sublimation, that we take as the radius at which $T = 100$ K. The channel width was set to 1 km s^{-1} and every channel was sampled at five different velocities. The source is assumed to be at a distance of 1000 pc and the resultant intensity as a function of velocity is convolved with a beam of 0.1 arcsec (FWHM).

Figure 3.16 shows the predicted NH_3(4,4) spectra for all models, corresponding to the integrated emission over the whole core. All spectra have similar integrated flux, ranging between 15 and 20 mJy, and similar satellite-to-main line intensity ratios ~ 0.6. The LPH and LS-over spectra are wider (~ 5 km s^{-1}) than those of the SIS and LS-sub models (~ 3 km s^{-1}), but

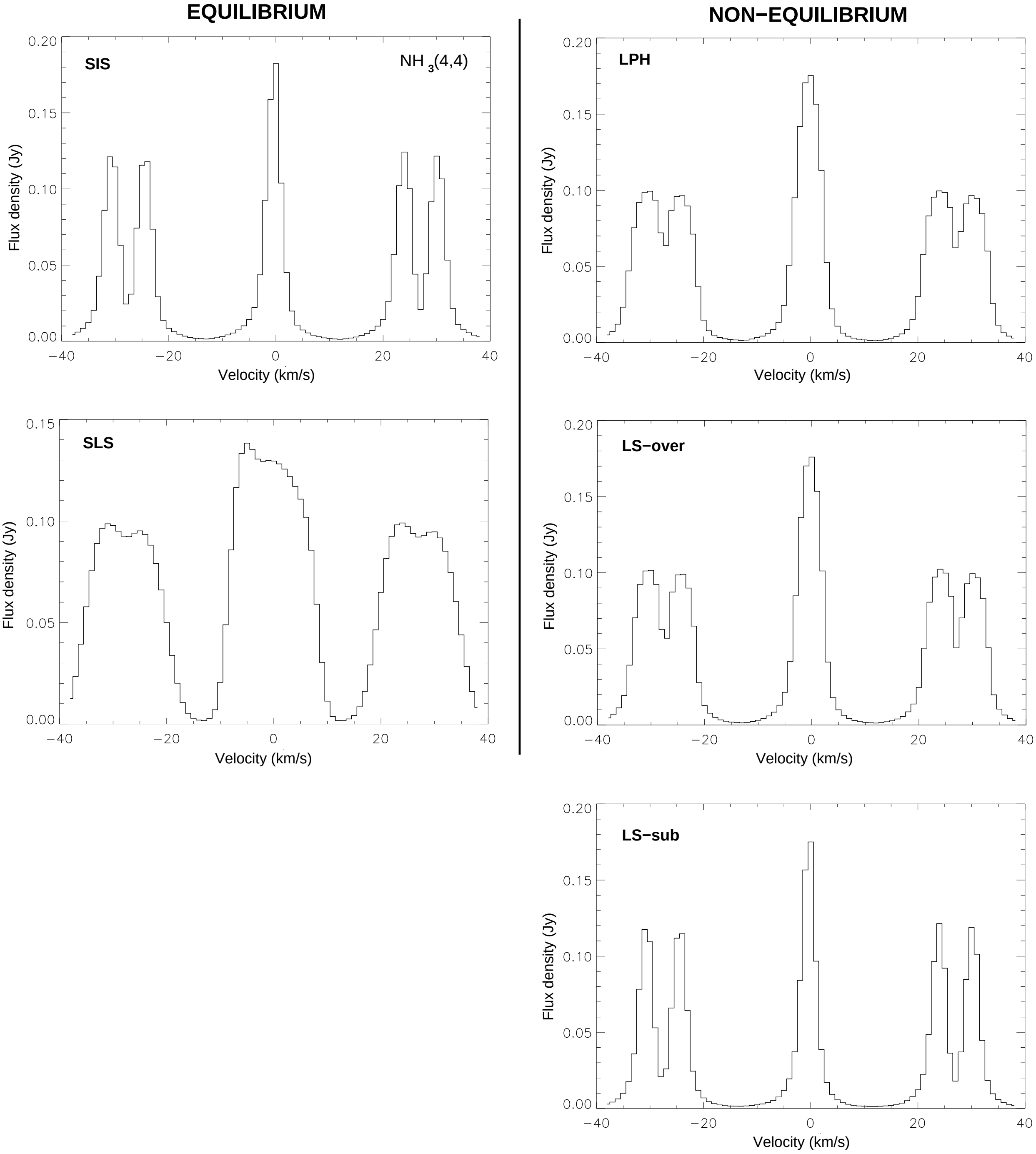

Figure 3.16: $NH_3(4,4)$ spectra predicted by the SIS, SLS, LPH, LS-over and LS-sub models, during the main accretion phase, at the moment when the total luminosity is of $L_{tot} = 1.5 \times 10^4$ $L_\odot$ and the accretion rate is $\dot{M} = 10^{-3}$ $M_\odot$ yr^{-1}. The spectra have been calculated using our own developed transfer code.

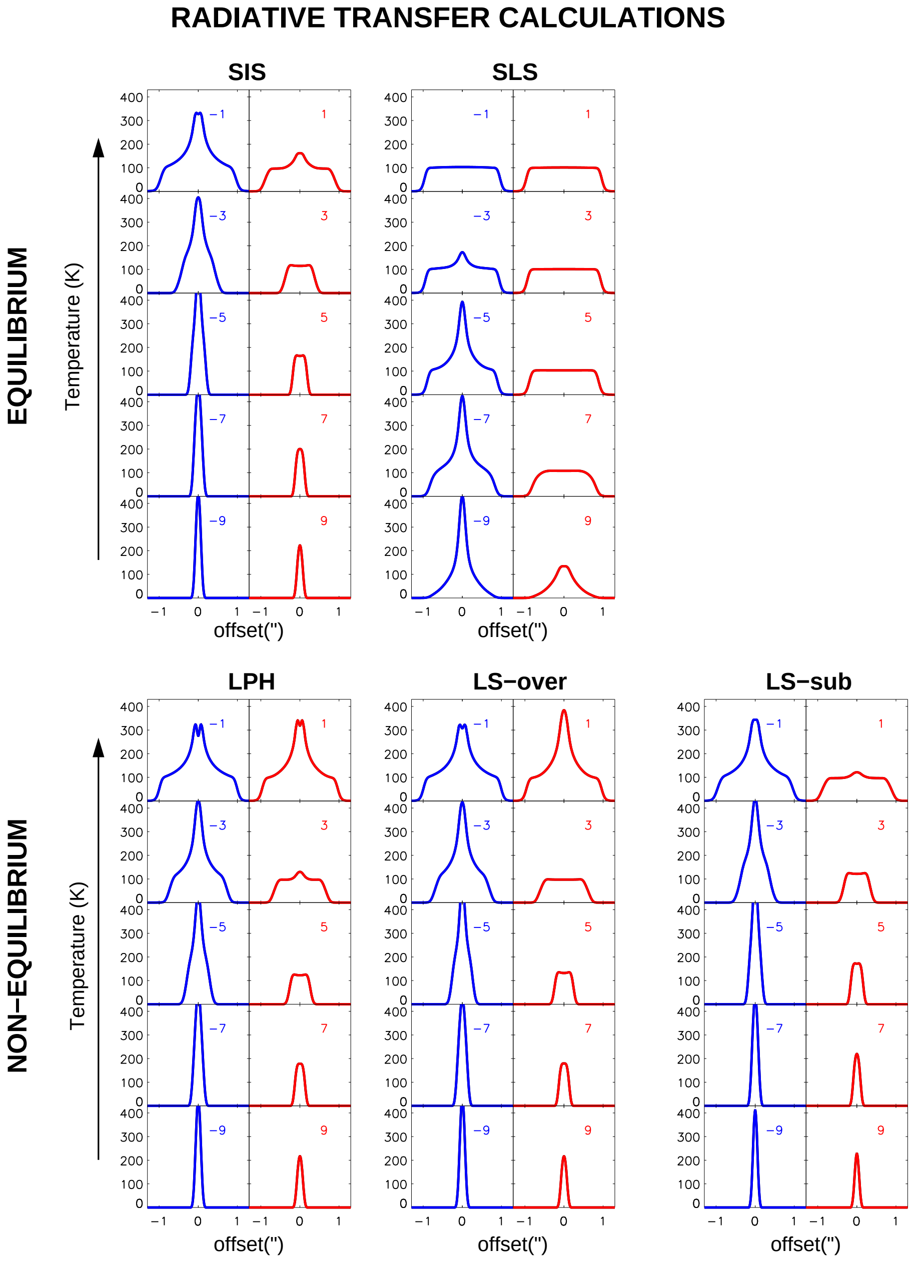

Figure 3.17: Intensity as a function of angular offset from the source center for different channel maps. Results are shown for the SIS, SLS, LPH, LS-over, and LS-sub models, during the main accretion phase, at the moment when the total luminosity is of $L_{tot} = 1.5 \times 10^4$ L$_\odot$ the accretion rate is of $\dot{M} = 10^{-3}$ M$_\odot$ yr^{-1}. These spatial intensity profiles have been obtained with our radiative transfer code (see Appendix). The velocities of the channel maps are shown in the upper right corner of each panel in units of km s^{-1}.

it is the SLS model the one with larger widths (~ 14 km s^{-1}). This is specially evident in the satellite lines, where inner and outer satellites merge in several channels.

The V$_z$-surfaces are the same as in Figure 3.14. Figure 3.17 shows the spatial intensity profiles of the different models obtained using the radiative transfer code. In general the spatial intensity profiles in Figure 3.15 and those shown in Figure 3.17 are very similar in shape and intensity. Small differences are appreciable towards the core center for those channels of lowest $|V_z|$, as the peak of intensity obtained through the radiative transfer code is lower than those obtained in the previous approach (see Section 3.4.2.2. and Figure 3.15). This difference is probably due to the velocity dispersion, which was not taken into account in Section 3.4.2.2. (Figure 3.15). Such a velocity dispersion is more important towards the center of the core because, first, the thermal dispersion is much larger towards the center due to the higher temperatures, and second, at the center all V$_z$-surfaces are met, so, although matter accumulates towards the center, the amount of matter per velocity unit can become smaller than in outer regions, so the emission arising from the core center becomes thin at some velocities.

The major difference between the spatial intensity profiles obtained through the radiative transfer code (Figure 3.17) and through the simplified methodology used in Section 3.4.2.2 (Figure 3.15) occurs at those profiles corresponding to the smallest open or incomplete V$_z$-surface. While in Section 3.4.2.2, the red-shifted profiles for such V$_z$-surface were centrally peaked, they are almost flat when obtain through the radiative transfer code (Figure 3.17). This discrepancy can be explained in terms of the thickness of the V$_z$-surfaces along a LOS. Thermal and turbulent widening makes the isovelocity surface (defined as all points having equal velocity component along the LOS) to have a certain width (see Figure 3.18), that is, the region that emits at a given LOS velocity, V$_z$, has a certain depth, with an internal and an external boundary. However, in the approach in Section 3.4.2.2 (and in Figure 3.15), we assumed that only a thin layer of the V$_z$-surfaces is visible, and considered the V$_z$-surfaces as infinitely thin surfaces, disregarding the thermal and turbulent widening. Therefore, in the approach in Section 3.4.2.2, when the outer boundary of the emitting region cut the V$_z$-surface making it incomplete, we overlooked the possibility that, because of the widening, the internal boundary of that thick isovelocity "surface" (or region) could be fully contained within the emitting region. If such is the case, the inner boundary of the V$_z$-surface would not appear incomplete and, therefore, the asymmetries would still be present at those velocities. Note that this simplification is not used in the radiative transfer code as it includes in its formulation the thermal and the turbulent widening. For the SLS, the spatial intensity profiles at velocities +1 and -1 km s^{-1} are flat (Figure 3.17) instead of sharp and centrally peaked as expected (Figure 3.15). This is also due to the extreme broadening of the lines, what makes the V$_z$-surfaces to be very thick.

As Figure 3.17 shows, the region of emission becomes smaller as $|V_z|$ increases, blue-shifted emission increases sharply towards the center, and the red-shifted emission is flat except at the lowest velocities, where it becomes centrally peaked because of the effect of incomplete and/or open V_z-surfaces. This behavior is in agreement with the predictions of the simplified formalism of A91, presented in Section 3.4.2.2. Accordingly, we conclude that the 3D infall signatures

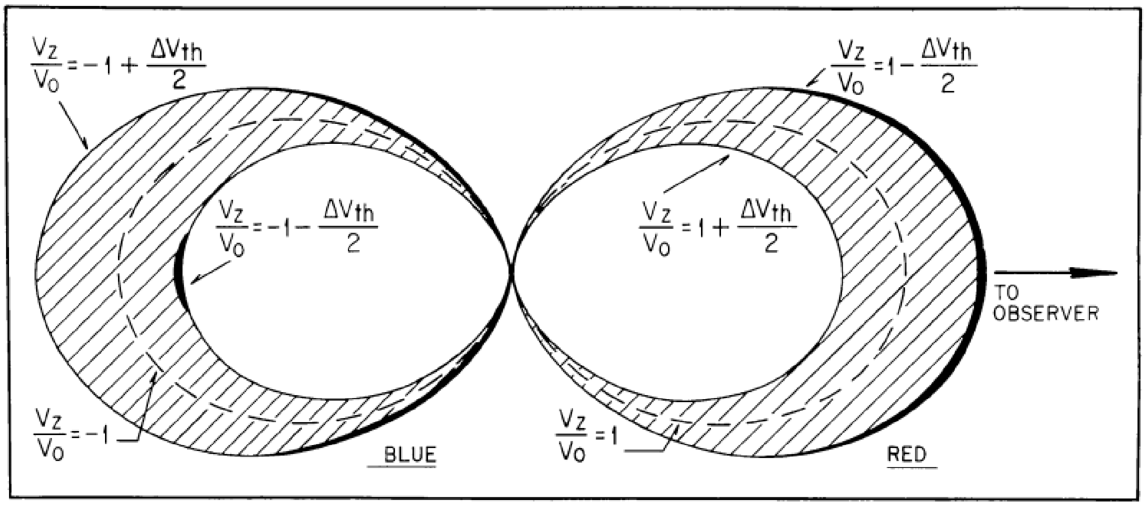

Figure 3.18: Emitting region in the z-p plane for $V_z/V_o = 1$ (shaded zone) for the example shown in Figures 2.4. ΔV_{th} is the broadening (FWHM) due to thermal velocities. The dark zone indicates the approximate extent of the region where the observed emission originates in very high opacity conditions. (Figure A1 from Anglada et al. 1987).

of A91 are present and should be observable in a contracting core for high enough velocities. Additionally, we also conclude that the 3D formalism of A91 provides reliable results in the prediction of the intensity maps as a function of the velocity.

3.5 Summary and Conclusions

We have analyzed the robustness of the (3D) "spectral imaging infall signature" of A91 for different models found in the literature that describe the collapse of star forming cores. The signature consists of an asymmetry in the spatial intensity profile between red- and blue-shifted velocity channels, for angularly resolved sources observed with optically thick lines. The red-shifted velocity channels present a nearly flat intensity distribution, while the blue-shifted velocity channels present a sharp increase in the intensity towards the core center. Additionally, the emission becomes more compact with increasing $|V_z|$. Two questions motivated the work presented in this chapter. To determine how robust is the 3D infall signature of A91 and, to determine whether it is possible to distinguish between different star formation models using this signature, which contains spatial and spectral information. For the latter purpose, we have taken special attention to possible differences between the models that start from equilibrium configurations and those that start from non-equilibrium configurations.

In order to calculate the spatial intensity profiles as a function of the velocity, first we have taken the predicted physical characteristics of each model from their self-similar formalism. We have found that, during the prestellar phase, when the central object has not yet formed, equilibrium models predict closed V_z-surfaces (Figure 3.6) and non-equilibrium models predict open V_z-surfaces (Figure 3.4). For the case of equilibrium, because the temperature is assumed to increase outwards, the spatial intensity profiles corresponding to blue-shifted velocities present a small dip towards the center, while for red-shifted velocities the spatial intensity profiles are flat. Additionally, for each pair of blue-/red-shifted velocities the average intensity is higher in the red-shifted channel than in the blue-shifted one. Hence, a 1D "red-asymmetry" on the spectral line profile, instead of the widely assumed "blue-asymmetry", would be expected for a prestellar collapsing core starting from equilibrium. Note that this may change if the thermalization condition is not met (Keto & Caselli 2008), and the inner parts of the cloud have higher excitation temperatures than the outer parts. For the case of non-equilibrium initial conditions, the spatial intensity profiles corresponding to both red- and blue-shifted velocities present a dip towards the central position of the core. However, because of the absence of an internal heating source, the temperature is expected to vary little throughout the core during this phase, and thus, such dips towards the core center should be small, being difficult to detect observationally.

For the study of the main accretion phase we used three approaches. First, we used a nondimensional approach, working on the space of the self-similar solutions to construct the V_z-surfaces, and assumed optically thick thermalized line emission to obtain the images and intensity profiles using the simplified formalism of A91 (i.e., that under the assumed conditions the velocity channel maps are images of the excitation temperature distribution over the side of the V_z-surfaces facing the observer). A second approach consisted in changing from dimensionless functions to physical functions in order to take into account the actual density and temperature distributions of each model to define the region where thermalization and high line opacity are fulfilled. In this second approach we consider the ammonia (4,4) inversion transition and used also the simplified formalism of A91 to obtain the spatial intensity profiles. Finally, we used a third approach, taking the same velocity, density, and temperature fields, but using our radiative transfer code to calculate the images and spatial intensity profiles of the ammonia (4,4) transition as a function of velocity.

With the nondimensional approach we have found that, during the main accretion phase, hybrid and polytropic collapse models that initiate from equilibrium configurations predict closed and nested V_z-surfaces, while hybrid collapse models that start from non-equilibrium configurations predict open V_z-surfaces at low velocities and closed and nested V_z-surfaces at high velocities (Figure 3.10). However, even non-equilibrium models in their polytropic generalization can present closed V_z-surfaces at all velocities (if $1 < \gamma < 2$), except for the case of the rapid collapse models (LS), whose non-zero inward velocities at large distances ($V(r \to \infty) \neq 0$), due to the supersonic converging flows, produce open V_z-surfaces for $|V_z| < |V(r \to \infty)|$. In the presence of an internal heating source, closed surfaces are expected to produce asymmetric red-vs-blue spatial intensity profiles under high line opacity conditions, but open surfaces do not. As a consequence, the rapid collapse model is not expected to show, at low velocities, the asymmetric red-vs-blue spatial intensity profiles that characterize infall, except in the subdense case (LS-sub) where, at low velocities, a rare combination of both an outer open surface and an inner closed surface (for the same V_z velocity) can mimic the effect of the infall asymmetry (Figures 3.10 and 3.11).

Another effect that can erase the infall signature in the spatial intensity profiles is the finite size of the emitting region that truncates the outer isovelocity surfaces. As a result, they become open surfaces and the asymmetry in the spatial intensity profiles of the corresponding velocities disappears in a similar way as it occurred in the collapse models that start from a non-equilibrium configuration. The nondimensional approach is not well suited to establish the scale where surface truncation occurs; this is better established using the second approach, with an application to specific, realistic physical conditions. Specifically, calculations were performed for the NH_3(4,4) inversion transition under the physical conditions predicted by the models when the central object has a luminosity of 1.5×10^4 $L_\odot$ and the accretion rate is of 10^{-3} $M_\odot$ yr^{-1}. The results obtained using this second approach are fully consistent with those obtained using the nondimensional approach. The main difference occurs at low velocities because of the inclusion of a better estimate of the truncation of the outer isovelociy surfaces (Figures 3.14 and 3.15). A more accurate calculation, relaxing the A91 simplifying assumptions, has been performed with our radiative transfer code (third approach). The previous results are confirmed by this third approach, indicating that the simplified A91 formalism turns to be a worthy methodology to predict the intensity distribution on velocity channel maps under conditions of high line opacity.

The main conclusion is that the "spectral imaging infall signature" of A91, which was originally predicted using the velocity field of the numerical simulations of Larson (1972), stands for all the collapse models studied, regardless of whether or not they evolve from equilibrium, as long as the cores are in the main accretion phase and the velocities considered are high enough. At lower velocities, differences between models starting from equilibrium (closed isovelocity surfaces, resulting in asymmetries between red and blue intensity profiles) and those starting from non-equilibrium (open isovelocity surfaces, resulting in similar red and blue intensity profiles) should appear. However, these differences could be masked by the finite size of the emitting region that might truncate the outer closed isovelocity surfaces, resulting in similar red/blue spatial intensity profiles (both sharply increasing towards the center). It should be noted that these results are obtained for the ammonia molecule, which is a high density tracer and therefore is mainly sensitive to the most internal parts of the core. It is possible that another molecule, sensitive to lower densities, might be a better tracer of the outer layers of the core so that the whole extent of the low velocity V_z surfaces were fully contained within the emitting region. In that case, the detection of an asymmetry between the blue/red spatial intensity profiles at the lowest velocities would unambiguously rule out the "overdensity" rapid collapse model (LS-over).

Chapter 4

The hot molecular core close to the HII region G31.41+0.31

4.1 Introduction

It is believed that the star-formation process should be dominated by gravitational infall motions that accrete material from the ambient cloud into a central protostellar object. Establishing the nature of infall motions and distinguishing them from other systematic motions in the cloud are not easy tasks, as infall motions have been always elusive to detect. So far, only a few observational signatures have been commonly used to claim for the presence of infall, and most of them are not univocal and need of further complementary observation. Another important matter of debate is the role of disks in the formation of high-mass stars. Detections of accretion disks of a few hundreds of AUs in radius around O-type stars would have a profound impact on high-mass star formation theories. However, the large distances and the confusion caused by the stellar crowding have prevented the systematic detection of disks in OB-type stars. Notwithstanding, larger structures (>1000 AU) named toroids, with velocity gradients suggesting rotation, have been observed around OB-type stars (Cesaroni et al. 1999, Beuther et al. 2004, Sollins & Ho 2005, Sollins et al. 2005, Beltrán et al. 2005, 2006, 2011, Furuya et al. 2008, Sandell et al. 2003; Beuther & Walsh 2008, Zapata et al. 2009), but their interpretation has often been controversial. The debate resides in the nature of such velocity gradient, which is sometimes interpreted as expansion instead of rotation, thus tracing a bipolar outflow rather than a rotating structure.

In the Chapters 2 and 3 we proved the robustness of the infall signature predicted by A91, and showed that it is expected even when a relatively small rotating component is present. We additionally derived from it new kinematic signatures on the first-order moment, the "central blue spot" (which traces infall), the "blue spot and dimmer red spot pair" and the "roller coaster" which trace infall combined with rotation. Despite the robustness and unambiguity of the spectral imaging signature of A91, it has not been used as a infalling signature in part because it requires either very sensitive observations or very strong molecular emission.

Here we present observational evidence of the spectral imaging infall signatures and of the rotation signatures (presented in Chapter 2) in the hot molecular core close to the ultracompact HII region G31.41+0.31 (hereafter G31 HMC). HMCs are small, dense, hot molecular clumps usually found in the proximity of UCHII regions, and are believed to trace one of the earliest observable stages in the life of massive stars (Section 1.3.3). G31 HMC, located at a distance of 7.9 kpc (Cesaroni et al. 1998), is one of the hottest molecular cores discovered so far, and it probably harbors an O-type protostar. G31 HMC is separated 5 arcsec from an UCHII region situated at its NE, and overlaps in projection on a diffuse halo of free-free emission possibly associated with the UCHII region itself (Cesaroni et al. 1998) (Figure 4.1a). It exhibits strong ammonia emission of high excitation transitions (Churchwell E., Walmsley C. M., & Cesaroni R., 1990; Cesaroni, Walmsley, & Churchwell 1992; Cesaroni et al. 1994, 1998) (Figure 4.1b), making G31 HMC one of the few sources where a high signal-to-noise ratio analysis of the spatially resolved molecular emission can be attempted. Cesaroni et al. (2010) reported a double radio continuum source towards the center of the ammonia core, that could trace the two jet lobes from a single central protostar or a binary system. Either way, it reveals the presence of deeply embedded YSOs and explains the temperature increase towards the core center (Beltrán et al. 2004, 2005). Infall motions in G31 HMC have already been inferred by Girart et al. (2009) through the detection of an inverse P-Cygni profile against the bright dust emission peak. Osorio et al. (2009) carried out a detailed modeling of the source. This model, which consists in a spherical envelope collapsing onto an O-type star, is able to reproduce the observed spectral energy distribution (SED) of the source as well as the spectra of the ammonia (4,4) transition obtained in the subarcsecond angular resolution VLA observations carried out by Cesaroni et al. (1998). Furthermore, methyl cyanide observations (CH_3CN; Cesaroni et al. 1994) showed the existence of a velocity gradient across the core in the NE-SW direction, also suggested by the distribution of OH masers (Gaume & Mutel 1987). This velocity gradient has also been observed in other molecules as methanol or ammonia. The nature of this gradient is controversial. Some authors support that it is tracing a molecular toroid (Olmi et al. 1996, Beltrán 2004, 2005, Cesaroni et al. 2011) while some others believe that it is tracing an outflow (Araya et al. 2008, Moscadelli et al. 2013). Other authors (Gibb et al. 2004), suggest that the outflow is not in the NW-SE direction but in the east-west direction.

In this chapter we present VLA observations of the (2,2) to (6,6) ammonia inversion transitions towards G31 HMC. The high angular resolution allows us to study the internal kinematics of the HMC. In Section 4.2 we describe our observations. In Section 4.3 we present the observational results. In Section 4.4 we discuss the presence of the spectral imaging infall signature and propose evidence of the "central blue spot" in G31 HMC. We also explore the effect of rotation in the kinematics of the source and propose evidence of the "blue spot and dimmer red spot pair" and the "roller coaster". In Section 4.5 we give our conclusions.

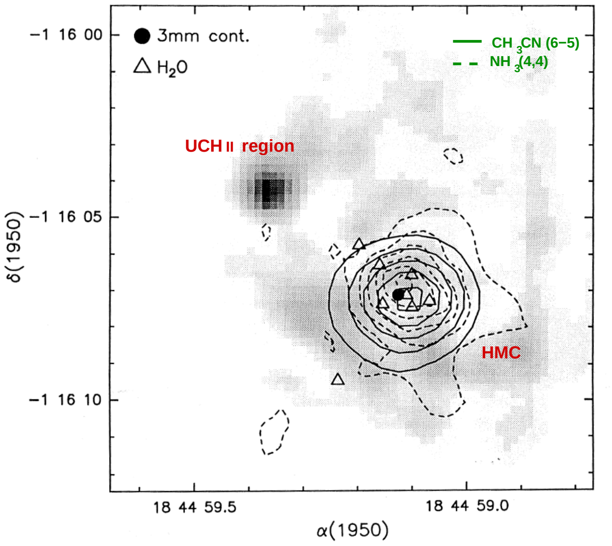

Figure 4.1: Image of the 3 mm free-free emission of the G31.41+0.31 HII region (gray scale) overlapped with the ammonia (dashed contours) and methyl cyanide (solid contours) emission of the HMC. The water masers (triangles) associated with the HMC are also shown (from Cesaroni et al. 1994).

4.2 Observations

Observations of the ammonia (2,2), (3,3), (5,5) and (6,6) inversion transitions were carried out on 2009, March 1 and 3, with the VLA of the NRAO[1] in the B-configuration (VLA Project Code: AM981) providing an angular resolution of $\sim 0\farcs3$. The phase center was set to RA(J2000) = $18^h47^m34.506^s$; DEC(J2000) = $-01^\circ12'42.97''$. We used the 4IF correlator mode with a bandwidth of 6.25 MHz ($\sim$80 km s^{-1}) and 31 channels of 195 kHz ($\sim$2.4 km s^{-1}) width each, plus a continuum channel that contains the central 75 per cent of the total bandwidth. This configuration allowed us to observe two inversion transitions simultaneously. To make sure that at least the main line and one pair of satellites fall within the observational bandwidth we centered the observation at a velocity in between the main line and the inner red-shifted satellite line.

Phase, flux and bandpass calibrators were 1851+005, 3C286, and 1773-130 respectively. Pointing corrections were derived from X-band observations for all the calibrators and applied on-line. At the time of the observations, the VLA interferometer was going through a transition period to turn into the Expanded VLA (EVLA) and 20 out of 27 antennas at that time were already EVLA antennas while the rest were still VLA antennas. The frequencies for the NH_3(5,5) and NH_3(6,6) inversion lines fell very close to the edge of the bandwidth of the VLA receivers and only the EVLA antennas were used for these two transitions. For the NH_3(2,2)

---

[1] The National Radio Astronomy Observatory is a facility of the National Science Foundation operated under cooperative agreement by Associated Universities, Inc.

Table 4.1: Observational parameters of the ammonia observations

Transition (J,K)	VLA Config.	Antenna[a] Type	Rest Frequency (GHz)	Bandwidth (MHz)	Spectral Resolution (km s^{-1})	Synthesized Beam[b] ($''$)	rms (mJy beam^{-1})
(2,2)	B	VLA(7)/EVLA(20)	23.7226333	6.25	2.468	0.33	0.7
(3,3)	B	VLA(7)/EVLA(20)	23.8701292	6.25	2.453	0.33	0.7
(4,4)	A	VLA(27)	24.1394163	12.5	2.426	0.16[c]	0.5
(5,5)	B	EVLA(20)	24.5329887	6.25	2.386	0.37	0.9
(6,6)	B	EVLA(20)	25.0560250	6.25	2.337	0.34	1.0

[a] Numbers in parenthesis indicate the number of antennas of either type.
[b] HPBW of the circular restoring beam.
[c] Interferometric visibilities have been tapered to increase the signal-to-noise ratio.

and NH_3(3,3) inversion lines both EVLA and VLA antennas were used.

Due to the narrowness of the bandwidth used, and because lines in this source are extremely broad, there were not enough line-free channels to subtract the continuum emission properly and additional continuum observations (VLA Project Code: AM994) were carried out on 2009, May 16 for this purpose. In this continuum observation we used the same flux and phase calibrators as in the line observations.

We also analyzed VLA archival data of the NH_3(4,4) transition taken in the A configuration (VLA Project Code: AC748; Cesaroni et al. 2010). These observations were carried out on 2004, October 15, 23, and November 5, using the Fast Switching technique with a 80/40 sec source-calibrator cycle. The bandwidth was 12.5 MHz ($\sim$160 km s^{-1}), with a channel width of 195 kHz ($\sim$2.4 km s^{-1}).

For all the transitions, data editing and calibration were carried out using the Astronomical Image Processing System (AIPS) package of NRAO following the standard high-frequency VLA procedures. We also followed the advice provided by the NRAO for observations with mixed EVLA and VLA antennas. Continuum was subtracted using the task UVSUB of AIPS. This correction was important only towards the position of the UCHII region and was negligible towards the HMC. Maps were obtained with “natural weighting” (with ROBUST parameter equal to 5) and were restored with a circular beam of the same are of the “unrestored” beam. For the (4,4) transition, which was observed in the A configuration, maps were obtained using a *uv* tapering of 1300 kλ to improve the signal-to-noise ratio. The observational set-up for all the line observations is summarized in Table 4.1.

4.3 Results

We detected ammonia emission in all the five studied transitions. This is the first interferometric detection of the ammonia (3,3), (5,5), and (6,6) inversion transitions in this source.

Figure 4.2 shows the spectra of the (2,2), (3,3), (5,5) and (6,6) inversion transitions obtained by integrating the flux over the entire HMC. Note that the blue-shifted pair of satellite lines did not entirely fit in our bandwidth. Lines are extremely broad (FWHM $\sim$ 13 km s^{-1}). In the (2,2), since the separation between the main line and the inner satellite line is only of 16.55 km s^{-1}, there is no channel free of emission, and possibly main line and inner satellite emission are blended at some channels. Moreover, the inner and outer satellite lines blend together. The latter happens for all transitions as consequence of the high broadening of the lines, even for the (2,2) transition, where the separation in velocity between satellite lines is larger, $\sim$ 9 km s^{-1}. The satellite to main-line intensity ratios are close to unity in the (2,2), (3,3) and (4,4) transitions, and this ratio is nearly 0.5 for (5,5) and (6,6) transitions. These ratios evidence the high line optical depth. An asymmetry in the main lines is also detected, with a blue side stronger than the red side, which may suggest the presence of infall (see Chapter 2).

The intensity channel maps of the (2,2), (3,3), (4,4), (5,5) and (6,6) transitions are shown in Figures 4.3, 4.4, 4.5, 4.6 and 4.7 respectively. Main and satellite line emission is detected in all transitions, showing a compact condensation ($< 1''$) roughly centered towards the 7 mm continuum sources of Cesaroni et al. (2010). There are morphological differences in the emission of the different velocity channels, which suggest changes in the kinematic structure of the condensation.

In Figure 4.8 we show an overlay of the zeroth-order moment (integrated intensity) and first-order moment (intensity-weighted mean velocity) of the ammonia (2,2), (3,3), (4,4), (5,5), and (6,6) main line emission. In the maps, the ammonia emission appears as a compact condensation, clearly associated with the double radio continuum source (angular separation = $0\rlap{.}''2$) reported by Cesaroni et al. (2010). The compact condensation appears somewhat elongated in the direction NE-SW. The NE-SW direction is also the direction of a (global) velocity gradient, present in all transitions, of about 5 km s^{-1} over 15000 AU, which corresponds to a gradient of $\sim$ 70 km s^{-1} pc^{-1}. The largest red-shifted velocities are found northeast of the condensation. This global velocity gradient coincides with the one found by Beltrán et al. (2005) from CH$_3$CN(12-11) observations. Furthermore, an excess of blue-shifted emission is observed near the peak of maximum emission. In the particular case of the NH$_3$(3,3) transition, low intensity emission extends to the E (red-shifted) and W (blue-shifted), creating two arms or protuberances not seen in the other transitions.

In Figure 4.9 we show an overlay of the maps of the zeroth-order moment (integrated intensity) and first-order moment (intensity-weighted mean velocity) of the observed ammonia (2,2), (3,3), (4,4), (5,5), and (6,6) satellite line emission. Because of the blending of inner and outer satellite lines, the emission from both lines is integrated together in the same map. As in the main line, the satellite ammonia emission also appears as a compact condensation associated with the double radio continuum source. The satellite emission extends over the same area of the main line for the lower excitation transitions, (2,2), (3,3) and (4,4). However, for the higher excitation transitions, (5,5) and (6,6), the FWHM of the satellite emission is smaller than that

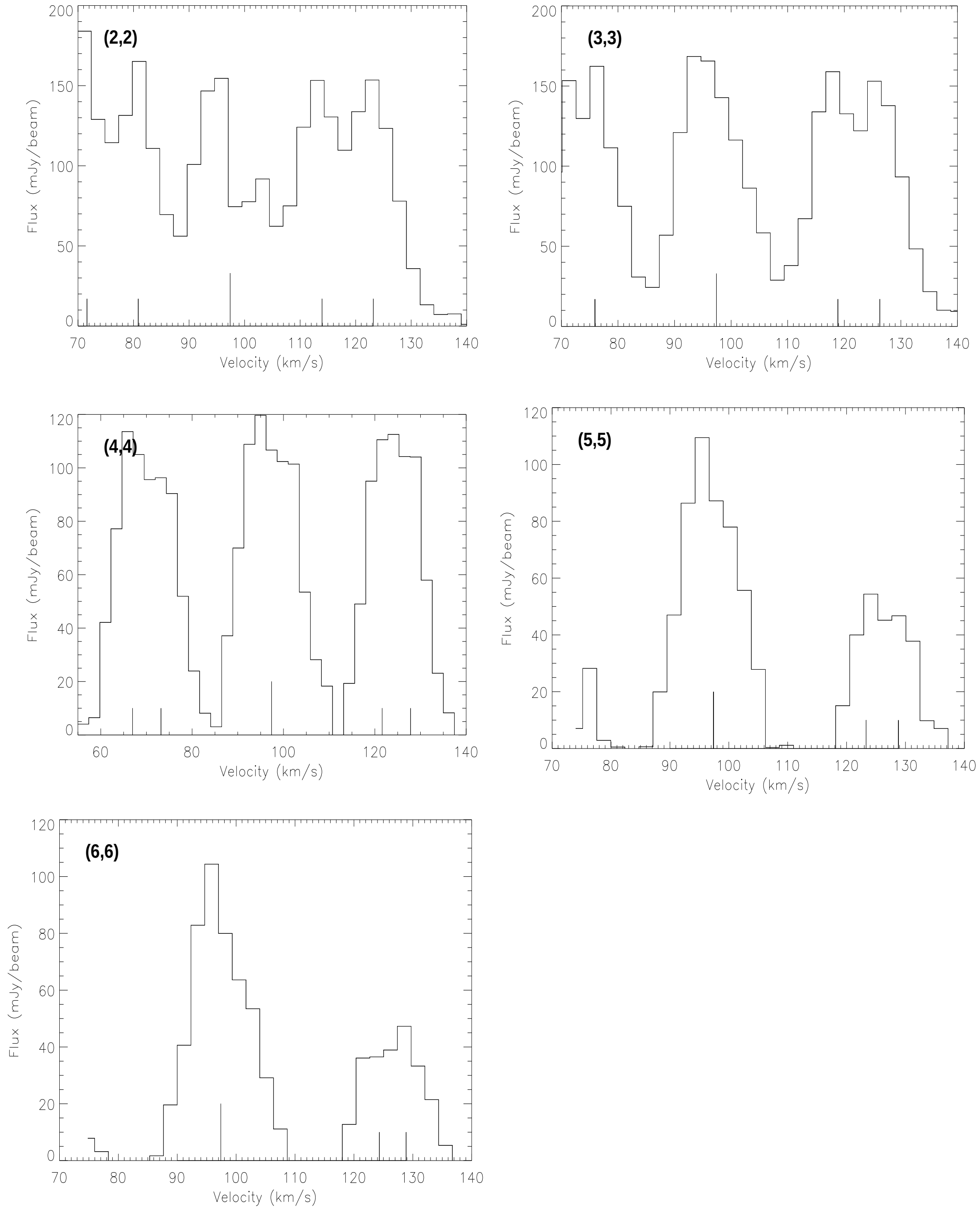

Figure 4.2: Spectra of the ammonia (2,2), (3,3), (4,4), (5,5) and (6,6) inversion transitions integrated over G31 HMC. The spectral resolution is of 195 kHz (~ 2.4 km/s). Adopting the rest velocity of the cloud of 97.4 km/s, the central velocity of the main line and of the satellite lines have been marked. Velocities have been calculated with respect to the rest frequency of the main line (Table A.2).

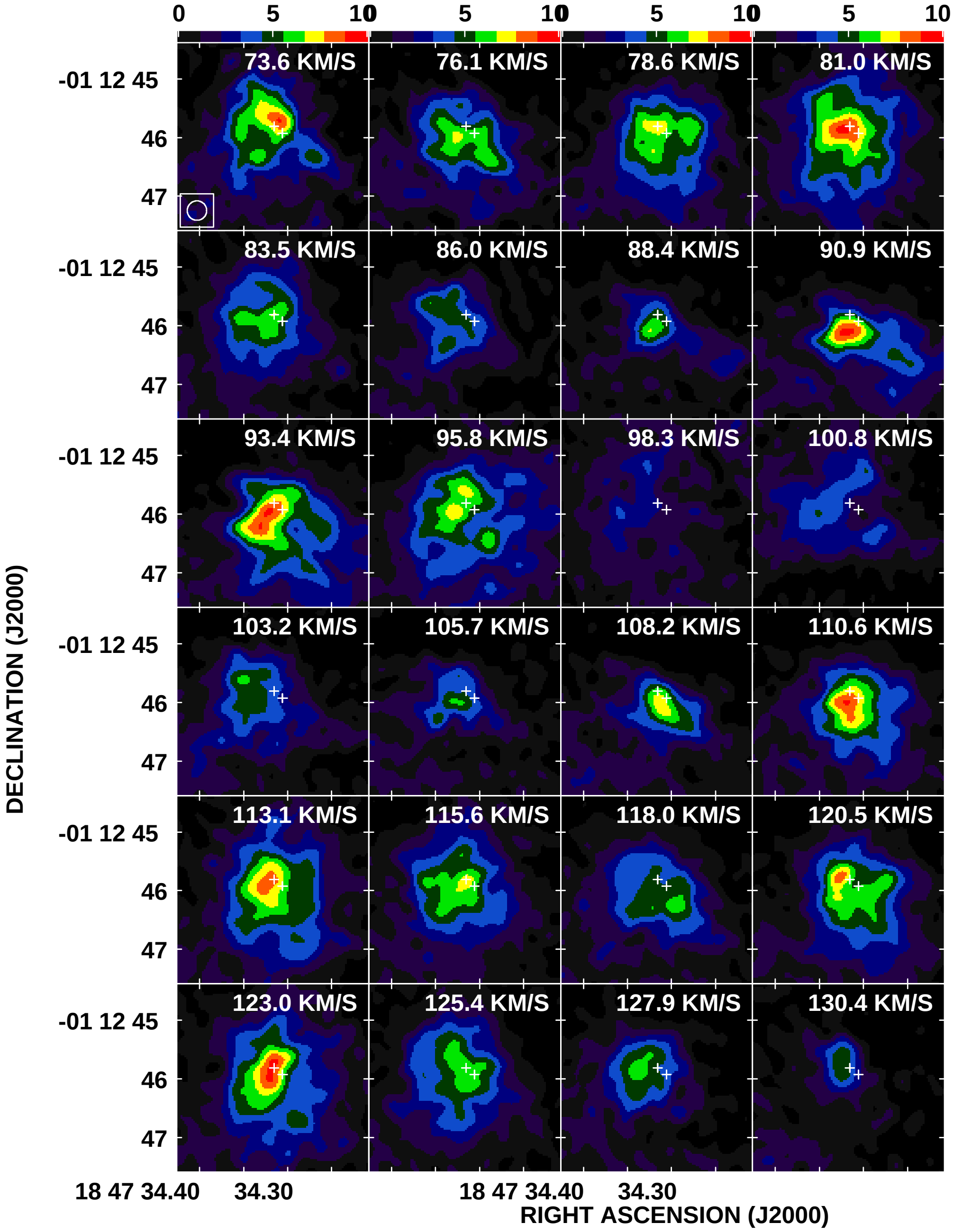

Figure 4.3: Channel maps of the NH_3(2,2) transition. The velocity of each channel has been calculated taking as a reference the rest frequency of the main line (Table A.2). Therefore, the velocity indicated in the upper part of each map gives the correct LSR velocity only for the main line emission. The LSR velocity of the satellite emission is shifted by ±16.55 km s^{-1} and ±25.78 km s^{-1} for the inner and outer satellites, respectively (Table A.2). The LSR velocity range of emission is ∼ 90 to 105 km s^{-1}. The synthesized beam is in the upper left corner of the first map. The two crosses indicates the position of the radio continuum sources detected by Cesaroni et al. (2010). The very last channel has been remove because of being flawed. The color bar indicates the intensity in mJy beam^{-1}.

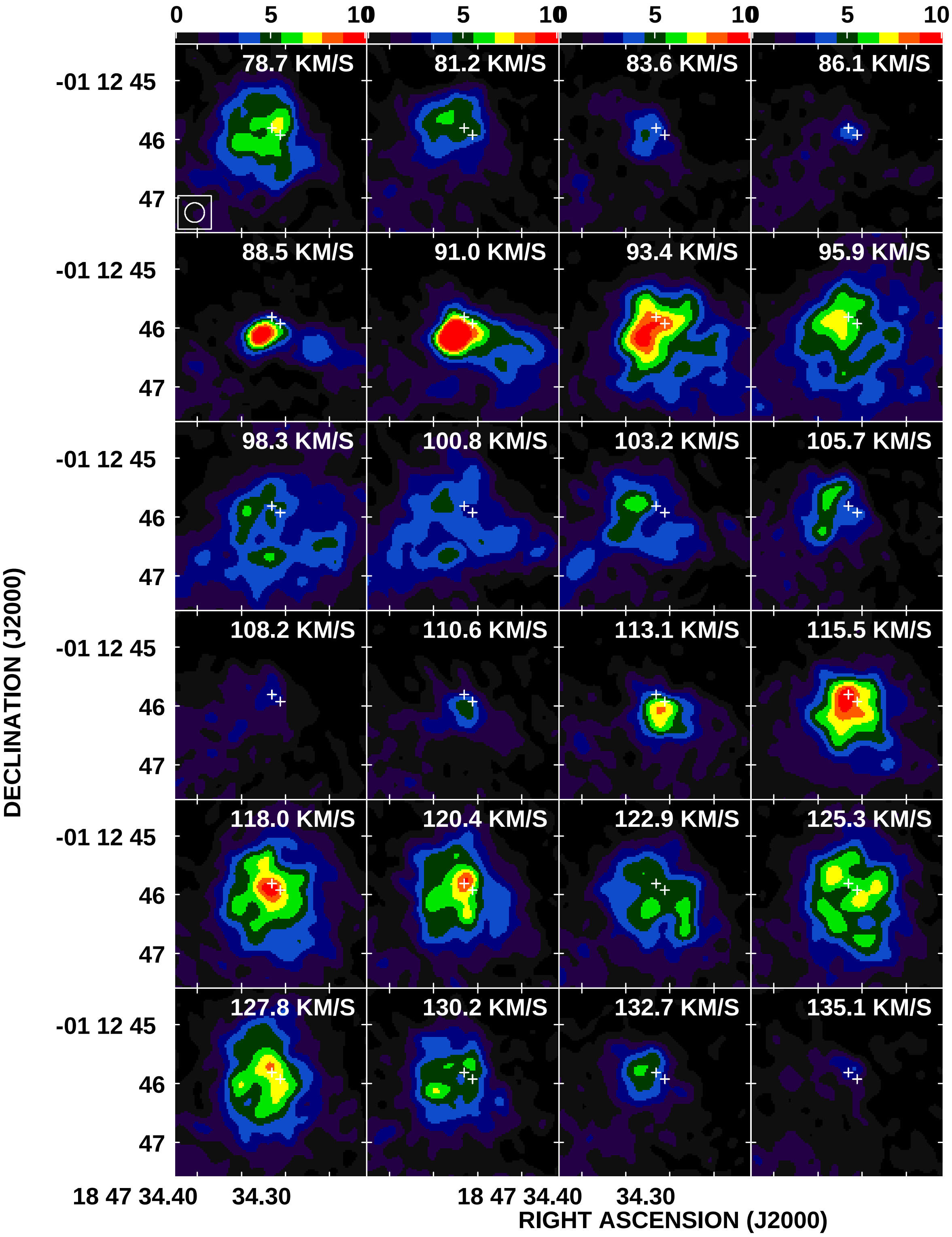

Figure 4.4: Same as Figure 4.3 but for the $NH_3(3,3)$ transition. The satellite line emission is shifted by ±21.47 km s^{-1} and ±28.88 km s^{-1} for the inner and outer satellites, respectively (Table A.2).

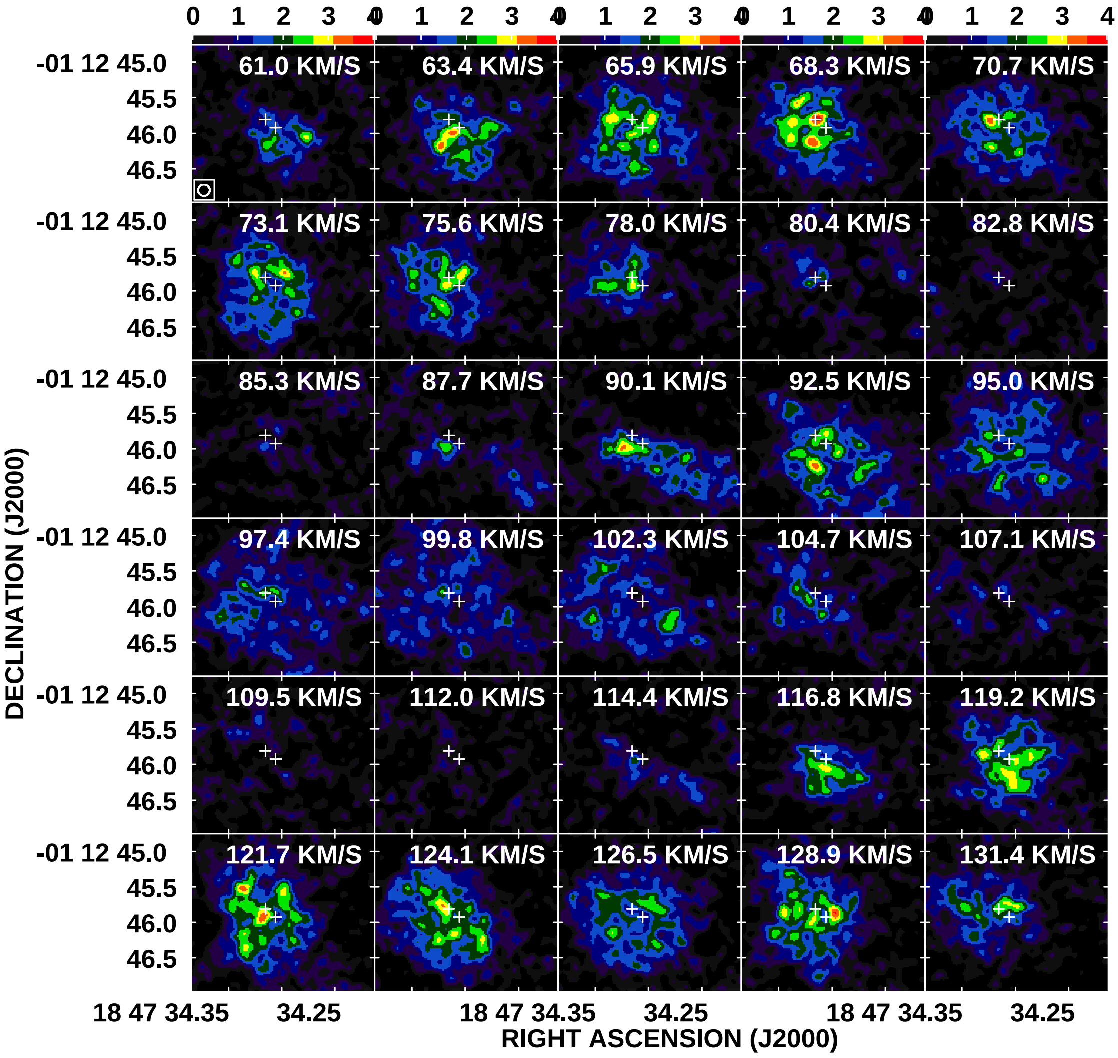

Figure 4.5: Same as Figure 4.3 but for the $NH_3(4,4)$ transition. The satellite line emission is shifted by ±24.21 km s^{-1} and ±30.43 km s^{-1} for the inner and outer satellites, respectively (Table A.2).

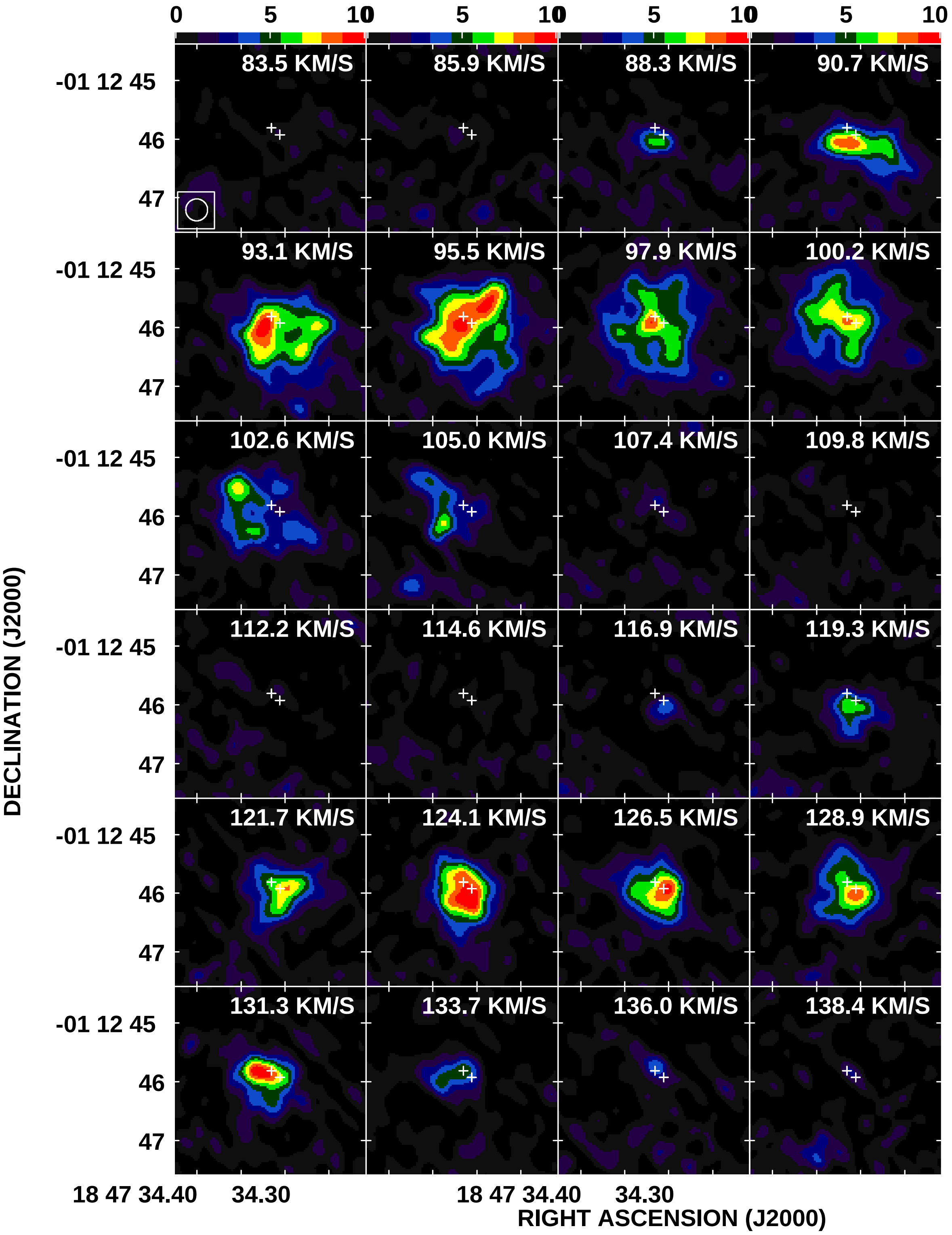

Figure 4.6: Same as Figure 4.3 but for the $NH_3(5,5)$ transition. The satellite line emission is shifted by +25.91 km s^{-1} and +31.40 km s^{-1} for the inner and outer satellites, respectively (Table A.2).

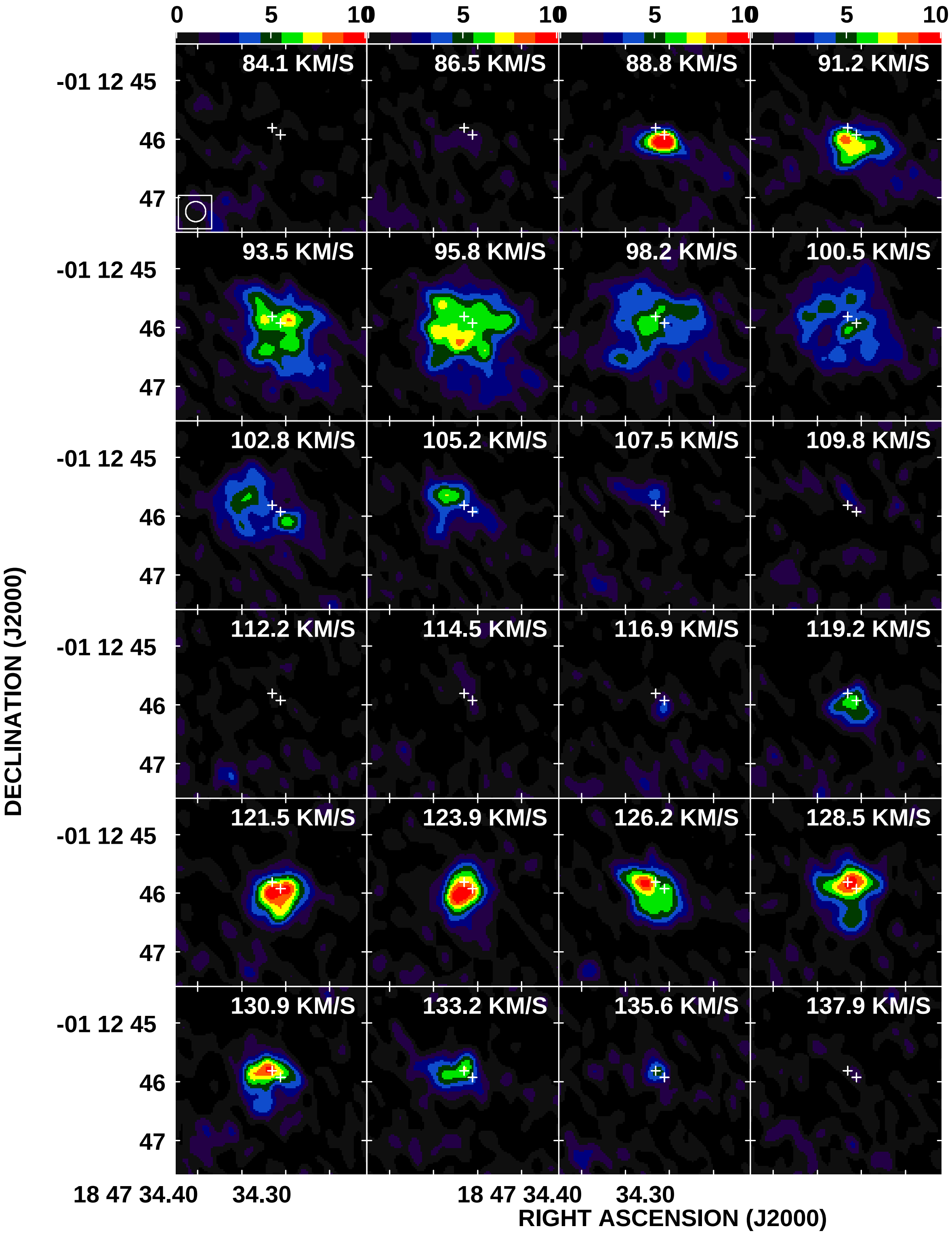

Figure 4.7: Same as Figure 4.3 but for the $NH_3(6,6)$ transition. The satellite line emission is shifted by +26.92 km s^{-1} and +31.46 km s^{-1} for the inner and outer satellites, respectively (Table A.2).

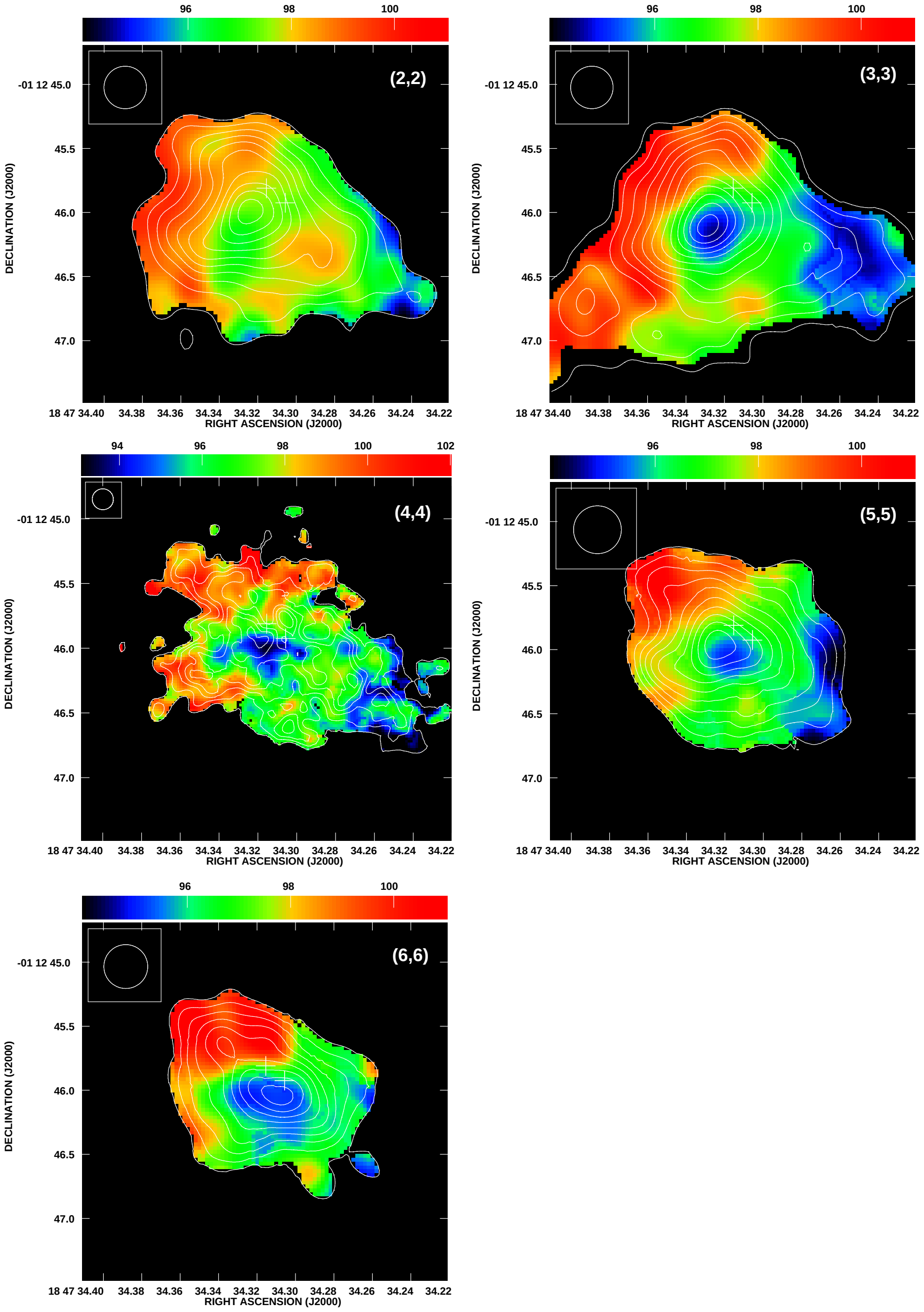

Figure 4.8: Overlay of the integrated intensity (zeroth-order moment; contours) and the intensity-weighted mean velocity (first-order moment; color scale) maps of the ammonia (2,2), (3,3), (4,4), (5,5), and (6,6) main line towards G31 HMC. Contour levels are 25, 30, 45, 60, 75, 90, 105, 120, 135, 150, 165, 180, 195, 210 mJy beam^{-1} km s^{-1}. The synthesized beam is shown in the upper left corner of each map. Color scale ranges from 93.2 to 102 km s^{-1}. Note the spot of blue-shifted emission towards the integrated intensity peak in all the maps.

of the main line (Figure 4.8). Also, the satellite emission appears less elongated, more rounded and more compact than the main-line emission. In the outer region the column density is not high enough to make the (5,5) and the (6,6) satellite lines optically thick, and so, the satellite emission of the (5,5) and (6,6) traces mainly the inner part of the core. The NE-SW velocity gradient is still evident in the velocity maps, but the excess of blue-shifted emission towards the emission peak observed in the main line maps is not seen here. As in the main line, the (3,3) satellite emission shows red-shifted gas of low intensity to the E of the main condensation. This feature also appeared in the (3,3) main line maps.

4.4 Discussion

4.4.1 Spatially resolved infall signature

To search for the spectral imaging infall signature (see section 2.2) we need to compare the observed intensity as a function of distance to the center of the core for pairs of velocity channels symmetrically located at both sides of the systemic velocity. In order to improve the signal-to-noise ratio, for every channel map we averaged the emission of the main line over circular annuli of different radii and $0\farcs15$ width, and then we plotted this average intensity as a function of the radius. The center of the annuli was chosen to be at RA(J2000) = $18^h47^m34.311^s$; DEC(J2000) = $-01°12'45.90''$, which corresponds to the position of the peak of the integrated intensity of the ammonia (6,6) satellite lines. This choice is based on the lowest opacity of the (6,6) satellite lines among all observed and therefore, so its emission may arise from the innermost, warmest regions, close to the central heating source. Our chosen central position lies roughly in between the positions of the two embedded radio continuum sources detected by Cesaroni et al. (2010), which are separated $\sim 0\farcs2$.

The systemic velocity of the cloud is not accurately determined. In the literature we find velocities ranging from 96.24 km s^{-1} (Beltrán et al. 2005; from ground state CH$_3$CN (12−11) observations) to 98.8 km s^{-1} (Cesaroni et al. 1994, from low resolution NH$_3$(4,4) observations). We have adopted the value of V_{LSR}=97.4 km s^{-1} (marked as dotted line in Figure 4.2) from the interferometric data of Beltrán et al. (2005), obtained by fitting simultaneously several components of different K-quantum number of the $v_8 = 1$ CH$_3$CN (5-4) transition. Since the original purpose of the observations presented here was not to search for infall signatures, they were not adequately designed for this study. The spectral resolution is poor ($\sim$ 2.4 km s^{-1}) and the observations of the different transitions were not centered exactly at the same velocity. Thus, we cannot obtain pairs of velocity channels that are exactly symmetric in velocity with respect to the systemic velocity of the cloud (97.4 km s^{-1}), which hinders an accurate comparison of red- and blue-shifted channel pairs. As our best approximation, we have compared channel pairs with the most similar velocity shifts with respect to the assumed systemic velocity of the cloud. Given the uncertainty in this central velocity and the large channel widths ($\sim$ 2.4 km s^{-1}), we have excluded the channel pair closest ($\sim \pm2$ km s^{-1}) to the systemic velocity in order to ensure that we are comparing emission with different velocity signs (i.e., red vs. blue).

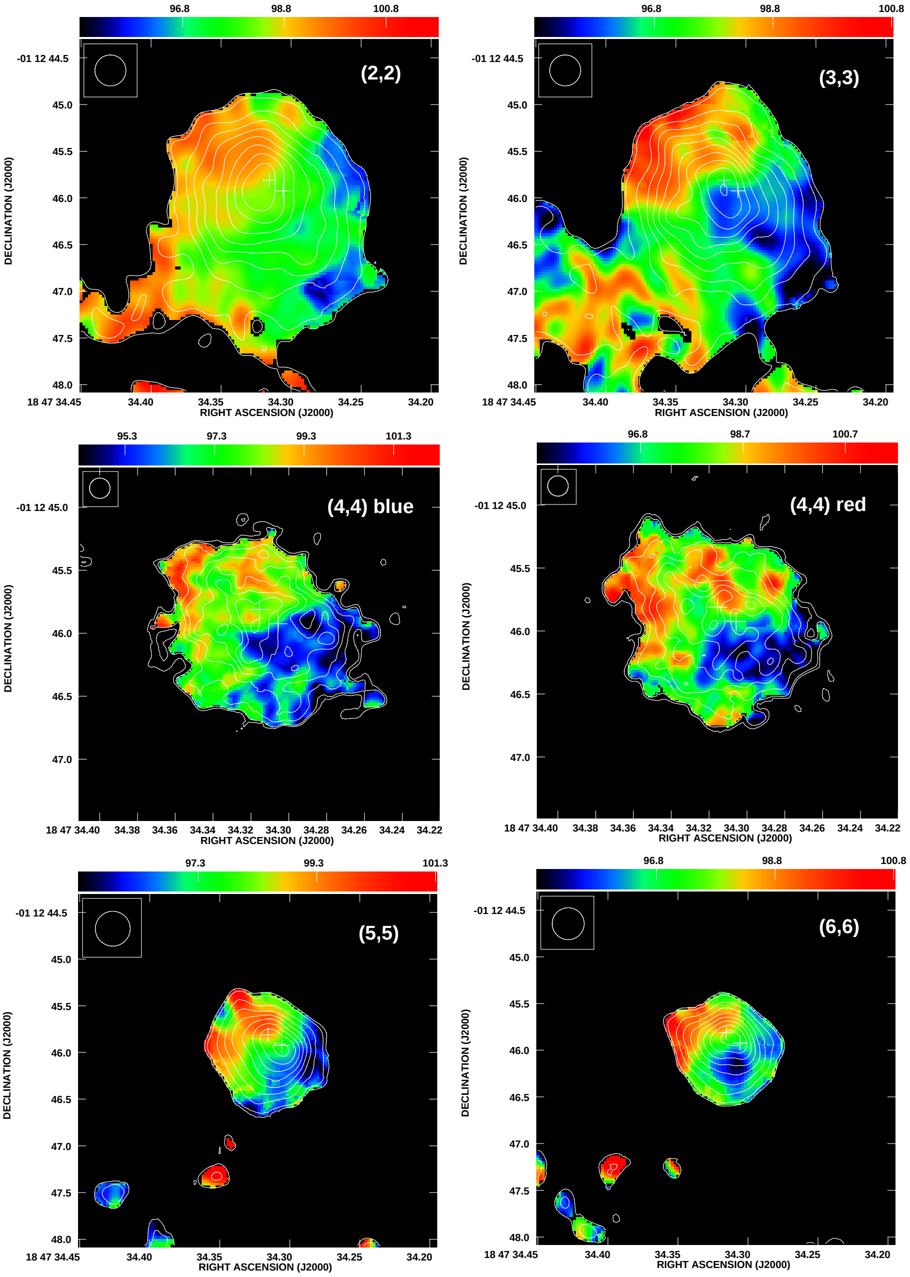

Figure 4.9: Overlay of the integrated intensity (zeroth-order moment; contours) and the intensity-weighted mean velocity (first-order moment; color scale) maps of the ammonia (2,2), (3,3), (4,4), (5,5), and (6,6) satellite lines towards G31 HMC. Maps correspond to the red-shifted pair of satellite lines, except for the (4,4) transition where maps for both pair of satellite lines are shown. Contour levels are 25, 30, 45, 60, 75, 90, 105, 120, 135, 150, 165, 180, 195, 210 mJy beam^{-1} km s^{-1}. The synthesized beam is shown in the upper left corner of each map. The two crosses mark the position of the two radio continuum sources detected by Cesaroni et al. (2010).

Figure 4.10 shows the observed intensity as a function of the projected distance to the core center for blue-shifted (blue continuous lines) and red-shifted (red dotted lines) velocity channels of the ammonia (2,2), (3,3), (4,4), (5,5) and (6,6) main lines. The main lines of all these transitions are certainly optically thick (as indicated by the main to satellite line ratio close to unity), and a pattern is clearly identifiable in the images of all the observed transitions. For each pair of blue/red channels, the intensity of the blue-shifted channel is stronger, and increases more sharply towards the center, than in the corresponding red-shifted channel, where the intensity distribution is flatter. Moreover, as the velocity departs from the systemic velocity, the emission becomes more compact (a narrower spatial intensity profile). This behavior, indicative of acceleration, is in agreement with the expected spectral imaging signature of infall for angularly resolved sources described by A91 (see Chapter 2 and 3), suggesting that gravitational infall motions strongly contribute to the kinematics of the G31 HMC. Since the satellite lines appear to be also optically thick (at least for the lowest excitation transitions), similar signatures would be expected in the satellite line channel maps. Unfortunately, since the satellite lines are broad and blended together a similar analysis cannot be carried out for the satellite emission.

To confirm the presence of these infall signatures more quantitatively, we compare our observational results with the predictions of the model for G31 HMC developed by Osorio et al. (2009). These authors modeled G31 HMC as a spherically symmetric envelope of dust and gas that is collapsing onto a recently formed massive star ($M_* \simeq 25$ M$_\odot$) that is undergoing an intense accretion phase ($\dot{M} \simeq 3 \times 10^{-3}$ M$_\odot$ yr^{-1}). The envelope consists of an inner, infalling region ($r < 2.3 \times 10^4$ AU) that is surrounded by a static part ($r_{\rm ew} < r < R_{\rm ext} \simeq 3 \times 10^4$ AU). The density and velocity structure of the envelope are obtained from the solution of the dynamical collapse of a singular logatropic sphere (see Section 3.4). The stellar radiation ($L_* \simeq 8 \times 10^4$ L$_\odot$) and the accretion luminosity ($L_{\rm acc} \simeq 1.5 \times 10^5$ L$_\odot$) provide the source of heating of the envelope, whose temperature as a function of the distance to the center is self-consistently calculated from the total luminosity. The excitation and absorption coefficients of the ammonia transitions are calculated according to the physical conditions along the envelope, and the radiative transfer is performed in order to obtain the emerging ammonia spectra. The parameters of the model are determined by fitting the observed spectral energy distribution (SED) and the VLA B-configuration NH$_3$(4,4) line spectra obtained in the observations of Cesaroni et al. (1998) that angularly resolve the source. Figure 4.11 shows the intensity predicted by the G31 HMC model as a function of the projected distance to the core center, for different pairs of blue/red-shifted channels of the ammonia (2,2) to (6,6) main lines. The angular and the spectral resolutions have been set equal to those of the observations.

As can be seen from Figure 4.11, the spatial intensity profiles predicted by the model of G31 HMC developed by Osorio et al. (2009) show the basic signatures of spatially resolved infall proposed by A91 from a simplified, general treatment of protostellar infall. The spatial intensity profiles of the blue-shifted channels are centrally peaked, while those of the red-shifted channels are flatter; and the emission in both red- and blue-shifted channels becomes more compact as

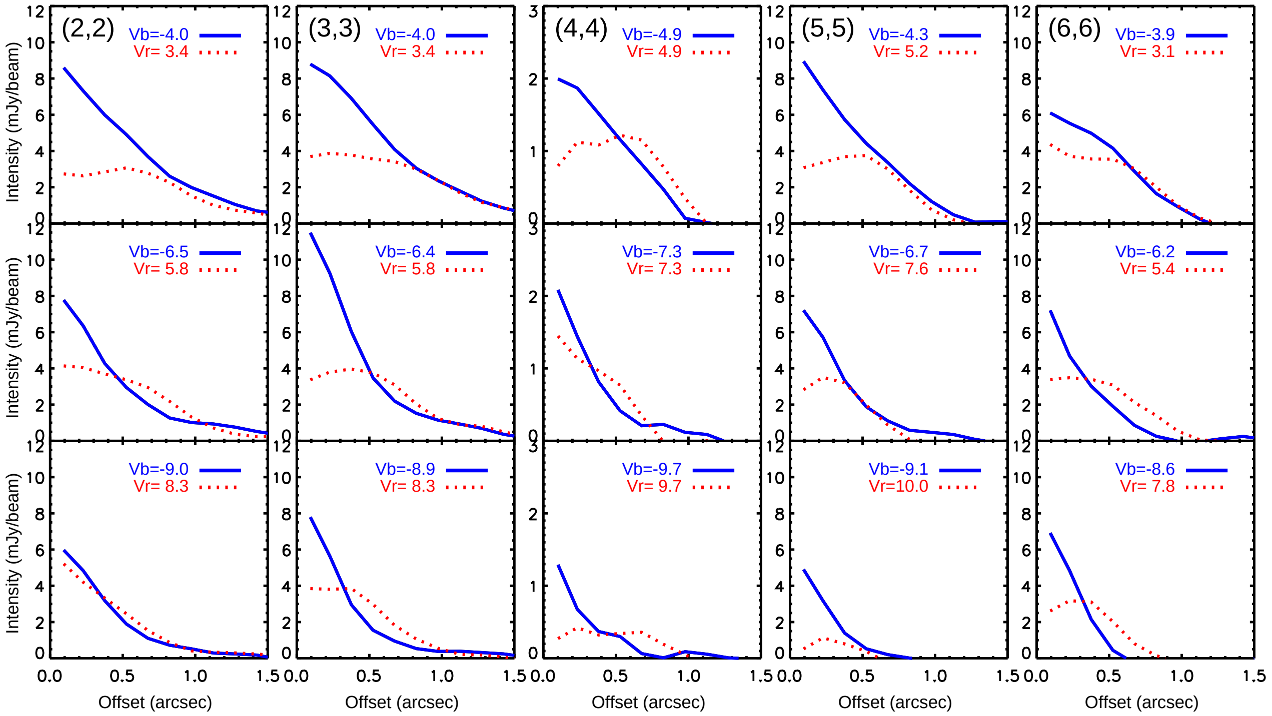

Figure 4.10: Circularly-averaged observed intensity as a function of angular distance to the center of G31.41 HMC, for different pairs of blue-shifted (solid blue line) and red-shifted (dotted red line) channel maps. Results for the ammonia (2,2), (3,3), (4,4), (5,5) and (6,6) transitions (from left to right) are shown. The sizes of the synthesized beams are given in Table 4.1. Labels indicate the channel velocity (in km s^{-1}) relative to the assumed systemic velocity of the cloud ($V_{\rm LSR}$ = 97.4 km s^{-1}).

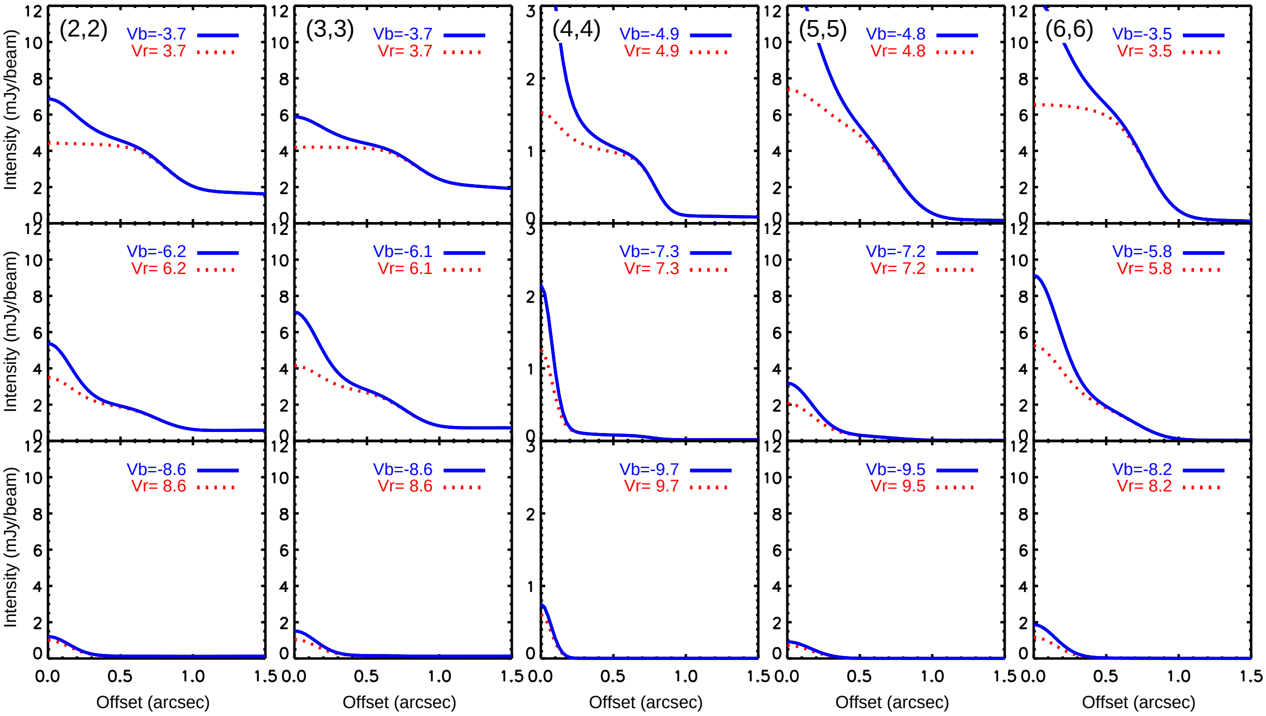

Figure 4.11: Intensity as a function of angular distance to the center, obtained with the model of G31 HMC by Osorio et al. (2009), for different pairs of blue-shifted (solid blue line) and red-shifted (dotted red line) channel maps. Results for the ammonia (2,2), (3,3), (4,4), (5,5) and (6,6) transitions (from left to right) are shown. Model results have been convolved with a Gaussian with a FWHM equal to that of the observational beam (see Table 4.1). Labels indicate the velocity (in km s^{-1}) relative to the systemic velocity of the cloud.

the relative velocity increases. Furthermore, by comparing Figures 4.10 and 4.11 we note that there is a remarkable quantitative agreement between the observations of G31 HMC and the model of this source, as the shape and range of values are similar in the observed and modeled spatial intensity profiles. Thus, we conclude that the general infall signatures described by A91 are present in G31 HMC, suggesting that infall motions have a significant contribution to the kinematics of this source. The quantitative agreement with the predictions of a specific model for G31 HMC indicates that these signatures are sensitive to the physical properties (in particular, the kinematics and temperature profile) of the source and, therefore, that they may be used to verify and/or improve source models.

Although there is a general agreement, the precise shape of the predicted and observed intensity profiles are not fully coincident. For example, at velocities farther away from the systemic one the model emission is in general weaker and more compact than observed (bottom panels in Figures 4.10 and 4.11). This implies that the model predicts thinner lines than those observed. Also, some of these discrepancies could be due to the fact that the pairs of velocity channels extracted from the observations are not exactly symmetric in velocity because of the large channel widths and the uncertainty in the central velocity. Observations with higher spectral resolution of optically thick lines, combined with additional observations of optically thin lines (to accurately determine the central velocity) are required to better study the trends presented here. Presence of rotation and outflow motions (e.g., Cesaroni et al. 2011) and, in general, departures from spherical symmetry, that are not considered in the modeling of Osorio et al. (2009) (e.g., the presence of a central binary), could affect the infall signatures, and account for some of the observed differences. In Section 4.4.2 we will examine the effects of rotation on the spatial intensity profiles.

The central blue spot signature

The observed first-order moments of the (2,2) to (6,6) main line transitions (Figure 4.8) show a velocity gradient from NE to SW, and a spot of blue-shifted emission towards the peak of the zeroth-order moment. The velocity gradient seen in the velocity maps suggests either rotation along an a axis with a PA $\simeq -30°$, or a bipolar outflow along a PA $\simeq 60°$. We identify the spots of blue-shifted emission towards the peak of the zeroth-order moment as the "central blue spot" signature. The clear detection of the "central blue spot" signature in G31 HMC indicates that infall motions play a fundamental role in the gas kinematics of this source. As can be seen in Figure 4.8, the blue spot signature is present in all the observed ammonia transitions, confirming that its detection is a robust result. It is less evident in the (2,2) transition, probably because in this transition the satellite lines are closer in velocity to the main line, resulting in a contamination of the high-velocity main line emission by satellite emission, given the large line-widths.

We note that the opacity is expected to decrease in the central part of the blue-shifted emitting region (see Section 3.4.2.3, and Appendices A and C of Anglada et al. 1987). This can reduce the degree of asymmetry and partially erase the blue spot signature in molecular transitions of moderately high optical depth. The observations and modeling suggest that this is not the case in G31 HMC.

We note that the "central blue spot" is not clearly seen in the satellite line maps, although the NE-SW velocity gradient is still evident. The satellite lines are optically thinner and we believe that the satellite lines are less sensitive to the outer part of the core, where infall dominates, and are more sensitive to the inner part of the core, where rotation may become at least as important as infall. As a consequence, the "central blue spot" is not clearly detectable with the satellite lines, but at the same time that makes the satellite line emission more suitable to the search of the infall plus rotation signatures described in Section 2.3.

4.4.2 On the effects of rotation

As can be seen in Figure 4.8 and Figure 4.9, the first-order moments (intensity-weighted mean velocity) of the ammonia emission in G31 HMC show a velocity gradient in the SW-NE direction, with velocities preferentially blue-shifted in the SW side and preferentially red-shifted in the NE side of the source. This velocity gradient has been previously reported by other authors using other molecular transitions as methyl cyanide (Cesaroni et al. 1994, Beltrán et al. 2004) or methanol (Araya et al. 2008). Its nature is controversial and has been attributed either to rotation or to a bipolar outflow. In Section 2.3 we studied the effects of rotation on the spatial intensity profiles, and found that, as long as rotation is not dominant, it does not mask the spectral imaging infall signatures, but produces asymmetric spatial intensity profiles with respect to the LOS towards the center. The equatorial intensity profiles will be more extended on the side where rotation and infall LOS velocity components have the same sign and more compact on the opposite side. Likewise, the spatial intensity profile of a given velocity channel is stretched on the side where the channel and rotation velocities are both red-shifted or both blue-shifted, while it is shrunk on the opposite side (Figure 2.7). Here we will explore whether the predicted rotation signatures on the spatial intensity profiles are in qualitative agreement with what is observed in G31 HMC.

To do so, we obtained the average intensity of the ammonia main line as a function of projected distance to the center (ring-averaged values, as in Section 4.4.1, to increase the signal-to-noise ratio), but we calculated this intensity separately in the half of the source that is blue-shifted (SW) and in the half that it is red-shifted (NE). Considering that the direction of the velocity gradient is PA$\sim$ 60°, for every observed velocity channel, we obtained the average intensity over half-annuli of different radii corresponding to the NE ($-30° <$ PA $< 150°$) and SW ($150° <$ PA $< 330°$) halves of the source. In Figure 4.12 we plotted the resulting spatial intensity profiles for different velocity channels of the observed ammonia transitions. As can be seen in the figure, the intensity profiles show the general trends predicted for a rotating collapsing core: (i) The spatial intensity profiles of the blue-shifted channels sharply increase towards the center, while those of the red-shifted channels are flatter; (ii) The profiles become

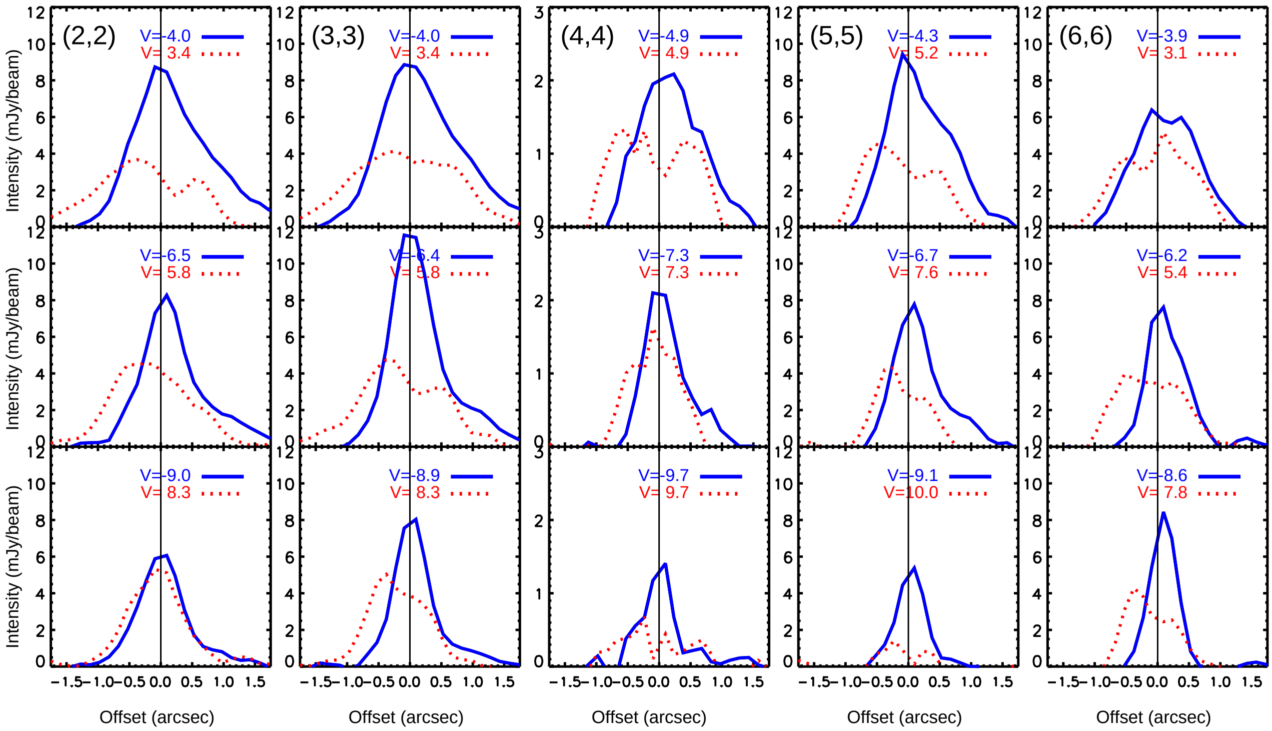

Figure 4.12: Observed intensity as a function of angular offset from the center of G31.41 HMC, for different pairs of blue-shifted (solid blue line) and red-shifted (dotted red line) channel maps. Intensities have been averaged over half-annuli at both sides of the rotation axis, here assumed to be at PA = 150°. Negative offsets correspond to the NE half of the source ($-30° < \mathrm{PA} < 150°$), where rotation velocities are red-shifted, and positive offsets correspond to the SW half of the source ($150° < \mathrm{PA} < 330°$), where rotation velocities are blue-shifted. Results for the ammonia (2,2), (3,3), (4,4), (5,5) and (6,6) transitions (from left to right) are shown. The sizes of the synthesized beams are given in Table 4.1. Color labels indicate the channel velocity (in km s^{-1}) relative to the assumed systemic velocity of the cloud ($V_{LSR} = 97.4$ km s^{-1}).

narrower as the velocity increases; (iii) The intensity profiles are asymmetric with respect to the central position, being the NE part (negative offsets) in the red-shifted channels more extended than the SE part (positive offsets), while the opposite is true for the blue-shifted channels. This behavior is in agreement with what is expected for infalling matter with clockwise rotation (as seen from north). Thus, we conclude that spatially resolved rotation and infall signatures can be identified in the images of the molecular ammonia emission of G31 HMC.

It should be noted that, so far, only a spherically symmetric model for the physical structure of G31 HMC has been constructed (Osorio et al. 2009); therefore, we can only evaluate the effects of rotation in a qualitative way. We plan to extend our study by carrying out an integral model of the source, where the observational data are fitted to an infalling rotating envelope.

We have shown that the rotation features may be present on the spatial intensity profiles, and so, our ammonia observations are probably sensitive to rotating material. However, as we have obtained such spatial intensity profiles by averaging over 180°, we could not determined accurately the direction of the rotation axis. In Section 2.3 we stated that, in order to determine the actual orientation of the equatorial plane (or, equivalently, the orientation of the rotation axis), we should examine the velocity gradient seen in the immediate vicinity of the core center rather than the large-scale velocity gradients. We additionally proposed some features that would indicate the orientation of the equatorial plane, as are the "roller coaster" feature, the presence of the "blue spot" and the "dimmer red spot" at opposite sides of the core center, the shift in the position of the "blue spot" with respect to the core center (when the "red spot" is not clearly detected because of being dimmer), or the "misplacement" of the actual core center (if known) with respect to the geometrical center of the contours of equal integrated emission. We will try to detect such features in G31 HMC in order to better determine the actual orientation of the rotation.

If we consider the average position of the two radio continuum sources detected by Cesaroni et al. (2010) as the core center, then it is interesting to note that this position does not fall at the geometric center of the integrated intensity emission (Figure 4.8). Instead, the two radio continuum sources appear as shifted to the N. We also note that the "central blue spot" of G31 HMC (Figure 4.8) appears systemically shifted to the south with respect to this central position. Both things suggest an equatorial plane in the N-S direction and a rotation axis nearly in the E-W direction (see Section 2.3.2).

We have observed in G31 HMC that, for the (5,5) and (6,6) transitions, the extension of the satellite emission is smaller than that of the main line (compare Figures 4.8 and 4.9). This suggests that the NH_3(5,5) and NH_3(6,6) satellite lines are, because of their much lower optical depth (see Table A.1), less sensitive to the outer parts of the core than the main line. Instead, these lines are emphasizing the most internal parts of the core, where rotation may become more important. This would be more noticeable for the (6,6) transition, where the ratio in optical depth between main line and satellite line is the greatest among the studied transitions. In the intensity-weighted mean velocity maps of the (6,6) satellite emission (Figure 4.13a), we found a spot of red-shifted emission to the north of the radio continuum sources, and a spot of blue-shifted emission to the south, both separated by only $0\farcs5$. The line joining the "blue and red spots" is orientated at PA=15°. We identify this feature as the "blue spot and dimmer red spot pair" signature predicted in Section 2.3.2. There are hints of this signature also in other transitions (Figure 4.9). Additionally, we find that, in general, towards the central region of the core the velocity gradient has preferentially a N-S orientation at small scales (Figures 4.9 and 4.13a). To the north of the radio continuum sources the emission is red-shifted, while to the south the emission is blue-shifted. Yet, there exist a large-scale velocity gradient in the E-W (red to blue-shifted emission).

The "dimmer red spot" is also detectable in the first-order moment of the (6,6) main line (Figure 4.13b), what indicates that the blending of inner and outer satellite does not distort the mean velocity map obtained from the satellite maps. In the first-order moment of the main line, the "blue spot" is much stronger than the "dimmer red spot" (Figure 4.13b), while in the satellite line first-order moment both have similar strength (Figure 4.13a). The former indicates that the main line, which is optically thicker, traces the large scale infall. The latter indicates that, either the satellite lines are optically thin, or either they may be tracing better the inner region of the core (scales of around 2000 AU) where rotation can be as important as infall.

We also searched for the "roller coaster" feature (Section 2.3.2). To do so we performed cuts of the first-order moment of the main line ammonia emission along different position angles covering the whole range of 360°. Figure 4.14 shows the cuts along the most significant PA. Only the cuts at PA$\simeq$ 20° show valleys and ridges that resemble those of the "roller coaster" feature (see Section 2.3.2). Such feature is present for all transitions, although the detection in the (2,2) transition is doubtful since the bluest velocity is not as blue as would be expected for the "roller coaster" signature. Note that the "roller coaster" feature is not present in the direction of the large-scale velocity gradient seen in Figure 4.8, PA$\simeq$ 60°. The direction marked by the detection of the "roller coaster" feature ($\sim$ 20°) is consistent with the presence of a rotating structure oriented nearly in the N-S direction, rather than at PA=60° as suggested by other authors (Olmi et al. 1996; Beltrán 2004, 2005; Cesaroni et al. 2011).

Moreover, Cesaroni et al. (2011) presented ^{12}CO(2-1) velocity channel maps towards G31 HMC. We have performed a map of the ^{12}CO(2-1) high-velocity emission from the data of Cesaroni et al. (2011) and we find that the bulk of the CO emission is distributed over three regions (Figure 4.15). There is red-shifted gas that extends 5 arcsec from the center of G31 HMC towards E. There is also blue-shifted gas that extends 3 arcsec from the HMC towards W, and finally there is a third area of blue-shifted gas, 5" SW from G31 HMC, that appears disconnected from the ammonia emission (Figure 4.15). The positions and orientations of the first and second regions of ^{12}CO(2-1) emission are compatible with an E-W bipolar CO outflow. The third area of high velocity emission to the SW has an unknown origin. Gibb et al. (2004) already pointed out the possibility of a H_2S outflow in the E-W direction.

The "roller coaster" feature, the "blue spot" and "dimmer red spot" orientation, the shift in position to the south of the "blue spot" with respect to the centimeter radio sources and the location of the radio sources off the peak of the integrated emission suggest that the rotating structure should be close to an N-S orientation. The presence of an outflow in E-W direction is also in agreement with the presence of a rotating structure in N-S direction.

We also noted that the red- and blue-shifted lobes of the CO outflow can be associated respectively with the red-shifted arm to the E, and with the blue-shifted arm to the W seen with the NH_3(3,3) main line emission (Figure 4.8 and Figure 4.15). Multiple studies have shown that there seems to be a tendency that the (3,3) transition is more sensitive to high-velocity motions than other ammonia transitions (Bachiller et al. 1993; Wilson et al. 1995; Umemoto et al. 1999; Takano et al. 2002, 2005; Mauersberger et al. 2003). For instance, Wilson et al. (1995) found differences between the (1,1) and the (3,3) transitions towards the massive star forming

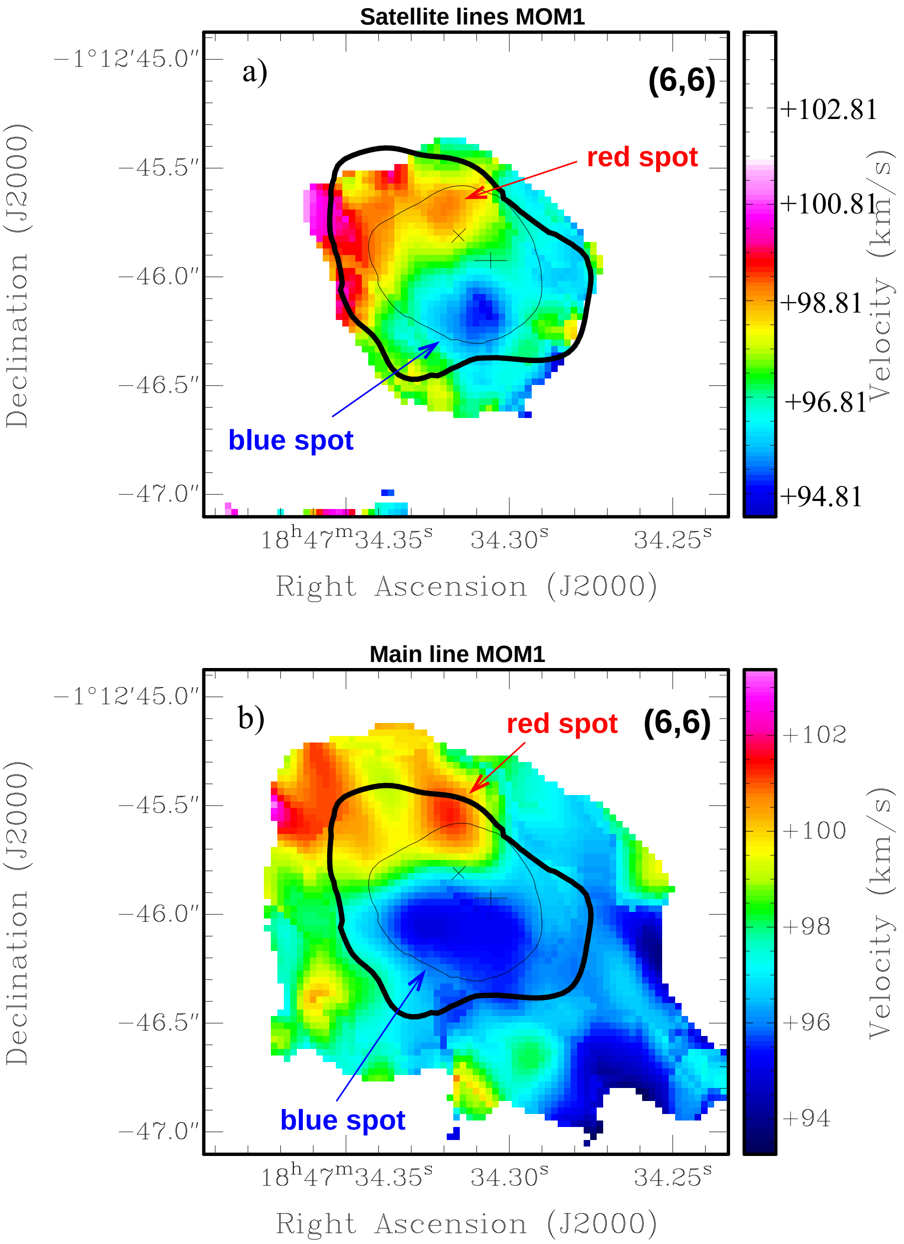

Figure 4.13: Intensity weighted mean velocity (first-order moment; color scale) maps of the ammonia (6,6) satellite emission (*Panel a*) and main line emission (*Panel b*). The maps are the same as those shown in Figure 4.9 but the color palette has been modified to enhance the velocity gradients in the region closer to the radio continuum sources that are assumed to trace the position of the embedded protostars. The contour at half maximum of the main line integrated emission (thick line) and of the satellite line integrated emission (thin line) are shown. Note that over the location of the two radio continuum sources the velocity gradient is preferentially in N-S direction.

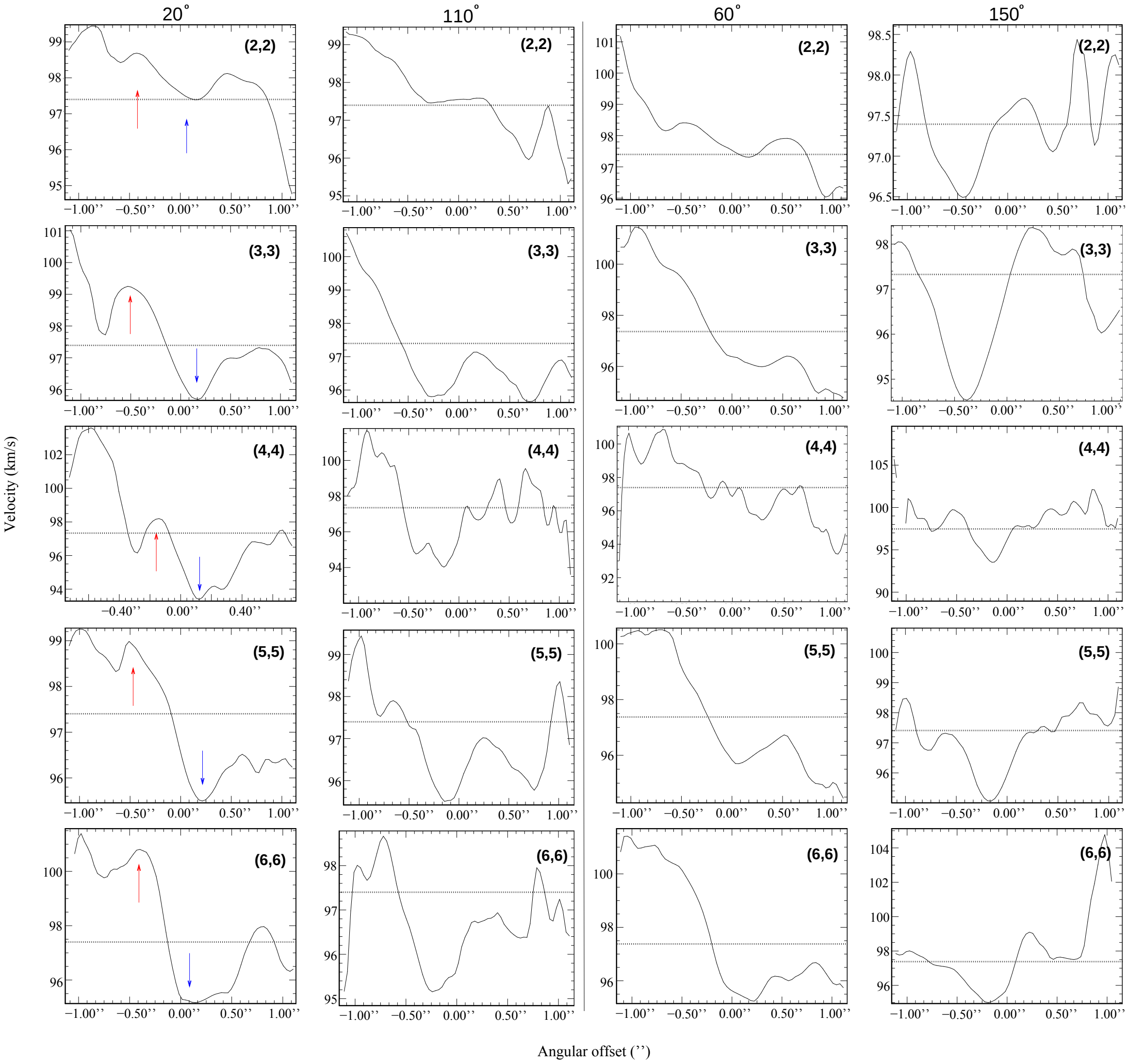

Figure 4.14: Cuts along PA=20° and PA=60° (and their corresponding perpendicular directions) of the first-order moment of the main line emission for the (2,2) to (6,6) ammonia transitions. The angles are measured east from north. For cuts of PA $<$ 90° positive offsets mean SE direction, and negative offsets mean NW direction. While for cuts with PA $>$ 90° positive offsets mean NE and negative offsets mean SW direction. The dotted horizontal lines indicate the systemic velocity of the cloud.

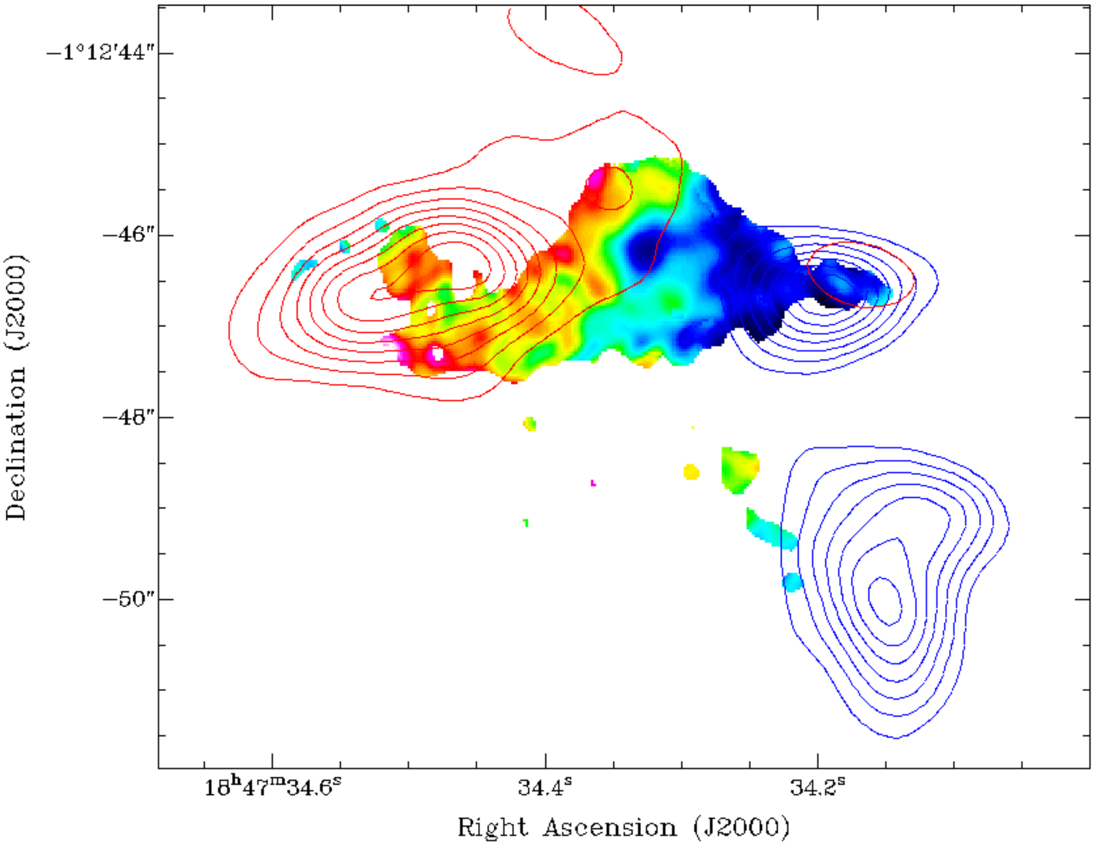

Figure 4.15: Map of the high velocity ^{12}CO(2-1) emission. Blue-shifted emission has been integrated from 69.4 km s^{-1} to 96.4 km s^{-1} (blue contours) while red-shifted emission has been integrated from 98.4 km s^{-1} to 132.4 km s^{-1} (red contours). The lowest contour corresponds to 8.2 Jy beam^{-1} km s^{-1} and increments are of 4.1 Jy beam^{-1} km s^{-1}. The first-order moment of the NH$_3$(3,3) main line emission (colors) is superposed.

region of DR 21 and explained that the (3,3) might be tracing hotter shocked gas associated with the outflow. In a similar way, the arms at E and W of the G31 HMC seen with the (3,3) transition might be tracing shocked gas associated with the outflow. The special sensitivity of the (3,3) transitions to high-velocity motions could explain why these arms associated with the CO outflow are only seen in the (3,3) transition (Figure 4.8).

Moscadelli et al. (2013) shows a distribution of water masers (at 22 GHz) that can be well fitted by an ellipse at a PA=8° (Figure 4.16). Note that this orientation would be almost perpendicular to the observed CO outflow (Figure 4.15). Such ellipse is centered towards the position of the radio continuum sources and its ratio between minor and major axis would suggest an edge-on circular ring. However, Moscadelli et al. (2013) interpreted such water maser group as an outflow. They based their interpretation on the fact that the ring inclination angle evaluated through the ratio of the velocity component projected along the LOS, V_z, and the velocity component along the ellipse minor axis, V_T, suggests an almost face-on configuration contradicting the edge-on orientation that the ratio of minor and major axis seems to indicate. However, the calculation of the ring inclination through the ratio of velocity components is based on the hypothesis of masers moving on the ring plane. We note that this assumption is not necessarily fulfilled. For example, motions along flared disks/structures do not lie onto a single plane, precessing disks develop velocities perpendicular to the plane of the disk (Shakura et al. 1999); warps in disks also produce velocities perpendicular to the plane of the disk as the warp propagates through the disk (Papaloizou & Lin 1995; Nelson & Papaloizou 1999; Lodato & Pringle 2007; Lodato & Price 2010; Lodato & Facchini 2013); also radiation pressure in flared disks can produce motions perpendicular to the disk plane (Kuiper et al. 2012, 2013). We suggest that, on basis of our findings, the ellipse of water masers is more likely tracing a ring inside a rotating structure. According to Moscadelli et al. (2013), if the water masers were tracing a rotating structure, the PA of the rotational axis should be PA$\sim$ 98° (or equivalently PA$\sim -82°$), and its inclination with respect to the line of sight of $i \sim 80°$.

If, indeed, water masers are tracing a rotating structure with an almost N-S orientation, the natural question that arises is: where does the observed velocity gradient at PA$\simeq$ 60° come from? Rodríguez & Bastian (1994) describe the kinematics of the source MWC 349 as a combination of two overlapped velocity gradients. They show that the velocity gradient caused by rotation and the one caused by an outflow, which are perpendicular, can sum up to produce an oblique overall velocity gradient (see Figure 4.17). In a similar way, this could be also the case of G31 HMC. The velocity gradient at PA$\simeq$ 60° would be caused by the overlapping of the velocity gradients due to rotation (N-S) and to outflow (E-W).

We propose that the following scenario is taking place in G31 HMC. Our interpretation consists of an almost spherical, environmental cloud (of $\sim 10^4$ AU in radius) which is preferentially detected with the main lines of the ammonia transitions. This ambient cloud is in a state of overall collapse, and therefore, the "spectral imaging infall signature" and the "blue spot" are detectable through the main line emission. The cloud is also rotating but rotation motions only become important in the most internal part of the cloud (at a radius of $\sim 2 \times 10^3$

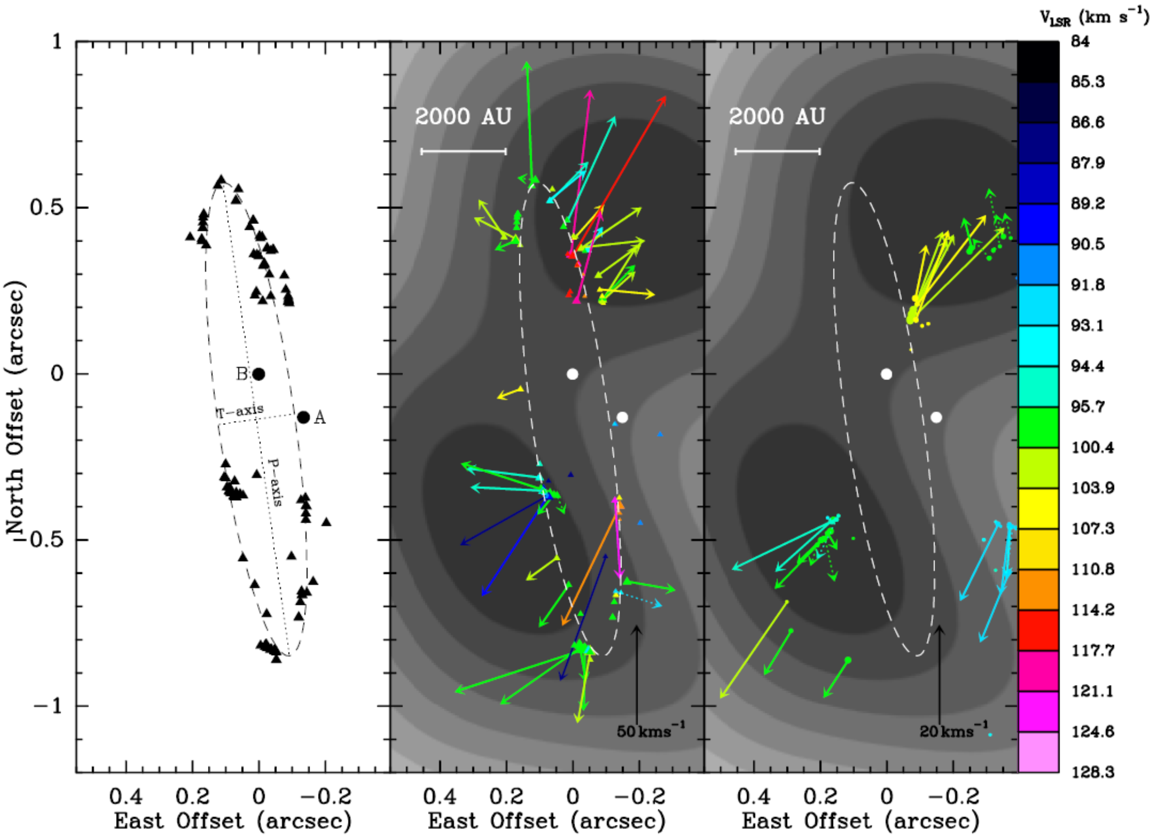

Figure 4.16: Snapshot of figure 5 in Moscadelli et al. (2013) which shows the ellipse-like distribution of the water masers group called J1, and their proper motions. *Left panel*: Black triangles denote the positions of the water masers. The dotted lines trace the major (labeled "P-axis") and minor ("T-axis") axis of the best-fit ellipse. Black dots give the positions of the radio continuum sources. *Central and Right panels*: Colored triangles and dots show the positions of the water (central panel) and methanol (right panel) masers, respectively. The gray-scale map reproduces the integrated emission of the CH_3CN $(12-11)$ K= 4 line (at 221 GHz) observed with the SMA (beam $\sim 0\farcs8$) by Cesaroni et al. (2011). The white big dots give the positions of the radio continuum sources. Colored vectors indicate the direction and the amplitude of the maser proper motions. The black vector in the bottom right corner of the panels indicates the amplitude scale of proper motions in kilometer per second. Dotted vectors are used for the most uncertain proper motions.

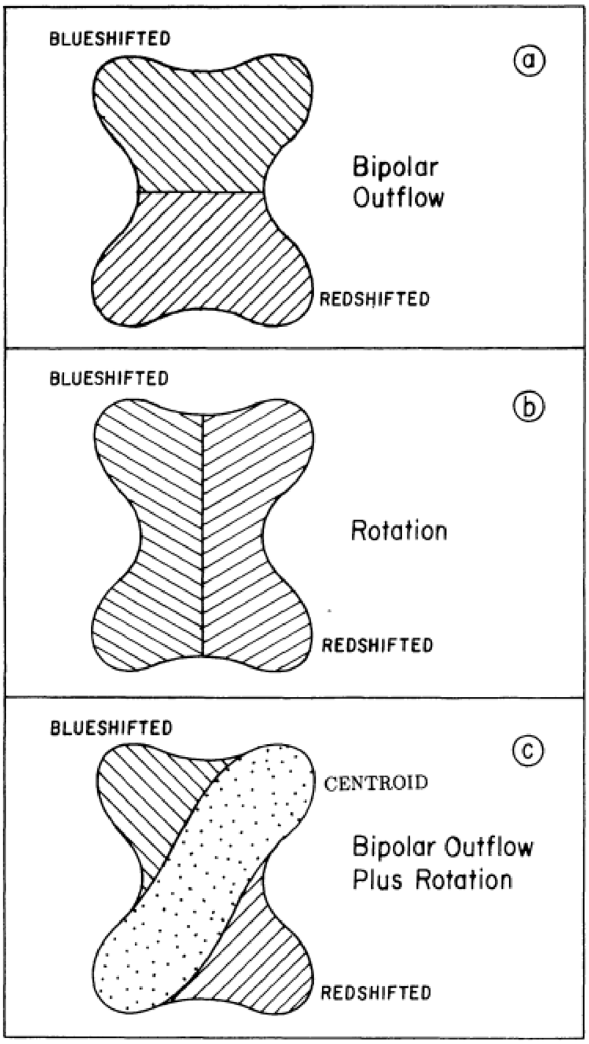

Figure 4.17: Schematic representation of the expected kinematic structure for (a) a bipolar outflow, (b) rotation, and (c) a bipolar outflow with rotation. Figure adapted from Rodríguez & Bastian (1994).

AU), which is better traced by the satellite lines of the highest excitation transitions. Rotation makes the internal density structure to be more concentrated along the equator plane. The ring-like appearance of the water masers may be tracing such a density enhancement along the equatorial plane, which has a rotation axis at PA$\sim -90°$. The high velocity CO emission traces an almost E-W bipolar outflow nearly perpendicular to such rotating density structure. The high velocity gas of the outflow produces shocks in the cavity walls; such shocks may be traced by the NH_3(3,3) line emission as "arms" or protuberances of low intensity emission extending to the E and W of the HMC. If this scenario is confirmed, then the controversial velocity gradient at $\sim 60°$ is probably not tracing neither rotation nor outflow, but a combination of the velocity gradients produced by the two of them. Additionally, if this scenario is proved, it would confirm that the "roller coaster" signature and the "blue spot and dimmer red spot pair" can be useful tools to distinguish if a velocity gradient is caused by outflow or by rotation, and that they can provide a much better approximations to the actual direction of rotation than what large-scale velocity gradients on maps may suggest. Though, high angular resolution and high line opacity are needed to detect these signatures.

4.4.3 Was G31 HMC a core initially at equilibrium?

In Chapter 3 we concluded that cores that evolve from equilibrium configurations and those that evolve from non-equilibrium configurations probably have similar (observational) spatial intensity profiles, but in the case of having any difference it should emerge in the channels of lowest velocities. Cores evolving from equilibrium are expected to have closed V_z-surfaces, which unless they are incomplete, they keep producing asymmetric spatial intensity profiles. Cores that evolve from non-equilibrium conditions are expected to have open V_z-surfaces for the lowest velocities, which produce equal spatial intensity profiles for red- and blue-shifted emission. The observations of G31 HMC were not well centered at the systemic velocity, impeding a proper comparison between symmetric pairs of velocity channels. Since our goal was to search for the spectral imaging infall signature (which happens preferentially in channels of high velocities; see Section 3.5), in our discussion on G31 HMC in Section 4.4.1 we excluded those channels of lowest velocity (relative to the systemic velocity). In Figure 4.18 we present the comparison between the spatial intensity profiles of blue- and red-shifted emission of low velocity channels for the five studied transitions. We found that the asymmetry in the spatial intensity profile is maintained in the (2,2) and (3,3), but is not clear in the (4,4), (5,5) and (6,6) transitions, although the blue-shifted emission keeps being stronger.

The fact that there is an asymmetry in the spatial intensity profile for (2,2) and (3,3) transitions at the lowest velocities suggest that the V_z-surfaces are not intrinsically open nor incomplete, otherwise the asymmetry will not be present. Hence, the overdensity case of the rapid collapse model, which predicts intrinsically open surfaces at low velocities, seems to be ruled out (see Section 3.5). Note that we can not rule out the LPH model, which is also a non-equilibrium model, because it predicts closed V_z-surfaces in its polytropic generalization (if $\gamma < 2$) (see Chapter 3). Note that this result have to be taken with caution because the central velocity is not well determined and we are not properly comparing symmetric pairs of channels.

4.5 Conclusions

We obtained high angular resolution images of the ammonia (2,2), (3,3), (4,4), (5,5), and (6,6) inversion transitions in the hot molecular core G31 HMC. We found that all the observed transitions show the “spectral imaging infall signature” proposed by A91: (i) Given a pair of red/blue-shifted channels at symmetric velocities with respect to the systemic velocity of the cloud, in the blue-shifted channels the intensity as a function of projected distance to the core center is stronger and sharply increasing towards the center, while it shows a more flattened distribution in the red-shifted channels; (ii) The emission becomes more compact as the velocity increases with respect to the systemic velocity of the cloud. We also found that the “central blue spot” infall signature, introduced in Chapter 2, is present in all the observed ammonia transitions of G31 HMC. These signatures are robust infall signatures that have been observationally identified here for the first time. These signatures cannot be easily mimicked by other motions, and indicate that infall motions play a fundamental role in the gas kinematics of G31 HMC.

In addition to the signatures indicating the presence of predominant infall motions, our observations of G31 HMC provide additional, more specific information on the properties of the infalling envelope. There is a good quantitative agreement, both in the shape and range of values, between the spatial intensity profiles predicted by the SLS model for G31 HMC developed by Osorio et al. (2009) and those observed in the channel maps of the ammonia (2,2) to (6,6) inversion transitions. This is particularly remarkable, as only the SED and (4,4) transition spectra were used in fitting the model parameters.

G31 HMC shows a NE-SW velocity gradient that suggests the presence of a rotation component. We searched for the rotation signature introduced in Chapter 2 by comparing radial intensity profiles averaged separately over the NE and SW halves of the source for red- and blue-shifted channels. We found that the spatial intensity profile of the image in a given velocity channel (red- or blue-shifted) is stretched towards the side where rotation has the same sign (red- or blue-shifted, respectively), and it is shrunk on the opposite side. That is to say, the red-shifted velocity channels are stretched towards the NE and they are shrunk to the SW, while the opposite is true for the blue-shifted channels. So, we conclude that the rotation signature is present in G31 HMC. Unfortunately, only a spherically symmetric model for the physical structure of G31 HMC has been constructed so far (Osorio et al. 2009); therefore, we can only evaluate the effects of rotation in a qualitative way. We plan to extend our study by carrying out an integral model of the source, where the observational data are fitted to an infalling rotating envelope, similarly to what we have already done for the W3(H_2O) HMC (see next chapter).

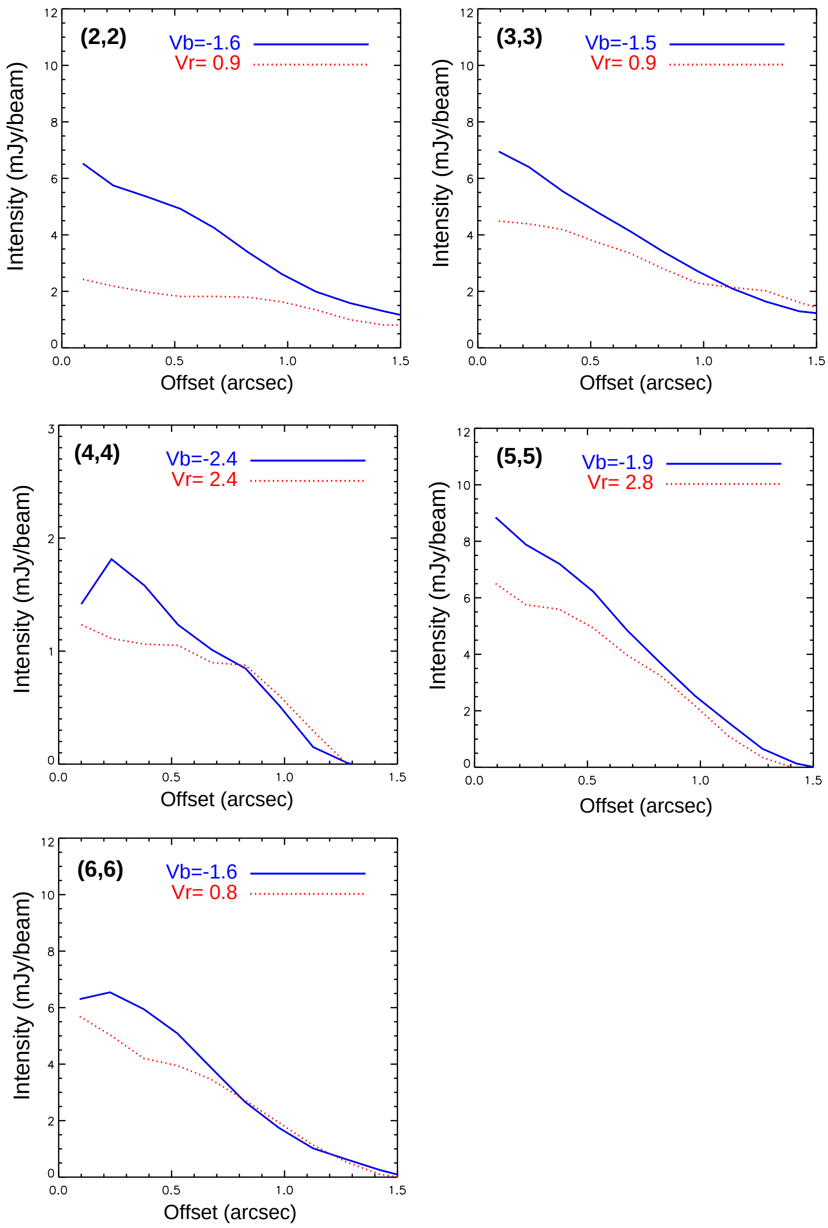

Figure 4.18: Circularly-averaged observed intensity as a function of angular distance to the center of G31.41 HMC, for the pairs of blue-shifted (solid blue line) and red-shifted (dotted red line) channel maps with lowest velocity. Results for the ammonia (2,2), (3,3), (4,4), (5,5) and (6,6) transitions are shown. The sizes of the synthesized beams are given in Table 4.1. Labels indicate the channel velocity (in km s^{-1}) relative to the assumed systemic velocity of the cloud ($V_{\rm LSR}$ = 97.4 km s^{-1}).

There is a long-standing debate regarding the nature (rotation vs. outflow) of the NE-SW velocity gradient observed in G31 HMC. As we found signs of the rotation signature in the spatial intensity profiles, we further investigated this issue in order to determine more accurately the direction of the rotation axis by using all the signatures introduced in Chapter 2, together with a re-analysis of the CO outflow. Our results suggest that the projection on the plane of the sky of the equatorial plane lies roughly in the N-S direction and that the axis of the CO bipolar outflow lies roughly in the E-W direction. Then, we conclude that the controversial NE-SW large-scale velocity gradient observed in G31 HMC could be produced by the combination of rotation and outflow velocity gradients in this infalling core.

We want to stress that G31 HMC is an exceptional source, with very strong molecular ammonia emission, making it possible to carry out high-angular resolution observations with a signal-to-noise ratio high enough to identify for the very first time the spectral imaging infall signatures in this source. The advent of large interferometers with improved sensitivity in the spectral line observing mode, such as ALMA, or the forthcoming facilities, such as the SKA or the ngVLA, should make it possible to detect these signatures in weaker sources and to extend this kind of studies to a large sample of sources in the near future.

Chapter 5

The hot molecular core W3(H_2O)

5.1 Introduction

In Chapter 2 we demonstrated that, when infall motions dominate the kinematics of a region, the "spectral imaging infall signatures" (3D) and their corresponding mapping signatures (2D) are expected to emerge for line emission of high optical depth. We also provided observational evidence of such signatures in the HMC near G31.41+0.31, where infall dominates the dynamics of the core gas, although both rotation and outflow motions are present. Rotation is thought to become increasingly important as collapse proceeds, because of the conservation of the angular momentum, and it must strongly influence the later stages of collapse. The main effect of rotation is to make the infalling mass to land on a centrifugally supported disk around the protostar, instead of landing directly on the stellar surface. In this chapter we perform a detailed study of the HMC W3(H_2O) in the proximities of the HII region W3(OH), in which we found that rotation motions are at least as important as infall motions.

W3(OH) is a well-studied UCHII region located at a distance of 2.04 kpc (Hachisuka et al. 2006). It is associated with a far-infrared source with a total luminosity of 10^5 $L_\odot$ (Campbell et al. 1989; Harper 1974), which corresponds to the luminosity of a main sequence star of spectral class O7 (Dreher & Welch 1981). W3(H_2O) is a HMC located $6''$ to the east of the UCHII region W3(OH). It was first detected and identified as a HMC by Turner & Welch (1984) with HCN observations. Based on the high brightness temperature and large width of the lines, as well as on the high extinction toward the center of the core, these authors suggested the presence of a massive young stellar object still in the process of formation within the core. The HMC is associated with water maser emission whose proper motions trace a bipolar outflow in the E-W direction (Alcolea et al. 1993). Reid et al. (1995) reported the presence of two cm radio continuum sources, separated by $\sim 1.2''$, with the easternmost source located towards the geometrical center of expansion of the masers. The emission of this radio source is non-thermal (spectral index $\simeq -0.6$) and shows an elongated morphology in the E-W direction, with a size that decreases with frequency (Size $\propto \nu^{-1.0}$), and was interpreted as a synchrotron bipolar jet. The western radio continuum source shows a thermal spectral index of $+0.9$. The two sources are better seen in the high sensitivity map at 3.6 cm obtained by Wilner et al. (1999) (Figure

5.1a), which shows the outstanding elongated morphology of the centimeter jet. These authors interpreted the western radio source as excited by a different YSO, and detected a third centimeter source $0''.5$ north-east of it.

Wyrowski et al. (1999) detected strong dust emission at 1.3 mm towards W3(H_2O) and found three peaks of emission, named A, B, and C from east to west (Figure 5.1a). A and C were associated with the easternmost and westernmost centimeter sources in Wilner et al. (1999) respectively, and are coincident with the two temperature peaks inferred from HNCO observations (Wyrowski et al. 1999). Source B coincides with a local maximum of molecular hydrogen column density at $\sim 0''.5$ east side of the westernmost cm source. However, the presence of source B has not been confirmed in subsequent mm/submm observations. Subarcsecond resolution observations at 0.89 mm (Zapata et al. 2011), 1.4 mm, and 2.88 mm (Chen et al. 2006) show two sources whose positions fall close to sources A and C. Zapata et al. (2011) identify their submm sources with the two 3.6 cm sources of Wilner et al. (1999). However, we note that there is a significant difference in position, that cannot be attributed to uncertainties in the absolute astrometry, since the separation between the submm positions ($0''.9$) is significantly smaller than that of the cm sources ($1''.2$). So we consider that additional information is required for an adequate identification between submm and cm sources.

A CO map (Zapata et al. 2011) reveals the presence of several collimated lobes of high velocity molecular gas that emerge from W3(H_2O) (Figure 5.1). Zapata et al. (2011) interpreted those lobes as two independent outflows with position angles (PA) of $-140°$ and $15°$ originating from sources A and C, respectively.

A velocity gradient along the east-west direction across the whole W3(H_2O) core was found (Wink et al. 1994, Wyrowski et al. 1997, Sutton et al. 2004). The most likely interpretation is that this gradient is due to the different velocities of the molecular gas associated with sources A and C, rather than tracing a single rotating structure or being a consequence of the interaction of the jet with the molecular gas. However, no previous molecular line observation has had enough angular resolution to separate the emission of sources A and C, let alone to resolve the internal substructure of the hot cores individually.

Here we present VLA observations at subarcsecond angular resolution of the ammonia (4,4) inversion transition towards W3(H_2O). Using these ammonia observations, together with the results of subarcsecond millimeter and submillimeter observations reported in the literature, we are able to resolve the two dust condensations in W3(H_2O) and model them as two independent cores. To do so, we developed a radiative transfer code that is presented in Appendix A.

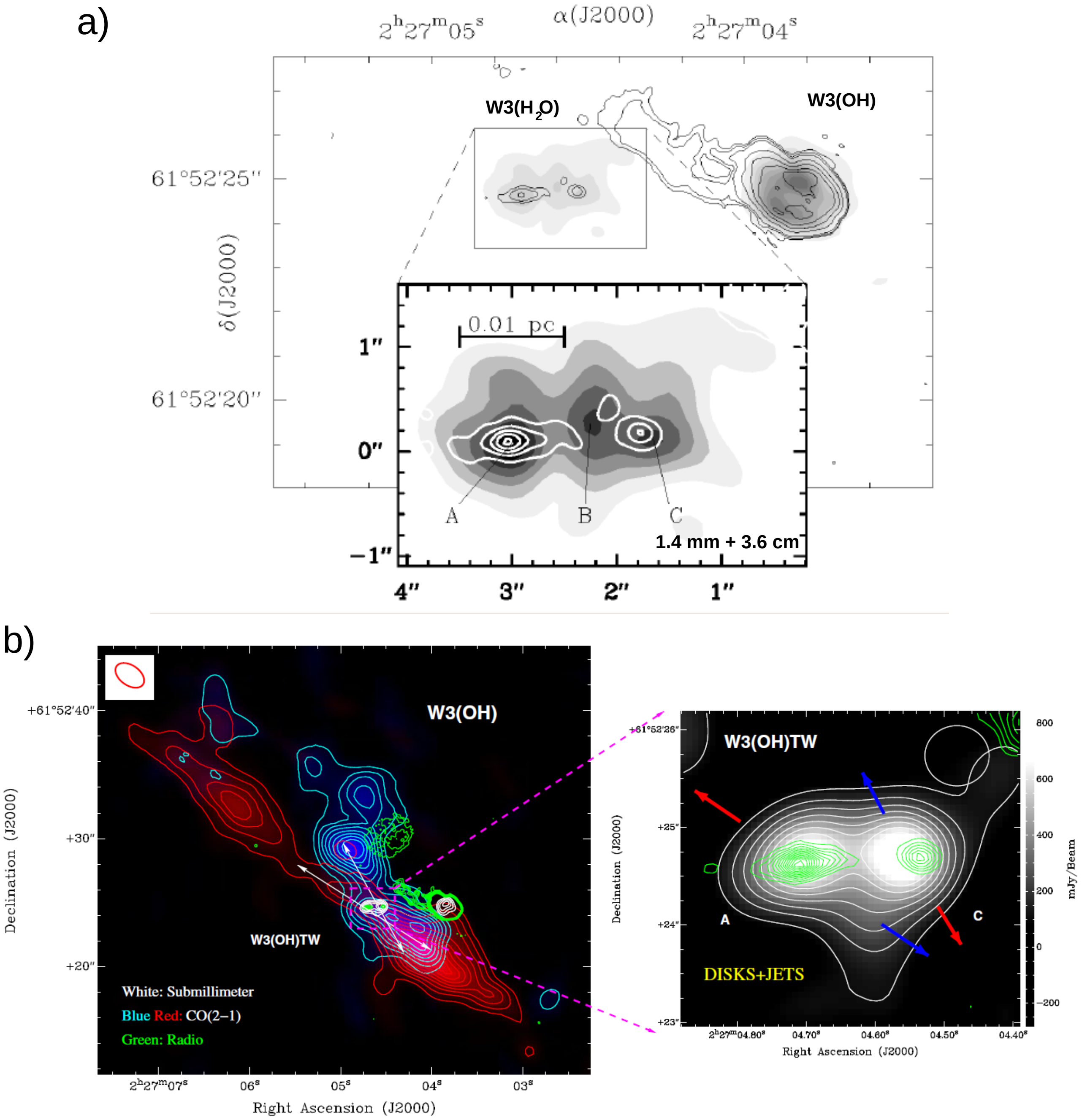

Figure 5.1: Maps of the W3(OH) region with a close-up of the W3(H_2O) HMC. *(a)* Map of continuum emission at 220 GHz (1.4 mm), obtained with the Plateau de Bure interferometer (Wyrowski et al. 1999, grayscale) and 8.4 GHz (3.6 cm) map obtained with the VLA (Wilner et al. 1999, contours). *(b)* Map of continuum emission at 0.89 mm (right; grayscale and white contours) and high-velocity CO(2-1) outflows (left; blue and red contours), obtained with the SMA. In both panels green contours represent the 8.4 GHz map of Wilner et al. (1999).

5.2 Observations

We carried out observations of the ammonia (4,4) inversion transition (rest frequency= 24.1394163 GHz) on 2001 May 24 and 25, with the VLA of the NRAO[1] in its B-configuration (VLA Project Code: AO158). The phase center was set to RA(J2000) = $02^h27^m04\overset{s}{.}7$; Dec(J2000) = $61°52'2''$. We used a total bandwidth of 6.25 MHz (~80 km s^{-1}) sampled with 63 channels of 97.7 kHz width each (~1.2 km s^{-1}), plus a continuum channel that contains the central 75% of the total bandwidth for calibration purposes. To make sure that at least the main line and one of the satellite lines of the ammonia inversion transition fall within the observational bandwidth we centered the observation at a frequency in between the main line and the inner red-shifted satellite line. The blue-shifted satellite lines lie outside our bandpass. Phase, flux and band-pass calibrators were J0228+673, J0137+331 (3C48), and J0319+415 respectively. Pointing corrections were derived from X-band observations for all the calibrators and applied on-line.

Data editing and calibration were carried out using the Astronomical Image Processing System (AIPS) package of NRAO following the standard high-frequency VLA recommendations. We used a robust parameter of 5 (equivalent to natural weighting, Briggs 1995) in task IMAGR of AIPS. We note that, at the time of our observations, 11 antennas were equipped with older receivers, while 16 had upgraded ones (which resulted in an improvement of a factor of 10 in their sensitivity). After a careful evaluation, we decided to keep the data from the antennas with old receivers, since their inclusion slightly improved the rms (from 1.1 mJy $beam^{-1}$ to 1.0 mJy $beam^{-1}$), while enlarging the beam area by 14% in maps with natural weight. This resulted in a better sensitivity to extended emission. The final synthesized beam was $0.29'' \times 0.28''$ and an rms of 1.0 mJy $beam^{-1}$ per channel was obtained.

Our VLA maps include both the W3(OH) UCHII region and the W3(H_2O) HMC. In the following we will describe the main characteristic of each of them.

5.3 Observational results on W3(OH)

The NH_3(4,4) inversion transition towards W3(OH) appears in absorption, both for the main line and the satellite lines (Figure 5.2). This is the first detection of the NH_3(4,4) transition towards the W3(OH) UCHII region. The ammonia (1,1) and (2,2) inversion transitions had also been seen in absorption showing a similar morphology (Reid et al. 1987; see also Wilson et al. 1993). The spatial distribution of the NH_3(4,4) absorption presents a cometary morphology, that overlaps the westernmost side of the UCHII region (Figure 5.3). This morphology coincides with the one shown by other molecules in W3(OH) such as CH_3OH, $HCOOCH_3$, H_2CO (Wyrowski et al. 1999), OH (Baudry & Menten 1995), and HNC (Kim et al. 2006). A group of OH masers (Bloemhof et al. 1992; Baudry & Diamond 1998; Wright et al. 2004;

---

[1] The National Radio Astronomy Observatory (NRAO) is a facility of the National Science Foundation operated under cooperative agreement by Associated Universities, Inc.

Fish et al. 2006; Fish & Sjouwerman 2007) and methanol masers (Menten et al. 1988; Etoka et al. 2005; Moscadelli et al. 2010; Matsumoto et al. 2011) also shows a similar N-S distribution.

The observed velocity gradient suggests that the masers are tracing a rotating structure along the N-S direction (Wright et al. 2004, Moscadelli et al. 2010). The proper motions of the OH masers indicate expansion (Wright et al. 2004; Fish & Sjouwerman 2007; Matsumoto et al. 2011), from which Wright et al. (2004) speculate that we are witnessing the destruction of the rotating structure by the expanding UCHII. Fish & Sjouwerman (2007) show that the OH masers fit well to an elliptical distribution, and speculate that they might be delineating the inner edge of a rotating torus. These authors believe that the masers may be tracing the interaction of an expanding shock with a rotating molecular torus that is identified with the structure seen in the ammonia absorption and in the above mentioned molecules. Matsumoto et al. (2011), who study the proper motions of 6.7 GHz methanol masers, found expansion motions similar to those of 1.6 GHz OH maser observations by Bloemhof et al. (1992) and Wright et al. (2004), and favor a rotating and expanding torus structure surrounding the UCHII region. The inclination of the ellipse traced by the OH masers and the ammonia distribution indicate that the western side of the HII region lies behind the molecular torus. The molecular gas seen in absorption corresponds to the half of the rotating structure in front of the UCHII. However, we do not detect a clear velocity gradient within the ammonia structure. The back side of the rotating structure, behind the ionized region, is not observed (Figure 5.4).

Recently, Dzib et al. (2013) detected a compact variable radio source projected near the center of W3(OH), suggesting that it traces partially optically free-free emission that could arise, among other scenarios, in a static ionized atmosphere around a fossil photoevaporated disk.

5.4 Observational results on W3(H_2O)

We detect emission of the ammonia (4,4) inversion transition towards W3(H_2O) from the main and satellite lines in the LSR velocity range from ~ -60 km s^{-1} to -40 km s^{-1} (Figures 5.5 and 5.6). The large line widths make both the inner and outer satellite lines blend together. Therefore, we cannot treat these satellite lines separately and, in the following, we will collectively use the term "satellite lines" for these blended lines.

In order to emphasize the large-scale behavior of the ammonia emission we have tapered the visibilities to obtain maps with slightly lower angular resolution (beam size = $0\farcs46 \times 0\farcs43$, PA = $-44.03°$). Figures 5.7, 5.8 and 5.9 show the tapered integrated intensity map (zeroth-order moment), intensity-weighted mean velocity map (first-order moment) and velocity dispersion map (second-order moment) of the main line of the whole W3(H_2O) region. Figure 5.7 reveals that the bulk of the emission arises from an elongated region of $2\farcs0 \times 0\farcs7$ in size, with two differentiated local maxima separated $\sim 1''$. The emission is $\sim 23\%$ stronger in the western

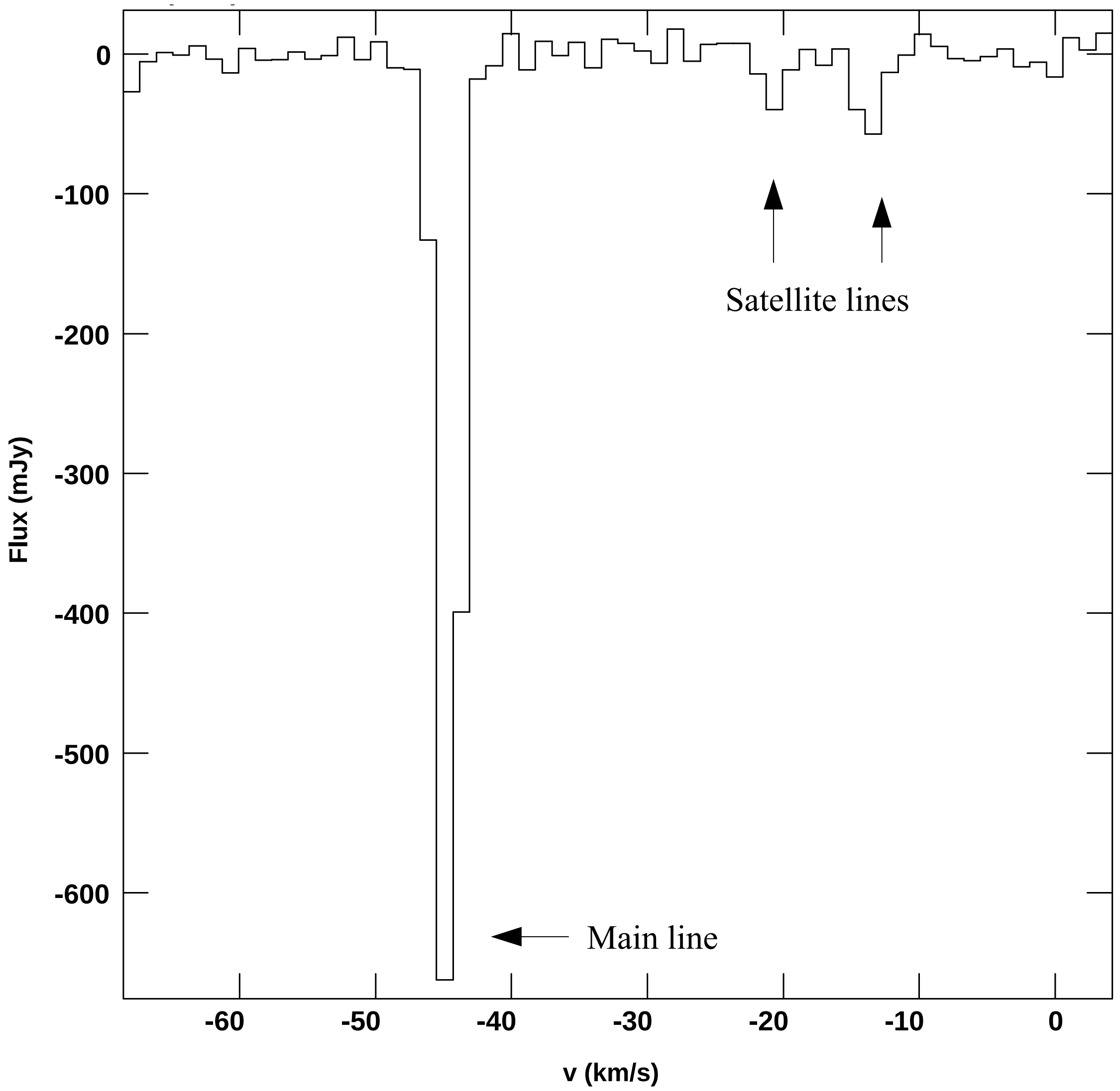

Figure 5.2: Spectrum of the NH_3 transition obtained with the VLA towards the UCHII region W3(OH). The main and satellite lines at lower frequencies are seen in absorption.

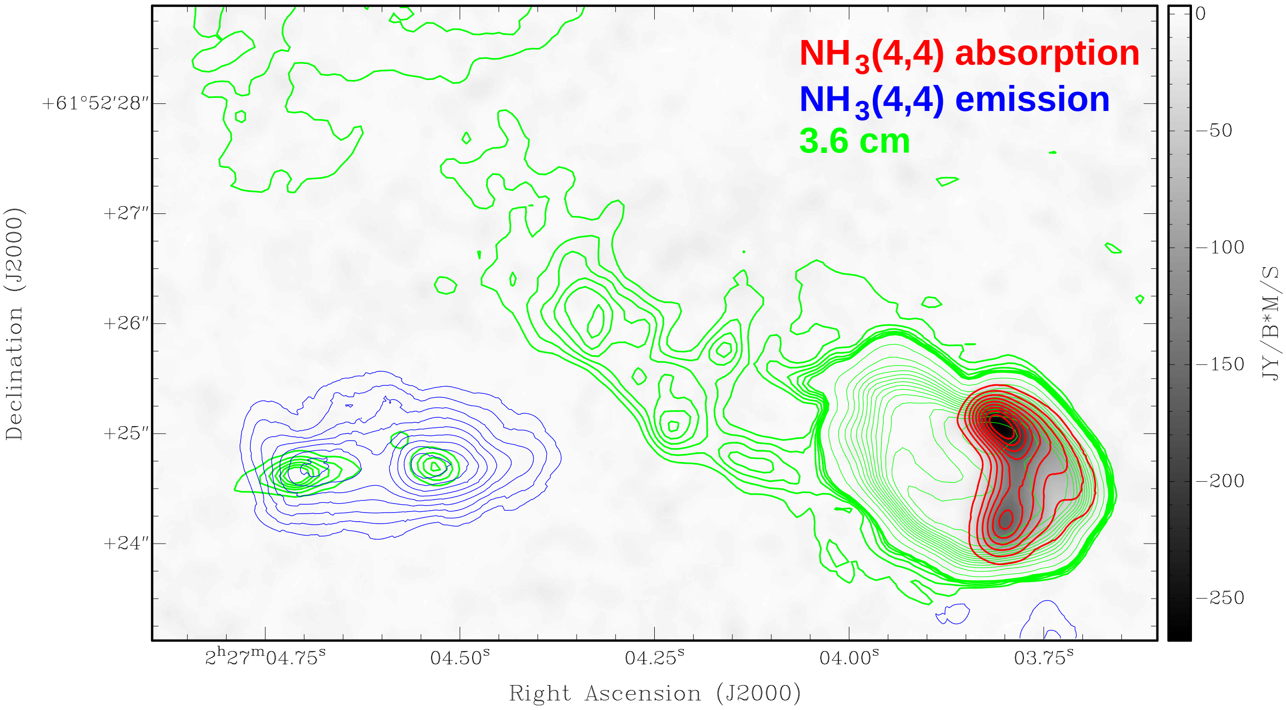

Figure 5.3: Integrated intensity VLA map of the NH_3(4,4) main line absorption towards W3(OH) (grayscale and red contours). The red lowest contour is -26.7 mJy beam^{-1} km s^{-1}, and the increment step is of -26.7 mJy beam^{-1} km s^{-1}. Green contours represent the 3.6 cm map of Wilner et al. (1999). Contours go from 0.182 mJy beam^{-1} to 0.58 mJy beam^{-1} in steps of 0.078 mJy beam^{-1}, and from 1.55 mJy beam^{-1} to 38.8 mJy beam^{-1}in steps of 2.7 mJy beam^{-1}. Blue contours represents the NH_3(4,4) emission towards W3(H_2O), the lowest contour is 25.5 Jy beam^{-1}, and the increment step is of 8.3 Jy beam^{-1}.

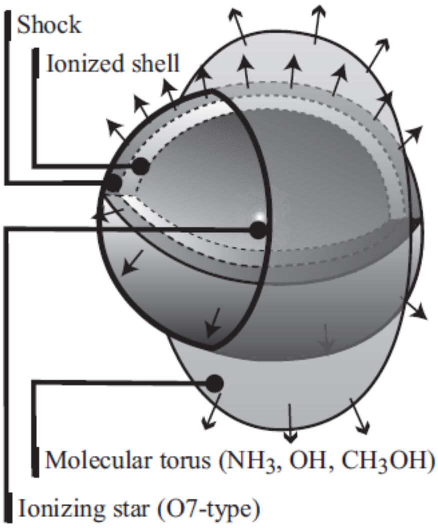

Figure 5.4: Model of the W3(OH) UCHII ergion proposed by Matsumoto et al. (2011). The UCHII region is expanding and has a shell structure as described in Dreher & Welch (1981). Maser emission and NH_3 absorption come from the molecular torus out of the UCHII region. Only the front side of the torus can be observed because the UCHII region is optically thick at those wavelengths. The molecular torus expands due to the expansion of the UCHII region.

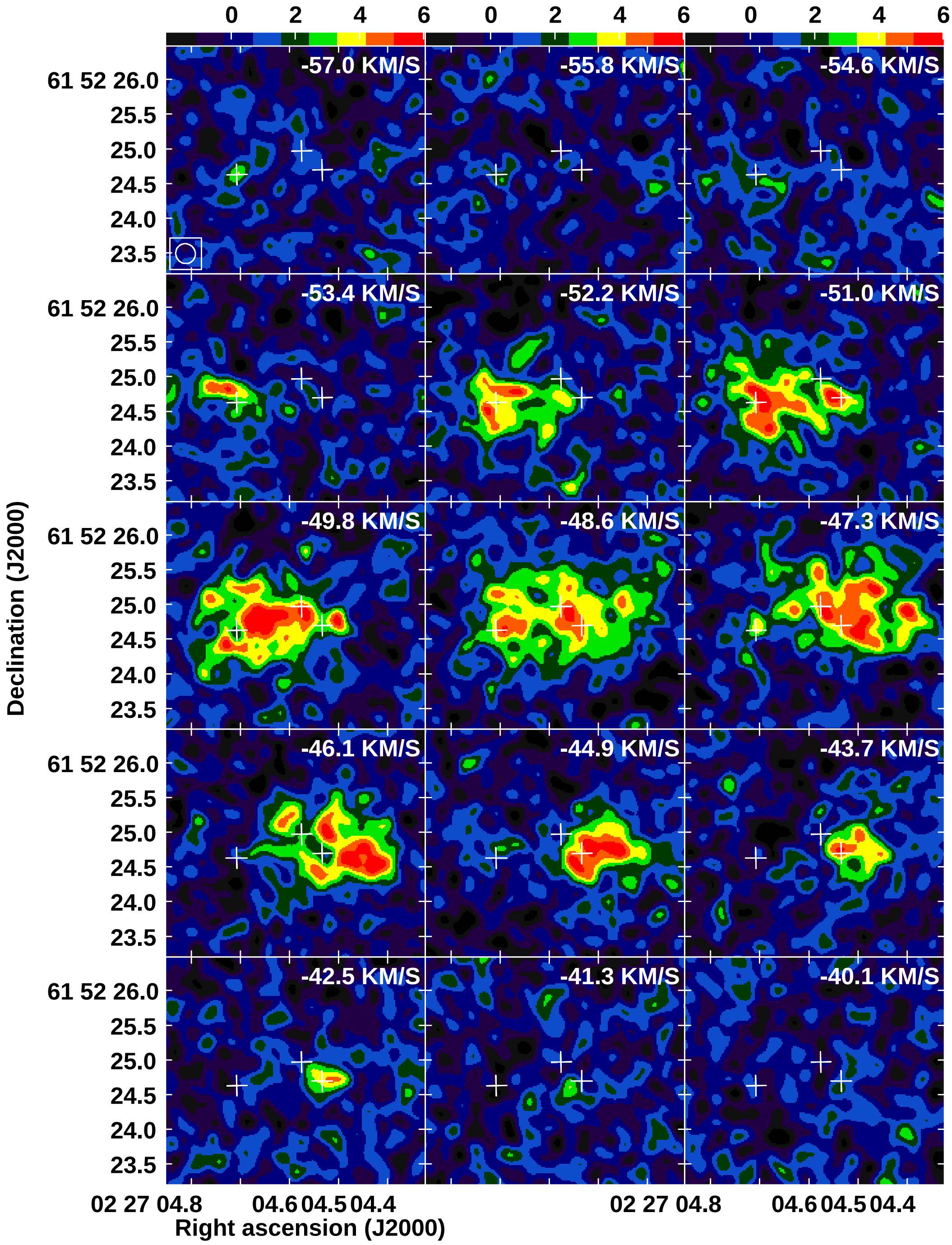

Figure 5.5: Channel maps of the NH_3(4,4) main line observed with the VLA. The velocity of each channel is indicated at the upper part of each map, the synthesized beam is shown at the bottom left corner of the first map. The three crosses indicate the positions of the centimeter sources detected by Wilner et al. (1999). The color bar indicates the intensity in mJy beam^{-1}.

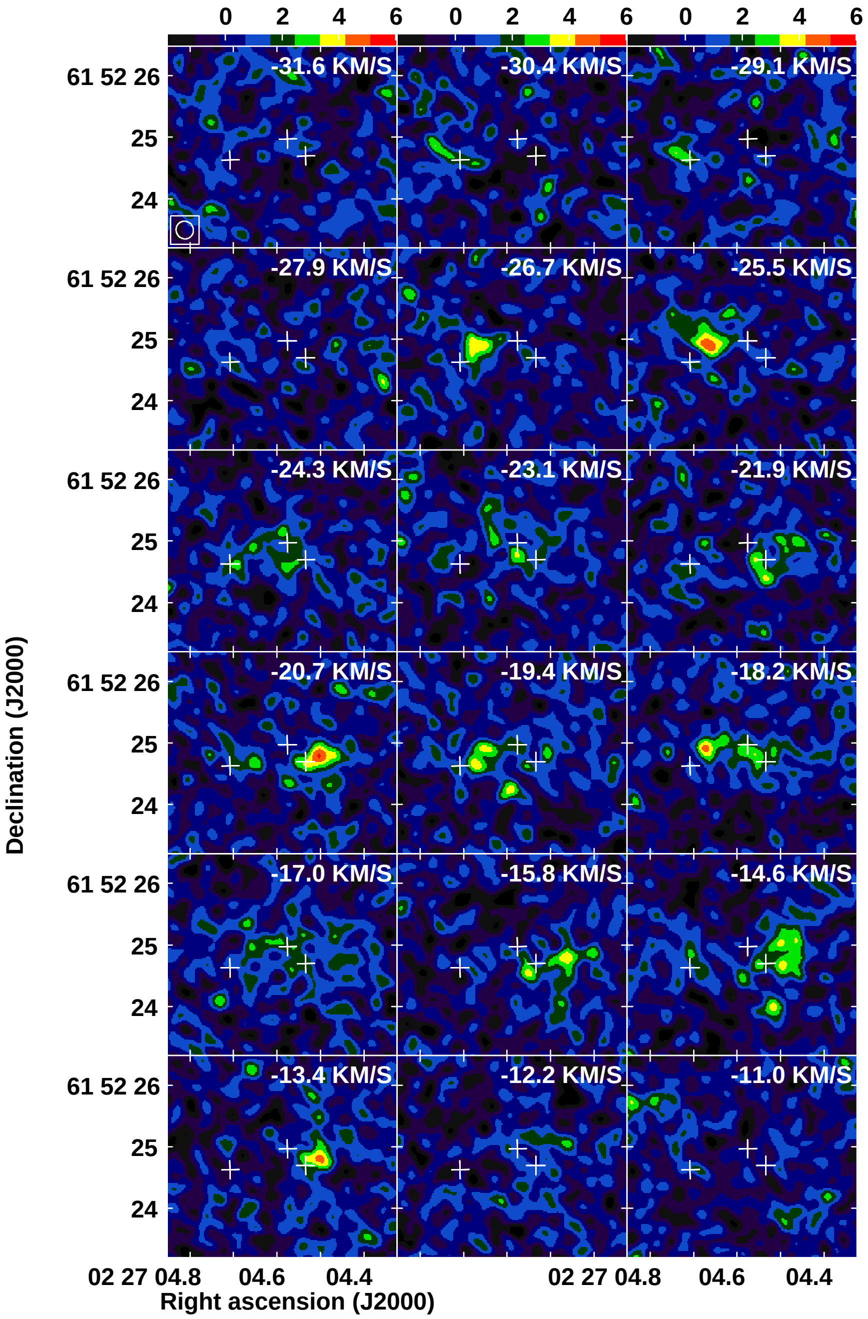

Figure 5.6: Channel maps of the NH_3(4,4) satellite lines observed with the VLA. The velocity of each channel has been calculated taking as a reference the rest frequency of the main line (Table A.2). The actual LSR velocity of the satellite emission is shifted by -24.21 km s^{-1} and -30.43 km s^{-1} for the inner and outer satellites, respectively (Table A.2). The LSR velocity range of emission is $\sim$ -43 to -55 km s^{-1}. The synthesized beam is in the lower left corner of the first map. The three crosses indicate the positions of the centimeter sources detected by Wilner et al. (1999). The color bar indicates the intensity in mJy beam^{-1}.

maximum than in the eastern one. Moreover, the western maximum is red-shifted ~ 5 km s^{-1} with respect to the other one (Figure 5.8), and its velocity dispersion is larger by 1 km s^{-1} (Figure 5.9). This supports that these maxima correspond to two independent cores, as suggested by Sutton et al. (2004) and Chen et al. (2006). These two cores coincide roughly in position with the two dust condensations seen by Zapata et al. (2011) (whose peak positions are marked as crosses in Figures 5.7, 5.8 and 5.9), Chen et al. (2006) and Sutton et al. (2004). We note that the submm peak positions of Zapata et al. (2011) are shifted with respect to the cm sources detected by Wilner et al. (1999). These shifts can not be attributed to uncertainties in the absolute positions, such as a misalignment of the maps or to phase errors in the calibration because the relative separation between the easternmost and westernmost sources is smaller in the submm map. We also note that the local maxima of ammonia emission coincide better with the submm peak positions than with the centimeter sources. Hereafter, we will denote the western ammonia core as W3(H_2O)-W, and the eastern one as W3(H_2O)-E. The millimeter source A (Wyrowski et al. 1999) and the synchrotron jet are observed towards W3(H_2O)-E, and sources B and C (Wyrowski et al. 1999) are observed towards W3(H_2O)-W.

Figures 5.10 and 5.11 show the natural weighted, untapered integrated intensity maps of the NH_3(4,4) main and satellite lines. These maps achieve a higher angular resolution, $0\farcs29 \times 0\farcs28$, which is good enough, not only to separate the two cores, but also to study their internal substructure, which is described in what follows.

5.4.1 The W3(H_2O)-W core

As can be seen in Figure 5.10, the integrated emission of the NH_3(4,4) main line towards W3(H_2O)-W shows two peaks separated $\sim 0\farcs45$. The eastern ammonia peak in W3(H_2O)-W coincides with the position of one of the submillimeter sources reported by Zapata et al. (2011). The westernmost centimeter source of Wilner et al. (1999) falls just in between the two ammonia peaks. We notice that the third centimeter source of Wilner et al. (1999) is located to the NE edge of the ammonia core.

The integrated emission of the satellite lines (Figure 5.11) also presents a double-peak morphology similar to the one seen in the main line. However, the orientation of this double-peak structure is somewhat different in the two maps. It is orientated nearly E-W (PA=85°) for the main line, and at PA=120° for the satellite lines. In Figure 5.12 we show a comparison of the main and satellite line integrated intensity maps. We labeled the eastern peak of the satellite lines as W1, and the western one as W2 .

Figure 5.13 shows the intensity-weighted mean velocity map (first-order moment) of W3(H_2O)-W obtained from the satellite line emission. We prefer to use the satellite lines instead of the main line because they are optically thinner ($\tau_{\rm sat} \simeq \tau_{\rm main}/60$ for the (4,4) transition). Thus, the satellite lines penetrate deeper inside the core and would trace more reliably the physical conditions and the velocity gradients. We note that the inner and outer satellite lines are blended

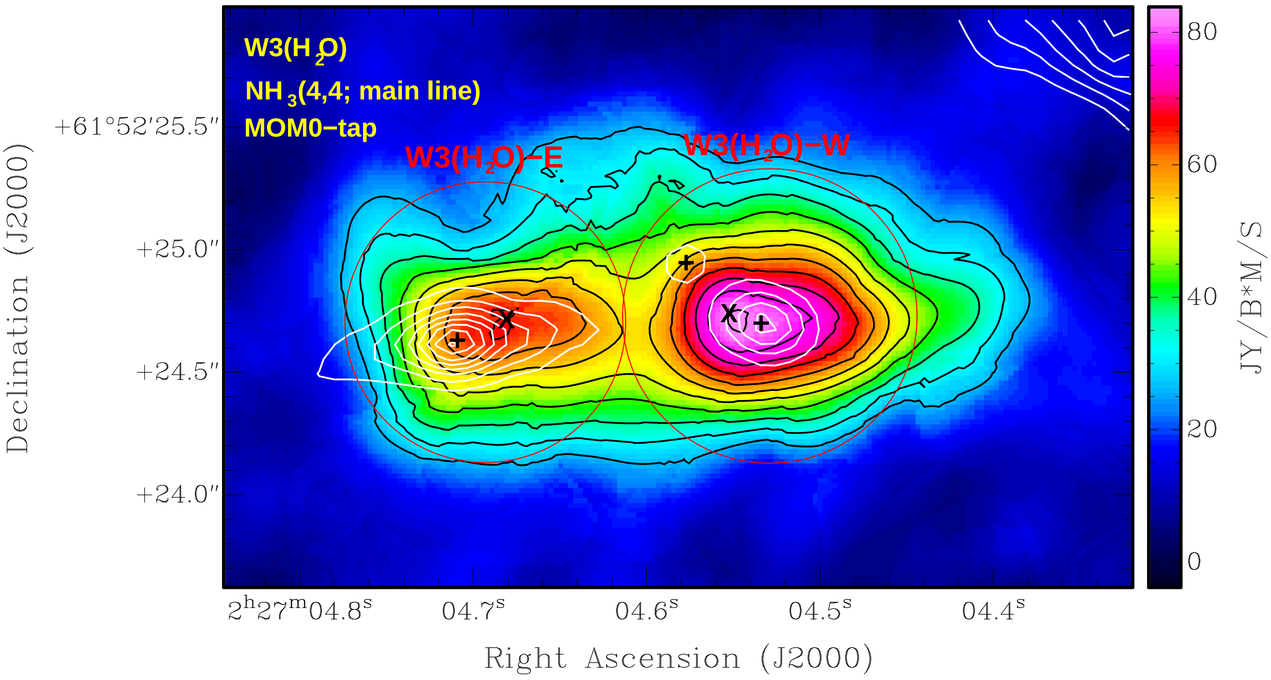

Figure 5.7: Integrated intensity map (zeroth-order moment) of the NH_3(4,4) main line, over the velocity interval -59.5 to -38.9 km s^{-1} (colors and black contours). A tapering of 400 kλ has been applied, resulting in a synthesized beam of the images of $0\farcs46 \times 0\farcs43$, PA= $-44°$. The lowest contour is 29 mJy $beam^{-1}$ km s^{-1} and the increment step is 5.37 mJy $beam^{-1}$ km s^{-1}. The 3.6 cm emission map of Wilner et al. (1999) is shown in white contours with the peak positions of the three sources indicated by + symbols. The lowest 3.6 cm contour is 0.18 mJy $beam^{-1}$ and the increment step is 0.08 mJy $beam^{-1}$. The × symbols correspond to the local maxima of the 890 μm emission (Zapata et al. 2011).

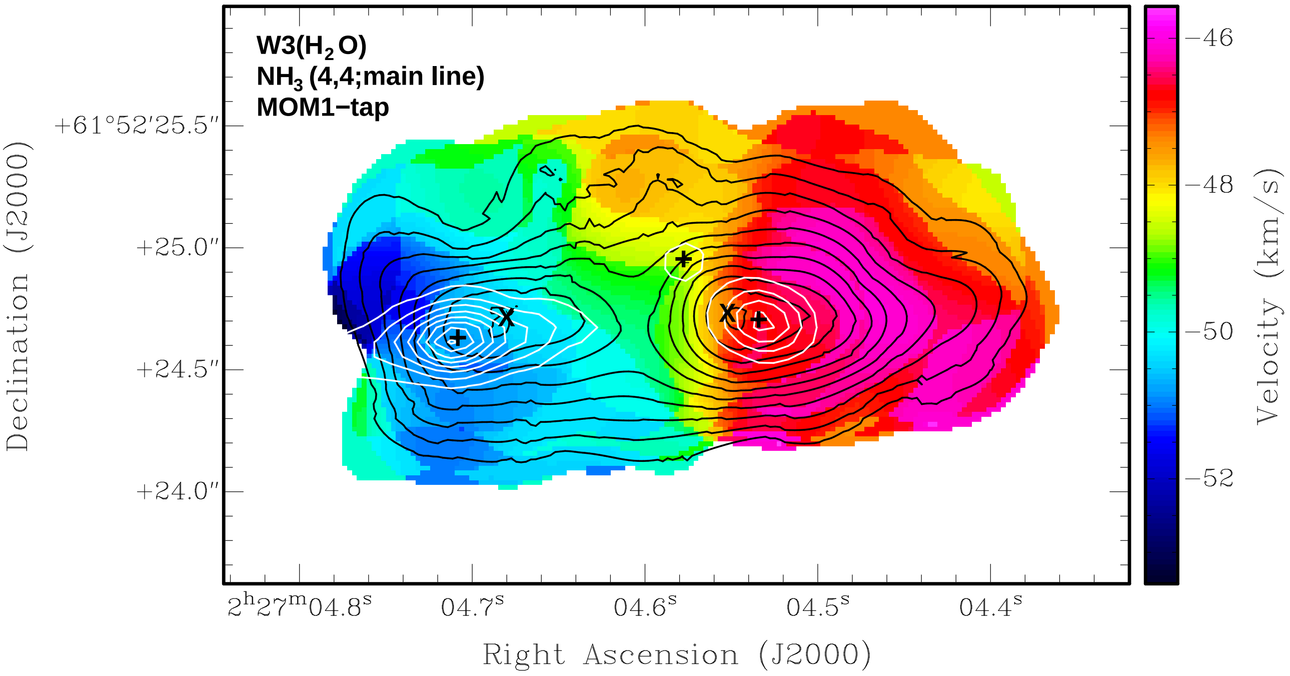

Figure 5.8: Intensity-weighted mean velocity map (first-order moment) of the NH_3(4,4) main line (colors). A tapering of 400 kλ has been applied, resulting in a synthesized beam of the images of 0.″46 × 0.″43 and PA= −44.0°. The integrated intensity of the NH_3(4,4) main line (Figure 5.7) and the 3.6 cm emission by Wilner et al. (1999) are shown as black and white contours, respectively. Contour levels and symbols are the same as in Figure 5.7.

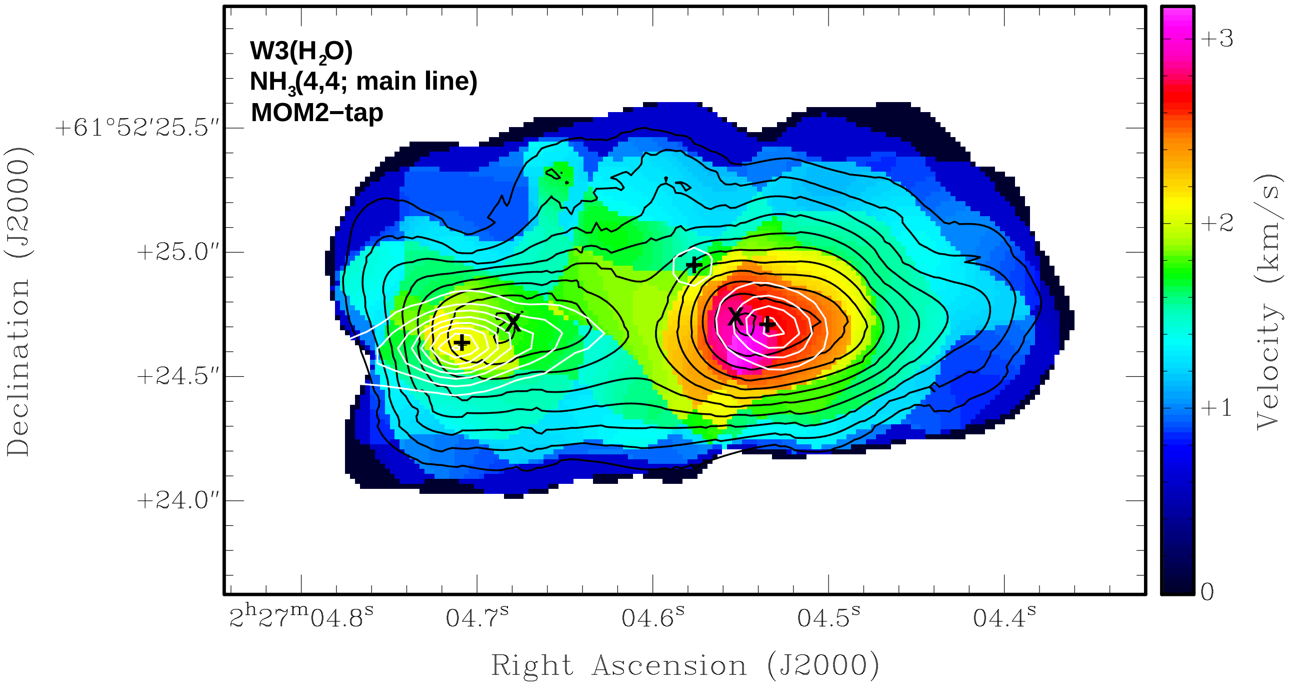

Figure 5.9: Velocity dispersion map (second-order moment) of the NH_3(4,4) main line (colors). A tapering of 400 kλ has been applied, resulting in a synthesized beam of the images of $0\farcs46 \times 0\farcs43$ and PA= $-44.0°$. The integrated intensity of the NH_3(4,4) main line (Figure 5.7) and the 3.6 cm emission by Wilner et al. (1999) are shown as black and white contours, respectively. Contour levels and symbols are the same as in Figure 5.7

.

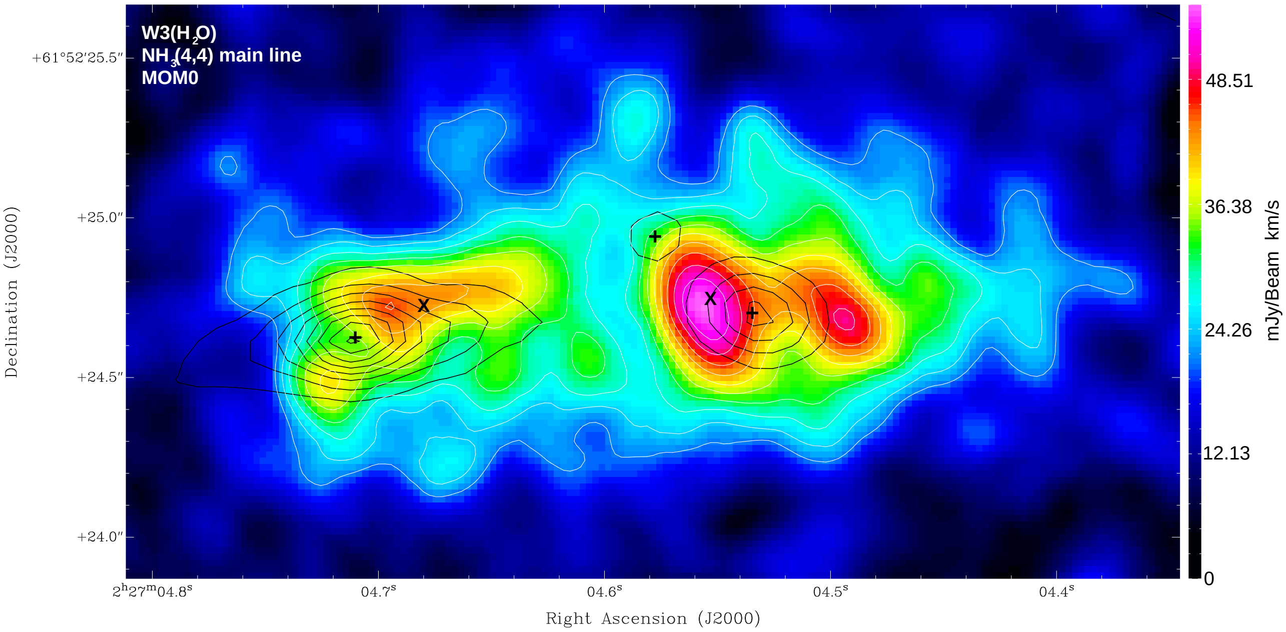

Figure 5.10: Integrated intensity map of the NH_3(4,4) main line, over the velocity range of -59.5 to -38.9 km s^{-1} (colors and white contours). The synthesized beam is $0\farcs29 \times 0\farcs28$, PA= $-44°$. The lowest contour is 19.5 mJy $beam^{-1}$ km s^{-1}, and the increment step is 3.6 mJy $beam^{-1}$ km s^{-1}. The 3.6 cm emission map of Wilner et al. (1999) is shown in black contours. The 3.6 cm contours and symbols are the same as in Figure 5.7.

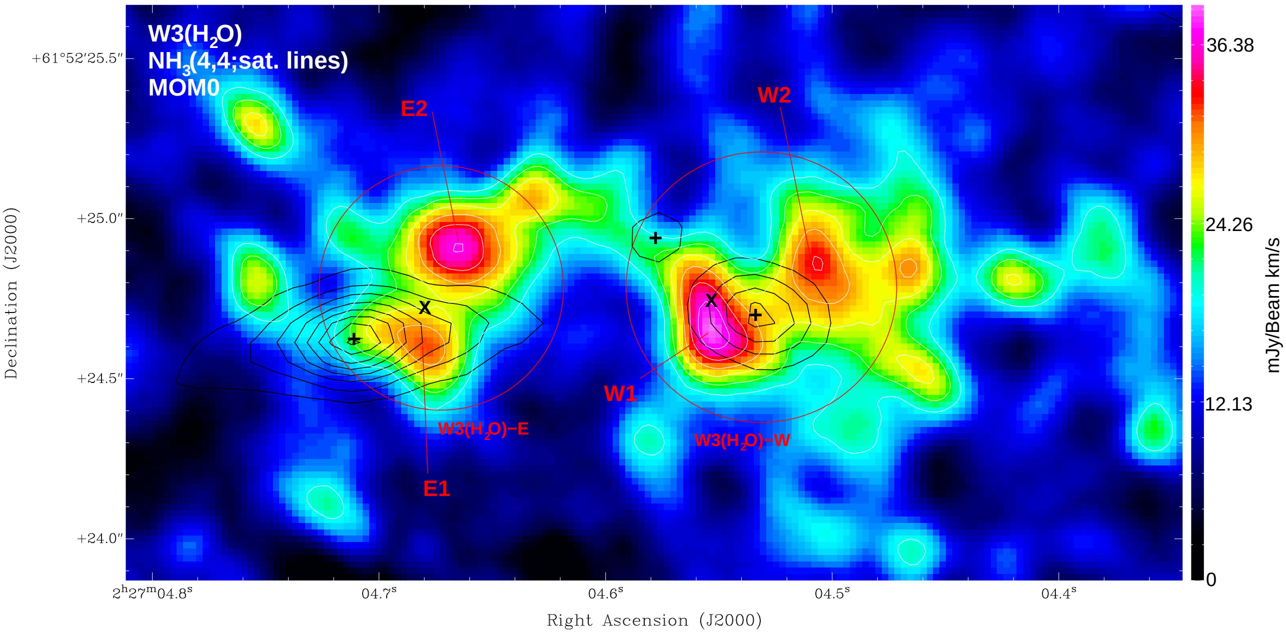

Figure 5.11: Integrated intensity map of the low frequency pair of NH_3(4,4) satellite lines integrated over the velocity range -59.5 to -38.9 km s^{-1} (colors and white contours). The beam and contour levels are the same as in Figure 5.10. The 3.6 cm emission map of Wilner et al. (1999) is shown in black contours. The 3.6 cm contours and symbols are the same as in Figure 5.7.

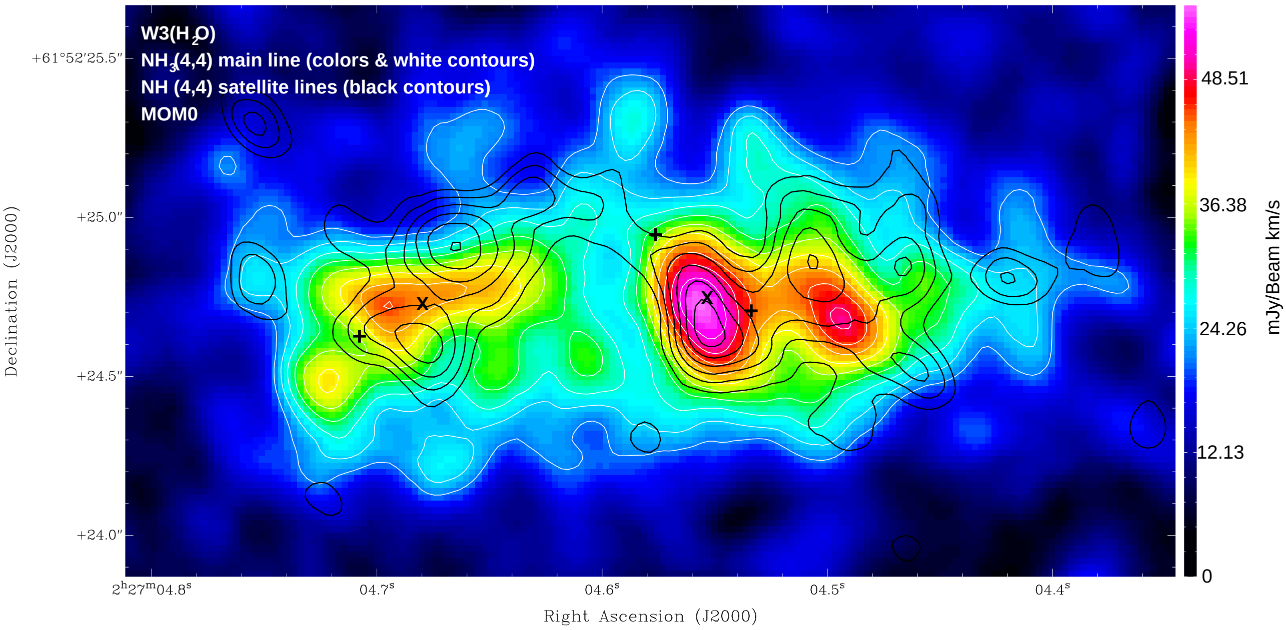

Figure 5.12: Comparison of the NH_3(4,4) main line (Figure 5.10; colors and white contours) and satellite lines (Figure 5.11; here in black contours) integrated intensity maps. Symbols are the same as in Figure 5.7.

together in W3(H_2O), which may complicate the interpretation of the first-order moment if the emission from one of them is absorbed by the other. However, this is not the case, since both satellite lines are optically thin throughout the region, and the first-order moment of the combined emission will reliably trace the velocity gradients. The first-order moment shows a velocity difference of 2.8 km s^{-1} over the 800 AU in projected distance between the two peaks of emission W1 and W2, with the former being blue-shifted with respect to the latter (Figure 5.13). Beyond the difference in velocity between the two peaks of emission W1 and W2, there are signs of velocity gradients at smaller scales, suggesting a complex velocity field within the core, probably a combination of infall and rotation motions.

5.4.2 The W3(H_2O)-E core

As can be seen in Figure 5.10, the integrated emission of the NH_3(4,4) main line in W3(H_2O)-E shows an elongated morphology that extends over approximately $0''\!.6$. Its orientation is at PA $\sim +81°$. Such elongated structure crosses over the submillimeter peak position, while the centimeter emission peak associated with the jet falls at the edge of the elongated structure.

On the other hand, the integrated emission of the satellite lines towards W3(H_2O)-E (Figure 5.11) presents a double-peaked morphology, similar to the one found in W3(H_2O)-W. The separation between the two peaks is $\simeq 0''\!.35$ (700 AU in projected distance). The double-peaked

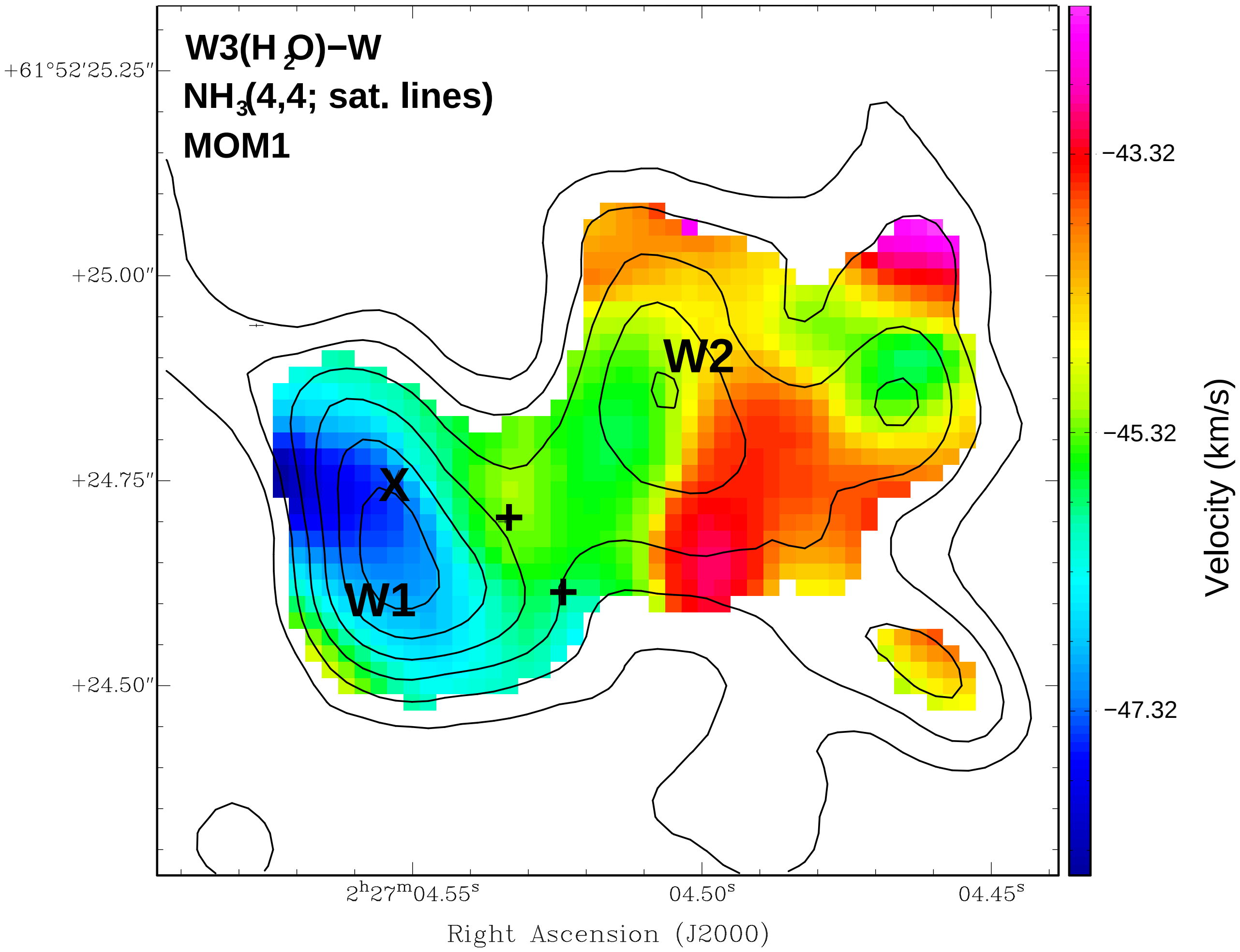

Figure 5.13: Intensity-weighted mean velocity map (colors) overlapped with the integrated emission map of the NH_3(4,4) satellite lines (contours) towards W3(H_2O)-W. The beam and the contour levels are the same as in Figure 5.11. Symbols have the same meaning as in Figure 5.7.

structure is oriented at PA= 210°. The submillimeter peak position (Zapata et al. 2011) falls right in between of the two peaks, while very scarce satellite line emission arises from the LOS towards the jet center. In Figure 5.12 there is a comparison of the ammonia main and satellite line integrated intensity maps. We labeled the two peaks of emission as E1 (southern) and E2 (northern). Note that the jet center falls outside the double-peaked structure, at the edge of E1.

We find that it is possible to separate the ammonia main line emission in two velocity components. The blue-shifted component, obtained by integrating emission over the velocity range -59.5 to -53.4 km s^{-1} (Figure 5.15), seems to be associated to the jet center. The red-shifted component, obtained by integrating the emission over the velocity range -52.2 km s^{-1} to -44.9 km s^{-1} (Figure 5.14), shows an elongated morphology, about $1''$ long, centered at the submm peak. At both sides of the submm peak, two low-contrast peaks of emission arise within the elongated morphology, similarly to what is detected with the main line emission (Figure 5.10). Note that the orientation of this new double-peaked structure is rotated $\sim 35°$ clockwise with respect to the orientation of the the double-peaked structure traced by the satellite emission (Figure 5.11). The fact that we can separate our NH_3(4,4) main line emission in two different velocity components, one associated with the center of the jet and a second one associated with the submm peak of emission, suggests that there are two different YSOs embedded within the W3(H_2O)-E core close in LOS. One YSO would fall at the center of the double-peaked structure traced by the satellite emission and would be the main responsible of the dust heating traced by the submm emission. The second YSO in the W3(H_2O)-E core would be the jet-driving source which, as mentioned, lies at the edge of the ammonia double-peaked structure. The ammonia emission associated with the jet is three times weaker than the one associated with the submm source within W3(H_2O)-E (Figure 5.14). This, together with the fact that only a small amount of satellite ammonia emission is seen towards the jet-center, suggests that the submm source has associated a larger amount of dense gas.

Figure 5.16 shows the intensity-weighted mean velocity map of the satellite line emission of W3(H_2O)-E. The ammonia emission associated with the peak E1 is red-shifted by $\simeq 1.5$ km s^{-1} with respect to that of E2. However, there is also some blue-shifted emission at the SE edge of the core, near the position of the jet. We believe that such blue-shifted emission is contamination coming from the molecular gas associated with the jet-driving source which is blue-shifted with respect that associated with the submillimeter source. It is important to point out that the velocity gradient traced by the NH_3(4,4) satellite lines (reddest velocities at SE and bluest velocities at NW) has opposite direction to the gradient reported by Zapata et al. (2011) obtained from methanol observations. We attribute this discrepancy to the poorer angular resolution ($0\overset{''}{.}8$) of the methanol observations with respect to that of our observations ($0\overset{''}{.}3$). The methanol observations are unable to resolve the two sources within W3(H_2O)-E, and we believe that the velocity gradient is, actually, produced by the different radial velocity of the two sources present within W3(H_2O)-E, and therefore is not tracing a disk-like structure as interpreted by Zapata et al. (2011).

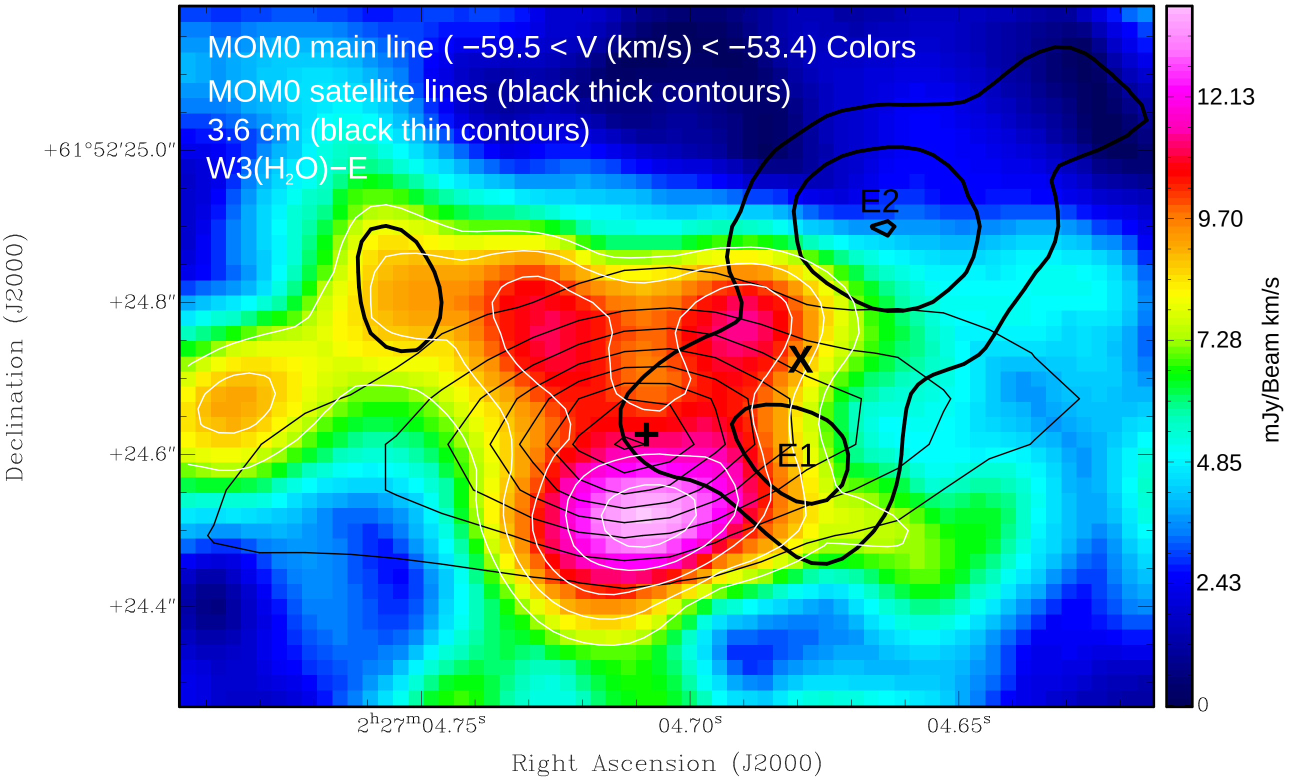

Figure 5.14: Integrated intensity map (zeroth-order moment) of the NH_3(4,4) main line, over the velocity range from −59.5 km s^{-1} to −53.4 km s^{-1} (colors and white contours), overlapped on the 3.6 cm continuum emission map of Wilner et al. (1999) (thin black contours). The lowest white contour is 7.3 mJy beam^{-1} km s^{-1} and the increment step is 1.46 mJy beam^{-1} km s^{-1}. The lowest thin black contour is 0.18 mJy beam^{-1} and the increment step is 0.08 mJy beam^{-1}. The + symbol corresponds to the position of the 3.6 cm source and the × symbol corresponds to the local maxima of the 890 μm emission (Zapata et al. 2011). The integrated intensity map of the satellite emission at the levels of 60% and 80% and 99% of the emission peak is also shown (thick black contours).

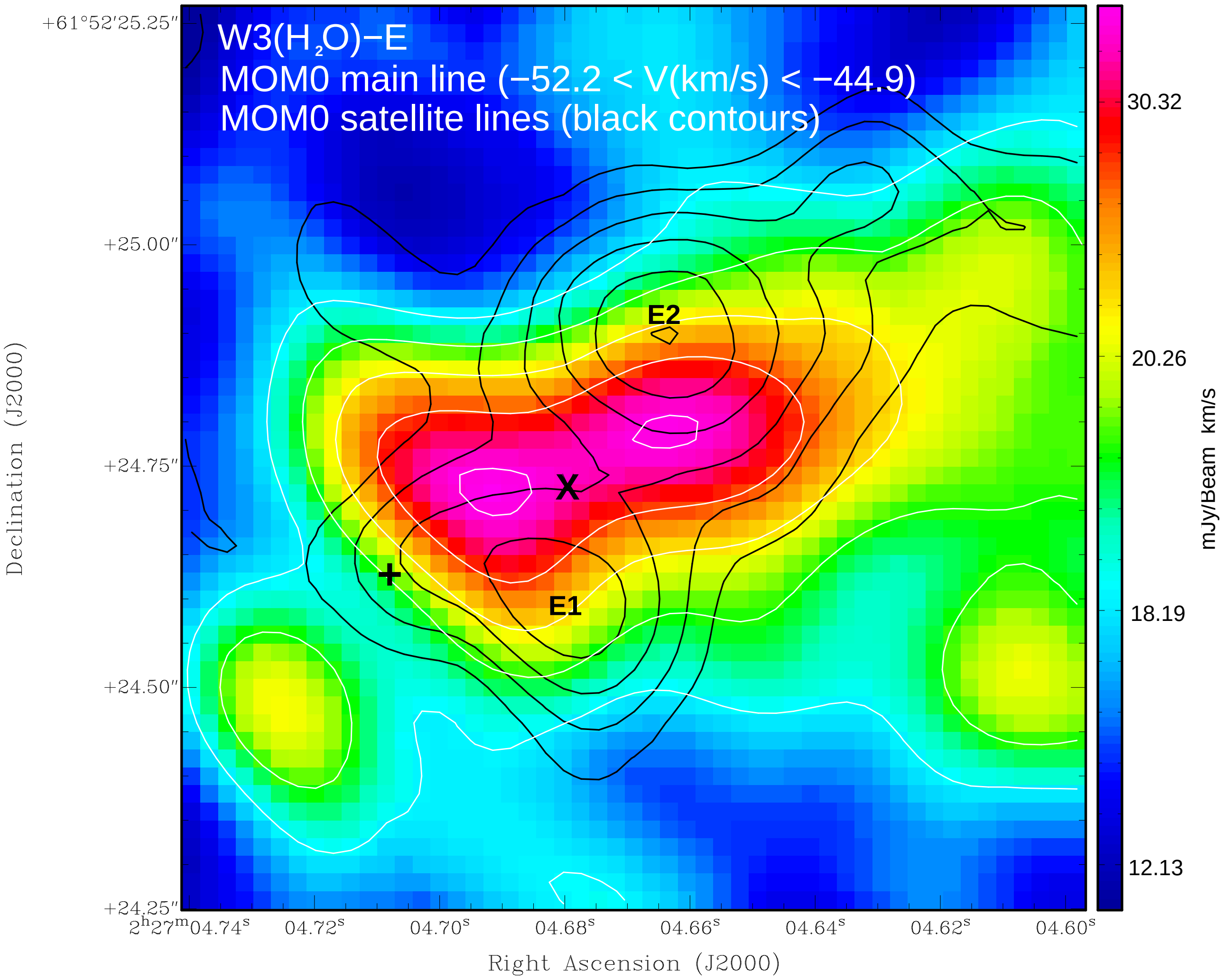

Figure 5.15: Integrated intensity map (zeroth-order moment) of the $NH_3(4,4)$ main line, over the velocity range from -52.2 km s^{-1} to -44.9 km s^{-1} (colors and white contours). The lowest contour is 18.5 mJy beam^{-1} km s^{-1} and the increment step is 3.4 mJy beam^{-1} km s^{-1}. The + symbol corresponds to the peak position of the 3.6 cm source and the × symbol corresponds to the local maximum of the 890 μm emission (Zapata et al. 2011). The integrated intensity map of the satellite lines (the same as in Figure 5.11) is shown in black contours.

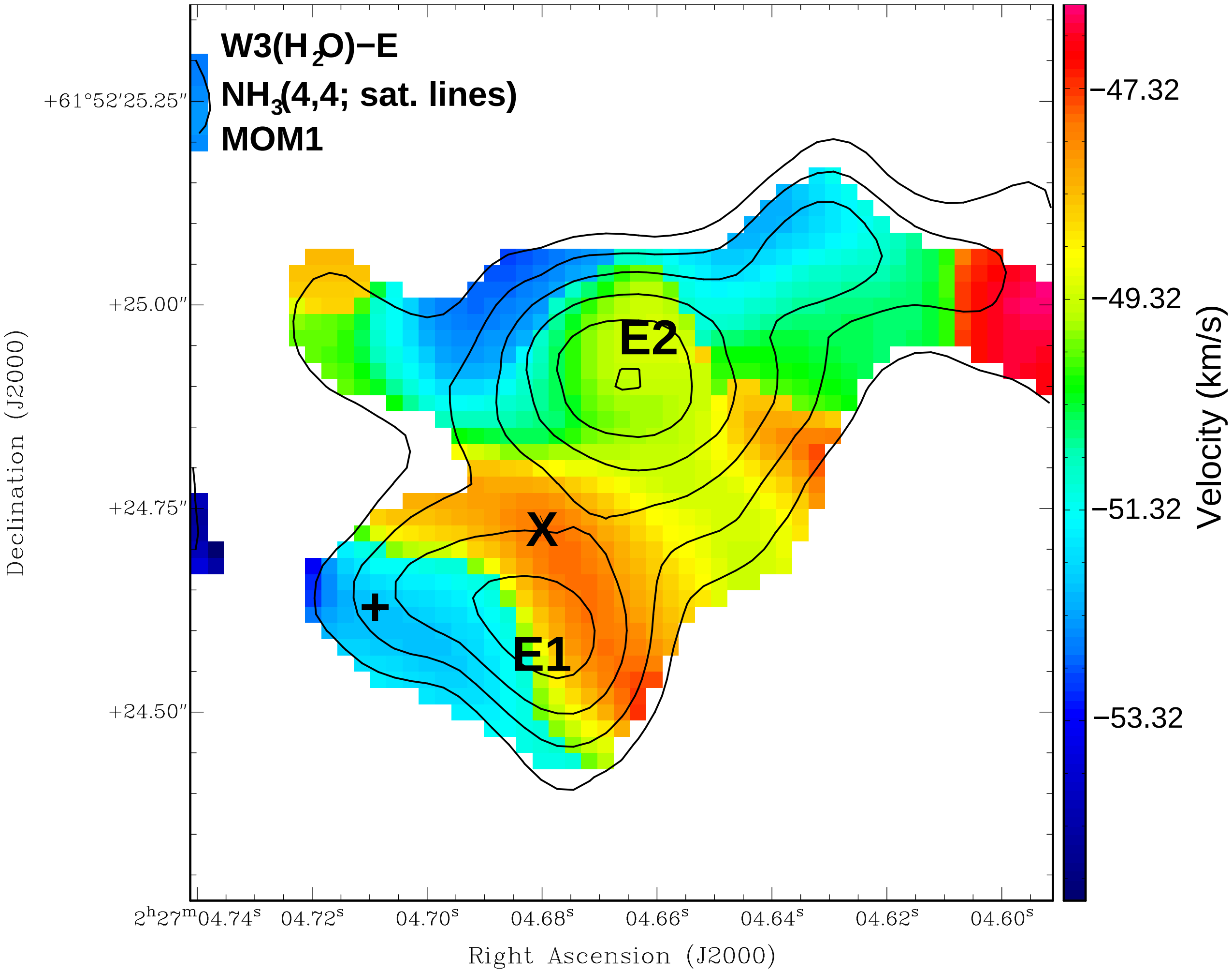

Figure 5.16: Intensity-weighted mean velocity map (colors) overlapped with the integrated emission map of the NH_3(4,4) satellite lines (contours) towards W3(H_2O)-E. The beam and the contour levels are the same as in Figure 5.10. Symbols have the same meaning as in Figure 5.7.

5.5 Description of the modeling procedure

Our NH_3(4,4) observations show that the W3(H_2O) HMC contains two main cores, W3(H_2O)-E and W3(H_2O)-W. Both cores exhibit internal substructure and velocity gradients. The intensity integrated maps of the satellite lines (which are optically thinner than the main line) reveal in both cases a double-peaked structure with the peaks separated by $\sim 0\farcs4$ ($\sim$ 800 AU) and centered on a YSO. The ammonia double-peaked structure in W3(H_2O)-W is associated with the westernmost centimeter source, and the one in W3(H_2O)-E is associated with the easternmost submillimeter source. Interestingly, the structures in the main line and in the satellite line maps have different orientations.

We interpret the ammonia double-peaked structure observed in W3(H_2O)-E and W3(H_2O)-W as toroids seen nearly edge-on. Under this interpretation, the observed double-peaked would correspond to the LOS that are nearly tangential to the internal edges of the toroid, where the highest column densities are reached. Dense molecular structures that have been interpreted as rotating toroids have been observed around protostar of different masses (Torrelles et al. 1994, Beltrán et al. 2005, Wang et al. 2007).

The complex velocity gradients observed in the W3(H_2O) cores would arise from a combination of rotation and infall motions within the toroidal structure. The differences in shape and orientation between the main and satellite line maps could be caused by opacity effects, since the opacity of the NH_3(4,4) satellite lines is $\sim$ 60 times smaller than that of the main line. Disentangling the effects of opacity, together with those of temperature, velocity and density gradients along the LOS is not an simple task and a detailed modeling is required.

In the following, we test our proposed scenario by modeling W3(H_2O)-E and W3(H_2O)-W as two independent cores. As our ammonia observations suggest the presence of flattened/toroidal structures, we explored collapse models that include rotation and flattening of the envelope. Infalling envelopes with a TSC density distribution (Terebey, Shu & Cassen 1984; see section 2.3) assume that the rotation of the infalling material becomes important only in the vicinity of the centrifugal radius. Therefore, TSC envelopes are flattened only in the inner region, being essentially spherical in the outer region. A more complex description can be given in terms of intrinsically flattened infalling envelopes, such as those with the density distribution resulting from the gravitational collapse of a sheet initially in hydrostatic equilibrium (Hartmann et al. 1994, 1996; hereafter “sheet collapse” models). These envelopes are flattened not only in their inner region, because of rotation, but also at large scales, due to the natural elongation of the cloud.

We will constrain the physical properties of the envelopes by fitting the observed SED of their continuum thermal dust emission (assuming a given dust-to-gas ratio). Additionally, our ammonia observations, which have enough angular resolution to resolve the substructure of each core, will provide further constraints, including the kinematics of the cores. We have developed a radiative transfer code that allows us to calculate the synthetic ammonia emission expected

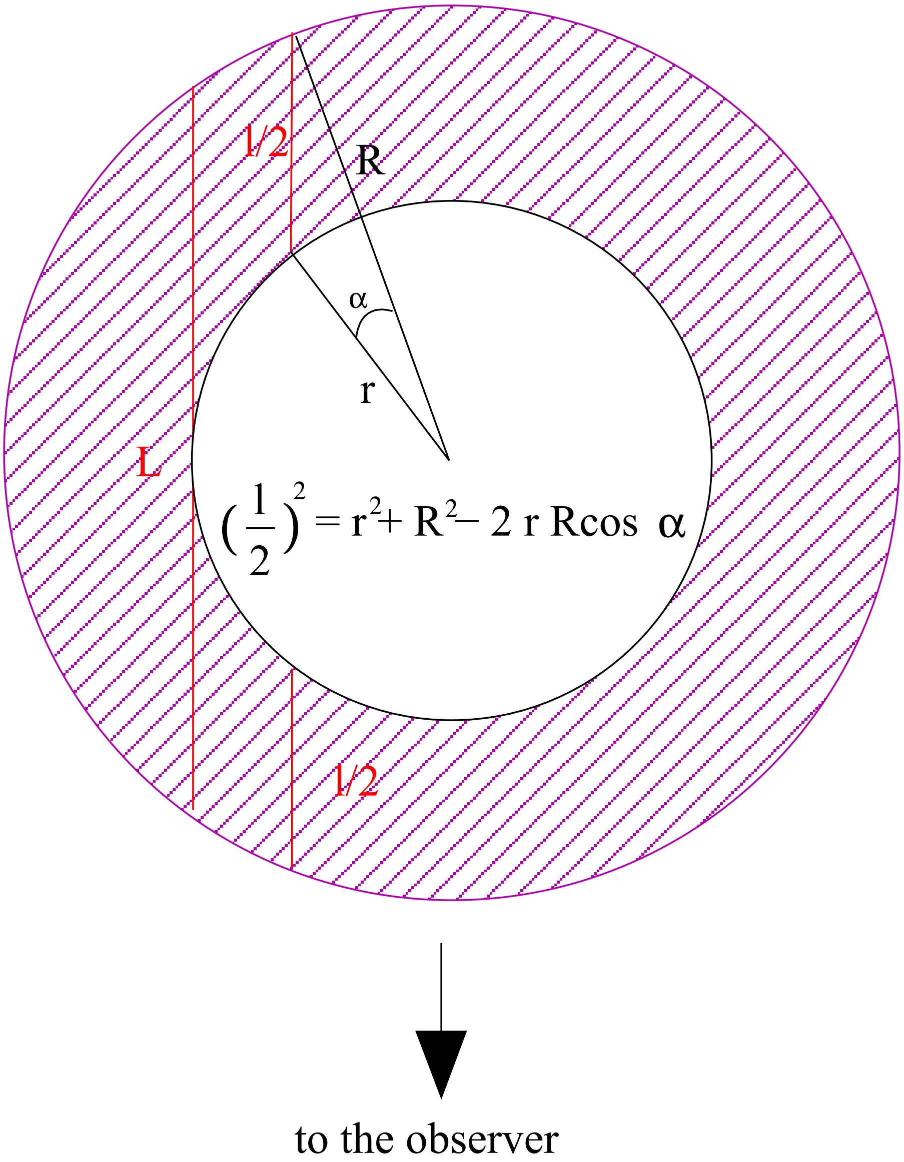

Figure 5.17: Sketch of the equatorial plane of a torus-like structure with constant density. The line of sight with larger optical depth is the one that crosses through the internal edge of the torus.

under the physical conditions obtained from the SED fit. The remaining free parameters in this calculation are the stellar mass, the velocity dispersion in the envelope, the ammonia abundance relative to hydrogen and the formation temperature of the ammonia. While the morphology of the observed ammonia emission in both W3(H_2O) condensations is suggestive of toroidal-like structures, the collapse models in general do not produce central holes in the density distribution. We attribute the observed decrease of ammonia emission towards the center of the double-peak structures to a decreases of the ammonia abundance. To account for this, we drop to zero the ammonia abundance in the region closer to the star in the calculation of the ammonia emission. The comparison of the synthetic and observed ammonia emissions will allow us to refine the models. We will take special consideration in trying to qualitatively explain the morphological differences found between the main and the satellite emission maps.

For completeness, we also tried an alternative modeling for the cores using a spherical collapse model, the SLS model (McLaughlin & Pudritz 1997, Osorio et al. 2009; see Section 3.4) but no satisfactory fits were obtained.

Thus, our modeling includes the effects of rotation, and flattening, by using the TSC and the sheet collapse formalisms, which provide a self-consistent description of the dynamical collapse of rotating molecular cores, and a framework for the study of the formation of stars. This improves the results of the previous modeling of W3(H_2O) carried out by Osorio et al. (1999) and by Chen et al. (2006), which considered spherical collapsing envelopes where rotation was not included. Also, while the model used by Osorio et al. (1999) uses a self-consistent formalism, it considers W3(H_2O) as a single core and does not separate the two condensations W3(H_2O)-E and W3(H_2O)-W. On the other hand, Chen et al. (2006), who model the two condensations separately, assume power-law dependences for the density and temperature, lacking a self-consistent description of their physical properties.

5.5.1 Description of the TSC model

When a rotational perturbation is introduced in the SIS model of Shu (1977), described in Section 3.4.1, the density distribution and the radial infall velocity are modified from those expected in a spherical collapse. The result is that most of the envelope matter does not fall directly onto the central protostar but settles onto a centrifugally supported disk around it (Terebey, Shu & Cassen 1984; Shu et al. 1987).

The rotational perturbation adopted by the TSC formalism is that of a rigid body with low angular velocity Ω. A particle at a given initial distance to the star, r_0, and an angular separation from the rotation axis, θ, would have a specific angular momentum of $h = \Omega r_0^2 \sin\theta$. Assuming that the pressure forces are negligible and that practically all the mass is contained in the central protostar, then the problem can be analyzed using ballistic trajectories and the particle orbit is given by the two-body parabolic motion around a central mass:

$$r = \frac{h^2}{GM_\star}\frac{1}{1-\cos\theta/\cos\theta_0}, \tag{5.1}$$

where G is the gravitational constant, $M_\star$ the mass of the central object, and θ_0 is the angle between the orbital plane of the particle and the rotation axis of the system. It can be demonstrated that the particle trajectories in the meridional plane can be written as:

$$\frac{r}{r_c} = \frac{\sin^2\theta_0}{1-\cos\theta/\cos\theta_0}, \tag{5.2}$$

where r_c is the centrifugal radius, which is defined as

$$r_c = r_0^4\Omega^2/GM_\star \tag{5.3}$$

and that represents the maximum distance at which matter at r_0 settles in the disk. Additionally, the velocity field in spherical coordinates is determined by the equations (Terebey, Shu & Cassen 1984):

$$\begin{aligned} v_r &= -\left(\frac{GM_\star}{r}\right)^{1/2}\left(1+\frac{\cos\theta}{\cos\theta_0}\right)^{1/2} \\ v_\phi &= \left(\frac{GM_\star}{r}\right)^{1/2}\left(1-\frac{\cos\theta}{\cos\theta_0}\right)^{1/2}\frac{\sin\theta_0}{\sin\theta} \\ v_\theta &= \left(\frac{GM_\star}{r}\right)^{1/2}(\cos\theta_0-\cos\theta)\left(\frac{\cos\theta_0+\cos\theta}{\cos\theta_0\sin^2\theta}\right)^{1/2} \end{aligned} \tag{5.4}$$

These equations imply that in the outer regions the gas falls almost radially, resembling the free-falling case. Rotation becomes important only in the vicinity of the centrifugal radius, where material falls non-radially and it accumulates in a flattened rotating structure.

The matter near the poles has lower angular momentum and, therefore, it will end up accumulated in the flattened rotating structure at a location relatively close to the star. On the contrary, near the equatorial plane, matter has a larger angular momentum and will end up in the rotating structure at larger radii, close to r_c. As collapse proceeds, matter that originally was located at larger distances becomes part of the disk and since it has larger angular momentum, r_c increases with time. The density is evaluated by assuming that the mass infall rate, $\dot{M}_{inf}$, is steady and is determined by the equation (Hartmann 1998):

$$\rho = \sqrt{2}\rho_1\left(1+\frac{\cos\theta}{\cos\theta_0}\right)^{-1/2}\left(\frac{\cos\theta}{\cos\theta_0}+\frac{2\cos^2\theta_0}{r/r_c}\right)^{-1}\left(\frac{r}{r_1}\right)^{-3/2}, \tag{5.5}$$

where the parameter $\rho_1 = \dot{M}_{inf}/(32\pi^2GM_\star r_1^3)^{1/2}$ corresponds to the density that a spherically symmetric free-falling envelope with the same mass infall rate, $\dot{M}_{inf}$, would have at the reference radius r_1, taken as 1 AU. At large radii, the density distribution tends to behave as

$\rho \propto r^{-3/2}$, as in the free-fall case. In the inner region the dependence goes roughly as $\rho \propto r^{-1/2}$.

Note that the TSC formalism considers that all the mass is concentrated in the central region and neglects the envelope mass. This assumption is not valid at large scales, where the internal envelope mass can be comparable or even larger than the stellar mass. Nevertheless, since most of the protostellar emission is concentrated towards the central region and at radii near r_c (where the density peaks) in practice such approximation is reasonable in the calculation of the line emission (Hartmann 1998).

5.5.2 Description of the Sheet collapse model

Star forming cores are usually elongated, with a length to width ratio of ~2:1 on average (Myers et al. 1991). Additionally, several authors suggest that the binarity or multiplicity of star-forming systems are best explained by the fragmentation of structures with filamentary or layer geometries, rather than purely spherical geometry (Boss 1993; Bodenheimer et al. 2000; Whithworth 2001). Since multiplicity is present in W3(H_2O), and the ammonia emission has a morphology that clearly departs from spherical symmetry, it is worth testing intrinsically flattened parental clouds as the initial conditions. The so-called sheet collapse model uses intrinsically flattened envelopes resulting from the gravitational collapse of a flat layer initially in hydrostatic equilibrium (Hartmann et al. 1994, 1996). Note that, unlike the TSC envelopes, these envelopes are flattened even at large scales. The density distribution of the infalling material can be expressed as:

$$\rho(r,\theta) = \rho_{TSC}(r,\theta)\eta \cosh^{-2}(\eta \cos\theta)[\tanh(\eta)]^{-1}, \tag{5.6}$$

where ρ_{TSC} is the density given by the TSC formalism. The parameter $\eta \equiv R_{out}/H$, where R_{out} is the outer radius of the envelope and H is the scale height, is a measure of the degree of flattening in these envelopes. Although the TSC and the sheet envelopes differ considerably at large scales, their behavior at small scales is similar. This, together with the fact that most of the line emission would arise from the inner parts of the envelope, allow us to approximate the velocity field in the sheet collapse formalism by the one of the TSC formalism (equations 5.4).

5.5.3 Modeling of the SED

In order to determine the density and temperature structure of the envelopes, we model their individual SEDs by calculating their dust emission. To do that, we adapt a radiative transfer code developed for low-mass protostars (Kenyon et al. 1993; Osorio et al. 2003). The code assumes a central star and a collapsing envelope of the TSC or sheet collapse type. The star emits photons that can be absorbed and re-emitted by the dusty envelope. The envelope density is zero close to the polar direction to mimic a bipolar cavity, whose aperture angle is θ_{cav}. The temperature of the envelope as a function of the distance to the central star is calculated from radiative equilibrium, assuming spherical compact dust grains of silicate, graphite, water, and troilite. This mixture of dust is assumed to have the typical grain-size distribution of the interstellar medium ($N(a) \propto a^{-3.5}$; where a represent the grain size) and a mass gas-to-dust ratio of 100. We have considered a stellar radius, R_*, of 10^{12} cm (Osorio et al. 1999; Hosokawa & Omukai 2008).

We have fitted the observed SED following the trends of SEDs given in De Buizer et al. (2005) for the high-mass protostar case. The explored parameters and values were: $L = 1000, 1500, 2000, 4000$, and 6000 $\mathrm{L}_\odot$ for the bolometric luminosity; $M_{env} = 8, 12, 16$, and 20 $\mathrm{M}_\odot$ for the envelope mass; $\eta = 0, 1.0, 1.5$, and 1.9 for the intrinsic flattening of the envelope ($\eta = 0$ corresponds to the TSC model); the inclination angle, i (the angle between the polar direction and the LOS; $0° < i < 90°$); $\theta_{cav} = 0°, 5°, 10°, 20°$ for the polar cavity aperture (full-angle); and $r_c = 300, 400, 500, 600$ AU for the centrifugal radius. The outer radius of the envelope is fixed at 1500 AU, and the inner radius is determined by the dust destruction front. Note that by setting the mass of the envelope and its outer radius we are setting ρ_1, which in its turn sets the density distribution together with r_c (equation 5.5).

5.5.4 Modeling of the ammonia line emission

The geometry (η, i and r_c), and the temperature and density fields obtained from the fitting of the SED are introduced in the radiative transfer code that we have developed for the calculation of the emergent ammonia emission (see Appendix A). We assume a gas-phase variable ammonia abundance relative to H_2, with a minimum abundance, X_{min}, in zones where the temperature is low and the ammonia molecules are frozen in grain dust mantles, and a maximum abundance, X_{max}, in zones where the temperature exceeds the sublimation temperature and, thus, the ammonia molecules are released to the gas-phase (Osorio et al. 2009). Following Osorio et al. (2009), we tested the possibility of direct sublimation of ammonia ices in grain mantles (at temperatures of ~ 60 K) and the possibility that ammonia molecules are mixed with water ice, being trapped in the grain mantles until temperatures high enough for sublimation of water molecules (~ 100 K) are reached. Furthermore, as noted above, we assume that the ammonia abundance has an inner hole whose radius is taken as a free parameter. We assume that the velocity dispersion has a thermal and a turbulent component. The turbulent component is parametrized using a generalization of the SLS formalism:

$$\Delta V_{\mathrm{tur}} = \sqrt{4 k_b \ln 2 \frac{P_{tur}}{\rho}} \tag{5.7}$$

where k_b is the Boltzmann's constant, and P_{tur} is a free parameter that determines the dependence of turbulence with density ρ. We tested constant turbulence over the core, and turbulence decreasing with increasing density. The remaining free parameter is the mass of the central (proto)star.

For the results presented here, we have used a grid of $100 \times 100 \times 100$ points with a linear cell size of 30 AU. In the computation of the intensity as a function of position and the velocity,

$I_\nu(x,z,v)$ (see Appendix), we sampled the velocity in increments of 0.1714 km s^{-1}. In order to compare the model results with our observations, we simulated the observational angular resolution by convolving the model intensity, $I_\nu(x,z,v)$, with a circular beam whose area is equal to the one of the synthesized beam in our data (beam $\simeq 0.29'' \times 0.28''$). To simulate the observational spectral resolution, we grouped the different samples of v in velocity channels of 1.2 km s^{-1} to coincide with that of the observations. For simplicity in the calculations, the rotational axis of the flattened structure was placed in the plane formed by the LOS and the north direction in the synthetic maps, (i.e., PA=0° in the synthetic maps). The synthesized ammonia spectra and maps were then compared with our ammonia observations to further constrain the physical characteristics of the cores.

5.6 Model results

We have been able to fit the SED and the ammonia emission for both W3(H_2O)-E and W3(H_2O)-W. The SED fitting is not unique, and several TSC and sheet collapse models are compatible with the observed SED. This is because several points of the SED, both for W3(H_2O)-E and for W3(H_2O)-W, are upper limits. These upper limits come either from low angular resolution observations that were not able to resolve the two cores, or from non-detections. Upper limits from non-detections were calculated using the formula for non-detected extended sources of Beltrán et al. (2001). The most restrictive piece of data in the SED fitting was the near infrared upper limit from Stecklum et al. (2002).

In general, we found that models with a cavity along the poles with an full aperture angle greater than 5° produce far-IR emission that exceeds the upper limits set by the observations. The SED fits with luminosities of 4000 and 6000 $L_\odot$ produce ammonia line emission much stronger than observed. The ammonia emission is better described with models where the ammonia molecules in dust grain mantles are trapped in water ice, and that use constant turbulence. We obtained good fit setting $X_{min} = 10^{-9}$ but note that lower values give similar results.

5.6.1 W3(H_2O)-W

The most satisfactory fit for W3(H_2O)-W was achieved with the sheet collapse formalism, with $\eta = 1.0$. The observed and fitted SEDs and NH_3(4,4) spectra are shown in Figure 5.18. The spectra have been obtained by integrating the intensity over a circular region of radius 0$''\!.$5 around the peak position of the centimeter source (Figure 5.12). As can be seen in Figure 5.18, the fit is very good both for the SED and the spectrum. The parameters of the model are listed in Table 5.6.1. The density and temperature fields corresponding to this model fit are also shown in Figure 5.18. The density has been averaged over the polar angle, θ, in order to represent its radial dependency that shows a local maximum at the centrifugal radius, where the material concentrates.

If we assume that the accretion shocks are produced on the stellar surface, then the luminosity due to accretion onto the star can be approximated by the formula of Ostriker & Shu (1995):

$$L = f_{acc} \frac{G M_* \dot{M}}{R_*} \tag{5.8}$$

where f_{acc} is the fraction of the gravitational potential energy released by accretion, which we assume to be 1. Using this formula, the accretion rate needed to produce the luminosity inferred for W3(H_2O)-W (2000 $L_\odot$) is of 1.5×10^{-4} $M_\odot$ yr^{-1}, which is sixty times lower than the inferred mass infall rate. Such difference between infall rate and accretion rate can be explained in terms of episodic accretion (Kenyon et al. 1990, McKee & Offner 2010). According to this hypothesis much of the protostellar mass would be accreted in short periods of time of very high accretion, but most of the time, the system disk-star is in a dormant phase of low accretion during which the disk accumulates mass through the infall process until an outburst of accretion occurs, providing of mass to the stars and releasing a much higher luminosity. The accretion rate 1.5×10^{-4} $M_\odot$ yr^{-1} would be that of the dormant phase.

Although the mass obtained for the central object ($M_\odot$=6 $M_\odot$) is typical of an intermediate-mass star rather than of a high-mass one, the value of the mass accretion rate derived is typical of a high-mass star (ranging between 10^{-4} and 10^{-2}). Taking into account that the mass-loss rate in the outflow is typically about the 10% of the accretion rate (Cabrit 2007, Antoniucci et al. 2008, Lee et al. 2008), then we can consider that most of the mass that falls from the molecular envelope to the disk is later accreted from the disk to the star. Note that this does not have to mean that the infall rate equals the accretion rate, $\dot{M}_{\rm inf} \simeq \dot{M}$, at all times. Our interpretation is that we are observing a high-mass protostar, which is still in the process of accreting most of its final mass from the molecular envelope that, with a mass of 16 $M_\odot$ can provide enough reservoir to further grow.

Moreover, accretion rates of the order of the one derived are considered high enough to quench the formation of an HII region (Osorio et al. 1999), and even to overcome the effects of radiation pressure. The latter is accomplished if:

$$\dot{M} \geq \frac{L}{u_d c} \tag{5.9}$$

where u_d is the velocity of the flow at the dust destruction front (Osorio et al. 1999). This condition is satisfied by our model.

Figure 5.19 shows the synthetic integrated intensity maps of the NH_3(4,4) main and satellite lines of the best-fit model. These maps reproduce well some qualitative characteristics of the observed maps (Figures 5.10 and 5.11). The synthetic maps show two peaks at both sides of the central position, that are more prominent in the satellite line maps, as in the observations.

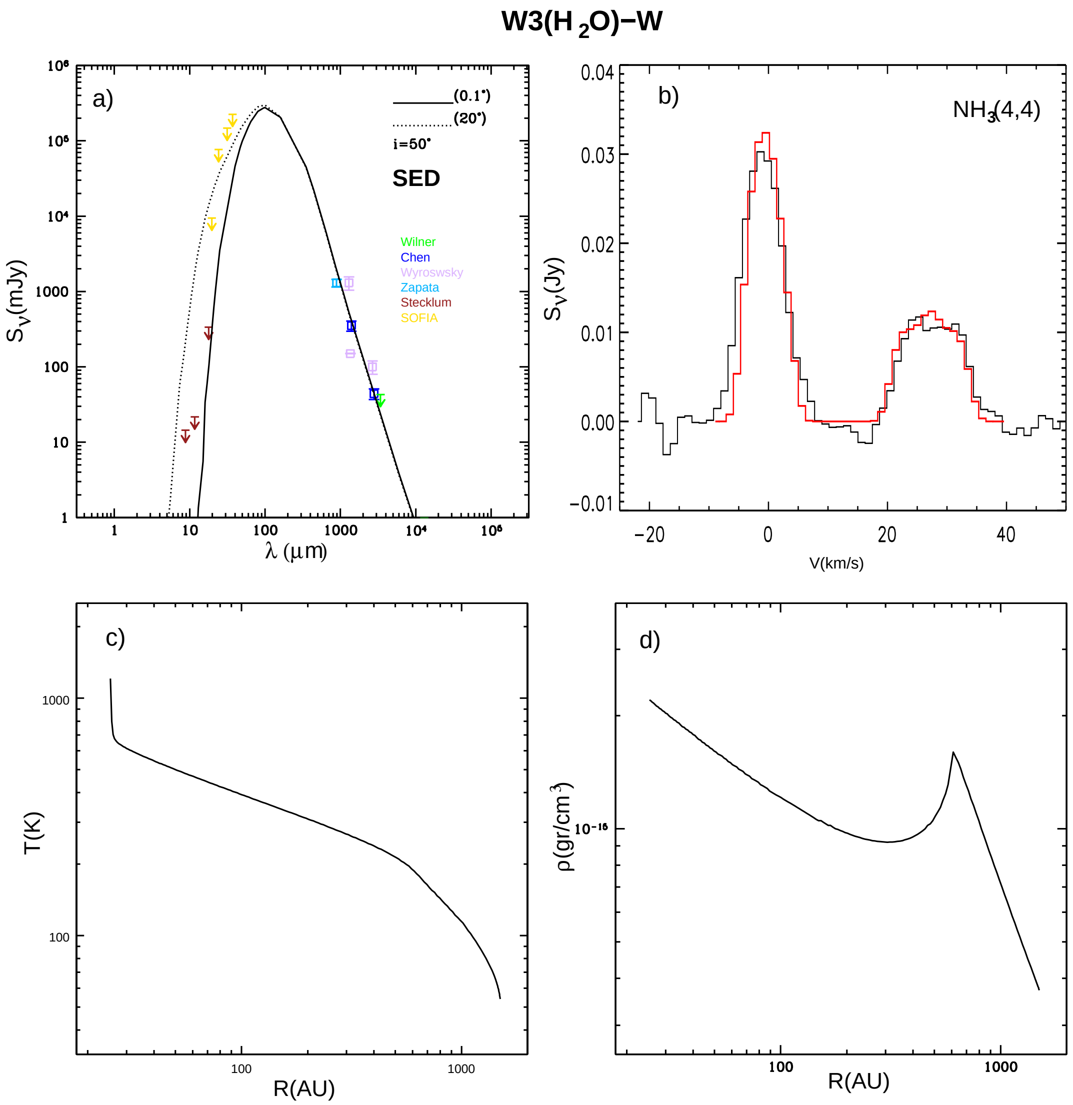

Figure 5.18: *(a)* Observed (symbols) and best-fit model (solid line) spectral energy distributions of W3(H_2O)-W. The data are from Chen et al. (2006), Wyrowski et al. (1997), Zapata et al. (2011), Wilner et al. (1995), Stecklum et al. (2002), and the SOFIA database. The dotted line, which clearly exceeds the mid-IR upper limits, represents the SED of the same model but with a cavity carved by an outflow of aperture angle 20°. *(b)* Observed (black line) and model (red line) spectra of the NH_3(4,4) transition. Emission has been integrated over a circular area of radius 0.″5 centered on the peak of the 3.6 source of Wilner et al. (1999). Velocities are relative to the systemic velocity of the core, assumed to be -46.0 km s^{-1}. *(c)* Temperature as a function of radius for the best-fit model. *(d)* Polar averaged density as a function of radius for the best-fit model.

Table 5.1: Parameters of the best fit models

Parameter	W3(H_2O)-W	W3(H_2O)-E	Notes[a]
$R_*{}^b$ (cm)	1×10^{12}	1×10^{12}	A
$R_{\rm out}{}^c$ (AU)	1500	1500	A
$r_c{}^d$ (AU)	600	500	F
$R_{\rm int}{}^e$ (AU)	480	500	F
$L_{\rm bol}{}^f$ ($L_\odot$)	2000	1500	F
$M_{\rm env}{}^g (M_\odot)$	16	20	F
$M_*{}^h$ ($M_\odot$)	6.0	2.2	F
$\dot{M}_{\rm inf}{}^i$ ($M_\odot$ yr^{-1})	9.98×10^{-3}	7.41×10^{-3}	C
η^j	1.0	...[k]	F
i^l (°)	50	60	F
$\theta_{\rm out}{}^m$ (°)	<5	<5	F
$X_{\rm max}{}^n$	2.95×10^{-7}	1.0×10^{-7}	F
$X_{\rm min}{}^o$	1.0×10^{-9}	1.0×10^{-9}	F
$\Delta V_{\rm turb}{}^p$ (km s^{-1})	0.5	0.4	F
$T_{\rm for}{}^q$ (K)	20	20	A

[a] A = Adopted, F = Fitted, C = Calculated.

[b] Radius of the central star (see Osorio et al. 1999).

[c] Outer radius of the envelope, inferred from observations.

[d] Centrifugal radius.

[e] Radius of the inner hole in ammonia abundance distribution.

[f] Bolometric luminosity.

[g] Mass of the envelope, obtained by integration of the density distribution.

[h] Mass of the central star.

[i] Mass infall rate.

[j] Degree of flattening.

[k] The TSC formalism provides the best fit.

[l] Angle between the rotational axis and the LOS.

[m] Full opening angle of the outflow cavity along the polar direction.

[n] Maximum ammonia abundance relative to the hydrogen in gas phase.

[o] Minimum ammonia abundance relative to the hydrogen in gas phase.

[p] Full width at half maximum of the velocity distribution due to turbulent motions.

[q] Formation temperature of the ammonia, which sets the ratio between ortho and para species.

The separation between the peaks in the synthetic maps is 0.″5 for the satellite lines, and 0.″4 for the main line, similar to what is observed (0.″45). Note that in a toroid of homogeneous density it is expected that the two emission peaks are separated twice the radius of the inner hole ($2R_{int}$). However, the model predicts that the centrifugal radius is larger than the radius of the ammonia hole ($r_c > R_{int}$; see Table 5.6.1); since the density distribution peaks at the centrifugal radius, the separation between the two emission peaks will be larger ($\sim 2r_c$). The synthetic maps also reproduce the observed difference in the orientation of the double-peaked structure between the main and satellite line maps. As in the observations, the structure traced by the main line appears rotated clockwise with respect to that of the satellite lines. However, this difference is somewhat smaller in the synthetic maps (27°) than in the observed maps (35°). We found that the difference in the orientation between maps increases as the inclination angle and the degree of flattening decreases. However, for $i < 50°$ the maps show a ring-like morphology rather than a double-peak structure, and for the TSC formalism (less flattened) the intensity of the peaks is too low. As a compromise, we took $i = 50°$ and $\eta = 1$. For the main line, the intensity of the peaks in the synthetic map ($\sim$ 35 mJy beam^{-1} km s^{-1}) is somewhat lower than in the observational maps ($\sim$ 50 mJy beam^{-1} km s^{-1}). The two peaks are not equal, but one is slightly stronger. For the satellite the model predicts two peaks of similar intensity, as also occurs in the observations. However, for the satellite lines, the discrepancy in the observed and model intensity of the peaks is higher, with the model peak intensity being about half of the observed value. The central mass also has an influence in the orientation between double-peak structures. The larger the central mass, the larger the difference in the orientation. However, the central mass is well constrained by the width of the lines, since a higher mass results in higher rotation velocities, and therefore in a larger line width. We also found that if the projection of the angular momentum along the LOS points towards the observer, then, the double-peak structure of the main line is rotated clockwise with respect to that of the satellite lines, while if the angular momentum LOS projection points away from the observer, then, the rotation is counterclockwise. The fact that in the observational maps, the double-peak structure of the main line appears rotated clockwise with respect to the structure of the satellite lines, indicates that the projection of the angular momentum must be pointing towards us. This has important implications in the interpretation, as we will show later.

Figure 5.20 shows the synthetic first-order moment of the satellite line emission. The model reproduces very well the velocity field since both, the observed and model maps agree in showing a velocity shift between peaks of $\sim$ 2.3 km s^{-1} and similar internal velocity gradients. The model successfully predicts that the strongest peak of the main line emission is blue-shifted with respect to the weaker one. We recall that the rotation axis of the flattened rotating structure was arbitrarily set to PA=0° in the model calculations. If we now rotate the synthetic map to make the blue- and red-shifted peaks coincide with the positions of the observed W1 (blue) and W2 (red) peaks, the axis of symmetry of the flattened structure would be located at PA= 23°. This is almost coincident with the orientation of the CO outflows (Zapata et al. 2011; see Figure 5.1), and therefore, the flattened and rotating structures traced by the NH_3(4,4) emission are nearly perpendicular to the outflow. Additionally, the fact that the model predicts that the projection of the angular momentum along the LOS should be pointing

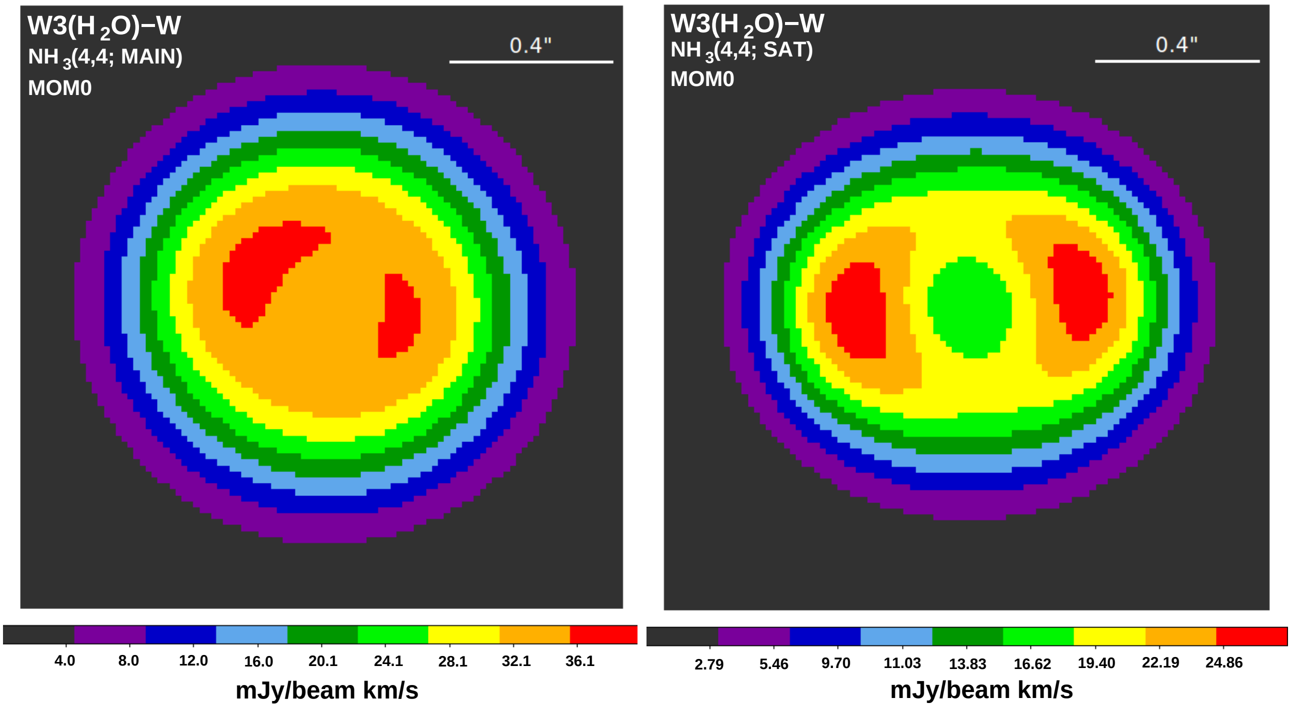

Figure 5.19: Synthetic integrated intensity map (zeroth-order moment) of the NH_3(4,4) main line (*left panel*) and satellite lines (*right panel*) for W3(H_2O)-W.

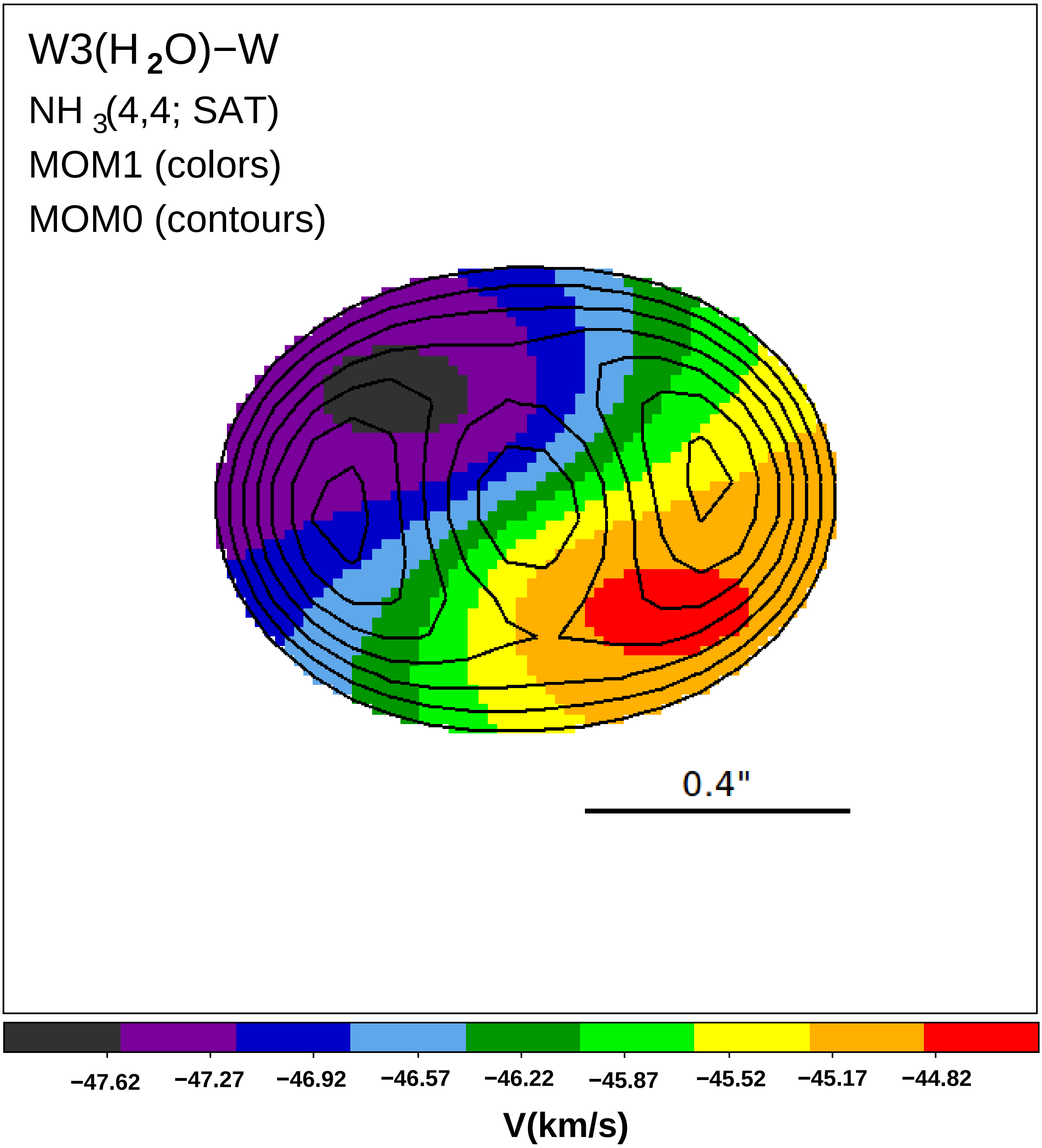

Figure 5.20: Synthetic intensity-weighted mean velocity map (first-order moment) of the NH_3(4,4) satellite lines (colors) overlapped on their synthetic integrated intensity map (contours), for W3(H_2O)-W. Contour levels are 13.8, 15.8, 17.8, 19.8, 21.8, 23.7, 25.7, 26.7 mJy beam^{-1} km s^{-1}.

towards us, together with the red-blue orientation of the double-peaked structure, implies that the blue-shifted lobe of an outflow should be North and the red-shifted lobe South, which is in agreement with the observations (Zapata et al. 2011). The fitting of the SED indicates that the outflow must be extremely collimated, with an opening angle $< 5°$ (see Figure 5.18a); otherwise the emission escaping through the poles would exceed the mid-IR upper limits in the SED.

The results of our calculation indicate that one should always be cautious when interpreting double-peaked morphologies in maps of molecular line emission. As we have seen, opacity effects in the presence of both rotational and infall motions can alter the orientation of the observed double-peak structures with respect to the real orientation of the flattened structures they are tracing. Observations of transitions with different optical depths are needed in order to correct for opacity effects of this type.

5.6.2 W3(H_2O)-E

The most satisfactory fit for W3(H_2O)-E was achieved with the TSC formalism. The observed and fitted SEDs and NH_3(4,4) spectra are shown in Figure 5.21. The spectra have been obtained by integrating the intensity over a circular region of radius $0\overset{''}{.}4$ around the peak position (to avoid contamination from nearby emission structures) of the submillimeter source (Figure 5.12). We note that the predicted ammonia spectrum (Figure 5.21b) is able to reproduce the observed line profiles of the main line and the satellite lines, except for a blue-shifted wing that is more evident in the main line profile. The emission of this wing corresponds to the velocity range (-59.47 to -53.40 km s^{-1}) that has been attributed to the ammonia associated with the jet driving source (see section 5.4.2). The fact that the ammonia spectrum predicted from the SED fitting naturally excludes this velocity range supports the proposed separation in two structures at different velocities. As can be seen in Figure 5.21, the fit is very good both for the SED and the spectrum. The parameters of the model are listed in Table 5.6.1. The density and temperature fields corresponding to this model fit are also shown in Figure 5.21. The density has been averaged over the polar angle, θ, in order to represent its radial dependency that shows a local maximum at the centrifugal radius, where the material concentrates.

Analogously to W3(H_2O)-W, we used equation 5.8 to obtain the accretion rate needed to produce the predicted luminosity (1500 $L_\odot$). We obtained a value of $\dot{M} = 3.1 \times 10^{-4}$ $M_\odot$ yr^{-1}. The required mass accretion rate is only 4% of the infall rate predicted by the model. This suggest that most of the mass is temporarily accumulated on the disk, until an outburst of accretion occurs. While the mass obtained for the central object (2.2 $M_\odot$) is small, the derived accretion rate is typically that of a high-mass protostar. As for W3(H_2O)-W, we interpret these results as a star that is in its initial phases of accretion, and that most of its final mass will be obtained later on from the reservoir provided by its 20 $M_\odot$ molecular envelope. Also similarly to what happens for W3(H_2O)-W, these accretion rates are high enough to quench the formation of an HII region and to overcome the radiation pressure, so the star can continue growing in mass.

Figure 5.22 shows the synthetic integrated intensity maps of the NH_3(4,4) main line, and of the NH_3(4,4) satellite lines. The main line emission shows an elongated morphology with two low-contrast local maximums symmetrically located with respect to the center, similar to what is observed (Figure 5.14). The synthetic map of the satellite lines shows an even more prominent double-peaked morphology, also in agreement with observations (Figure 5.11). However, the intensity of the peaks in the synthetic maps is a factor of two lower than in the observational maps, as it also happens in W3(H_2O)-W. The structure traced by the main line is rotated clockwise with respect to the one traced by the satellite lines. The sense of the rotation agrees with what is observed, although the angle is smaller in the model ($\simeq 15°$ vs. $\simeq 35°$ in the observations). As the rotation is clockwise, the projection of the angular momentum along the LOS must be pointing towards the observer (see 5.6.1). The separation between peaks of emission of the synthetic maps is of $0\farcs40$, similar to the observed value of $0\farcs35$. Increasing the inclination angle would help obtain a larger angular difference between the orientation of the satellite and main line structures, also reducing the inner ammonia hole would reduce the separation between peaks. However, by doing so, the synthetic main line map would deviate from what is observed since the double-peak structure is lost.

The map of the synthetic first-order moment for W3(H_2O)-E is shown in Figure 5.23. The velocity field, due to the combination of infall and rotation motions, agrees relatively well with what is observed if the red-shifted peak in the synthesized model is identified with E1 and the blue-shifted one with E2 (Figure 5.16). However, we suggested that the SE edge of the observed condensation (near E1) has a contamination from blue-shifted emission associated with the jet source (see Sec 5.4.2). This contamination prevents a more detailed comparison between model and observations.

We recall that the rotation axis of the flattened structure was arbitrarily set to PA = 0° in the calculations. If we now rotate the synthetic map, to make the blue- and red-shifted peaks coincide with the positions of the observed E1 (red) and E2 (blue) peaks, the axis of symmetry of the flattened structure would be located at PA = $-155°$. This is almost coincident with the orientation of the CO outflow (Zapata et al. 2011, see Figure 5.1), and therefore, the flattened and rotating structures traced by the NH_3(4,4) emission are nearly perpendicular to the outflow. This suggests that the CO outflow has this orientation from its origin, and that its driving source is at the center of the rotating flattened structure traced by the ammonia emission. Its location is marked by the submm emission peak, while the cm jet corresponds to a different object with its own outflow activity. Note that this interpretation differs from the one given by Zapata et al. (2011), who already noticed the different orientation between the CO outflow (PA = $-155°$) and the jet (PA = $-90°$). However, these authors considered that the submm emission was directly associated with the jet driving source, and proposed three possible explanations to account for the discrepancy between the orientation of the jet and the CO outflow: i) the CO outflow with a large-scale PA= $-140°$ originally has an E-W orientation but it bends at a scale of $5''$ from the origin due to an interaction with a high density clump located to the E of W3(H_2O)-E (the preferred option by the authors); ii) the outflow

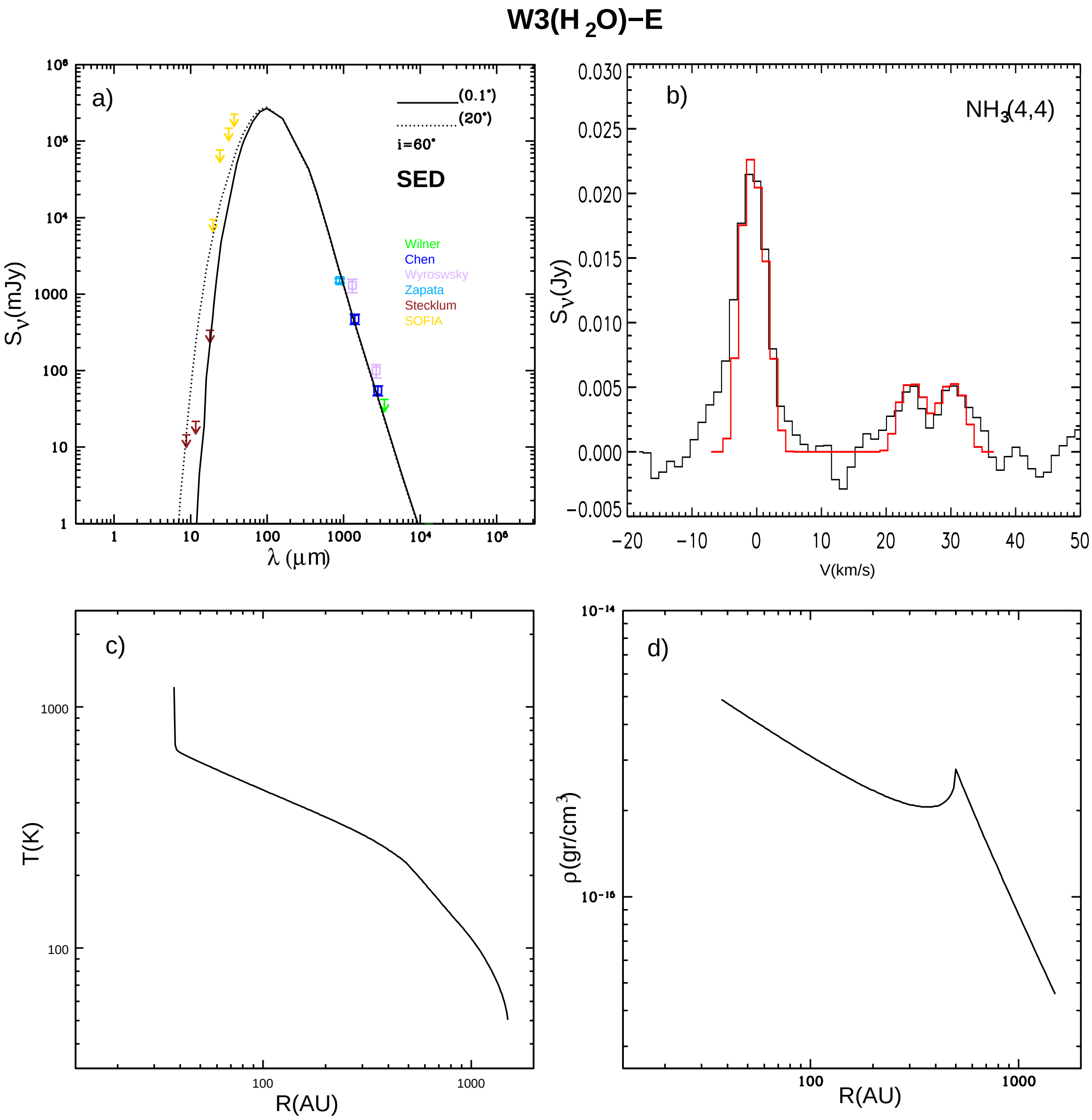

Figure 5.21: *(a)* Observed (symbols) and best-fit model (solid line) spectral energy distributions of W3(H_2O)-E. The data are from Chen et al. (2006), Wyrowski et al. (1997), Zapata et al. (2011), Wilner et al. (1995), Stecklum et al. (2002), and the SOFIA database. The dotted line, which clearly exceeds the mid-IR upper limits, represents the SED of the same model but with a cavity carved by an outflow of aperture angle 20°. *(b)* Observed (black line) and model (red line) spectra of the NH_3(4,4) transition. Emission has been integrated over a circular area of radius 0.″4 centered on the peak of the 3.6 source of Wilner et al. (1999). Velocities are relative to the systemic velocity of the core, assumed to be -49.8 km s^{-1}. *(c)* Temperature as a function of radius for the best-fit model. *(d)* Polar averaged density as a function of radius for the best-fit model.

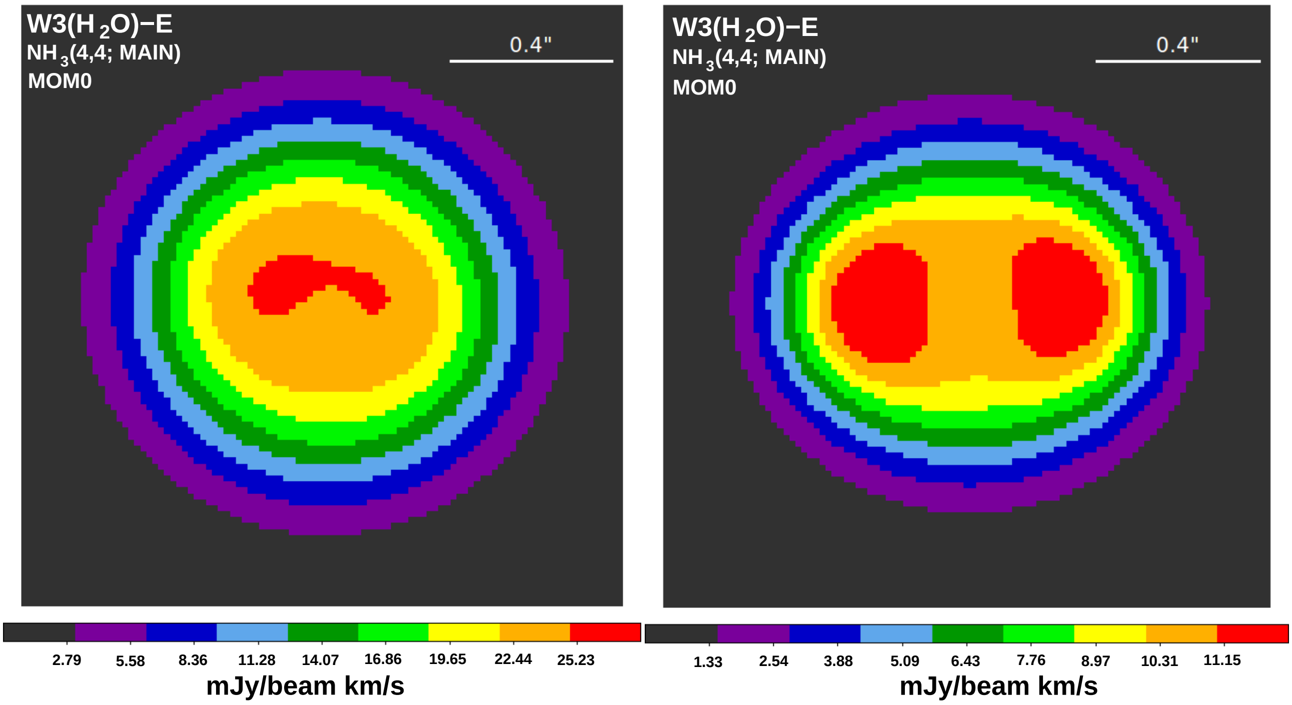

Figure 5.22: Synthetic integrated intensity map (zeroth-order moment) of the NH_3(4,4) main line (*left panel*) and satellite lines (*right panel*) for W3(H_2O)-E.

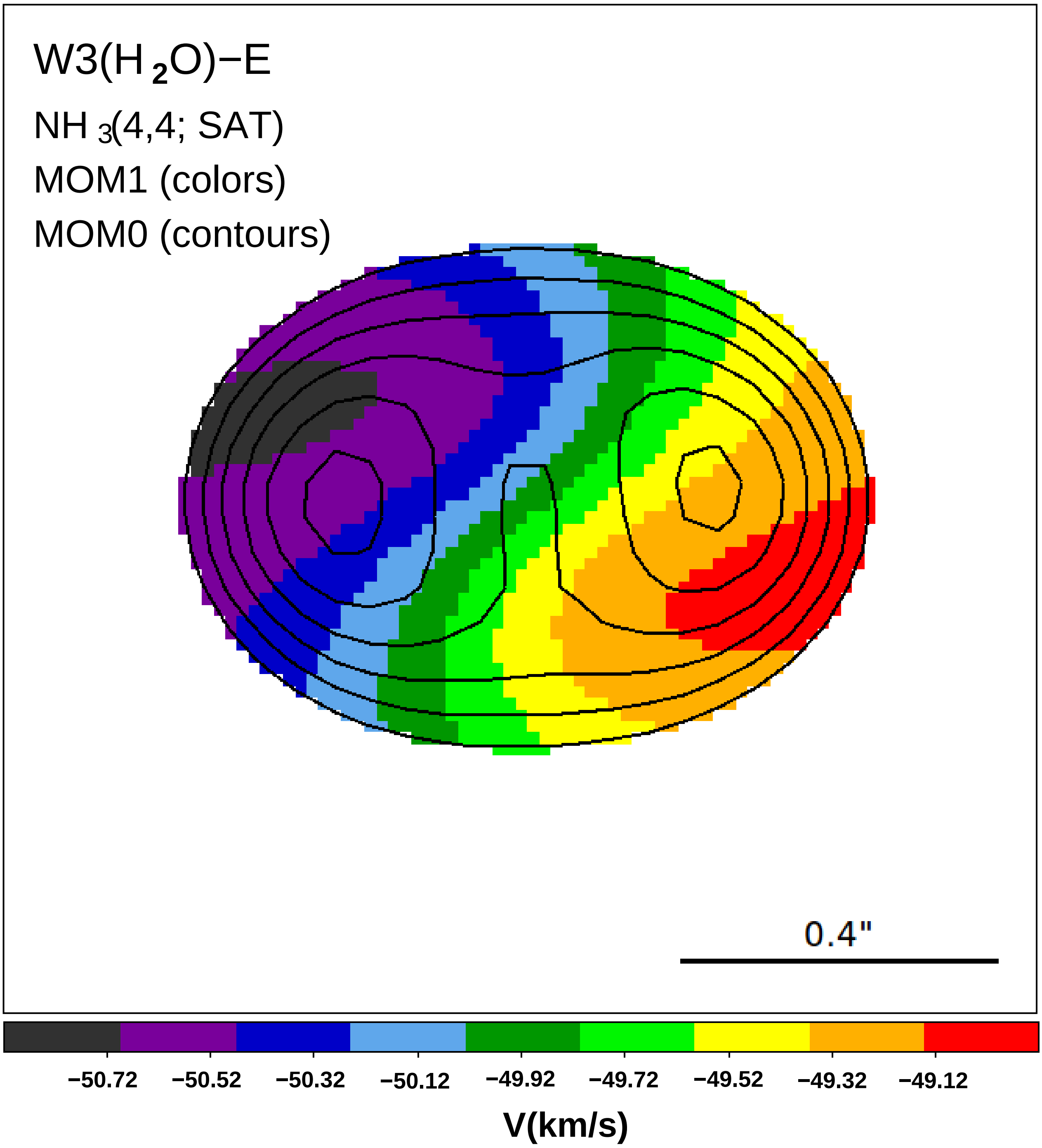

Figure 5.23: Synthetic intensity-weighted mean velocity map (first-order moment) of the NH_3(4,4) satellite lines (colors) overlapped on their synthetic integrated intensity map (contours), for W3(H2O)-E. Contour levels are 6.9, 8.1, 9.3, 10.6, 11.6, 12.9 mJy beam^{-1} km s^{-1}.

changes its orientation because of precession; or iii) the presence of a second, undetected source different from the jet driving source responsible for the CO outflow. Our results rule out their first two interpretations, and support the scenario of two distinct sources. In our interpretation, the outflow driving source is the same object that produces the submm emission and it is associated with most of the ammonia emission in W3(H_2O)-E. Additionally, the fact that the model predicts that the projection of the angular momentum along the LOS points towards us, together with fact that the peak E1 is red-shifted with respect to E2 implies that the blue-shifted lobe of the outflow is predicted to be at SW and the red-shifted lobe at NE. This is exactly what it is observed. Thus, the model successfully predicts the orientation of the outflow.

5.7 Discussion

We have studied the hot molecular core W3(H_2O) through high angular resolution ($\sim 0.3''$) VLA observations of the NH_3(4,4) inversion transition. We have detected main and satellite line emission from two molecular subcores, W3(H_2O)-E and W3(H_2O)-W, separated by $\sim 1''$ and whose LSR velocities differ by ~ 5 km s^{-1}. The dense molecular gas traced by the NH_3(4,4) satellite emission shows two local maxima and complex velocity gradients within each of the subcores. These velocity gradients do not follow the expected pattern of pure rotation or outflow. Also, the observed orientation of the structures is different in the main and satellite maps. We interpret such morphologies and velocity gradients as tracing infalling and rotating ammonia toroids around two young stellar objects.

We modeled W3(H_2O)-E and W3(H_2O)-W as flattened and rotating infalling structures of molecular gas using the TSC and sheet collapse models, respectively. From the physical structure obtained from these models we calculated the ammonia emission with our radiative transfer code. In this calculation we dropped to zero the ammonia abundance in the inner region in order to mimic the central hole of the ammonia toroids. Our models are able to: (i) Reproduce the SED and the NH_3(4,4) spectra; (ii) Reproduce the double-peak morphology of the NH_3(4,4) emission maps; (iii) Qualitatively explain the differences between the main and satellite line emission maps; and (iv) Reproduce the intensity-weighted mean velocity maps. We have obtained values of the (proto)stellar masses of 2.2 and 6 $M_\odot$ (typical of intermediate-mass stars), very high mass infall rates of 7.4×10^{-3} $M_\odot$ yr^{-1} and 9.8×10^{-3} $M_\odot$ yr^{-1} (typical of massive star-formation), and envelope masses of 20 and 16 $M_\odot$, for W3(H_2O)-E and W3(H_2O)-W respectively. We interpret these results as two accreting high-mass protostars that have not yet acquired most of its final mass from its surrounding envelope.

The rotation axes of the two flattened infalling structures we have modeled are aligned with the axes of the two highly collimated CO outflows present in the region. The models can successfully reproduce also the observed red-blue distribution of the CO outflow lobes. This suggest that the outflows are originally ejected in the same directions as are observed at large scale, with no change in direction.

We also conclude that at least two YSOs are present within the W3(H_2O)-E subcore. One of them, associated with the observed submillimeter source and located at the center of the flattened rotating double-peak ammonia structure, would be driving the CO outflow. The second YSO would be driving the observed synchrotron jet, whose center lays out of the double-peaked structure of the satellite line ammonia emission, and whose orientation (E-W) does not coincide with the CO outflow orientation.

The results of our modeling and radiative transfer calculations indicate that the orientation and morphology observed in molecular line maps of complex regions depend significantly on the optical depth of the observed transition, and may not reflect the actual orientation of the density structures that are tracing. We have also found that detailed models, taking properly into account the whole physical structure (velocity and temperature gradients, opacity effects,...) are required in order to obtain reliable values of parameters such as the mass, while simplified calculations can lead to very wrong estimates.

5.7.1 Comparison with previous ammonia observations

Wilson et al. (1993) observed the NH_3(1,1) and NH_3(2,2) transitions towards W3(H_2O) with the VLA in its D-configuration. Their beam size ($3\farcs8$) was too large to separate between the two cores. We have used the physical conditions inferred from our modeling to calculate with our radiative transfer code the NH_3(1,1) and NH_3(2,2) expected spectra over the whole region in order to compare them with the observational spectra of Wilson et al. (1993). The results are shown in Figure 5.24.

As can be seen in the figure, the predicted intensity is half that observed by Wilson et al. (1993) but the shape of the spectra is similar. Our synthetic spectra compare better with the observed ones than those obtained in the previous modeling by Osorio (2000). The deficit of emission in the model spectra can be due to the presence of an extended cold component that was not included in our model. Our models were aimed to fit the hot compact component that is traced by the high-angular resolution VLA B-configuration NH_3(4,4) observations, while the NH_3(1,1) and NH_3(2,2) VLA D-configuration observations are expected to be also sensitive to a colder extended component of gas with relative high ammonia abundances that is expected to surround the protostellar cores (Aikawa et al. 2012).

5.7.2 Comparison of our results with other calculations

We realize that the masses predicted by our models did not match well with previous estimates by other authors. Our model results predict (proto)stellar masses of 2.2 $M_\odot$ and 6 $M_\odot$, and envelope masses of 20 $M_\odot$ and 16 $M_\odot$, for W3(H_2O)-E and W3(H_2O)-W respectively. On the other hand, Chen et al. (2006) calculate envelope masses of 4-6 $M_\odot$ and 3-4 $M_\odot$, for W3(H_2O)-E and W3(H_2O)-W respectively, which they obtained by using spherically symmetric models and

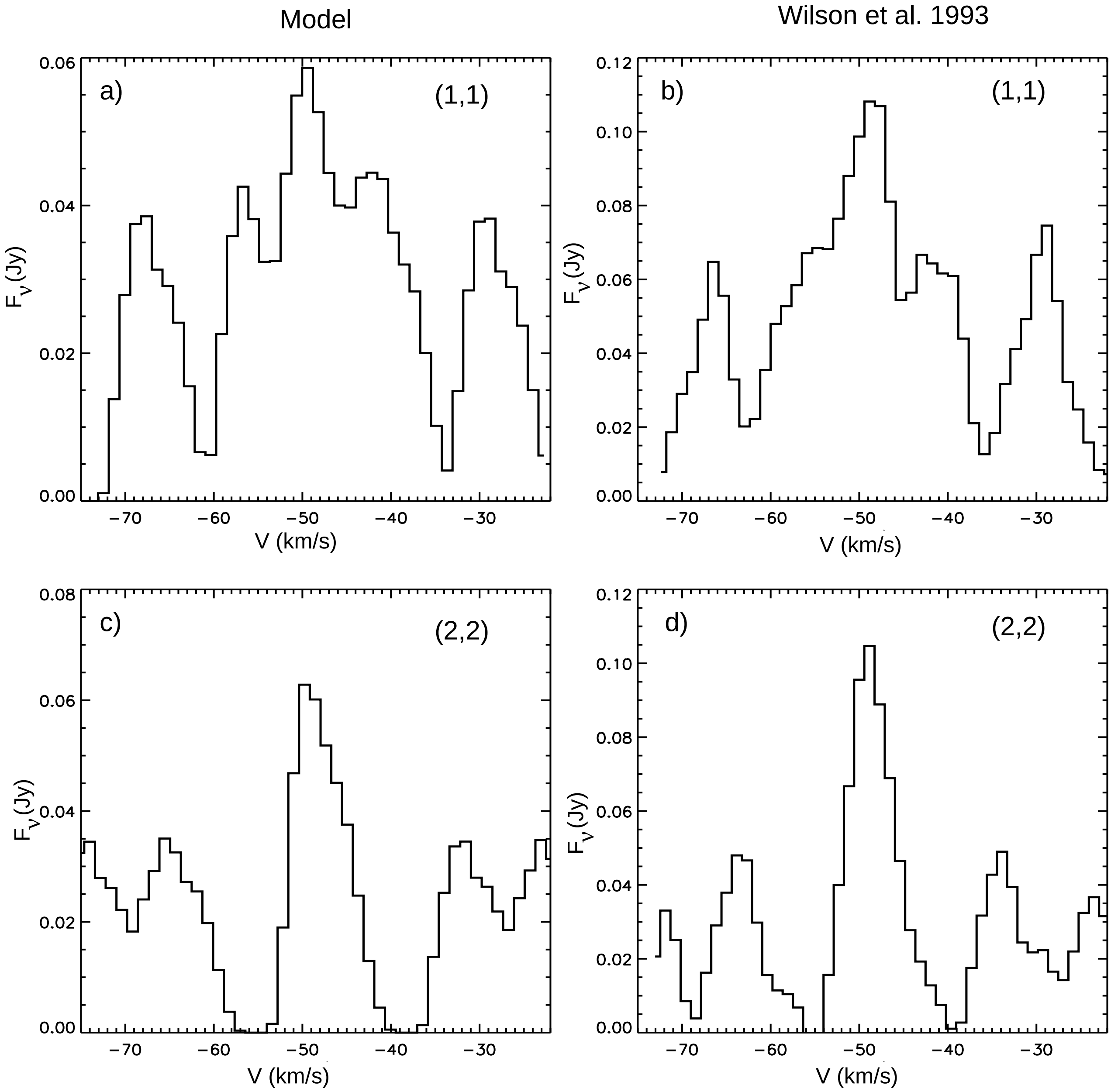

Figure 5.24: *(a)* Synthetic spectrum for the NH_3(1,1) inversion transition over the whole region W3(H_2O) as predicted by our models. *(b)* NH_3(1,1) spectrum towards W3(H_2O) observed by Wilson et al. (1993). Spectral Hanning smoothed was applied to the original spectra of Wilson et al. (1993). *(c)* Same as panel (a) but for the NH_3(2,2) inversion transition. *d)* same as panel (b) but for the NH_3(2,2) inversion transition.

assuming power-law dependences of density and temperature on radius. These authors fitted the continuum SEDs of the two cores and used CH_3CN line data to infer the physical properties of the envelopes, obtaining that the density distributions must be close to the free-fall case. The envelope masses obtained by Chen et al. (2006) are much lower than those obtained by our models. Nevertheless, their modeling is not as self-consistent as the TSC and the sheet formalisms we used in our fits, and the angular resolution of their CH_3CN observations ($\sim 1''$) is not high enough to properly separate W3(H_2O)-E and W3(H_2O)-W nor to resolve their internal kinematics. Our subarcsecond angular resolution NH_3(4,4) observations have shown that rotation motions are important, so the cores are likely far from being in a free-fall state, casting some doubts on their results.

Zapata et al. (2011) give dynamical masses of 13 and 4 $M_\odot$ for the protostars in W3(H_2O)-E and W3(H_2O)-W respectively, which they obtained from the velocity gradient observed in their methanol observations. However, these authors associate the submillimeter emission in the easternmost core with the jet-driving source, but our results (see Section 5.6) suggest that this submillimeter emission is associated with a different source, which is the driving source of the CO outflow. We believe that the velocity gradient detected by Zapata et al. (2011) towards W3(H_2O)-E does not trace rotation, but simply the velocity difference between the gas associated with two sources (the jet and the driving source of the CO outflow), so their mass calculation is flawed.

We note that even using the observed velocity gradients associated with the individual sources, a simple calculation of the dynamical mass assuming that the velocity gradient is due to Keplerian rotation, can give very inaccurate results. When a velocity gradient is detected observationally, it is common to assume that it is due to Keplerian rotation and to calculate the dynamical mass ($M_{\rm dyn}$) needed for equilibrium assuming that the separation between the two points with the largest difference in velocity is twice the radius of the rotating structure (R_o) and that the difference in velocity between these two points is twice the rotation velocity (V_r). The dynamical mass is calculated with the expression $M_{\rm dyn} = V_r^2 R_o/G \sin^2 i$. We used the velocity difference between the peaks of emission E1 and E2 (Figures 5.16) and its (projected) separation to perform the calculation of the dynamical mass in W3(H_2O)-E. We did the same for W3(H_2O)-W but using the velocity difference and distance between W1 and W2 (Figures 5.13). We obtained dynamical masses of 0.3 $M_\odot$ for W3(H_2O)-E and 0.5 $M_\odot$ for W3(H_2O)-W, assuming inclination angles of 60° and 50°, respectively. The values obtained for the dynamical masses are much smaller than the masses of the internal objects predicted by the models. This discrepancy led us to conclude that the expression $M_{\rm dyn} = V_r^2 R_o/G \sin^2 i$ can provide mass estimations that depart largely form the actual masses.

Our results indicate that simplified assumptions do not provide reliable masses, and that more detailed models, like the one presented here, are necessary to obtain appropriate physical parameters for this type of sources.

5.7.3 On the origin of the central ammonia hole. Other alternative scenarios

As mentioned above, the double peaks observed in the ammonia satellite emission maps have been considered to trace the points with the highest column density along the internal edges of a toroid (see Figure 5.17). In our interpretation, the toroid internal hole is produced by a sudden drop in the ammonia abundance. There are several examples in the literature of torus-like ammonia structures whose central hole has been attributed to a sudden decrease of ammonia abundance in the vicinity of the protostellar object (Mundy et al. 1990, Zhou et al. 1991, 1993a, Fuller & Wooten 2000). However, most of these cases correspond to low-mass protostars, where the ammonia abundance decrease can be explained in terms of freezout of the ammonia molecules onto the surface of dust grains (Aikawa et al. 2005). In the case of HMCs like W3(H_2O), where high temperatures are reached, ammonia molecules have been sublimated in the inner parts of the core and are found in the gas phase. Therefore, the former explanation is not applicable to high-mass protostars. However, ammonia toroids have also been observed around other massive protostars; for instance, through NH_3(1,1) observations towards IRAS 18196-1331 (Wang et al. 2007). Several studies suggest that the central hole in ammonia abundance can be caused by chemical reactions. Turner (1995) indicates that, very close to the star, ammonia is expected to be destroyed by a reaction with carbon ion. Lee, Bergin & Evans (2004) indicate that the CO, indirectly, is the major destroyer of NH_3 and found that the NH_3 abundance may drop by three orders of magnitude in a central region of the core that may have sizes of several hundreds of AU of radius.

There are other alternative mechanisms, in addition to chemistry, that are able to produce an internal hole in the ammonia emission. One of them has an excitation origin. Temperatures over 400 K move most of the ammonia population at high K metastable states, unpopulating the (4,4) level in favor of the (5,5), (7,7) and subsequent para-ammonia metastable levels. Note that in this case, there is no ammonia hole. Ammonia is still present in the inner region of the core, but the lowest excitation rotational states (including the (4,4) level) are unpopulated because of the high temperatures. To test this possibility we checked if the high temperatures in the inner region of the core predicted by the SED model would be able by themselves to unpopulate the (4,4) level, favoring other transitions in levels of higher excitation. To do so, we ran our radiative transfer code without any restriction in the ammonia abundance in the inner region of the core. A double-peak morphology was still detectable in the satellite line emission map due to the increase of density at the centrifugal radius. However, we were not able to reproduce the double-peak morphology observed in the main line maps, and the predicted main line spectra were too intense; therefore, this excitation effect was ruled out.

Other alternative scenarios involve the presence of an actual hole in the total gas density, not only in the ammonia distribution. For example, a bipolar outflow can sweep out the infalling material along the polar axis, creating cavities in the core. However, we rule out the outflow/cavity scenario because in order to produce the holes needed to fit the ammonia observations, outflow opening angles of $\sim 50^\circ$ would be required (Calvet et al. 1994), which is inconsistent with the high collimation of the molecular outflows observed in this region, as can be seen in the CO maps of Zapata et al. (2011).

Another scenario that can result in the creation of an actual hole in the gas distribution is the presence of a binary system. In a system consisting of a stellar binary surrounded by an accretion disk there is a continuous exchange of angular momentum between the binary and the disk. As the binary is orbiting with a shorter period than the disk material it is generating positive angular momentum waves in the disk which, upon dissipating, deposit their energy and angular momentum in the disk. Hence, there is a continuous transfer of angular momentum from the binary to the nearby outer disk. Upon receiving this angular momentum, the disk speeds up, and the material moves away from the binary, leaving a region of very low density around the central binary, a so called "inner gap". The width and form of the gap depends on disk parameters, such as the temperature and viscosity, and on the orbital parameters of the binary, such as separation or eccentricity (Artymowicz et al. 1991; Artymowicz & Lubow 1994). Artymowicz & Lubow (1994) and Escala et al. (2005) predict that a binary system maintains a central hole in the viscously relaxed disk with radius equal to about twice the binary semimajor axis. Then, wide binaries, which can have separations of a few hundred of AU (Tobin 2014), can account for holes with sizes of the order we need ($\sim$ 500 AU) to explain the observations. On this basis, we considered the possibility that the ammonia emission could be tracing an accretion circumbinary disk instead of an infalling and rotating envelope. However, we found that the difference in orientation between the main and the satellite line emissions depends on the degree of flattening of the rotating structure. The more spherical the structure, the larger the difference in orientation. Thus, to account for the observed difference in orientation we need of relatively spherical models ($\eta \leq 1$), suggesting that we are seeing the environmental cloud rather than an accretion disk, which is expected to be a flattened structure. Additionally, the observed intensity-weighted mean velocity maps (Figures 5.13 and 5.16) present velocity gradients that cannot be explained with pure rotation, a combination of infall and rotation motions is required.

We also considered the possibility that the four ammonia emission peaks, E1, E2, W1, and W2, were associated with four independent YSOs. In this scenario, there would be four independent ammonia condensations instead of two ammonia structures with central holes. If E1, E2, W1, and W2 were tracing the positions of four independent YSOs with similar properties, one would expect to observe four CO outflows instead of two. Furthermore, it would be difficult to explain the nature and location of the observed continuum sources (cm and submm), as none of them coincide in position with the ammonia emission peaks. The differences in morphology and orientation of the main and satellite line emissions would also be difficult to interpret.

Shchekinov & Sobolev (2004) suggested that the available observations (until that date) could be explained in a completely different scenario. These authors proposed the presence of a large (4000 AU) circumstellar disk, oriented E-W, with one or more stars within it. In this scenario the non-thermal emission (interpreted as a synchrotron jet by Reid et al. 1995) is interpreted as emission originated from the interaction of a stellar wind with an irregularity on the disk surface, and the western centimeter source would be part of the disk heated by internal stars. Under this interpretation the masers in the region would not be tracing an outflow but a molecular torus seen edge-on. However, this scenario could hardly explain the double-peak morphology of the ammonia emission or the complex kinematic structure observed by the intensity-weighted mean velocity maps (Figures 5.13 and 5.16).

Because of its capacity to explain the characteristics of the region, we favor an interpretation of the observed NH_3(4,4) emission as tracing flattened infalling and rotating structures with a central drop in ammonia abundance originated by chemical effects.

Despite the very good qualitative agreement between our model results and the observations, we note that there are some quantitative differences. For example, the intensity of the peaks in the synthetic NH_3(4,4) maps is a factor of two lower than in the observed maps, for both W3(H_2O)-W and W3(H_2O)-E. Also, the synthetic spectra for the whole W3(H_2O) region, calculated from our model for the NH_3(1,1) and NH_3(2,2) transitions, are less intense that those observed by Wilson et al. (1993). Nevertheless, the morphology of the maps and the shape of the line profiles are in good agreement with the observations. The lack of a detailed agreement may be a consequence of the somewhat "idealized" models that we used to interpret the data, such as the TSC and the sheet formalisms, that probably do not describe in full detail the real conditions of the rotating and collapsing molecular environment. Calculations probably could be improved, for instance, by relaxing the approximation of neglecting the envelope mass relative to the central object mass, the absence of viscosity, or the adoption of a 1D temperature field. The radiative transfer code that calculates the emergent ammonia emission could be improved also, for example, by using a better treatment of the ammonia excitation, and by considering the population of both metastable and non-metastable levels. Nevertheless, the formalisms adopted have been proved to be suitable in explaining quite well the main observational features in the case of collapse with rotation.

5.7.4 A proposed evolutionary scheme

It is worth noting that in the whole region comprising W3(H_2O) and W3(OH), with an extension of $\simeq$ 14000 AU in projected size, there are at least four distinct YSOs, each of them showing different characteristics. We speculate that the observed differences are due to differences in the evolutionary stage of these YSOs, and we propose the following sequence:

The youngest source would be the submillimeter source embedded in W3(H_2O)-E, which is not detected at centimeter wavelengths. The central mass is currently only 2.2 $M_\odot$, but there is still plenty of mass in the envelope to further increment the protostellar mass and to finally become a massive object. The infall and accretion processes are very intense and probably provide most of the luminosity of the core. Assuming that the infall rate (Table 5.1) is constant and that most of the infalling material is then accreted onto the protostar, we derive a protostellar age of $\sim$ 300 yr. The protostar would increment its mass through episodic events of high accretion from the disk, while the accretion disk accumulates mass from the infalling envelope. Since accretion is correlated with the presence of outflows, this object could be the driving source of the collimated molecular outflow detected in CO (Zapata et al. 2011).

The YSO in W3(H_2O)-W has already reached 6 $M_\odot$, almost three times the mass of the embedded source in W3(H_2O)-E. Using the same assumptions as in W3(H_2O)-E, we derive a protostellar age of $\sim$ 600 yr, older than that of the protostar in W3(H_2O)-E. The embedded YSO presents centimeter emission, and appears to be located between the two high-density peaks revealed by the ammonia emission. Wilner et al. (1999) found that the spectral index of the centimeter emission was compatible with that of an ionized stellar wind or unresolved jet.

A more evolved evolutionary stage may correspond to the source of the non-thermal jet, in the southern part of the W3(H_2O)-E core. This source appears to be associated with a smaller amount of dense gas (and probably also a smaller amount of dust), as the ammonia emission is weaker towards this object, possibly because its environmental cloud has mostly consumed.

Once the central star reaches a mass and temperature high enough to develop a significant flux of ionizing photons ($\lambda <$ 912 Å), it can photoionize the surrounding medium and create an UCHII region. W3(OH) would represent this evolutionary stage. The NH_3(4,4) absorption possibly is tracing a remaining toroidal structure of molecular gas around the star, which had mostly concentrated near the equatorial plane (red contours in Figure 5.3). The interaction of the inner part of the molecular torus with the ionized front may obstruct the expansion of the HII region, producing shocks that give rise to the OH masers that outline the inner edge of the torus (Menten et al. 1988, Fish & Sjouwerman 2007). After this phase, most of the material around the star will be blown away, revealing the star at optical wavelengths, and the source will become a classical HII region.

Our results suggest that at least four massive YSOs in different evolutionary stages are found in the region containing W3(OH) and W3(H_2O). Therefore, this region constitutes a very promising laboratory to study the early evolution of massive stars. Further high-angular resolution multiwavelength observations will be necessary to characterize individually these YSOs in order to better study the multiplicity in the region and the processes taking place in each individual source.

5.8 Conclusions

We have studied the hot molecular core W3(H_2O) through high angular resolution ($\sim 0.3''$) VLA observations of the NH_3(4,4) inversion transition. We have detected main and satellite line emission from two molecular subcores, W3(H_2O)-E and W3(H_2O)-W, separated by $\sim 1''$ and whose LSR velocities differ by $\sim$ 5 km s^{-1}. The dense molecular gas traced by the NH_3(4,4) satellite emission shows two local maxima and complex velocity gradientes within each of the subcores. These velocity gradients do not follow the expected pattern of pure rotation nor outflow. Also, the observed orientation of the structures is different in the main and satellite maps. We interpret such morphologies and velocity gradients as tracing infalling and rotating ammonia toroids around two young stellar objects.

We modeled W3(H_2O)-E and W3(H_2O)-W as flattened and rotating infalling structures of molecular gas using the TSC and sheet collapse models, respectively. From the physical structure obtained from these models we calculated the ammonia emission with our radiative transfer code. In this calculation we dropped to zero the ammonia abundance in the inner region in order to mimic the central hole of the ammonia toroids. Our models are able to: (i) Reproduce the SED and the NH_3(4,4) spectra; (ii) Reproduce the double-peak morphology of the NH_3(4,4) emission maps; (iii) Qualitatively explain the differences between the main and satellite line emission maps; and (iv) Reproduce the intensity-weighted mean velocity maps. We have obtained values of the (proto)stellar masses of 2.2 and 6 $M_\odot$ (typical of intermediate-mass stars), very high mass infall rates of 7.4×10^{-3} $M_\odot$ yr^{-1} and 9.8×10^{-3} $M_\odot$ yr^{-1} (typical of massive star-formation), and envelope masses of 20 and 16 $M_\odot$, for W3(H_2O)-E and W3(H_2O)-W respectively. We interpret these results as two accreting high-mass protostars that have not yet acquired most of its final mass from its surrounding envelope.

The rotation axes of the two flattened infalling structures we have modeled are aligned with the axes of the two highly collimated CO outflows present in the region. The models can successfully reproduce also the observed red-blue distribution of the CO outflow lobes. This suggest that the outflows are originally ejected in the same directions as are observed at large scale, with no change in direction.

We also conclude that at least two YSOs are present within the W3(H_2O)-E subcore. One of them, associated with the observed submillimeter source and located at the center of the flattened rotating double-peak ammonia structure, would be driving the CO outflow. The second YSO would be driving the observed synchrotron jet, whose center lays out of the double-peaked structure of the satellite line ammonia emission, and whose orientation (E-W) does not coincide with the CO outflow orientation.

The results of our modeling and radiative transfer calculations indicate that the orientation and morphology observed in molecular line maps of complex regions depend significantly on the optical depth of the observed transition, and may not reflect the actual orientation of the density structures that are tracing. We have also found that detailed models, taking properly into account the whole physical structure (velocity and temperature gradients, opacity effects,...) are required in order to obtain reliable values of parameters such as the mass, while simplified calculations can lead to very wrong estimates.

Chapter 6

Conclusions

In this thesis work we have studied the physical conditions of the ambient gas around massive (proto)stars paying special attention to its kinematics. This has been done in two ways. In a first theoretical part, we have considered different self-consistent models found in the literature to investigate the observable characteristic features resulting from the model kinematics. We have started our study using the 3D "spectral imaging infall signature" proposed by Anglada et al. (1991) (A91) using a simplified formalism. This signature describes which are the distinctive features of infall motions on the observed intensity images as a function of velocity (i.e., the channel maps, or $I_\nu(x, y, V)$) of molecular transitions. This signature predicts that for angularly resolved collapsing cores, if the line opacity is high enough, blue-shifted channels would present a centrally peaked spatial intensity distribution, while red-shifted channels would present an almost constant intensity distribution. Additionally, the emission would become more compact as the difference in velocity with respect to the systemic velocity of the cloud increases. In a second part, we have focused on the study of two particular hot molecular cores through observations of the NH_3 molecule. Our main findings can be summarized as follows:

We introduced a new signature of infall, the "central blue spot", consisting in a spot of blue-shifted emission in the first-order moment (intensity-weighted mean velocity map) towards the peak position of the zeroth-order moment (integrated intensity map). This signature is a result of the "spectral imaging infall signature" of A91, but it has the advantages of being easily identifiable and does not requiring of an accurate determination of the systemic velocity of the core.

We identified the signature of a rotating infalling core. The spatial intensity profile of the image in a given velocity channel is stretched towards the side where rotation has the same sign as the channel velocity, and it is shrunk on the opposite side. We conclude that rotation makes the spatial intensity profiles asymmetric with respect to the central position but it does not mask the A91 infall signatures.

We also found that rotation makes the "central blue spot" bluer and moves it off the center towards the blue rotating half of the core. Additionally, a "dimmer red spot" appears on the opposite side. As a consequence of this "blue spot and dimmer red spot pair", a cut along the equatorial direction will reveal a sequence of successive valleys (bluer values) and ridges (redder values) that we call the “roller-coaster” signature. We propose that the orientation of the “blue spot and dimmer red spot pair” or the appearance in a cut of the “roller-coaster” signature could be used in high angular resolution observations to infer the equatorial direction of an infalling and rotating core. These small-scale signatures are likely more reliable in tracing the rotation axis than large-scale velocity gradients.

We have analyzed the robustness of the (3D) “spectral imaging infall signature” of A91 for different models of collapsing star-forming cores. We have studied both the pre-stellar phase and the main accretion phase, taking special attention to possible differences between the models that start from equilibrium configurations and those that start from non-equilibrium configurations.

For the study of the prestellar phase, when the central object has not yet formed, we have taken the predicted physical characteristics of each model from their self-similar formalism. We have found that, because the excitation temperature is assumed to increase outwards (unless the thermalization condition is not fulfilled), for equilibrium models the spatial intensity profiles corresponding to blue-shifted velocities present a small dip towards the center, while for red-shifted velocities the intensity is expected to be higher and the spatial profiles to be flat. For the case of non-equilibrium initial conditions, the spatial intensity profiles of both red- and blue-shifted velocities present a dip towards the central position. However, these dips should be small because of the absence of an internal heating source in this phase, being difficult to detect observationally. So, we conclude that it is difficult to identify an unambiguous infall signature for the pre-stellar phase.

For the study of the main accretion phase we took three different approaches. We took a nondimensional approach, working on the space of the self-similar solutions, and using the simplified formalism of A91. We changed to physical functions and considered the case of the ammonia (4,4) inversion transition to define for each model the region where thermalization and high line opacity are fulfilled. Finally, we carried out the calculations using our radiative transfer code. The main conclusion is that the “spectral imaging infall signature” of A91 stands for all the collapse models studied, regardless of whether or not they evolve from equilibrium, as long as the cores are in the main accretion phase and the velocities considered are high enough. At lower velocities, differences between models starting from equilibrium (closed isovelocity surfaces, resulting in asymmetries between red and blue spatial intensity profiles) and those starting from non-equilibrium (open isovelocity surfaces, resulting in similar red and blue intensity profiles) should appear. However, these differences could be masked by the finite size of the emitting region that might truncate the outer closed isovelocity surfaces, resulting in similar red/blue spatial intensity profiles (both sharply increasing towards the center). It should be noted that these results are obtained for the ammonia molecule, which is a high density tracer and therefore is mainly sensitive to the most internal parts of the core. It is possible that another molecule, sensitive to lower densities, might be a better tracer of the outer layers of the core so that the whole extent of the low velocity V_z surfaces were fully contained within the emitting region. In that case, the detection of an asymmetry between the blue/red spatial intensity profiles at the lowest velocities would unambiguously rule out the “overdensity” rapid collapse model.

We obtained high angular resolution images of ammonia inversion transitions in the hot molecular core G31 HMC. We found that all the observed transitions (from the (2,2) to the (6,6)) show the “spectral imaging infall signature” proposed by A91. We also found that the “central blue spot” infall signature, introduced in this thesis, is present in all the observed ammonia transitions of G31 HMC. These signatures are robust infall signatures that have been observationally identified here for the first time. These signatures cannot be easily mimicked by other motions, and indicate that infall motions play a fundamental role in the gas kinematics of G31 HMC.

Our observations of G31 HMC provide specific information on the properties of the infalling envelope. There is a good quantitative agreement, both in the shape and range of values, between the spatial intensity profiles predicted by the SLS model for G31 HMC developed by Osorio et al. (2009) and those observed in the channel maps of all the ammonia inversion transitions. This is particularly remarkable, as only the SED and the spectra of a single transition were used in fitting the model parameters.

There is a long-standing debate regarding the nature (rotation vs. outflow) of the NE-SW velocity gradient observed in G31 HMC. We searched for the rotation signature introduced in this thesis by comparing radial intensity profiles averaged separately over the NE and SW halves of the source and we conclude that the rotation signature is present in G31 HMC. Unfortunately, only a spherically symmetric model for the physical structure of G31 HMC has been constructed so far (Osorio et al. 2009); therefore, we can only evaluate the effects of rotation in a qualitative way. We used the remaining signatures introduced in this thesis, together with a re-analysis of the CO outflow data, to determine more accurately the direction of the rotation axis. Our results suggest that the rotation and outflow axes lie roughly in the E-W direction, and we conclude that the controversial NE-SW large-scale velocity gradient observed in G31 HMC could be produced by the combination of rotation and outflow velocity gradients in this infalling core. We plan to extend our study by carrying out an integral model of the source, where the observational data are fitted to an infalling rotating envelope, similarly to what we have already done for the W3(H_2O) HMC.

We emphasize that G31 HMC is an exceptional source, with very strong molecular ammonia emission, making it possible to carry out high-angular resolution observations with a signal-to-noise ratio high enough to identify for the very first time the spectral imaging infall signatures in this source. The advent of large interferometers with improved sensitivity in the spectral line observing mode, such as the Atacama Large Millimeter/submillimeter Array (ALMA), or forthcoming facilities, such as the Square Kilometre Array (SKA) or the next generation Very Large Array (ngVLA), should make it possible to detect these signatures in weaker sources and to extend this kind of studies to a large sample of sources in the near future.

We have studied the hot molecular core W3(H_2O) through high angular resolution ($\sim 0.3''$) VLA observations of the $NH_3(4,4)$ inversion transition. We have detected main and satellite line emission from two molecular subcores, W3(H_2O)-E and W3(H_2O)-W, separated by $\sim 1''$ (~ 2000 AU) and with different LSR velocities. The dense molecular gas traced by the $NH_3(4,4)$ satellite emission shows two local maxima and complex velocity gradientes within each of the subcores. These velocity gradients do not follow the expected pattern of pure rotation or outflow. Also, the observed orientation of the structures is different in the main and satellite maps. We interpret such morphologies and velocity gradients as tracing infalling and rotating ammonia toroids around two young stellar objects.

We modeled W3(H_2O)-E and W3(H_2O)-W as flattened and rotating infalling structures of molecular gas using the TSC and sheet collapse models, respectively, but dropping to zero the ammonia abundance in the inner region in order to mimic the central hole of the ammonia toroids. Our models are able to: (i) Reproduce the SED and the $NH_3(4,4)$ spectra; (ii) Reproduce the double-peak morphology of the $NH_3(4,4)$ emission maps; (iii) Qualitatively explain the differences between the main and satellite line emission maps; (iv) Reproduce the intensity-weighted mean velocity maps; and (v) Reproduce the orientation and the blue-red lobe distribution of the two highly collimated CO outflows present in the region. We have obtained values of the (proto)stellar masses typical of intermediate-mass stars, very high mass infall rates typical of massive star-formation, and large envelope masses compared with the masses of the central objects. We interpret these results as two accreting high-mass protostars that have not yet acquired most of its final mass from its surrounding envelope. Our results also suggest that the outflows are originally ejected in the same directions as are observed at large scale, with no change in direction. We also conclude that at least two young stellar objects are present within the W3(H_2O)-E subcore, one of them associated with a submillimeter source and the modeled ammonia structure, would be driving the CO outflow, while second, more evolved object would be driving the observed synchrotron jet.

The results of our modeling and radiative transfer calculations indicate that the orientation and morphology observed in molecular line maps of complex regions depend significantly on the optical depth of the observed transition, and may not reflect the actual orientation of the density structures that are tracing. We have also found that detailed models, taking properly into account the whole physical structure (velocity and temperature gradients, opacity effects,...) are required in order to obtain reliable values of parameters such as the mass, while simplified calculations can lead to very wrong estimates.

Bibliography

Adams, F. C., Lada, C. J., & Shu, F. H. 1987, ApJ, 312, 788

Adams, J. D., Herter, T. L., Osorio, M., et al. 2012, ApJL, 749, L24

Adelson, L. M., & Leung, C. M. 1988, MNRAS, 235, 349

Aikawa, Y., Herbst, E., Roberts, H., & Caselli, P. 2005, ApJ, 620, 330

Aikawa, Y., Wakelam, V., Hersant, F., Garrod, R. T., & Herbst, E. 2012, ApJ, 760, 40

Alcolea, J., Menten, K. M., Moran, J. M., & Reid, M. J. 1993, Astrophysical Masers, 412, 225

Allen, A., Li, Z.-Y., & Shu, F. H. 2003, ApJ, 599, 363

Allen, A., Shu, F. H., & Li, Z.-Y. 2003, ApJ, 599, 351

Alves, J. F., Lada, C. J., & Lada, E. A. 2001, Nature, 409, 159

André, P., Belloche, A., Motte, F., & Peretto, N. 2007, A&A, 472, 519

André, P., Ward-Thompson, D., & Barsony, M. 1993, ApJ, 406, 122

Anglada, G. 1995, Revista Mexicana de Astronomia y Astrofisica Conference Series, 1, 67

Anglada, G. 1996, Radio Emission from the Stars and the Sun, 93, 3

Anglada, G., Estalella, R., López, R., Rodríguez, L.F., & Cantó, J., 1991, A&A, 252, 639 (A91)

Anglada, G., Rodríguez, L. F., Cantó, J., Estalella, R., & López, R., 1987, A&A, 186, 280

Anglada, G., Rodríguez, L. F., & Carrasco-Gonzalez, C. 2015, Advancing Astrophysics with the Square Kilometre Array (AASKA14), 121

Anglada, G., Rodriguez, L. F., Canto, J., Estalella, R., & Torrelles, J. M. 1992, Apj, 395, 494

Anglada, G., Villuendas, E., Estalella, R., et al. 1998, AJ, 116, 2953

Antoniucci, S., Nisini, B., Giannini, T., & Lorenzetti, D. 2008, A&A, 479, 503

Araya, E., Hofner, P., Kurtz, S., Olmi, L., & Linz, H. 2008, ApJ, 675, 420

Artymowicz, P., Clarke, C. J., Lubow, S. H., & Pringle, J. E. 1991, ApJ, 370, L35

Artymowicz, P., & Lubow, S. H. 1994, ApJ, 421, 651

Bachiller, R., Martin-Pintado, J., & Fuente, A. 1993, ApJ, 417, L45

Bacmann, A., André, P., Puget, J.-L., et al. 2000, A&A, 361, 555

Bacmann, A., André, P., & Ward-Thompson, D. 2001, From Darkness to Light: Origin and Evolution of Young Stellar Clusters, 243, 113

Ballesteros-Paredes, J., Gazol, A., Kim, J., et al. 2006, ApJ, 637, 384

Ballesteros-Paredes, J., Klessen, R. S., & Vázquez-Semadeni, E. 2003, ApJ, 592, 188

Ballesteros-Paredes, J., Vázquez-Semadeni, E., & Scalo, J. 1999, ApJ, 515, 286

Bate, M. R. 1998, ApJ, 508, L95

Baudry, A., & Diamond, P. J. 1998, A&A, 331, 697

Baudry, A., & Menten, K. M. 1995, A&A, 298, 905

Beltrán, M. T., Cesaroni, R., Codella, C., et al. 2006, Nature, 443, 427

Beltrán, M. T., Cesaroni, R., Neri, R., et al. 2005, A&A, 435, 901

Beltrán, M. T., Cesaroni, R., Neri, R., & Codella, C. 2011, A&A, 525, A151

Beltrán M. T., Cesaroni R., Neri R., Codella C., Furuya R. S., Testi L., Olmi L., 2004, ApJ, 601, L187

Beltran, M. T., & de Wit, W. J. 2015, arXiv:1509.08335

Beltrán, M. T., Estalella, R., Anglada, G., Rodríguez, L. F., & Torrelles, J. M. 2001, AJ, 121, 1556

Beuther, H., Churchwell, E. B., McKee, C. F., & Tan, J. C. 2007, Protostars and Planets V, 165

Beuther, H., Hunter, T. R., Zhang, Q., et al. 2004, ApJ, 616, L23

Beuther, H., Schilke, P., Gueth, F., et al. 2002a, A&A, 387, 931

Beuther, H., Schilke, P., Menten, K. M., et al. 2002b, ApJ, 566, 945

Beuther, H., & Walsh, A. J. 2008, ApJ, 673, L55

Bloemhof, E. E., Reid, M. J., & Moran, J. M. 1992, ApJ, 397, 500

Bodenheimer, P., Burkert, A., Klein, R. I., & Boss, A. P. 2000, Protostars and Planets IV, 675

Bonnell, I. A., & Bate, M. R. 2006, MNRAS, 370, 488

Bonnell, I. A., Bate, M. R., & Zinnecker, H. 1998, MNRAS, 298, 93

Bonnell, I. A., & Davies, M. B. 1998, MNRAS, 295, 691

Bonnell, I. A., Vine, S. G., & Bate, M. R. 2004, MNRAS, 349, 735

Bonnor, W. B. 1956, MNRAS, 116, 351

Boss, A. P. 1993, ApJ, 410, 157

Bourke, T. L., Myers, P. C., Robinson, G., & Hyland, A. R. 2001, ApJ, 554, 916

Briggs, D. S. 1995, Bulletin of the American Astronomical Society, 27, #112.02

Burrows, C. J., Stapelfeldt, K. R., Watson, A. M., et al. 1996, ApJ, 473, 437

Cabrit, S. 2007, Lecture Notes in Physics, Berlin Springer Verlag, 723, 21

Cabrit, S., & Bertout, C. 1992, A&A, 261, 274

Calvet, N., Hartmann, L., Kenyon, S. J., & Whitney, B. A. 1994, ApJ, 434, 330

Campbell, M. F., Lester, D. F., Harvey, P. M., & Joy, M. 1989, ApJ, 345, 298

Carey, S. J., Clark, F. O., Egan, M. P., et al. 1998, ApJ, 508, 721

Carrasco-González, C. 2010, Ph.D. Thesis, University of Granada

Carrasco-González, C., Osorio, M., Anglada, G., et al. 2012, ApJ, 746, 71

Caselli, P., & Myers, P. C. 1995, ApJ, 446, 665

Cassen, P., & Moosman, A. 1981, Icar, 48, 353

Cesaroni, R., Beltrán, M. T., Zhang, Q., Beuther, H., & Fallscheer, C. 2011, A&A, 533, A73

Cesaroni, R., Churchwell, E., Hofner, P., Walmsley, C.M., Kurtz, S. 1994, A&A, 288, 903

Cesaroni, R., Felli, M., Jenness, T., et al. 1999, A&A, 345, 949

Cesaroni, R., Hofner, P., Araya, E., & Kurtz, S. 2010, A&A, 509, A50

Cesaroni, R., Hofner, P., Walmsley, C. M., & Churchwell, E. 1998, A&A, 331,709

Cesaroni R., Walmsley C. M., Churchwell E., 1992, A&A, 256, 618

Chandrasekhar, S., & Fermi, E. 1953, ApJ, 118, 116

Chen, H.-R., Welch, W. J., Wilner, D. J., & Sutton, E. C. 2006, ApJ, 639, 975

Cheng, A. F. 1978, ApJ, 221, 320

Cheung, A. C., Rank, D. M., Townes, C. H., Knowles, S. H., & Sullivan, W. T., III 1969, ApJ, 157, L13

Churchwell, E. 1997, ApJ, 479, L59

Churchwell E., Walmsley C. M., Cesaroni R., 1990, A&AS, 83, 119

Crutcher, R. M. 1999, ApJ, 520, 706

Crutcher, R. M., & Troland, T. H. 2000, ApJ, 537, 139

Crutcher, R. M., & Troland, T. H. 2008, ApJ, 685, 281

Curiel, S., Rodriguez, L. F., Bohigas, J., et al. 1989, Astrophysical Letters and Communications, 27, 299

Danby, G., Flower, D. R., Valiron, P., Schilke, P., & Walmsley, C. M. 1988, MNRAS, 235, 229

Davis, C. J., Varricatt, W. P., Todd, S. P., & Ramsay Howat, S. K. 2004, A&A, 425, 981

De Buizer, J. M., Osorio, M., & Calvet, N. 2005, ApJ, 635, 452

de Gregorio-Monsalvo, I., Ménard, F., Dent, W., et al. 2013, A&A, 557, A133

Di Francesco, J., Myers, P. C., Wilner, D. J., Ohashi, N., & Mardones, D. 2001, ApJ, 562, 770

Dobbs, C. L., Bonnell, I. A., & Clark, P. C. 2005, MNRAS, 360, 2

Dreher, J. W., & Welch, W. J. 1981, ApJ, 245, 857

Dzib, S. A., Rodríguez-Garza, C. B., Rodríguez, L. F., et al. 2013, ApJ, 772, 151

Ebert, R. 1957, Z. Astrophys., 42, 263

Eddington, A. S. 1924, MNRAS, 84, 308

Egan, M. P., Shipman, R. F., Price, S. D., et al. 1998, ApJ, 494, L199

Escala, A., Larson, R. B., Coppi, P. S., & Mardones, D. 2005, ApJ, 630, 152

Estalella, R. & Anglada, G. 1999

Estalella, R., Mauersberger, R., Torrelles, J. M., et al. 1993, ApJ, 419, 698

Etoka, S., Cohen, R. J., & Gray, M. D. 2005, MNRAS, 360, 1162

Evans, N. J., II, Rawlings, J. M. C., Shirley, Y. L., & Mundy, L. G. 2001, ApJ, 557, 193

Fatuzzo, M., Adams, F. C., & Myers, P. C. 2004, ApJ, 615, 813

Fish, V. L., Brisken, W. F., & Sjouwerman, L. O. 2006, ApJ, 647, 418

Fish, V. L., & Sjouwerman, L. O. 2007, ApJ, 668, 331

Foster, P. N., & Chevalier, R. A. 1993, ApJ, 416, 303

Fuller G. A., Williams S. J., Sridharan T. K., 2005, A&A, 442, 949

Fuller, G. A., & Wootten, A. 2000, ApJ, 534, 854

Furlan, E., Megeath, S. T., Osorio, M., et al. 2014, ApJ, 786, 26

Furuya, R. S., Cesaroni, R., Takahashi, S., et al. 2008, ApJ, 673, 363

Galli, D., & Shu, F. H. 1993a, ApJ, 417, 220

Galli, D., & Shu, F. H. 1993b, ApJ, 417, 243

Gao, Y., Lou, Y.-Q., & Wu, K. 2009, MNRAS, 400, 887

Garay, G., & Lizano, S. 1999, PASP, 111, 1049

Garay, G., Ramirez, S., Rodriguez, L. F., Curiel, S., & Torrelles, J. M. 1996, ApJ, 459, 193

Garay, G., Rodriguez, L. F., Moran, J. M., & Churchwell, E. 1993, ApJ, 418, 368

Gaume, R. A., & Mutel, R. L. 1987, ApJS, 65, 193

Gibb, A. G., Wyrowski, F., & Mundy, L. G. 2004, ApJ, 616, 301

Girart, J. M., Beltrán, M. T., Zhang, Q., Rao, R., & Estalella, R. 2009, Science, 324, 1408

Girichidis, P., Federrath, C., Banerjee, R., & Klessen, R. S. 2011, MNRAS, 413, 2741

Goldreich, P., & Kwan, J. 1974, ApJ, 189, 441

Gómez, J. F., Sargent, A. I., Torrelles, J. M., et al. 1999, ApJ, 514, 287

Goodman, A. A., Benson, P. J., Fuller, G. A., & Myers, P. C. 1993, ApJ, 406, 528

Gouliermis, D., Keller, S. C., Kontizas, M., Kontizas, E., & Bellas-Velidis, I. 2004, A&A, 416, 137

Gregersen, E. M., & Evans, N. J., II 2000, ApJ, 538, 260

Gregersen, E. M., Evans, N. J., II, Zhou, S., & Choi, M. 1997, ApJ, 484, 256

Gregersen, E. M., Mardones, D., Evans, N. J., II, et al. 2000, Bulletin of the American Astronomical Society, 32, 1286

Hachisuka, K., Brunthaler, A., Menten, K. M., et al. 2006, ApJ, 645, 337

Harper, D. A. 1974, ApJ, 192, 557

Hartmann, L. 1998, Accretion processes in star formation / Lee Hartmann. Cambridge, UK ; New York : Cambridge University Press, 1998. (Cambridge astrophysics series ; 32) ISBN 0521435072.,

Hartmann, L. 2008, Accretion Processes in Star Formation, by Lee Hartmann, Cambridge, UK: Cambridge University Press, 2008,

Hartmann, L., Boss, A., Calvet, N., & Whitney, B. 1994, ApJ, 430, L49

Hartmann, L., & Burkert, A. 2007, ApJ, 654, 988

Hartmann, L., Calvet, N., & Boss, A. 1996, ApJ, 464, 387

Heiles, C., Goodman, A. A., McKee, C. F., & Zweibel, E. G. 1993, Protostars and Planets III, 279

Heitsch, F., Mac Low, M.-M., & Klessen, R. S. 2001, ApJ, 547, 280

Herbst, E. 1994, The Structure and Content of Molecular Clouds, 439, 29

Herbst, E., & Klemperer, W. 1973, ApJ, 185, 505

Hillenbrand, L. A., & Hartmann, L. W. 1998, ApJ, 492, 540

Ho, P. T. P. 1977, Ph.D. thesis, Massachusetts Institute of Technology

Ho, P. T. P., & Haschick, A. D. 1981, ApJ, 248, 622

Ho, P. T. P., & Townes, C. H. 1983, ARA&A, 21, 239

Ho, P. T. P., & Young, L. M. 1996, ApJ, 472, 742

Holden, L., Hoppins, K., Baxter, B., & Fatuzzo, M. 2009, PASP, 121, 485

Hosokawa, T., & Omukai, K. 2008, Massive Star Formation: Observations Confront Theory, 387, 255

Hunter, C. 1977, ApJ, 218, 834

Jeans, J. H. 1902, Royal Society of London Philosophical Transactions Series A, 199, 1

Jeans, J. H. 1928, Cambridge [Eng.] The University press, 1928.

Jijina, J., & Adams, F. C. 1996, ApJ, 462, 874

Jijina, J., Myers, P. C., & Adams, F. C. 1999, ApJS, 125, 161

Kahn, F. D. 1974, A&A, 37, 149

Kandori, R., Nakajima, Y., Tamura, M., et al. 2005, AJ, 130, 2166

Kenyon, S. J., Calvet, N., & Hartmann, L. 1993, ApJ, 414, 676

Kenyon, S. J., Hartmann, L. W., Strom, K. M., & Strom, S. E. 1990, AJ, 99, 869

Keto, E. 2007, ApJ, 666, 976

Keto, E., & Caselli, P. 2008, ApJ, 683, 238

Keto, E., & Caselli, P. 2010, MNRAS, 402, 1625

Keto, E., & Field, G. 2005, ApJ, 635, 1151

Keto, E. R., Ho, P. T. P., & Haschick, A. D. 1987, ApJ, 318, 712

Keto, E. R., Ho, P. T. P., & Haschick, A. D. 1988, ApJ, 324, 920

Keto, E., & Wood, K. 2006, ApJ, 637, 850

Kim, S.-J., Kim, H.-D., Lee, Y., et al. 2006, ApJS, 162, 161

Kitamura, Y., Momose, M., Yokogawa, S., et al. 2002, ApJ, 581, 357

Klaassen, P. D., & Wilson, C. D. 2007, ApJ, 663, 1092

Klessen, R. S. 2000, ApJ, 535, 869

Klessen, R. S., Ballesteros-Paredes, J., Vázquez-Semadeni, E., & Durán-Rojas, C. 2005, ApJ, 620, 786

Klessen, R. S., & Burkert, A. 2000, ApJS, 128, 287

Klessen, R. S., & Burkert, A. 2001, ApJ, 549, 386

Klessen, R. S., Burkert, A., & Bate, M. R. 1998, ApJ, 501, L205

Konigl, A., & Pudritz, R. E. 2000, Protostars and Planets IV, 759

Krumholz, M. R. 2006, ApJ, 641, L45

Krumholz, M. R., Klein, R. I., & McKee, C. F. 2005a, Massive Star Birth: A Crossroads of Astrophysics, 227, 231

Krumholz, M. R., Klein, R. I., McKee, C. F., Offner, S. S. R., & Cunningham, A. J. 2009, Science, 323, 754

Krumholz, M. R., & McKee, C. F. 2008, Nature, 451, 1082

Krumholz, M. R., McKee, C. F., & Klein, R. I. 2005b, Nature, 438, 332

Krumholz, M. R., McKee, C. F., & Klein, R. I. 2005c, ApJ, 618, L33

Kuiper, R., Klahr, H., Beuther, H., & Henning, T. 2012, A&A, 537, A122

Kuiper, R., Klahr, H., Beuther, H., Henning, T., & Yorke, H. W. 2013, Protostars and Planets VI Posters, 47

Kurtz, S., Cesaroni, R., Churchwell, E., Hofner, P., & Walmsley, C. M. 2000, Protostars and Planets IV, 299

Lada, C. J. 1987, Star Forming Regions, 115, 1

Larson, R. B. 1969, MNRAS, 145, 271

Larson, R. B. 1972, MNRAS, 157, 121

Larson, R. B. 1981, MNRAS, 194, 809

Larson, R. B. 1982, Annals of the New York Academy of Sciences, 395, 274

Larson, R. B. 1985, MNRAS, 214, 379

Larson, R. B., & Starrfield, S. 1971, A&A, 13, 190

Lee, C.-F., Hirano, N., Palau, A., et al. 2009, ApJ, 699, 1584

Lee, C.-F., Ho, P. T. P., Bourke, T. L., et al. 2008, ApJ, 685, 1026

Lee, C. W., Myers, P. C., & Tafalla, M. 1999, ApJ, 526, 788

Lee, C. W., Myers, P. C., & Tafalla, M. 2001, ApJS 136, 703

Lee, J.-E., Bergin, E. A., & Evans, N. J., II 2004, ApJ, 617, 360

Leung, C. M., & Brown, R. L. 1977, ApJ, 214, L73

Li, Z.-Y., & Shu, F. H. 1996, ApJ, 472, 211

Li, Z.-Y., & Shu, F. H. 1997, ApJ, 475, 237

Lizano, S., & Shu, F. H. 1989, ApJ, 342, 834

Lodato, G., & Facchini, S. 2013, MNRAS, 433, 2157

Lodato, G., & Price, D. J. 2010, MNRAS, 405, 1212

Lodato, G., & Pringle, J. E. 2007, MNRAS, 381, 1287

Lou, Y.-Q., & Shen, Y. 2004, MNRAS, 348, 717

Lou, Y.-Q., & Wang, W.-G. 2006, MNRAS, 372, 885

Mac Low, M.-M., & Klessen, R. S. 2004, Reviews of Modern Physics, 76, 125

Mardones, D., Myers, P. C., Tafalla, M., et al. 1997, ApJ, 489, 719

Martí, J., Rodríguez, L. F., & Reipurth, B. 1993, ApJ, 416, 208

Matsumoto, N., Honma, M., Isono, Y., et al. 2011, PASJ, 63, 1345

Mauersberger, R., Henkel, C., Weiß, A., Peck, A. B., & Hagiwara, Y. 2003, A&A, 403, 561

Mayen-Gijon, J. M., Anglada, G., Osorio, M., et al. 2014, MNRAS, 437, 3766

McKee, C. F., & Offner, S. S. R. 2010, ApJ, 716, 167

McKee, C. F., & Tan, J. C. 2002, Nature, 416, 59

McKee, C. F., & Tan, J. C. 2003, ApJ, 585, 850

McKee, C. F., & Zweibel, E. G. 1995, ApJ, 440, 686

McKee, C. F., Zweibel, E. G., Goodman, A. A., & Heiles, C. 1993, Protostars and Planets III, 327

McLaughlin, D. E., & Pudritz, R. E. 1996, ApJ, 469, 194

McLaughlin, D. E., & Pudritz, R. E. 1997, ApJ, 476, 750

Menten, K. M., Johnston, K. J., Wadiak, E. J., Walmsley, C. M., & Wilson, T. L. 1988, ApJ, 331, L41

Mestel, L., & Spitzer, L., Jr. 1956, MNRAS, 116, 503

Mezger, P. G., Altenhoff, W., Schraml, J., et al. 1967, ApJ, 150, L157

Millar, T. J., MacDonald, G. H., & Gibb, A. G. 1997, A&A, 325, 1163

Motte, F., & André, P. 2001, A&A, 365, 440

Moscadelli, L., Li, J. J., Cesaroni, R., et al. 2013, A&A, 549, A122

Moscadelli, L., Xu, Y., & Chen, X. 2010, ApJ, 716, 1356

Mouschovias, T. C. 1977, ApJ, 211, 147

Mouschovias, T. C. 1991, NATO ASIC Proc. 342: The Physics of Star Formation and Early Stellar Evolution, 61

Mouschovias, T. C., & Spitzer, L., Jr. 1976, ApJ, 210, 326

Mueller, K. E., Shirley, Y. L., Evans, N. J., II, & Jacobson, H. R. 2002, Hot Star Workshop III: The Earliest Phases of Massive Star Birth, 267, 395

Mundy, L. G., Wootten, H. A., & Wilking, B. A. 1990, ApJ, 352, 159

Myers, P. C., Fuller, G. A., Goodman, A. A., & Benson, P. J. 1991, ApJ, 376, 561

Myers, P. C., & Goodman, A. A. 1988, ApJ, 329, 392

Myers, P. C., Mardones, D., Tafalla, M., Williams, J. P., & Wilner, D. J. 1996, ApJ, 465, L133

Nagayama, T., Omodaka, T., Handa, T., et al. 2009, PASJ, 61, 1023

Nakamura, F., & Li, Z.-Y. 2005, ApJ, 631, 411

Nakano, T. 1989, ApJ, 345, 464

Nakano, T., Hasegawa, T., & Norman, C. 1995, ApJ, 450, 183

Narayanan, G., & Walker, C. K. 1998, ApJ, 508, 780

Nelson, R. P., & Papaloizou, J. C. B. 1999, MNRAS, 309, 929

Ogino, S., Tomisaka, K., & Nakamura, F. 1999, PASJ, 51, 637

Oka, T., Shimizu, F. O., Shimizu, T., & Watson, J. K. G. 1971, ApJ, 165, L15

Olmi, L., Cesaroni, R., Neri, R., & Walmsley, C. M. 1996, A&A, 315, 565

Osorio, M. 2000, Ph.D. Thesis,

Osorio, M., Anglada, G., Lizano, S., & D'Alessio, P. 2009, ApJ, 694, 29

Osorio, M., D'Alessio, P., Muzerolle, J., Calvet, N., & Hartmann, L. 2003, ApJ, 586, 1148

Osorio, M., Lizano, S., & D'Alessio, P. 1999, ApJ, 525, 808

Ostriker, E. C., & Shu, F. H. 1995, ApJ, 447, 813

Padgett, D. L., Brandner, W., Stapelfeldt, K. R., et al. 1999, AJ, 117, 1490

Padoan, P., Juvela, M., Goodman, A. A., & Nordlund, Å. 2001a, ApJ, 553, 227

Padoan, P., Nordlund, Å., Rögnvaldsson, Ö. E., & Goodman, A. 2001b, From Darkness to Light: Origin and Evolution of Young Stellar Clusters, 243, 279

Palla, F., & Stahler, S. W. 1993, ApJ, 418, 414

Papaloizou, J. C. B., & Lin, D. N. C. 1995, ApJ, 438, 841

Patel, N. A., Curiel, S., Sridharan, T. K., et al. 2005, Nature, 437, 109

Penston, M. V. 1969, MNRAS, 144, 425

Perault, M., Omont, A., Simon, G., et al. 1996, A&A, 315, L165

Peretto, N., Hennebelle, P., & André, P. 2007, A&A, 464, 983

Pillai, T., Wyrowski, F., Carey, S. J., & Menten, K. M. 2006, A&A, 450, 569

Plume, R., Jaffe, D. T., Evans, N. J., II, Martín-Pintado, J., & Gómez-González, J. 1997, ApJ, 476, 730

Prasad, S. S., Tarafdar, S. P., Villere, K. R., & Huntress, W. T., Jr. 1987, Interstellar Processes, 134, 631

Preibisch, T., Weigelt, G., & Zinnecker, H. 2001, The Formation of Binary Stars, 200, 69

Purcell, C. R., Balasubramanyam, R., Burton, M. G., et al. 2006, MNRAS, 367, 553

Raga, A., & Cabrit, S. 1993, A&A, 278, 267

Raga, A. C., Canto, J., Calvet, N., Rodriguez, L. F., & Torrelles, J. M. 1993, A&A, 276, 539

Reid, M. J., Argon, A. L., Masson, C. R., Menten, K. M., & Moran, J. M. 1995, ApJ, 443, 238

Reid, M. J., Myers, P. C., & Bieging, J. H. 1987, ApJ, 312, 830

Rodríguez, L. F., & Bastian, T. S. 1994, ApJ, 428, 324

Rodríguez, L. F., Canto, J., Torrelles, J. M., Gomez, J. F., & Ho, P. T. P. 1992, ApJ, 393, L29

Rodriguez, L. F., Carral, P., Ho, P. T. P., & Moran, J. M. 1982, ApJ, 260, 635

Rodríguez, L. F., Ho, P. T. P., & Moran, J. M. 1980, ApJ, 240, L149

Rodríguez, L. F., Moran, J. M., Franco-Hernández, R., et al. 2008, AJ, 135, 2370

Rodríguez, L. F., Myers, P. C., Cruz-Gonzalez, I., & Terebey, S. 1989, ApJ, 347, 461

Rudolph, A., Welch, W. J., Palmer, P., & Dubrulle, B. 1990, ApJ, 363, 528

Sandell, G., Wright, M., & Forster, J. R. 2003, ApJ, 590, L45

Sandford, S. A., & Allamandola, L. J. 1993, ApJ, 417, 815

Shakura, N. I., Prokhorov, M. E., Postnov, K. A., & Ketsaris, N. A. 1999, A&A, 348, 917

Shchekinov, Y. A., & Sobolev, A. M. 2004, A&A, 418, 1045

Shen, Y., & Lou, Y.-Q. 2004, ApJ, 611, L117

Shepherd, D. S., & Churchwell, E. 1996, ApJ, 472, 225

Shepherd, D. S., Claussen, M. J., & Kurtz, S. E. 2001, Science, 292, 1513

Shepherd, D. S., Watson, A. M., Sargent, A. I., & Churchwell, E. 1998, ApJ, 507, 861

Shu, F. H. 1977, ApJ, 214, 488

Shu, F. H., & Adams, F. C. 1987, Circumstellar Matter, 122, 7

Shu, F. H., Adams, F. C., & Lizano, S. 1987, ARA&A, 25, 23

Snell, R. L., & Loren, R. B. 1977, ApJ, 211, 122

Snell, R. L., Loren, R. B., & Plambeck, R. L. 1980, ApJ, 239, L17

Sobolev, V. V. 1957, SvA, 1, 678

Sollins, P. K., & Ho, P. T. P. 2005, ApJ, 630, 987

Sollins, P. K., Zhang, Q., Keto, E., & Ho, P. T. P. 2005, ApJ, 631, 399

Solomon, P. M., Rivolo, A. R., Barrett, J., & Yahil, A. 1987, ApJ, 319, 730

Spitzer, L. 1978, New York Wiley-Interscience, 1978. 333 p.,

Stahler, S. W. 1984, ApJ, 281, 209

Stecklum, B., Brandl, B., Henning, T., et al. 2002, A&A, 392, 1025

Stodólkiewicz, J. S. 1963, Acta Astron., 13, 30

Stolte, A., Brandner, W., Brandl, B., & Zinnecker, H. 2006, AJ, 132, 253

Suto, Y., & Silk, J. 1988, ApJ, 326, 527

Sutton, E. C., Sobolev, A. M., Salii, S. V., et al. 2004, ApJ, 609, 231

Szymczak, M., Bartkiewicz, A., & Richards, A. M. S. 2007, A&A, 468, 617

Tafalla, M., Myers, P. C., Caselli, P., & Walmsley, C. M. 2004, A&A, 416, 191

Takano, S., Hofner, P., Winnewisser, G., Nakai, N., & Kawaguchi, K. 2005, PASJ, 57, 549

Takano, S., Nakai, N.,& Kawaguchi, K. 2002, PASJ, 54, 195

Tan, J. C., & McKee, C. F. 2003, IAU Symposium, 221, 274P

Tassis, K., & Mouschovias, T. C. 2004, ApJ, 616, 283

Terebey S., Shu F. H., Cassen P., 1984, ApJ, 286, 529

Tobin, J. J. 2014, American Astronomical Society Meeting Abstracts, 223, #417.01

Torrelles, J. M., Gomez, J. F., Ho, P. T. P., et al. 1994, ApJ, 435, 290

Torrelles, J. M., Patel, N. A., Curiel, S., et al. 2007, ApJ, 666, L37

Townes, C. H., & Schawlow, A. L. 1975, Microwave spectroscopy., by Townes, C. H.; Schawlow, A. L.. New York, NY (USA): Dover Publications, 698 p.,

Turner, B. E. 1995, ApJ, 444, 708

Turner, J. L., & Welch, W. J. 1984, ApJ, 287, L81

Ulrich, R. K. 1976, ApJ, 210, 377

Umemoto, T., Mikami, H., Yamamoto, S., & Hirano, N. 1999, ApJ, 525, L105

Ungerechts, H., Walmsley, C. M., & Winnewisser, G. 1980, A&A, 88, 259

Vázquez-Semadeni, E., Ballesteros-Paredes, J., Klessen, R. S., & Jappsen, A. K. 2008, Massive Star Formation: Observations Confront Theory, 387, 240

Vázquez-Semadeni, E., Gazol, A., & Scalo, J. 2000, ApJ, 540, 271

Vázquez-Semadeni, E., Gómez, G. C., Jappsen, A.-K., Ballesteros-Paredes, J., & Klessen, R. S. 2009, ApJ, 707, 1023

Vázquez-Semadeni, E., Kim, J., Shadmehri, M., & Ballesteros-Paredes, J. 2005, ApJ, 618, 344

van der Tak, F. F. S., van Dishoeck, E. F., Evans, N. J., II, & Blake, G. A. 2000, ApJ, 537, 283

van Dishoeck, E. F., & Blake, G. A. 1998, ARA&A, 36, 317

Walker C. K., Narayanan G., Boss A. P., 1994, ApJ, 431, 767

Walmsley, C. M. 1997, IAU Symposium, 170, 79

Wang, W.-G., & Lou, Y.-Q. 2007, Ap&SS, 311, 363

Wang, W.-G., & Lou, Y.-Q. 2008, Ap&SS, 315, 135

Wang, Y., Wu, Y., Zhang, Q., Mao, R.-Q., & Miller, M. 2007, A&A, 461, 197

Welch, W. J., Dreher, J. W., Jackson, J. M., Terebey, S., & Vogel, S. N. 1987, Science, 238, 1550

Whitworth, A. P. 2001, From Darkness to Light: Origin and Evolution of Young Stellar Clusters, 243, 171

Williams, J. P., Blitz, L., & McKee, C. F. 2000, Protostars and Planets IV, 97

Wilner, D. J., Ho, P. T. P., & Rodriguez, L. F. 1996, ApJ, 470, L117

Wilner, D. J., Reid, M. J., & Menten, K. M. 1999, ApJ, 513, 775

Wilson, T. L., Gaume, R. A., & Johnston, K. J. 1993, ApJ, 402, 230

Wilson, T. L., Gaume, R. A., Johnston, K. J., & Tieftrunk, A. R. 1995, ApJ, 452, 693

Wink, J. E., Duvert, G., Guilloteau, S., et al. 1994, A&A, 281, 505

Wolfire, M. G., & Cassinelli, J. P. 1987, ApJ, 319, 850

Wood, D. O. S., & Churchwell, E. 1989, ApJS, 69, 831

Wood, D. O. S., Myers, P. C., & Daugherty, D. A. 1994, ApJS, 95, 457

Wright, M. M., Gray, M. D., & Diamond, P. J. 2004, MNRAS, 350, 1253

Wu, J., & Evans, N. J., II 2003, ApJ, 592, L79

Wu, J., Sridharan, T., Fuller, G. A., Zhang, Q., & Evans, N. J. 2007, Bulletin of the American Astronomical Society, 39, 881

Wu, Y., Wei, Y., Zhao, M., et al. 2004, A&A, 426, 503

Wyrowski, F., Hofner, P., Schilke, P., et al. 1997, A&A, 320, L17

Wyrowski, F., Schilke, P., Walmsley, C. M., & Menten, K. M. 1999, ApJ, 514, L43

Yahil, A. 1983, ApJ, 265, 1047

Yorke, H. W. 1986, ARA&A, 24, 49

Yorke, H. W., & Bodenheimer, P. 1999, ApJ, 525, 330

Zapata, L. A., Ho, P. T. P., Schilke, P., et al. 2009, ApJ, 698, 1422

Zapata, L. A., Rodríguez-Garza, C., Rodríguez, L. F., Girart, J. M., & Chen, H.-R. 2011, ApJ, 740, L19

Zhang, Q., & Ho, P. T. P. 1997, ApJ, 488, 241

Zhang, Q., Ho, P. T. P., & Ohashi, N. 1998, ApJ, 494, 636

Zhou, S., Evans, N. J., II, Butner, H. M., et al. 1990, ApJ, 363, 168

Zhou, S., Evans, N. J., II, Guesten, R., Mundy, L. G., & Kutner, M. L. 1991, ApJ, 372, 518

Zhou, S., Evans, N. J., II, Koempe, C., & Walmsley, C. M. 1993, ApJ, 404, 232

Zhou, S., Evans, N. J., II, Kompe, C., & Walmsley, C. M. 1994, IAU Colloq. 140: Astronomy with Millimeter and Submillimeter Wave Interferometry, 59, 226

Zhou, S., Evans, N. J., II, Mundy, L. G., & Kutner, M. L. 1993a, ApJ, 417, 613

Zinnecker, H., McCaughrean, M. J., Rayner, J. T., Wilking, B. A., & Moneti, A. 1993b, Reviews in Modern Astronomy, 6, 191 2000, ApJ, 537, L139

Zinnecker, H., & Yorke, H. W. 2007, ARA&A, 45, 481

Appendix A

A radiative transfer code to calculate the ammonia line emission

A.1 The ammonia molecule

The ammonia molecule has been widely used in the study of star formation regions for the following reasons:

- Ammonia is a high density tracer. Its critical density for thermalization ($n_{crit} \sim 10^4$ cm^{-3} for the (1,1) inversion transition) is of the order of the dense clumps in molecular clouds, which allows to isolate them from the rest of the cloud. Moreover, it is a relatively abundant molecule, with an abundance relative to H_2 of $X_{\mathrm{NH_3}} \sim 10^{-9}$-$10^{-5}$.
- The inversion transitions of ammonia have similar frequencies, so several transitions can be observed with the same radio telescope and with similar instrumental setups. This is important to obtain similar spectral and angular resolution for all transitions under study.
- These transitions have hyperfine structure, which allows the calculation of physical parameters, such as opacity and excitation temperature from the study of a single inversion transition. There is no need of complementary observations of different isotopic species.
- The most studied ammonia transitions have wavelengths $\simeq$ 1 cm, which allow us to study them with high angular resolution ($< 1''$) and sensitivity using interferometers like the (E)VLA.

Ho & Townes (1983) present an excellent review about the properties of the ammonia molecule and how to use it to obtain physical parameters of the region under study. Here we will present a summary of its properties, to better understand the ammonia observations presented in this thesis work.

The NH_3 molecule has a pyramidal geometry, with its axis of symmetry perpendicular to the plane determined by the three hydrogen atoms. The rotational levels of the NH_3 molecule are described by two quantum numbers, J and K, which correspond to the total angular momentum, and its projection along the axis of symmetry respectively, with $|K| \leq J$. The energy associated with the (J, K) rotational level is given by:

$$E(J,K) = h[BJ(J+1) + (C-B)K^2] \;; \quad J = 0,1,2,\dots \;; \quad K = 0, \pm 1, \dots, \pm J, \tag{A.1}$$

where B=2.98×10^{11} Hz and C=1.89 ×10^{11} Hz.

In the absence of vibrational motions perpendicular to the axis of symmetry, the electric dipole moment points in the axis direction and the allowed radiative transitions must fulfill $\Delta K = 0$ and $\Delta J = 0, \pm 1$. Interactions between rotational and vibrational motions can induce a small electric dipole moment perpendicular to the axis of symmetry, causing transitions with $\Delta K = \pm 3$ (Oka et al. 1971) but such transitions have a much lower probability. The result is that rotational states are divided into ladders, defined by their K quantum number, with very rare radiative transitions between ladders. Within each K-ladder, states with $J > K$ decay rapidly through the $\Delta J = -1$ radiative transition, down to the lowest level $J = K$. In the normal conditions of the interstellar medium, the energy input (radiation fields or collisions) is not enough to repopulate upper-J levels, so we can consider that only states with $J = K$ are populated. These states are called "metastable", while those of $J \neq K$ are "non-metastable". As radiative transitions between states with different K have low probability, in general, transitions between metastable levels can only be achieved via collisions. For this reason the excitation temperature that relates the population levels of different metastable levels, usually called rotational temperature, T_{rot}, is a good estimate of the kinetic temperature of the gas, and satisfies

$$\frac{n_{(J_2,K_2)}}{n_{(J_1,K_1)}} = \frac{g_{(J_1,K_1)}}{g_{(J_2,K_2)}} e^{-(E_{(J_2,K_2)} - E_{(J_1,K_1)})/k_b T_{rot}} \;, \tag{A.2}$$

where k_b is the Boltzmann constant, $n_{(J,K)}$ is the population of the (J, K) rotational level, and $g_{(J,K)}$ is its statistical weight (Townes & Schalow 1975):

$$g_{(J,K)} = \begin{cases} 4(2J+1), & K \neq \dot{3} \\ 8(2J+1), & K = \dot{3} \\ 4(2J+1), & K = 0 \;. \end{cases} \tag{A.3}$$

The ratio between ortho and para species: the formation temperature

There are two different species of NH_3, depending on the relative orientation of the spins of the hydrogen atoms. In the ortho species, all hydrogen spins have the same orientation, while in the para species one of the hydrogen spins is inverted. The two species populate different K-ladders: states with K multiple of 3 ($K = \dot{3}$) correspond to ortho, while those with $K \neq \dot{3}$ are for the para species. Radiative or collisional transitions that may change the spin orientation have very low probability (Cheung et al. 1969) so transitions from ortho to para states or vice versa are forbidden under normal conditions in the interstellar medium. Therefore, it is not possible to relate the population of states corresponding to ortho to those of the para species using the Boltzmann equation at an arbitrary temperature. Only the population of molecules of the same species can be related in this way. However, at the formation temperature, the populations are actually related by Boltzmann equation, and this determines the ortho-to-para ratio.

The ratio between the spin statistical weights of ortho and para molecules is 4:2. On the other hand, the number of para rotational levels is twice that of ortho levels. These two factors compensate one another and, thus, the ortho-to-para ratio approaches unity when NH_3 is produced under high-temperature conditions ($\gtrsim$ 40 K), but the ortho-to-para ratio increases when the molecules are produced at lower temperatures. This is because at low temperatures most molecules reside in the lowest rotational state, $(J, K) = (0, 0)$, an ortho level. The relationship between the ortho-to-para ratio and the formation temperature is plotted in Figure A.1. Ortho-to-para ratios in massive star-forming regions have been found to be about $C_{\mathrm{o-p}} = 1.5$-3.5, which correspond to ammonia formation temperatures, $T_{\mathrm{for}} = 20$-11 K (Takano et al. 2002; Nagayama et al. 2009).

The inversion transitions

The three hydrogen atoms of the NH_3 molecule create a potential barrier along their plane that, in classical mechanics, would prevent the nitrogen atom from flipping over the other side of this plane, unless the molecule has a very high vibrational energy. However, it can traverse the potential barrier via quantum tunneling. For any energy state of the molecule, there are two possible degenerate states (with the same energy), depending on the location of the nitrogen atom (we will call them "up" and "down"). Starting from one of these configurations, the tunnel effect will produce a time-variable probability of finding the molecule in the opposite configuration. The result is that the up/down states do not represent eigenstates of the molecule. The actual eigenstates are the symmetric and antisymmetric combination of the up and down states. These eigenstates have different energies, with this difference depending on the probability associated to the tunneling. In summary, the possibility of tunneling for the nitrogen atom splits each energy level of the ammonia molecule in two sublevels with slightly different energies. The transitions between these sublevels are called "inversion transitions". In this thesis we study the inversion transitions within the rotational levels (J, K) of the ammonia molecule.

The electric quadrupole interaction between the angular momentum of the molecule and the electric charge distribution created by the electrons produces hyperfine structure in the ammonia energy levels due to the different relative orientations of the nuclear spins. The hyperfine splitting is dominated by the spin of the nitrogen atom. Considering the spin alone, the total angular momentum of the molecule would be $\vec{F} = \vec{I}_N + \vec{J}$, where $\vec{I}_N$ is the spin of the nitrogen atom (whose quantum number is $I = 1$), and $\vec{J}$ is the rotational angular momentum of the molecule. Due to the electric quadrupole interaction, the energy of the molecule in a rotational state depends on the quantum number F, in addition to K and J. Depending on

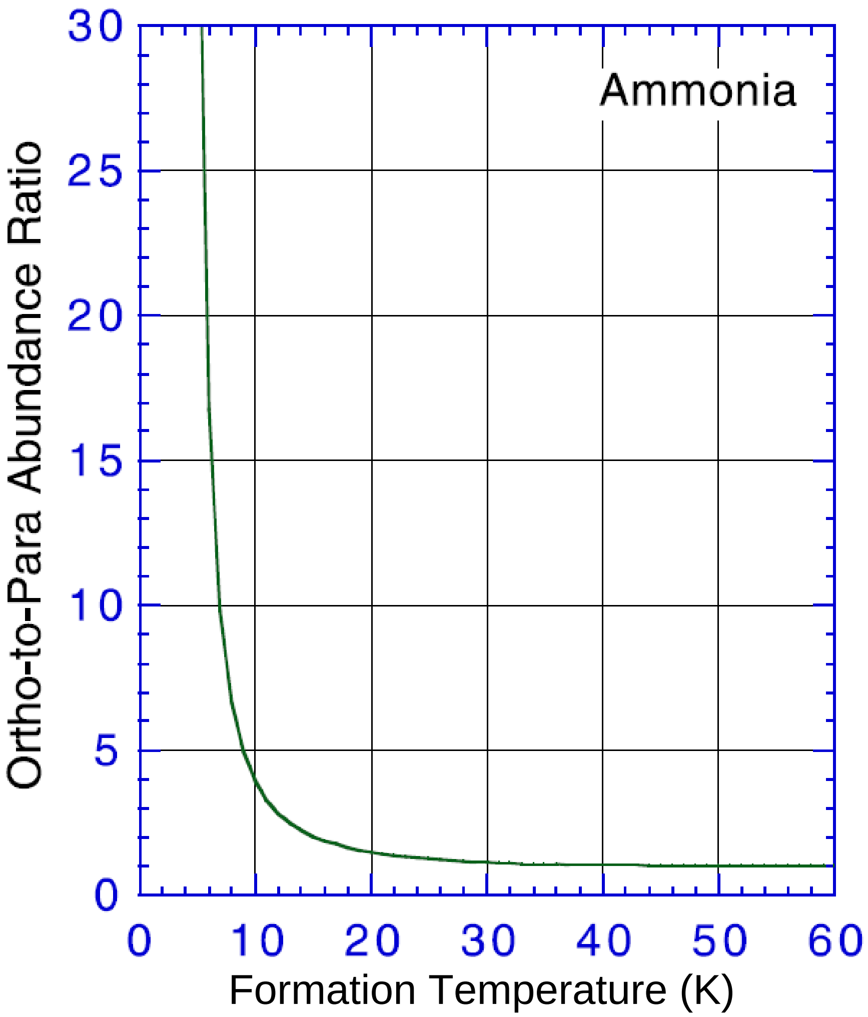

Figure A.1: Calculated ortho-to-para abundance ratio of NH_3 as a function of the formation temperature, which determines the distribution between ortho and para species. Figure from Takano et al. (2002).

Table A.1: NH_3 inversion transitions

Transitions (J,K)	ν_0 (GHz)	A_{ul} (s^{-1})
(1,1)	23.6944955	1.66838×10^{-7}
(2,2)	23.7226333	2.23246×10^{-7}
(3,3)	23.8701292	2.55865×10^{-7}
(4,4)	24.1394163	2.82264×10^{-7}
(5,5)	24.5329887	3.08642×10^{-7}
(6,6)	25.0560250	3.38201×10^{-7}

Frequency and Einstein's Coefficient of Spontaneous Emission.

the relative orientation of $\vec{J}$ and $\vec{I_N}$, the total angular momentum can have values $F = J, J \pm 1$. Thus, each energy level is further split into three sublevels. Selection rules impose that allowed inversion transitions have $\Delta F = 0, \pm 1$. The transitions with $\Delta F = 0$ have very similar frequencies and usually result indistinguishable, and so appear as a single line called the main line. The transitions $\Delta F = \pm 1$ are observed as two pairs of lines symmetrically located in frequency with respect to the main line. In total five lines are observed. Table A.2 shows the quadrupolar hyperfine structure of the ammonia molecules for inversion transitions from (1,1) to (6,6). Further hyperfine splitting of these five hyperfine components is produced due to spins of the hydrogen atoms, but the frequency shift of the resulting lines is much smaller, and they can only be distinguished in quiescent clouds, where thermal broadening of the spectral profile is small.

A.2 The radiative transfer code

In order to compare molecular line observations towards HMCs with the predictions of the core models we have developed a simple radiative transfer code that calculates the emergent line emission from the physical conditions of gas density (ρ), kinetic temperature (T_k), and velocity (V) given by the model. The code uses a three dimensional Cartesian grid to describe the geometry, and places the star at the center of the grid. In the following we will show how the code obtains the resultant intensity, I_ν, by simulating the propagation of the radiation throughout the core.

The radiative transfer differential equation is:

$$\frac{dI_\nu}{dy} = -\kappa_\nu I_\nu + j_\nu \ , \qquad (A.4)$$

where κ_ν is the absorption coefficient, j_ν the emission coefficient, and y is the spatial dimension

Table A.2: Electric quadrupole hyperfine structure of NH_3 inversion transitions[a]

i	$F \rightarrow F'$	$\Delta\nu_i$ (MHz)	V_i (km s^{-1})	x_i	Notes
			(1,1)		
1	$0 \rightarrow 1$	1.531	−19.37	0.11111	OS
2	$2 \rightarrow 1$	0.613	−7.75	0.13889	IS
3	$1 \rightarrow 1 + 2 \rightarrow 2$	0	0	0.08333+0.41667 = 0.50000	M
4	$1 \rightarrow 2$	−0.613	7.75	0.13889	IS
5	$1 \rightarrow 0$	−1.531	19.37	0.11111	OS
			(2,2)		
1	$1 \rightarrow 2$	2.04	−25.78	0.05000	OS
2	$3 \rightarrow 2$	1.31	−16.55	0.05185	IS
3	$1 \rightarrow 1 + 2 \rightarrow 2 + 3 \rightarrow 3$	0	0	0.15000+0.23148+0.41481 = 0.79629	M
4	$2 \rightarrow 3$	−1.31	16.55	0.05185	IS
5	$2 \rightarrow 1$	−2.04	25.78	0.05000	OS
			(3,3)		
1	$2 \rightarrow 3$	2.30	−28.88	0.02645	OS
2	$4 \rightarrow 3$	1.71	−21.47	0.02678	IS
3	$2 \rightarrow 2 + 3 \rightarrow 3 + 4 \rightarrow 4$	0	0	0.21164+0.28009+0.40178 = 0.89352	M
4	$3 \rightarrow 4$	−1.71	21.47	0.02678	IS
5	$3 \rightarrow 2$	−2.30	28.88	0.02645	OS
			(4,4)		
1	$3 \rightarrow 4$	2.45	−30.43	0.01620	OS
2	$5 \rightarrow 4$	1.95	−24.21	0.01629	IS
3	$3 \rightarrow 3 + 4 \rightarrow 4 + 5 \rightarrow 5$	0	0	0.24305+0.30083+0.39111 = 0.93500	M
4	$4 \rightarrow 5$	−1.95	24.21	0.01629	IS
5	$4 \rightarrow 3$	−2.45	30.43	0.01620	OS
			(5,5)		
1	$4 \rightarrow 5$	2.57	−31.40	0.01090	OS
2	$5 \rightarrow 6$	2.12	−25.91	0.01094	IS
3	$4 \rightarrow 4 + 5 \rightarrow 5 + 6 \rightarrow 6$	0	0	0.26181+0.31148+0.38299 = 0.95629	M
4	$6 \rightarrow 5$	−2.12	25.91	0.01094	IS
5	$5 \rightarrow 4$	−2.57	31.40	0.01090	OS
			(6,6)		
1	$5 \rightarrow 6$	2.63	−31.46	0.00783	OS
2	$6 \rightarrow 7$	2.25	−26.92	0.00785	IS
3	$5 \rightarrow 5 + 6 \rightarrow 6 + 7 \rightarrow 7$	0	0	0.27422+0.31765+0.37677 = 0.96863	M
4	$7 \rightarrow 6$	−2.25	26.92	0.00785	IS
5	$6 \rightarrow 5$	−2.63	31.46	0.00783	OS

Table from Osorio et al. (2009). Shifts in frequency and velocity of the lines with respect to the main line, and intrinsic relative intensity, x_i, of the lines with respect the total emission of the inversion transition (Townes & Schawlow 1975). Notes: M, IS and OS indicate main line, inner satellite line and outer satellite line respectively.

in the direction of the propagation of light. The absorption coefficient, κ_ν, and the emission coefficient, j_ν, can be expressed as follows:

$$\kappa_\nu = \frac{n_u A_{ul} c^2}{8\pi\nu_0^2}(e^{h\nu_0/k_b T_{ex}} - 1)\Phi(\nu)\ , \tag{A.5}$$

$$j_\nu = \frac{n_u A_{ul}}{4\pi} h\nu_0 \Phi(\nu)\ , \tag{A.6}$$

where the index u and l indicate the upper and lower levels involved in the transition respectively, A$_{ul}$ is the Einstein spontaneous emission coefficient of the transition, Φ is the line profile function which contains information about the motions of the gas particles and of the hyperfine structure of the molecule, ν_0 is the transition rest frequency, n_u is the number density of molecules in the upper level of the transition under consideration, and T_{ex} is the excitation temperature of the transition, which relates the population of the upper and lower levels,

$$\frac{n_u}{n_l} = \frac{g_u}{g_l} e^{(-h\nu_0/k_b T_{ex})}\ , \tag{A.7}$$

where g_u and g_l are the statistical weights (equation A.3). Using equations A.5 and A.6 in equation A.4 it is obtained:

$$\frac{dI_\nu}{dy} = -\frac{n_u A_{ul} c^2}{8\pi\nu_0^2}(e^{h\nu_0/k_b T_{ex}} - 1)\Phi(\nu) I_\nu + \frac{n_u A_{ul}}{4\pi} h\nu_0 \Phi(\nu)\ . \tag{A.8}$$

In order to facilitate calculations we will work in the velocity domain. We make use of the Doppler conversion to pass from frequency dependence to velocity dependence. Knowing that:

$$I_\nu = \frac{dE}{dt\, dA \cos\theta\, d\Omega\, d\nu}, \tag{A.9}$$

and

$$d\nu = \frac{\nu}{c} dV, \tag{A.10}$$

we define

$$I_V \equiv \frac{\nu}{c} I_\nu. \tag{A.11}$$

Taking into account that:

$$\int \Phi(\nu) d\nu = \int \Phi(\nu) \frac{d\nu}{dV} dV = \int \Phi(\nu) \frac{\nu}{c} dV = \int \Phi(V) dV, \tag{A.12}$$

we can rewrite equation A.8 as:

$$\frac{dI_V}{dy} = -\frac{n_u A_{ul} c^3}{8\pi\nu_0^3}(e^{h\nu_0/k_b T_{ex}} - 1)\Phi(V) I_V + \frac{n_u A_{ul}}{4\pi} h\nu_0 \Phi(V)\ . \tag{A.13}$$

We approximate equation A.13 by using finite increments to get the recursive equation:

$$I_V(y+dy) = \left(1 - \frac{n_u A_{ul} c^3}{8\pi\nu_0^3}(e^{h\nu_0/k_bT_{ex}} - 1)\Phi(V)\ dy\right) I_V(y) + \frac{n_u A_{ul}}{4\pi} h\nu_0 \Phi(V)\ dy\ . \tag{A.14}$$

For the case of the inversion transition of the ammonia molecule, each (J,K) rotational level is splited in two different sublevels. Taking into account equation A.7 we can relate n_u with T_{ex} and the total number density of molecules in the rotational level, $n_{(J,K)}$:

$$n_{(J,K)} = n_u + n_l = n_u(1 + \frac{n_l}{n_u}) = n_u\left(1 + \frac{g_l}{g_u} e^{(h\nu_0/k_bT_{ex})}\right)\ , \tag{A.15}$$

which introduced in equation A.14 gives:

$$\begin{aligned} I_V(y+dy) = &\left(1 - \frac{n_{(J,K)} A_{ul} c^3}{8\pi\nu_0^3} \frac{(e^{h\nu_0/k_bT_{ex}} - 1)}{\left(1 + \frac{g_l}{g_u} e^{(h\nu_0/k_bT_{ex})}\right)} \Phi(V)\ dy\right) I_V(y) \\ &+ \frac{n_{(J,K)} A_{ul}}{4\pi\left(1 + \frac{g_l}{g_u} e^{(h\nu_0/k_bT_{ex})}\right)} h\nu_0 \Phi(V)\ dy. \end{aligned} \tag{A.16}$$

This equation applied to the code grid results in:

$$\begin{aligned} I_V(x,y-1,z) = &\left(1 - \frac{n_{(J,K)} A_{ul} c^3}{8\pi\nu_0^3} \frac{(e^{h\nu_0/k_bT_{ex}} - 1)}{\left(1 + \frac{g_l}{g_u} e^{(h\nu_0/k_bT_{ex})}\right)} \Phi(V)\ l\right) I_V(x,y-1,z) \\ &+ \frac{n_{(J,K)} A_{ul}}{4\pi\left(1 + \frac{g_l}{g_u} e^{(h\nu_0/k_bT_{ex})}\right)} h\nu_0 \Phi(V)\ l. \end{aligned} \tag{A.17}$$

where $I_V(x,y,z)$ is the “intensity” (considered as energy per unit of velocity instead of frequency) at a certain velocity, V, at the cell (x,y,z) of the grid; and l is the length of a cell in the grid. The line of sight in the code has been considered to be along the y axis, with the observer located at $y = -\infty$.

We have obtained an expression, equation A.17, that relates the intensity in the cell (x,y,z) at a certain velocity, V, with: i) the intensity in the adjacent cell, ii) the parameters A_{ul}, ν_0, g_u, g_l, and iii) the fields $T_{ex}(x,y,z)$, $n_{(J,K)}(x,y,z)$, and $\Phi(x,y,z,v)$. The parameters A_{ul}, ν_0, g_u, g_l are specific of a molecular transition. As we will see later, the fields $T_{ex}(x,y,z)$, $n_{(J,K)}(x,y,z)$, and $\Phi(x,y,z,V)$ will come determined by the physical conditions provided by the core model such as the gas density (ρ), the kinetic temperature (T_k), and the velocity (V) fields. In these relationships, parameters as the molecule abundance and the turbulent dispersion will appear and will be considered as free parameters of the code. Once the molecular transition involved is specified (A$_{ul}$, ν_0, g_u and g_l are set), $T_{ex}(x,y,z)$ and $n(x,y,z)$ are calculated for each cell (x,y,z), then the code evaluates $\Phi(V)$ for a large sample of velocity values and uses equation A.17 to get the resultant $I_V(x,z,V)$. The result is converted back to the frequencies domain, and convolved with a circular beam in order to match observations. In the following we will derive the relationship of T_{ex}, $n_{(J,K)}$, and $\Phi(V)$ with the model's fields T_k, ρ, and V.

Calculation of T_{ex} as a function of the inputs provided by the model

The code uses the two-level model to estimate T_{ex} as a function of T_k, which is an input of the code given by the core model. The two level model assumes that the two levels of a given transition are isolated. In order to obtain the excitation temperature, the two-level model balances the rates of excitation and de-excitation (considering both radiative and collisional processes) in the form:

$$n_u A_{ul} + n_u B_{ul} I_\nu + n_u n_{H_2} \gamma_{ul} = n_l B_{lu} I_\nu + n_l n_{H_2} \gamma_{lu}, \tag{A.18}$$

where A_{ul}, B_{ul}, B_{lu}, are the Einstein coefficients, whose relations are:

$$g_l B_{lu} = g_u B_{ul}, \;\; A_{ul} = \frac{2h\nu_0^3}{c^2} B_{ul}, \tag{A.19}$$

where γ_{ul} and γ_{lu} are the collisional coefficients, I_ν is the local intensity, and n_{H_2} is the H_2 density. This balance assumes that dominant collisions are those with the H_2 molecule. Equation A.18 can be rewritten as:

$$\frac{n_u}{n_l} = \frac{B_{lu} I_\nu + n_{H_2}\gamma_{lu}}{A_{ul} + B_{ul} I_\nu + n_{H_2}\gamma_{ul}} = \frac{g_u}{g_l} e^{(-h\nu_0/k_b T_{ex})}. \tag{A.20}$$

Using the relation between collisional coefficients,

$$\frac{\gamma_{lu}}{\gamma_{ul}} = \frac{g_u}{g_l} e^{-h\nu_0/k_b T_k}, \tag{A.21}$$

and the Boltzmann equation one can obtain:

$$T_{ex} = \frac{h\nu_0/k_b}{\ln\left[\frac{\left(1+\frac{A_{ul}}{n_{H_2}\gamma_{ul}}\right)e^{h\nu_0/k_b T_k}-1}{\frac{A_{ul}}{n_{H_2}\gamma_{ul}}\left(\frac{c^2}{2h\nu_0^3} I_\nu e^{h\nu_0/k_b T_k}\right)+1} + 1\right]}. \tag{A.22}$$

Equation A.22 gives an expression that relates T_{ex} with the transition parameters (A_{ul}, γ_{ul} and ν_0), the intensity I_ν (which is taken to be the intensity that reaches the cell of the grid), and the fields T_k and n_{H_2} (provided by the model). Note that n_{H_2} is the H_2 density in number of particules, which is directly related with the mass density provided by the model by $n_{H_2} = \rho/m_{H_2}$. Such expression is introduced in equation A.17 of the code in order to calculate the emergent intensity via the iterative process.

Although our radiative transfer code is of general applicability to any molecular transition, in this thesis we have used it for the particular case of the ammonia inversion transitions. For the cases of the ammonia inversion transitions of metastable rotational levels, the values of A_{ul}

and ν_0 are those given in the table A.1; g_u, g_l are given by equation A.3; and the collisional de-excitation coefficients for the ammonia molecule are given by (Ho 1977):

$$\gamma_{ul} = 2.27 \times 10^{-11} \left(\frac{T_k}{\mathrm{K}}\right)^{1/2} \mathrm{s}^{-1}\mathrm{cm}^3 \ . \tag{A.23}$$

Note that, in the case of the ammonia molecule, the calculation of T_{ex} by using the two-level model is well justified because radiative transitions between rotational levels are forbidden ($\Delta K \neq 0$), and because collisional transitions within the inversion doublet are much more frequent than between different rotational levels (Ho & Townes 1983, Danby et al. 1988).

Calculation of $n_{(J,K)}$ as a function of the inputs provided by the model

Here we will explain how the number density of molecules in the rotational level (J, K), $n_{(J,K)}$, in equation A.17 relates with the total mass density, ρ, and the kinematic temperature, T_k, provided as inputs of the code by the model. As we can consider that only metastable levels are populated (see A.1), then, $n_{(J,K)} = n_{(J,J)}$. We will use the Boltzmann equation to relate the population of a (J, J) metastable level with the total ammonia density, n_{NH_3}, through the rotational temperature, T_{rot} (equation A.2). As explained earlier, in general, transitions between metastable levels can only be achieved via collisions, so the rotational temperature is usually a good estimate of the kinetic temperature of the gas, $T_k \simeq T_{rot}$. However, two distinct species of $\mathrm{NH_3}$ exist, ortho ($K = \dot{3}$) and para ($K \neq \dot{3}$), and transitions between ortho and para are forbidden (see A.1). That implies that only metastable levels of the same specie can be related through the Boltzmann equation and that the ratio between the number of ortho and para molecules remains constant in time. According to this, the total number of ammonia molecules is:

$$n_{\mathrm{NH_3}} = n_{(0,0)} + n_{(1,1)} + n_{(2,2)} + n_{(3,3)} + n_{(4,4)} + n_{(5,5)} + ... \ , \tag{A.24}$$

gathering all the ortho and para species separately:

$$n_{\mathrm{NH_3}} = n_{(0,0)}(T_{rot}) \ \left(1 + [\frac{n_{(3,3)}}{n_{(0,0)}}](T_{rot}) + ...\right)$$

$$+n_{(1,1)}(T_{for}) \ \left(1 + [\frac{n_{(2,2)}}{n_{(1,1)}}](T_{rot}) + [\frac{n_{(4,4)}}{n_{(1,1)}}](T_{rot}) + ...\right) \ , \tag{A.25}$$

where (T_{rot}) indicates dependences on the rotation temperature, T_{rot}. Defining the partition functions of the ortho and para species as:

$$Q_{ortho}(T_{rot}) = \left(1 + [\frac{n_{(3,3)}}{n_{(0,0)}}](T_{rot}) + [\frac{n_{(6,6)}}{n_{(0,0)}}](T_{rot}) + ...\right) \ , \tag{A.26}$$

and

$$Q_{para}(T_{rot}) = \left(1 + [\frac{n_{(2,2)}}{n_{(1,1)}}](T_{rot}) + [\frac{n_{(4,4)}}{n_{(1,1)}}](T_{rot}) + ...\right) \ , \tag{A.27}$$

we can rewrite the total number of ammonia molecules as a function of T_{rot} and the number of ammonia molecules in the rotational level $(0,0)$ and $(1,1)$ as:

$$n_{\mathrm{NH_3}} = n_{(0,0)}(T_{rot})\, Q_{ortho}(T_{rot}) + n_{(1,1)}(T_{rot})\, Q_{para}(T_{rot}) \ . \tag{A.28}$$

As the ratio between the number of ortho and para molecules remains constant in time,

$$[\frac{n_{(0,0)}}{n_{(1,1)}}](T_{rot})\frac{Q_{ortho}(T_{rot})}{Q_{para}(T_{rot})} = C_{o-p} \ , \tag{A.29}$$

where C_{o-p} is a constant. Using this constant, equation A.28 can be expressed as:

$$n_{\mathrm{NH_3}} = n_{(1,1)}(T_{rot})\ Q_{para}(T_{rot})\ (1 + C_{o-p}) \ . \tag{A.30}$$

On the other hand, since we know, from the Boltzmann equation, that, for a para species:

$$n_{(J,J)} = n_{(1,1)}\frac{g_{(J,J)}}{g_{(1,1)}}e^{\frac{\left(E_{(1,1)}-E_{(J,J)}\right)}{k_b T_{rot}}} \ . \tag{A.31}$$

where $E_{(1,1)}$ is the energy of the (1,1) inversion transition which is given by equation A.1. Introducing equation A.33 in equation A.31, the number density of a given rotational level for para species can be rewritten as:

$$n_{(J,J)} = \frac{n_{\mathrm{NH_3}}}{Q_{para}(T_{rot})}\frac{g_{(J,J)}}{g_{(1,1)}}e^{(E_{(1,1)}-E_{(J,J)})/k_b T_{rot}}\frac{1}{1 + C_{o-p}} \ , \tag{A.32}$$

Equation A.32 relates the population of a metastable level, $n_{(J,J)}$, of a para specie, with the total ammonia population, n_{NH_3}, the rotational temperature, T_{rot} (which equals the kinetic temperature; obtained from the model), and the constant C_{o-p}. This can be done also for ortho species, in that case equation A.33 would be replaced by:

$$n_{\mathrm{NH_3}} = n_{(0,0)}(T_{rot})\ Q_{ortho}(T_{rot})\ (1 + \frac{1}{C_{o-p}}) \ . \tag{A.33}$$

As the ratio of ortho and para ammonia molecules is constant in time, equation A.29 should be satisfied, also, at the particular moment of the formation of the ammonia, at temperature T_{for}, and so equation A.29 yields to:

$$[\frac{n_{(0,0)}}{n_{(1,1)}}](T_{for})\frac{Q_{ortho}(T_{for})}{Q_{para}(T_{for})} = C_{o-p} \ . \tag{A.34}$$

At the moment of formation, the populations of all levels (without distinction between ortho and para) were indeed distributed following the Boltzmann equation with a single rotational temperature (Takano et al. 2002), so:

$$[\frac{n_{(0,0)}}{n_{(1,1)}}](T_{for})\frac{Q_{ortho}(T_{for})}{Q_{para}(T_{for})} = \frac{g_{00}}{g_{11}} e^{(E_{11}-E_{00})/k_b T_{for}} \frac{Q_{ortho}(T_{for})}{Q_{para}(T_{for})} = C_{o-p} \ , \tag{A.35}$$

where the number of ammonia molecules has been assumed that does not change with time. The numerical value of C_{o-p} is set once T_{for} is given according to equation A.35. The formation temperature is a fixed parameter in the code that it is taken as $T_{for} = 20$ K (see later for further explanation).

Note that equation A.32 relates the density of ammonia molecules in a given rotational level, $n_{(J,J)}$, with the total density of ammonia molecules n_{NH_3}. However, this equation refers to density in number of particles in gas phase per unit of volume, while the model provides the total gas density in units of mass per unit of volume, ρ. Thus,

$$n_{\mathrm{NH_3}} = \frac{\rho}{\mu} X_{\mathrm{NH_3}} \ , \tag{A.36}$$

where $\mu = 2.33\, m_{\mathrm{H}}$ is the mean molecular weight, and $X_{\mathrm{NH_3}}$ is the ammonia abundance in gas phase relative to the $\mathrm{H_2}$, which is not necessarily constant. The code uses the same approach as Osorio et al. (2009) for the calculation of $X_{\mathrm{NH_3}}$. Such approach assumes that the total abundance of ammonia molecules (both in solid and gas phase) is constant all over the core. However, the relative proportion of ammonia in gas and solid phase changes as a result of deposition and sublimation processes due to temperature variations. In particular, at low temperatures most of the ammonia molecules are frozen and trapped into water ice on the surface of dust grains (with a residual gas-phase ammonia abundance with respect to hydrogen, X_{min}), but when the temperature reaches 100 K, water sublimates and ammonia is released to the gas phase, up to a maximum gas-phase ammonia abundance, X_{max}. The gas-phase abundance can be estimated following Osorio et al. (2009):

$$X_{\mathrm{NH_3}} = \frac{X_{\mathrm{max}} - X_{\mathrm{min}}}{1+\eta} + X_{\mathrm{min}} \ , \tag{A.37}$$

where η is the ratio of molecules in the solid to gas phase that is given by Sandford & Allamandola (1993):

$$\eta = 8 \times 10^{-30} \left(\frac{\rho}{\mathrm{cm^{-3}}}\right) \left(\frac{T_k}{\mathrm{K}}\right)^{1/2} e^{5070\,\mathrm{K}/T_k} \ , \tag{A.38}$$

in the presence of water ice, where ammonia molecules can be trapped. In the absence of water ice, ammonia sublimates at 60 K and η takes the form:

$$\eta = 5 \times 10^{-30} \left(\frac{\rho}{cm^{-3}}\right) \left(\frac{T_k}{\mathrm{K}}\right)^{1/2} e^{3075\,\mathrm{K}/T_k} \ . \tag{A.39}$$

We take the values of X_{max} and X_{min} as free parameters in the code. In summary, by setting the values of the ammonia abundance (X_{max} and X_{min}), and by obtaining from the adopted model of protostellar collapse the kinetic temperature, T_k (which in its turn determines T_{rot}), and the total density, ρ, inside the molecular core, we can use equations A.32, A.36 and A.37 to obtain an expression for $n_{(J,J)}$ that can be introduced in the equation A.17 of the code.

Determination of Φ as a function of the inputs provided by the model

The line profile function, Φ, contains information about the thermal motions, the systemic velocity, the turbulent motions, and the hyperfine structure of the molecule. In the case of ammonia inversion transitions, to take into account the hyperfine structure of the molecule, the profile function is split into five Gaussian functions, each of them centered at a different velocity, corresponding to the ammonia hyperfine components. Each of them is weighted by its relative intensity, x_i (Table A.2), and its width depends on the thermal and turbulent motions:

$$\Phi(V) = \sum_{i=1}^{5} x_i \Phi_i(V) \ , \tag{A.40}$$

where V is the LOS velocity field. Since the profile function of the transition is normalized as $\int \Phi(V)dV = 1$, and the relative intensities of the hyperfine components satisfy the condition $\sum x_i = 1$, the profile for each hyperfine component is normalized as:

$$\Phi_i(V) = \frac{1}{\sqrt{2\pi k_b}} \frac{1}{\sqrt{\frac{T_k}{m_{\mathrm{NH_3}}} + \frac{P_{tur}}{\rho}}} e^{-\frac{(V - V_{\mathrm{LSR}} - V_i)^2}{2k_b\left(\frac{T_k}{m_{\mathrm{NH_3}}} + \frac{P_{tur}}{\rho}\right)}} \ , \tag{A.41}$$

where m_{NH_3} is the ammonia molecular weight, V_i is the separation in velocity between the hyperfine line i and the main line, V_{LSR} is the systemic velocity of the gas (which has to be evaluated for each cell of the grid), T_k is the kinetic temperature (that sets the thermal velocity dispersion), and P$_{tur}$ is a parameter (with units of pressure) that, together with the density ρ, sets the velocity dispersion due to turbulence. The FWHM of the velocity dispersion due to turbulence is given by:

$$\Delta V_{tur} = \sqrt{8 \ln 2 k_b \frac{P_{tur}}{\rho}} \ . \tag{A.42}$$

We take P_{tur} as a free parameter in our code. Note that, if P_{tur} is constant (as in the SLS model), then the turbulent velocity dispersion decreases with increasing density, as described in the "Larson relations" (Section 1). If $P_{tur} \propto \rho$, then the turbulent velocity dispersion is constant throughout the core.

About the formation temperature used the code

To obtain the population of a given metastable level, $n_{(J,J)}$, from the total amount of ammonia molecules (equation A.32), n_{NH_3}, our radiative transfer code takes into account the presence of two separate species of ammonia (ortho and para), and considers that radiative or collisional transitions from one to another are not allowed. The SLS model used to fit the ammonia emission in G31 HMC in Chapter 4 does not take into account this differentiation between ortho and ammonia species. The radiative transfer code described here and used to fit the ammonia emission towards W3(H_2O) in Chapter 5 is, in this sense, more complete because it does differentiate between ortho and para species. However, the code, in the calculation of n_{NH_3} (equation A.24), only accounts for the metastable levels, neglecting the population in the non-metastable levels (this approximation is also adopted in the SLS model for G31 HMC). This can be also a rough approximation under some physical conditions. In order to quantify the error in the calculation of n_{NH_3} introduced by the exclusion of the non-metastable levels, we calculated the ortho-para ratio, C_{o-p}, predicted by the code for values of the formation temperature of 20 and 11 K and compared them with the value obtained by Takano et al. (2002), which does take into account the non-metastable levels. While our code provides values of $C_{o-p} = 1$ and 6, Takano et al. (2002) obtain values of $C_{o-p} = 1.5$ and 3.5, for formation temperature of 20 and 11 K respectively. Because we are considering regions of high-mass star formation, which are hot (Infrared Dark Clouds have typically temperatures $10 - 20$ K), and because the error is lower for 20 K than for 11 K, we adopt in our code calculations $T_{for} = 20$ K.

We also tried to quantify the differences between the population of the metastable levels predicted by the SLS model in Chapter 4 and the ones predicted by our radiative transfer code. To do so, we have calculated the relative population of the metastable levels, $n_{(J,J)}/n_{NH_3}$, as a function of T_{rot} and T_{for}, when differentiating between ortho and para molecules and when not differentiating. Results are shown in Figure A.2. We conclude that for low formation temperatures, $T_{for} \simeq 10$ K, there are significant differences. At higher formation temperatures, $T_{for} \simeq 20$ K, the differences are small. This is because at low formation temperatures most of the population is ortho, but at higher formation temperatures the ortho-to-para ratio approaches unity.

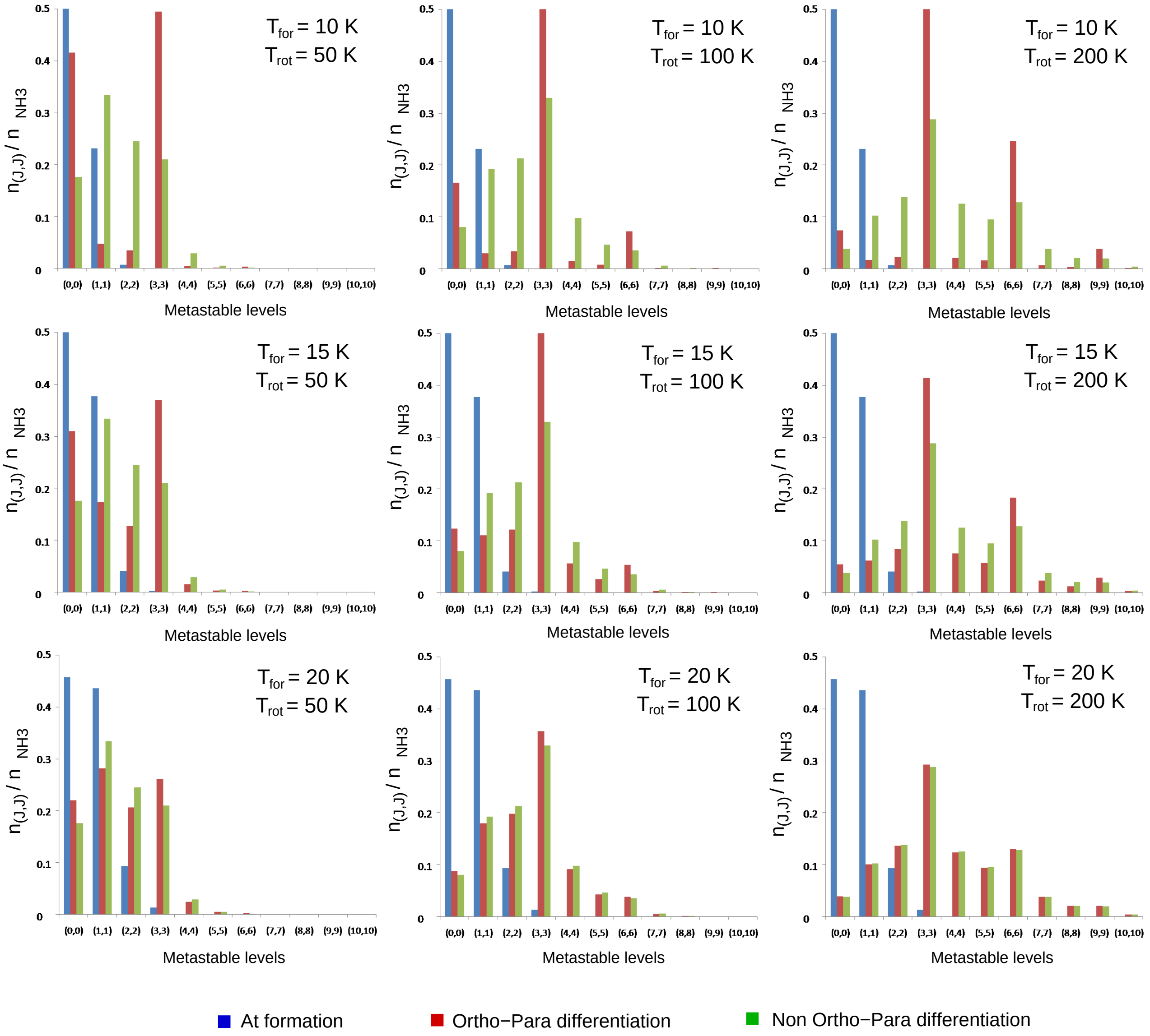

Figure A.2: Comparison between relative population of metastable levels, $n_{(J,J)}/n_{\mathrm{NH_3}}$, when ortho-para differentiation is performed (red bars) and not performed (green bars). The blue bars represents the relative population in the metastable levels at the moment of the ammonia formation (at this time there is no ortho-para differentiation; Takano et al. 2002). The (J, J) values in the horizontal axis represents the metastable level (J, J). The vertical axis represents the fraction of molecules in the metastable level (J, J) relative to the total amount of ammonia molecules.